Charles University
Faculty of Science
Institute of Petrology and Structural Geology

Study program: Geology

Assembly of the Saxothuringian orogenic wedge: the Variscan *P–T–t* record of the metasediments of Erzgebirge, Bohemian Massif

Tvorba saxothuringického orogenního klínu: variský *P–T–t* záznam vývoje metasedimentů Krušných hor, Český masiv

MSc. Marine Jouvent

Doctoral dissertation

Supervisor: doc. Mgr. Ondrej Lexa, Ph.D.
Advisor: doc. RNDr. Petr Jeřábek, Ph.D.

Prague, 2022

Acknowledgments

This thesis would never become a reality without the large contribution and support from many people which I would like to thank here. I am very grateful to my supervisor Ondrej Lexa, who gave me the opportunity to work on this amazing topic and for being always available and reactive to discuss interpretations and tectonic ideas and for giving me a lot of freedom. I would like to thank my advisor Petr Jeřábek, who provided helpful suggestions, and for carefully reading and correcting the article manuscripts. This work would also be far away to be in this shape without the help and large contributions of Vít Peřestý who was always here to discuss geological processes or anything related to this work. I also would like to thank Stéphane Scaillet who supervised me in the lab during my stay in Orléans, and who gave me precious advice on the ^{40}Ar/^{39}Ar dating strategy and on results interpretation. Florian Duval is thanked for his patience to teach me the rudiments of the ^{40}Ar/^{39}Ar ages acquisition. Thank you to Andrew Kylander-Clark for having acquired a huge amount of monazite ages for this study, and for being very responsive and helpful with monazite data processing and interpretations. I am grateful to Martin Racek and Radim Jedlička for their help with microprobe and SEM analyses, for always having found some free schedule on EMPA or SEM lab, and for being very nice friends and company during many lunches. I would never have known about this PhD opportunity and started it without the support of Karel Schulmann, Anne-Sophie Tabaud and Pavla Stipska, who all gave me good geological background and support before starting this work. I am grateful to Pavel Pitra and Marion Tichomirova for the review of this thesis. Thank you also to Tomáš Fischer for giving me the access to the phyllite drill-core in Litoměřice. A děkuji mnohokrát to Dominika Linzerová and Radim Jedlička for Czech translation of the abstract.

Working at faculty was always a pleasant time thanks to the friendship of (by alphabetical order): Dominika best figure skating teacher, Drahu super secretary, Eliška the ballet dancer, Hezbullah, Honza the hockey-man master of tea, Igor Nikolaevitch, Karin the best italian cook, Kuba Vodička, a ty taky Kubo, Lena the plant lifesaver, Leta, Marketa, Martin the cheese amateur, Ondřej Krýza the snail lover, Petarda the croatian Pongrac, Radim the futur Tour de France winner, Rafael the portuguese wine amateur, Tadeáš the raclette guy, Tereza, Turbold, Vasek the cool farmer, Viktoria the drawing artist and Vítek the cerevenken turistev. I would also like to thank my french friends, especially my chicken (even if she unfortunately does not produce eggs), the VACARM, the conpotes and the friends I met in Strasbourg and in Pau, as well as my family, for their support during and before this PhD. And last but not least, I am very grateful to my boyfriend Cédric for his support, advice, love and patience during all this PhD period, and also for having washed all the dishes during this summer thesis writing!

This work was financially supported by the Grant Agency of The Czech Republic (GAČR 17-22207S), the Center for Geosphere Dynamics (UNCE/SCI/006) and the Grant Agency of Charles University (GAUK 384721).

Prohlašuji, že jsem závěrečnou práci vypracovala samostatně, a že jsem uvedla všechny použité informační zdroje a literaturu. Tato práce ani její podstatná část nebyla předložena k získání jiného nebo obdobného druhu vysokoškolské kvalifikace. Výsledky práce jsou produktem mé vlastní práce nebo práce ve výzkumném týmu.

V Praze dne 28.08.2022 . . . .

I declare that this thesis is a result of my own work and that I have cited all the resources and literature. Neither this thesis nor its substantial part has been submitted to fulfill requirements for any other academic degree. The results of the thesis are my own work or the product of collaboration with other members of the research team.

In Prague, 28.08.2022 . . . .

List of papers and authors contribution

This thesis is a monography combined with one published paper, one manuscript submitted and one manuscript in preparation. The candidate is the first author of all of them.

Published article in the *Journal of Metamorphic Geology*:

Jouvent, M., Lexa, O., Peřestý, V., & Jeřábek, P. (2022). New constraints on the tectonometamorphic evolution of the Erzgebirge orogenic wedge (Saxothuringian Domain, Bohemian Massif). *Journal of Metamorphic Geology*, 40(4), 687-715. https://doi.org/10.1111/jmg.12643

- The original article forms the part I of the thesis. The candidate was responsible for the fieldwork to obtain the structural data, field documentation, sampling, structural data processing, petrographic descriptions, collection of mineral analyses and pseudosection modelling. The candidate prepared the figures and the manuscript body with preliminary interpretations, which were then consulted with the co-authors. (Author's contribution 70%).

Manuscript submitted to *Tectonics*:

Jouvent, M., Lexa, O., Peřestý, V., Jeřábek, P. & Kylander-Clark, A. (submitted). Assembly of the Saxothuringian orogenic wedge: monazite U-Pb geochronology of the tectonic events of Erzgebirge metasediments (Bohemian Massif).

- This submitted manuscript is a major constituent of part II of the thesis. The candidate was responsible for the field work, field documentation, sampling, petrographic descriptions, collection of mineral analyses, mounts preparation, geochronological data and REE processing. The candidate prepared the figures and the manuscript body with early interpretations. The careful reading and modifications of the text were made by co-authors. (Author's contribution 60%).

Manuscript in preparation for a submission to *Geochimica et Cosmochimica Acta*:

Jouvent, M., Scaillet S., Lexa, O., Peřestý, V., & Jeřábek, P. (*in prep.*). The Saxothuringian orogenic wedge exhumation and reactivation: Evidence from mica ^{40}Ar/^{39}Ar geochronology in Erzgebirge (Bohemian Massif).

- The data and preliminary interpretations of this article in preparation are given in part II of the thesis. The candidate was responsible for the field work, field documentation, structural data processing, sampling, samples selection, petrographic descriptions, collection of mineral analyses, samples preparation before irradiation, sample dating in the ^{40}Ar/^{39}Ar laboratory and geochronological data interpretation. The candidate prepared the figures and manuscript body and the early interpretations were discussed with the co-authors. (Author's contribution 75%).

I certify that the above records are an accurate representation of the involvement of the candidate in the aforementioned research papers.

Signed:

Doc. Mgr. Ondrej Lexa, PhD.
Project supervisor

ABSTRACT

The formation of collisional orogenic wedges involves complex polyphase deformation and metamorphism. This study reveals the tectonic evolution, internal architecture and the timing of the Variscan orogenic wedge evolution in the Saxothuringian Domain (Bohemian Massif). The studied area is the Erzgebirge Crystalline Complex, characterized by numerous occurrences of the *(U)HP* rocks. In contrast, the surrounding metasediments have been scarcely studied, although they provide an important link between deep subduction and mid-crustal processes. Using field structural geology, petrology, thermodynamic modelling and geochronology (monazite U-Pb and mica ^{40}Ar/^{39}Ar dating), we constrained the *P–T* conditions and timing of four deformation events (D1-D4) identified by structural analysis. Several transects from the low-grade hanging wall phyllites to the footwall medium-grade micaschists have been investigated.

The first M1-D1 event is characterized by *HP–LT* minerals (garnet, chloritoid, phengite, paragonite, and rutile) defining the S1 foliation with an M1 peak pressure conditions increasing from 13 kbar and 520°C in phyllites to 25 kbar and 560°C in micaschists. The corresponding geothermal gradient of 6–11°C/km is typical for subduction environments. The M2-D2 event corresponds to the deformation and metamorphic overprint of the S1 fabric during partial decompression. The M3-D3 event is mainly developed in micaschists and becomes more intense towards the footwall. It is accompanied by the development of subhorizontal S3 cleavage and formation of *MP–MT* minerals (biotite, staurolite, muscovite and ilmenite). The M3 event reaches the peak temperature conditions of 5–9 kbar and 595°C representing a barrovian-type geothermal gradient of 17–30°C/km. Finally, all metamorphic fabrics were heterogeneously affected by the low-grade M4-D4 upright folding.

In order to link the ages with individual tectonometamorphic events, eight samples have been dated by monazite Laser-Ablation Split-Stream Inductively Coupled Plasma Mass Spectrometry and the ^{40}Ar/^{39}Ar geochronometer was used on micas to date 19 samples with CO_2-laser step-heating and *in-situ* UV-laser ablation. The resulting monazite ages and Rare Earth Elements patterns, coupled with white mica ^{40}Ar/^{39}Ar ages revealed that the phyllites experienced prograde metamorphism around 350 Ma followed by an exhumation at 345–340 Ma. The prograde *HP-LT* evolution in micaschists is constrained by large monazites in the matrix and oldest monazites enclosed in garnet core to be at least 339 Ma old. This suggests that the micaschists possibly entered the wedge slightly later than the phyllites. A following ductile thinning associated with the M3-D3 event was dated at 338–330 Ma. The monazite ages in micaschists and few ^{40}Ar/^{39}Ar ages in the deepest phyllites show that the region is then strongly affected by an event at ~330 Ma, interpreted as a lower-grade overprint during final exhumation or possible younger reactivation.

This study highlights the tectonic evolution marked by transition from the accretion of the subducted continental material to the building of the Saxothuringian orogenic wedge from ~360 to ~340 Ma. This process is manifested by thickening and partial exhumation within the wedge accompanied by ductile thinning in upper crustal levels. Finally, the late Variscan intracontinental deformation was responsible for orthogonal shortening, heterogeneous reactivation and final exhumation at 330 Ma. Based on our new data, we suggested that the Saxothuringian orogenic wedge could be divided into a younger inner part, formed by micaschists and *UHP* rocks, and an older outer part, formed by phyllites, both showing distinct metamorphic and structural evolution. The restoration of the wedge architecture reveals an early E-W zonation with *P–T* conditions increasing eastward and complexity of structural record as well as the change in lithology from units dominated by metasediments to units dominated by gneisses. The development of the current shape of the Erzgebirge antiformal dome resulted from subsequent orthogonal N-S shortening.

Keywords: Variscan orogeny, Saxothuringian orogenic wedge, Erzgebirge metasediments, thermodynamic modelling, monazite U-Pb and mica ^{40}Ar/^{39}Ar geochronology

ČESKÝ ABSTRAKT

Proces tvorby kolizních orogenních klínů zahrnuje komplexní polyfázovou deformaci a metamorfózu. Tato studie zkoumá tektonický vývoj, vnitřní stavbu a časový rámec vývoje variského orogenního klínu v saxothuringické doméně (Český masív). Studovanou oblastí je krušnohorský krystalinický komplex, charakterizovaný četnými výskyty *(U)HP* hornin. Ve srovnání s těmito horninami byly okolní metasedimenty studováni pouze okrajově, přestože představují důležité propojení mezi hlubokou subdukcí a procesy střední kůry. Za pomocí terénní strukturní geologie, petrologie, termodynamického modelování a geochronologie (datování monazitů pomocí U-Pb a slíd pomocí ^{40}Ar/^{39}Ar) jsme vymezili *P–T* podmínky a časové rozpětí čtyř deformačních událostí (D1-D4), které byly identifikovány strukturní analýzou. Bylo prozkoumáno několik profilů od nadložních slabě metamorfovaných fylitů až po středně metamorfované svory v podloží.

První deformační událost M1-D1 je charakterizována výskytem *HP–LT* minerálů (granát, chloritoid, fengit, paragonit a rutil), které definují foliaci S1 s podmínkami maximálního tlaku M1, zvyšujícími se od 13 kbar a 520 °C ve fylitech na 25 kbar a 560 °C ve svorech. Odpovídající geotermální gradient 6–11 °C/km je typický pro subdukční prostředí. Deformační událost M2-D2 odpovídá deformaci a metamorfnímu přetisku S1 stavby během částečné dekomprese. Událost M3-D3 je zachycena především ve svorech a její intenzita stoupá směrem do podloží. Je doprovázena rozvojem subhorizontální kliváže S3 a tvorbou *MP–MT* minerálů (biotit, staurolit, muskovit a ilmenit). Tato deformační událost dosahuje vrcholných P-T podmínek za 5–9 kbar a 595 °C, což představuje geotermální gradient barrovianského typu (17–30 °C/km). Za závěr byly všechny přítomné metamorfní stavby heterogenně postiženy kolmým vrásněním M4-D4.

Aby bylo možné přiřadit stáří k jednotlivým tektonometamorfním událostem, osm vzorků monazitů bylo datováno pomocí laserové ablace s indukčně vázanou plazmovou hmotovou spektrometrií a ^{40}Ar/^{39}Ar geochronometr byl použit na slídách k datování 19 vzorků pomocí *in-situ* UV-laserové ablace s postupným zahříváním CO_2 laseru. Výsledné stáří monazitů a variace prvků vzácných zemin ve spojení se stářím světlých slíd ^{40}Ar/^{39}Ar odhalily, že fylity prodělaly postupnou metamorfózu kolem 350 Ma, po níž následovala exhumace při 345–340 Ma. Postupný *HP-LT* vývoj svorů je zdokumentována na velkých monazitech v matrix, kdežto starší monazity, uzavřené v jádrech granátů,vykazují stáří minimálně 339 Ma. Tato data naznačují, že se svory staly součástí akrečního klínu o něco později než fylity. Následné duktilní ztenčování spojené s událostí M3-D3 bylo datováno na 338–330 Ma. Stáří monazitů ve svorech a několik ^{40}Ar/^{39}Ar stáří v nejhlubších fylitech poukázalo na silný vliv deformační události okolo 330 Ma na celý region, která je interpretována jako přetisk nižšího stupně během konečné exhumace nebo možné mladší reaktivace.

Tato studie vyzdvihuje tektonický vývoj, vyznačený přechodem od akrece subdukovaného kontinentálního materiálu k budování saxothuringického orogenního klínu mezi ~360 Ma a ~340 Ma. Tento proces se projevuje ztluštěním a částečnou exhumací uvnitř klínu doprovázenou duktilním ztenčením ve svrchních částech kůry. Závěrečná pozdně variská intrakontinentální deformace byla zodpovědná za ortogonální zkrácení, heterogenní reaktivaci a konečnou exhumaci okolo 330 Ma. Na základě našich nových dat navrhujeme rozdělení saxothuringického orogenního klínu na mladší vnitřní část, tvořenou svory a *UHP* horninami, a starší vnější část tvořenou fylity, přičemž obě části vykazují zřetelný metamorfní a strukturní vývoj. Restaurování stavby klínu odhalilo ranou E-W zonalitu s *P–T* poměry rostoucími směrem na východ, výraznou spletitost strukturního záznamu, a postupnou změnu v litologii od jednotek dominovanými metasedimenty, až po jednotky s převažujícími rulami. Vývoj Krušnohorského antiformního dómu do současné podoby vyplynul z následného ortogonálního zkrácení v S-J směru.

Klíčová slova: variská orogeneze, saxothuringický orogenní klín, krušnohorské metasedimenty, termodynamické modelování, slídová ^{40}Ar/^{39}Ar a monazitová U-Pb geochronology

TABLE OF CONTENTS

PART II: ASSEMBLY OF THE SAXOTHURINGIAN OROGENIC WEDGE: GEOCHRONOLOGY

PREFACE

1 - INTRODUCTION

1.1 - OROGENIC WEDGE ASSEMBLY: THE EXAMPLE OF ERZGEBIRGE IN THE SAXOTHURINGIAN DOMAIN

The collisional orogens are an impressive manifestation of plate tectonics (Beaumont et al., 1996; Malavieille, 2010). It involves pre-collisional subduction of the oceanic lithosphere with the formation of accretionary prism, development of orogenic wedge (Dahlen, 1984; Linnemann et al., 2008; Platt, 1986; Willett et al., 1993), formation and exhumation of ultra-high-pressure *(UHP)* rocks and the subduction of crustal material (Beaumont et al., 1996; Burov et al., 2014; Sizova et al., 2014). However, the building and evolution of collisional orogens is very complex. The study of metamorphic rocks is a key for the comprehension of the assembly of orogenic wedges as they well-preserve the geothermal gradients, which are contrasting for the subduction and subsequent collisional evolution. Additionally, the metamorphic rocks record important parameters such as depth of burial, peak metamorphic conditions and allow to reconstruct prograde/retrograde *P–T* paths which combined spatially provide an information about lateral metamorphic field gradients, all of which critically constrain tectonic settings and crustal architecture (Jamieson et al., 2002; Peacock, 1987; Spear, 1993). Among the metamorphic rocks that are usually present in orogenic wedges, the metasediments are sensitive enough to trace the changes of *P–T* conditions over time and thus provide an important link between deep subduction and mid-crustal processes. However, many of the studies are commonly focused on rocks recording the extreme *P–T* conditions, while their link to the rock at middle and upper crust is commonly neglected in the literature. This is also the case of Erzgebirge, where investigation of *P–T–t* evolution of low- to medium-grade metasediments in link with the surrounding

(U)HP rocks is still missing, despite it has a potential to bring important knowledge on the tectonic evolution of the Variscan belt and on other orogens worldwide.

The Saxothuringian Domain in the European Variscan belt is a spectacular example of plate convergence with the subduction of the Saxothuringian lower-plate under the hanging wall Tepla-Barrandian Domain (Franke, 1989; Kroner et al., 2007; Schulmann et al., 2014; Willner et al., 1997, 2000). The record of the resulting Saxothuringian orogenic wedge is present in the Erzgebirge Crystalline Complex. Many authors studied this complex in the past decades but the whole wedge assembly is still controversial. While the Saxothuringian *(U)HP-HT* rocks of have been frequently studied, the extent of their shared evolution with the overlying lower-grade metasediments has been only scarcely explored (Faryad & Kachlík, 2013; Roetzler et al., 1998; Rahimi & Massonne, 2018, 2020). In addition, the geochronological link of the two contrasting domains remains unresolved.

1.2 - ERZGEBIRGE DICHOTOMY AND AIMS OF THE STUDY

The complex present-day geometry of the Saxothuringian orogenic wedge raises several questions which we tried to answer in this study.

The Erzgebirge complex forms an antiformal dome structure with units appearing in concentric zones. The dome is composed of high-grade rocks on the core overlain by low-grade metasediments on the dome envelope (Figure 0.1). The area comprises a sequence of units as follows, from the structurally higher to the structurally lower units, i.e. from the hanging-wall to the foot-wall: low-grade (Garnet)-Phyllite Unit, medium-grade Micaschist/Eclogite Unit, high-grade Gneiss/Eclogite Unit, and medium-grade parautochton or Red-and-Grey gneisses (Figure 0.1). The envelope of the Erzgebirge dome is composed of the structurally higher allochthonous units, and the core of the dome is made of the deeper units. Such spatial arrangement of individual units created an uncommon pattern of metamorphic field gradients (Figure 0.1). Indeed, from the envelope to the core, a normal metamorphic zoning is observed with low- and medium-grade metasediments above high-grade gneisses (Kröner et al., 1995; Schmädicke & Evans, 1997; see the arrow for normal metamorphic zoning in Figure 0.1). However, towards the Erzgebirge core, the high-grade gneisses are above the medium-grade parautochton creating an inverted metamorphic gradient (Hallas, 2020; Kryl et al., 2021; Schmädicke et al., 1995; Werner & Lippolt, 2000;

Willner et al., 2000; see the arrow for inverse metamorphic zoning in Figure 0.1). This complex spatial distribution of normal and inverted metamorphism created a dualism in the definition of the tectonic evolution in Erzgebirge and led to different interpretations of the orogen assembly and its evolution. Several authors interpreted the Erzgebirge dome as a gneiss dome developed during extensional unroofing (Kröner & Willner, 1998; Willner et al., 2000) or as a metamorphic core complex (Kröner et al., 1995; Schmädicke & Evans, 1997; Seifert & Sandmann, 2006; Tichomirowa & Köhler, 2013). Franke & Stein (2000) affirm that the Erzgebirge antiform is the result of a late compressive feature, and not an extensional core complex. Other authors (Konopásek et al., 2001) associated the doming with a large scale folding of a nappe stack of *HP* units assembled during exhumation from the subduction channel, and a channel exhumation model is favored also by Hallas et al. (2021). One of the aims of this study is to understand why we nowadays observe an apparent normal metamorphic zoning in a subduction environment. Indeed, even if normal metamorphic gradient in antiformal nappe stacks was also reported from other complexes of continental subduction (Agard & Vitale-Brovarone, 2013; Plunder et al., 2012; Brovarone et al., 2013), the accretionary wedges are usually related to inverted metamorphic gradients (Peacock, 1987).

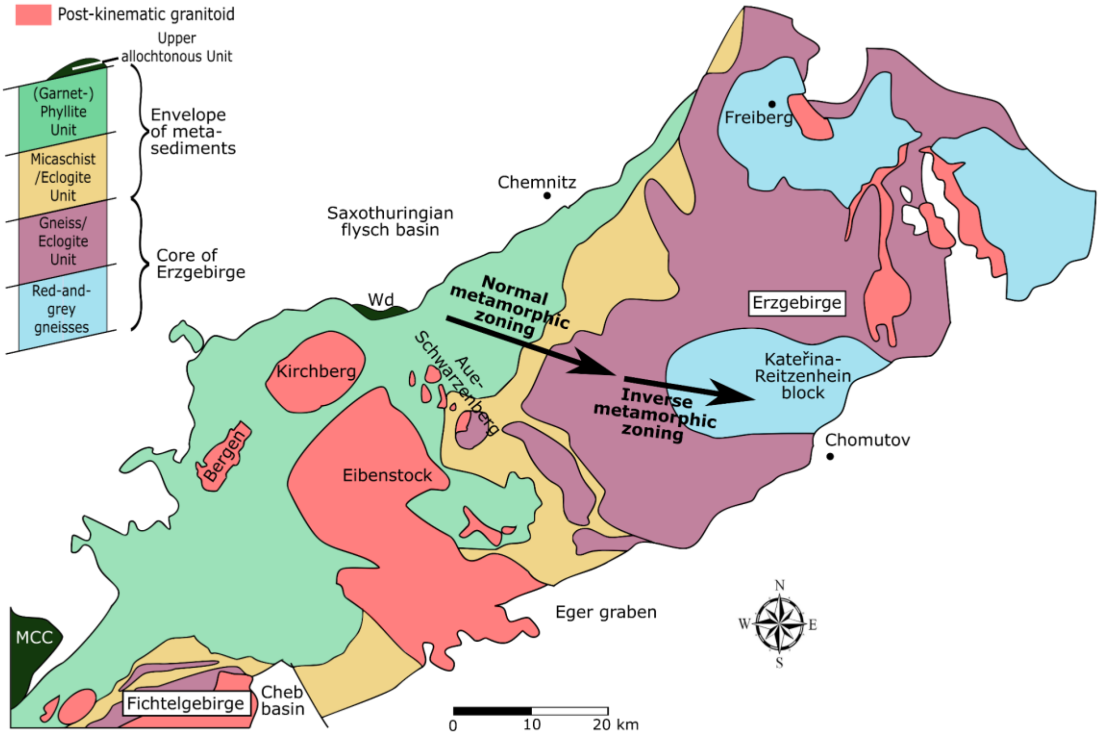

Figure 0.1: Simplified geological map of the Erzgebirge and Fichtelgebirge with the structural position of the main units. The metamorphic field gradients (normal and inverted) are schematically shown by the two arrows. MCC: Münchberg Crystalline Complex; Wd: Wildenfels Massif. Modified after Werner & Lippolt, 2000.

The overall architecture of the units with low-grade metasediments lying on top of high-grade gneisses is generally accepted in Erzgebirge literature (Figure 0.1; Faryad & Kachlík, 2013; Mingram, 1998; Rahimi & Massonne, 2018, 2020; Roetzler et al., 1998; Schmädicke et al., 1992; Werner & Lippolt, 2000). However, the nature of the contact in between these units and the tectonic processes proposed to explain such current architecture does not reach a consensus. The rock sequence is sometimes characterized by nappe stacking followed by extensional collapse. Roetzler et al. (1998) suggested that the entire micaschists unit represents a major detachment horizon. Schmädicke & Evans (1997) proposed that the contact between high-grade crystalline units and overlying low-grade sequences can be explained by tectonic juxtaposition, probably along an extensional detachment as typical of metamorphic core complexes. Hallas et al. (2021) suggests a pre-orogenic nappe stacking, followed by a channel exhumation flow nowadays overlain by the Kateřina-Reitzenhein parautochton and by the micaschists. Such ideas are based on knowledge from Himalaya and from other orogens (Beaumont et al., 2001; Godin et al., 2006; Grujic, 2006; Jamieson et al., 2002), where the channel extrusion could result in an inverted metamorphic zonality below the channel and in a normal zonality above the channel. As shown in the south Qiangtang terrane in Tibet, (Li et al., 2022; Zhao et al., 2014, 2015, 2017, 2020), the rocks could also be exhumed by pulling out of a slab, (e.g. due to the rolling back of another slab backward of the subduction zone), instead of an exhumation in a subduction channel.

The above mentioned highly contrasting tectonic models proposed for the Erzgebirge area raise following major questions, which are being answered in this thesis:

- What is the nature of contacts between different units of different metamorphic grades?
- How were these units juxtaposed?
- How was the whole orogenic wedge built?
- More tectonic questions…..

To answer these questions, several in-depth problems have to be resolved:

- Which tectonometamorphic events can be recognized in the Erzgebirge metasediments?
- What are the *P–T* conditions of each of these tectonic events?
- How similar is the metamorphic history in the metapelites and the surrounding units?

- What is the timing of the individual events in each unit?
- What was the former spatial position and depth reached by each unit in the accretionary prism and/or orogenic wedge?

This study brings a new view on the orogenic evolution in the Saxothuringian Domain, which can be adapted to other orogens worldwide. The structural and metamorphic evolution of the area is described in part I of the thesis, and part II shows the timing of the individual event and proposes a tectonic model and geometry of the Saxothuringian orogenic wedge.

1.3 - MULTIDISCIPLINARY APPROACH

The study of complex orogenic systems with polyphase deformation and juxtaposition of contrasting rock units requires the use of a multidisciplinary approach. The use of one or two approaches only or the restriction to only one rock type or one deformation event can lead to contrasting interpretations (channel exhumation flow, metamorphic core complex, nappe stacking and extensional collapse, etc).

This work is the combination of several methods comprising field and structural geology, petrology, geochemistry, phase-equilibria modelling and geochronology (monazite U-Pb and mica $^{40}Ar/^{39}Ar$ dating). Almost 300 outcrops have been documented. About 200 rock pieces have been studied petrographically and ~50 of them were analyzed on Secondary Electron Microscope (SEM) or electron microprobe. The most important representative samples are described and summarized in Table 0.1, together with an overview of results.

It can be noticed that we faced some challenges by using a multidisciplinary approach, and sometimes even during the use of one method itself. To link the results obtained by various methods, a single selected sample was studied with as many methods as possible. However, not all the samples were suitable for all of the available methods (Table 0.1). In addition, the use of monazite U-Pb geochronology by LASS-ICP-MS (Laser-Ablation Split-Stream Inductively Coupled Plasma Mass Spectrometry), which allows very precise dating of monazites *in-situ* together with the acquisition of Rare Earth Elements (REE) from the same volume of mineral, did not allow us to date the tiny monazites present in inclusion in the garnet core as their size was lower than 7 µm. Similarly, it was sometimes not possible to measure by electron microprobe the composition of tiny minerals like paragonite or muscovite in extremely fine-grained phyllite samples or garnet inclusions, leading to potential lack of information to determine *P–T* conditions. The too small size of muscovites was also prejudicial to date extremely fine-grained phyllites samples from the north-west of the phyllite unit with the ^{40}Ar/^{39}Ar geochronology. The use of the K/Ar geochronometer would be necessary and can be considered for future work.

Distance to Erzgebirge high-grade core	Sample	Unit	Lithology	Method					Mineralogy																				P-T conditions + Monazite U-Pb dating						Mica Ar-Ar dating
				P-T modelling	Monazite U-Pb dating		Mica Ar-Ar dating		q	g	mu	bi	pa	ma	ctd	st	chl	ru	ilm	ab	ksp	cal	ep	all	mag	sph	hem	tur	M1				M2 matrix	M3/M4 matrix	
					in mount	in thin-section	by step-heating	by in-situ																					g core	g rim I	g rim II	M1 matrix			
Close to Erzgebirge meta-sediments	MJ44	Phyllite	ctd phyllite	X	X				x		x		x		x		x	x	x													13 kbar, 520°C 340.8 ± 1.1 339.7 ± 1.0			
	MJ182		chl phyllite		X				x		x		x				x	x	x									x				350.0 ± 1.1 345.3 ± 1.2			
↓	MJ69G		chl phyllite				X		x		x						x	x	x																343.1 ± 1.1
	MJ52		ctd phyllite		X		X		x		x		x		x		x	x	x													349.6 ± 1.1 347.7 ± 0.8			343.4 ± 1.3 340.0 ± 0.9
	MJ22		ab phyllite				X	X	x		x						x	x	x	x		x						x							333.2 ± 3.3 332.6 ± 3.5
	MJ92C		chl phyllite				X		x		x		x				x	x	x																328.9 ± 0.4
	S3		chl-ab phyllite				X		x		x		x				x	x	x	x								x							328.2 ± 0.5 325.7 ± 0.7 330.7 ± 0.6
	MJ46E		ab-chl phyllite				X		x		x		x				x	x	x	x															324.8 ± 0.6
	MJ6D		quartzitic g phyllite	X					x	x	x				x		x	x	x										10-15 kbar, 460-500°C	12-20 kbar, 480-530°C			8-10 kbar, 490-550°C		
	MJ213A	Micaschist	ep micaschist				X		x		x		x	x			x	x	x	x			x	x	x										332.8 ± 0.5
	MJ218A		ctd-g micaschist	X		X			x	x	x	x	x		x		x	x	x										11-15 kbar, 480-510°C	12-15 kbar, 500-530°C 338.7 ± 2.4	24-26 kbar, 555-570°C 333.7 ± 2.0	333.5 ± 1.7	15-18 kbar, 545-565°C	9 kbar, 580°C 326.0 ± 1.8	
	MJ216		g micaschist				X		x	x	x	x					x	x	x	x															327.8 ± 0.5
	MJ58		st-g micaschist	X	X	X			x	x	x	x	x		x	x	x	x	x									x	12-15 kbar, 480-510°C	13-16 kbar, 510-535°C 331.0 ± 1.0	18-21 kbar, 565-580°C	338.1 ± 0.7 334.6 ± 1.1	13-17 kbar, 545-605°C	5-8 kbar, 550-595°C 329.6 ± 1.4	
	MJ11		quartzitic g micaschist			X	X	X	x	x	x	x			x		x	x	x											336.0 ± 2.2	334.0 ± 1.2			328.7 ± 0.8	330 ± 0.5 335 ± 0.3
	MJ62		g micaschist			X	X		x	x	x	x	x		x		x	x	x	x	x						x	x		330.7 ± 1.9	330.3 ± 1.9	330.8 ± 0.9		330.7 ± 1.3	327.6 ± 0.6
Close to Erzgebirge core	MJ61B	Gneiss	g paragneiss				X		x	x	x	x					x	x	x	x	x					x									335.7 ± 0.6 320.2 ± 0.5 (bi)
	MJ212		orthogneiss				X		x		x	x	x	x			x	x	x	x	x														329.1 ± 0.6

Table 0.1: Simplified sample description and summary of the results of this thesis involving petrography, *P–T* modelling, monazite U-Pb dating and mica ^{40}Ar/^{39}Ar dating.

2 - STRUCTURE OF THE THESIS

This thesis comprises two parts. It first presents the tectonometamorphic evolution of the metasediments of the Erzgebirge Crystalline Complex, essential in understanding the tectonics of the whole wedge and similar orogens. The second part details the assembly, exhumation and reactivation of the Saxothuringian wedge and its timing using monazite U-Pb and mica $^{40}Ar/^{39}Ar$ geochronology. The first part is self-contained and independent and the second part uses results and interpretations from the first part.

The figures and the tables of the thesis are labeled as follows: the first letter corresponds to the number of the chapter (i.e. preface, part I or II), followed by the number of the figure itself in the chapter. The figures in the preface start by “0”. For example, the figure 0.8 corresponds to the figure 8 of the preface, and the figure II.12 corresponds to the figure 12 of the part II. The tables from the appendix are numbered starting by “S”, followed by the number of the corresponding chapter and then the number of the table itself (e.g. Table S.II.2 for the table 2 refered in the part II in the appendix).

Part I: New constraints on the tectonometamorphic evolution of the Saxothuringian orogenic wedge

The first part of the thesis describes the structure and evolution of the Saxothuringian wedge. The metasedimentary rocks are carefully studied and combine data from structures, microstructures, petrology, mineral chemistry, mineral assemblage and phase-equilibria modelling. These new data are compared with existing literature on the study area. The new results associate detailed structural and metamorphic data on the metasediments, and bring progress for the geological understanding of the Saxothuringian orogenic wedge, which can be applied to other orogens. Here for the first time, the tectonometamorphic evolution of the metasediments is described in detail and is linked with the formation and evolution of the whole Saxothuringian wedge, explaining the position of each unit in the wedge and the present-day spatial arrangement of the units, apparently incoherent with a subduction environment. This part was published as an article in the Journal of Metamorphic Geology (Jouvent et al., 2022) and is presented in an unchanged form, apart from the abstract, which was removed, and from the geological setting, which is extended in the section 3 of the Preface.

Part II: Assembly of the Saxothuringian orogenic wedge: geochronology

The second part of the thesis focuses on the Saxothuringian orogenic wedge assembly and its timing (prograde, peak metamorphism, exhumation and reactivation). It is based on the first part of the thesis keeping the logic of distinguished successive tectonometamorphic events and inferred *P–T* paths. The tectonic and metamorphic evolution of the wedge is fit into the time framework using the strength of detailed *in-situ* monazite U-Pb geochronology performed by LASS-ICP-MS, and mica ^{40}Ar/^{39}Ar geochronology. This part brings for the first time a complete dating on the metapelites with 8 samples (phyllites and micaschists) dated by monazite U-Pb and 19 samples dated by step-heating and *in-situ* ^{40}Ar/^{39}Ar geochronology. The process of Saxothuringian wedge building, exhumation and reactivation is discussed and a zoning of the wedge is shown. This part covers the topics from a manuscript submitted to Tectonics (based on data from the monazite U-Pb dating) and from a manuscript in preparation (based on data from the mica ^{40}Ar/^{39}Ar dating).

3 - GEOLOGICAL SETTING

3.1 - THE VARISCAN BELT

The Variscan belt is a collisional orogen formed during the Paleozoic by the closure of the Rheic Ocean and long-lasting convergence of the paleocontinents Laurentia, Baltica and Gondwana (Nance et al., 2012; Schulmann et al., 2014; Figure 0.2).

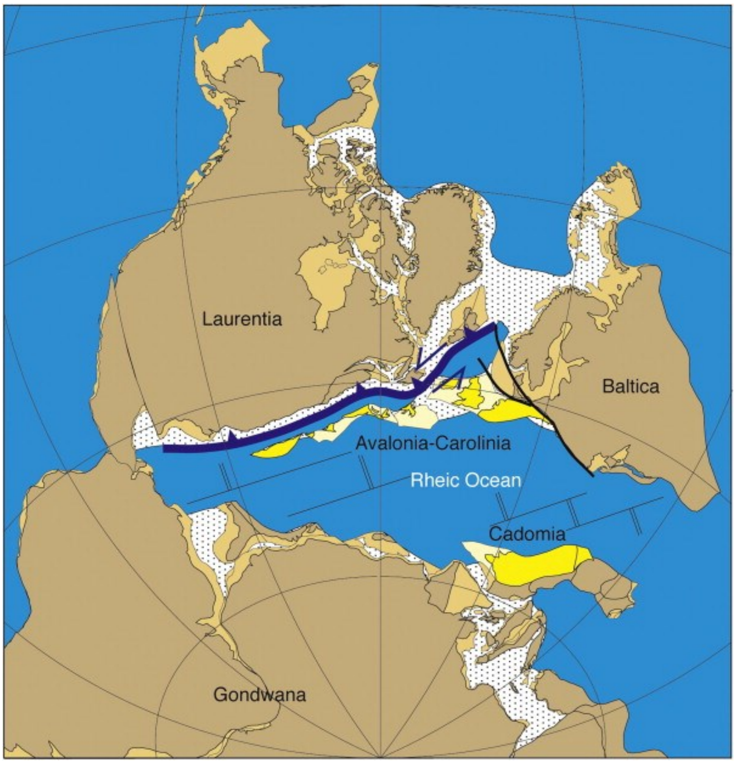

Figure 0.2: Early Silurian reconstruction of the Rheic Ocean immediately prior to the closure of Iapetus by way of subduction (toothed purple line) beneath Laurentia. From Nance et al., 2012.

Following the closure of the Iapetus Ocean during the Silurian, the opening of the Rheic Ocean caused the rifting of Avalonia (Nance et al., 2010) and the development of a large continental passive margin, the Peri-Gondwana, at the southern shelf of the Rheic Ocean. The Peri-Gondwana was heterogeneously extended and separated in Cadomian blocks of thinned and mostly juvenile continental crust, i.e. the Armorican Terrane Assemblage (Franke, 2000; Nance & Murphy, 1994). The closure of the Rheic Ocean and the continent-continent collision of the Gondwana and Laurussia (Laurentia-Baltica-Avalonia) plates formed the Variscan belt and final assembly of the Pangea supercontinent (Kroner & Romer, 2013; Muttoni et al., 2003; Nance, 2022). The main orogenesis occurred in late Devonian and Carboniferous and formed a large and heterogeneous orogen. The central part represented by European Variscides is traditionally interpreted as a result of two zones of subduction on the northern flank and one on the southern flank of the belt (Figure 0.3; Franke, 2006; Massonne, 2005; Schulmann et al., 2014). In the literature, there is still a debate about the number of oceans, the subduction direction, the geodynamic views, etc, to explain the Variscan collision (Franke, 2000; Franke, 2006; Kroner & Romer, 2013; Matte, 1986; O'Brien, 2000; Zeh & Gerdes, 2010; Figure 0.3).

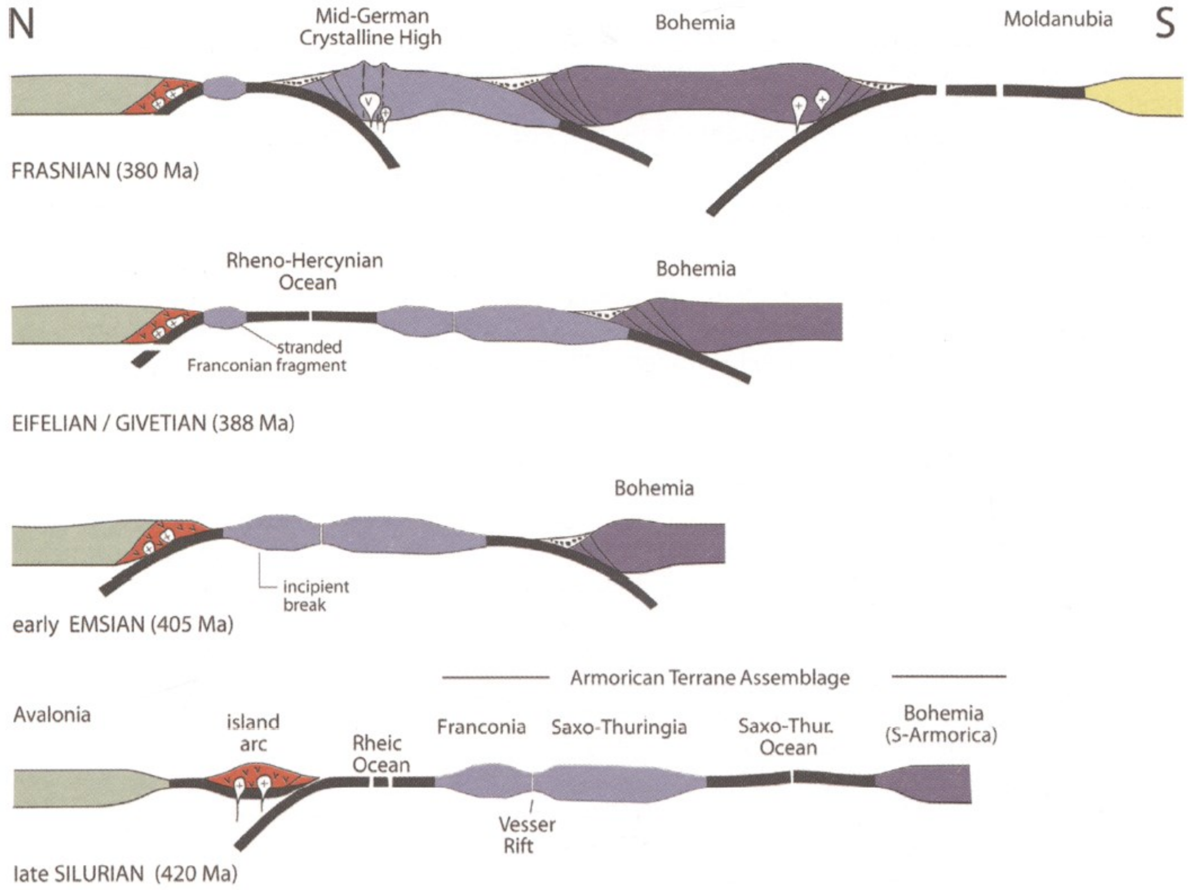

Figure 0.3: Evolution of the major and minor plates of the European Variscides (from Franke, 2006) over time. The Bohemia terrane corresponds to the NE margin of the Teplá-Barrandian unit.

3.2 - THE VARISCAN BELT IN CENTRAL EUROPE

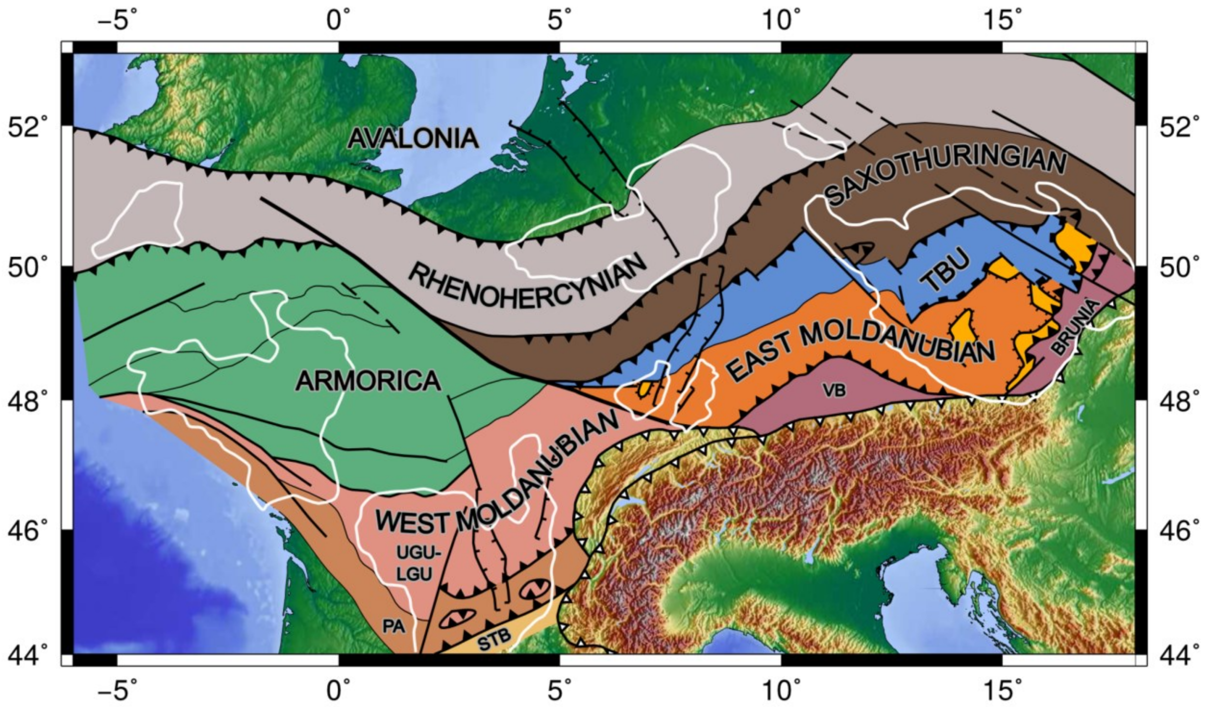

Figure 0.4: Simplified geotectonic map of the European Variscides with positions of terranes, main sutures, and thrust zones. White outlines show positions of Variscan outcrops. TBU = Teplá-Barrandian Unit; North-Gondwana-derived blocks: Brunia and VB = Vindelicia (modified after Maierová et al., 2016).

In Europe, the Variscan belt is preserved in many areas from the Iberian Peninsula on the West to the Bohemian Massif on the East, including the French Massif Central, the Vosges, the Ardennes, the Armorica, etc. It is the bedrock of several sedimentary basins (e.g. Parisian or Aquitaine basins) and the basement of more recent mountain chains (Alps, Pyrenees, Carpathians, Sardinia, Algeria, etc). The European Variscan belt consists of several blocks of at least Paleozoic age, resulting from successive convergence of microplates. From the North to the South, these blocks are the Westphalian, the Rhenohercynian, the Mid-German Crystalline High, the Saxothuringian, the Teplá-Barrandian, the Moldanubian and the Brunovistulian (Figures 0.3, 0.4 and 0.5; Franke, 2006; Konopásek et al., 2001; Kossmat, 1927).

3.3 - THE SAXOTHURINGIAN DOMAIN AND THE ERZGEBIRGE REGION

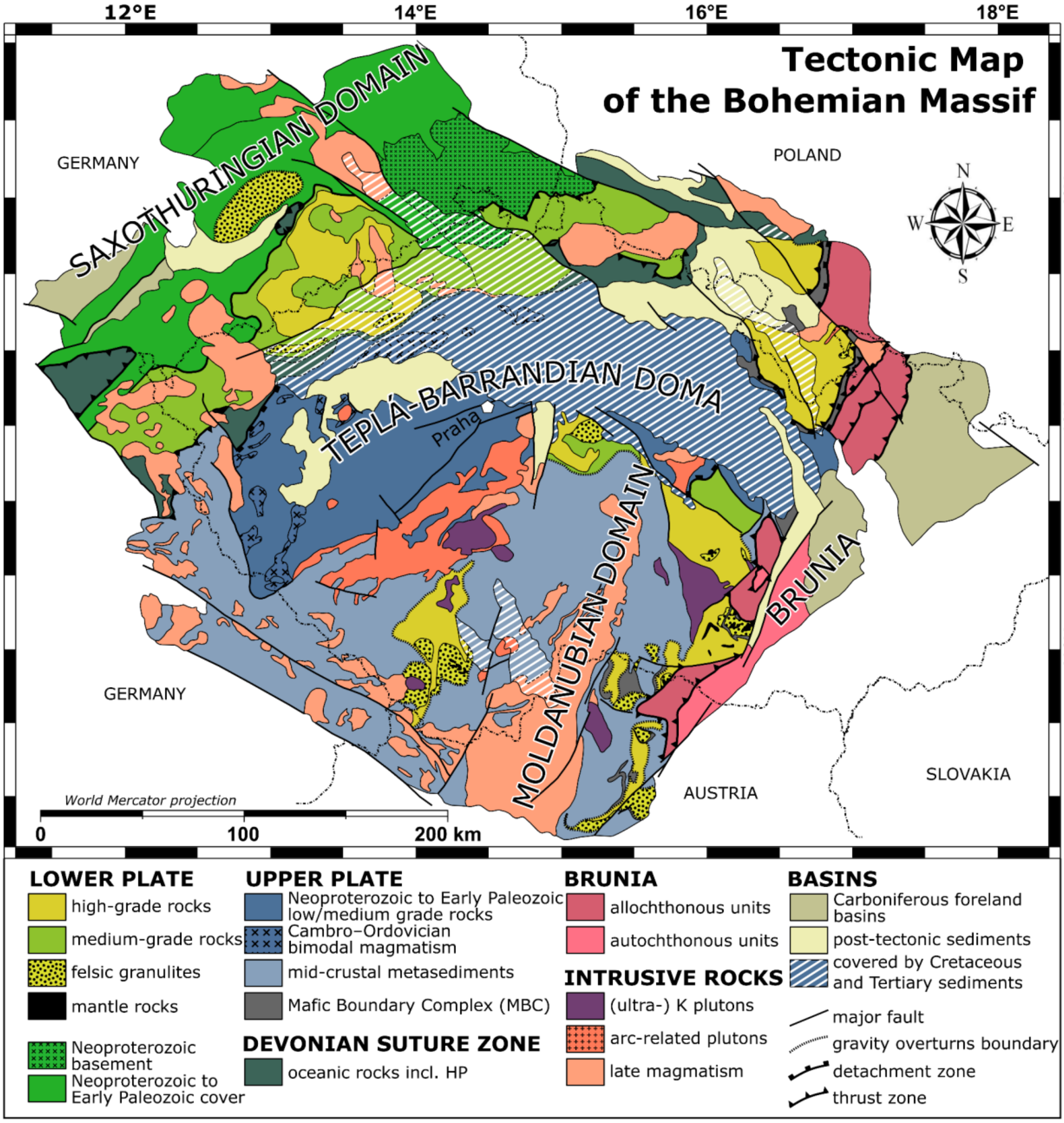

Figure 0.5: Tectonic map of the Bohemian Massif (modified after Schulmann et al., 2014). Lower plate tectonic units are autochthonous (SaxoThuringian domain, dark green) or allochthonous (SaxoThuringian and Moldanubian domains, light green-yellow). Upper plate tectonic units are represented by supracrustal rocks (Teplá-Barrandian domain, dark blue), medium-grade mainly metasedimentary rocks (Moldanubian domain, light blue) and Cambrian–Ordovician mafic boundary complex (dark gray).

The Bohemian Massif in Central Europe represents a large segment in the East of the Variscan belt. It is subdivided in the Saxothuringian, the Teplá-Barrandian and the Moldanubian Domains (Figures 0.4 and 0.5). The Saxothuringian Domain is subducted underneath the Teplá-Barrandian Domain (Figures 0.3, 0.4 and 0.5). The *HP-UHP* rocks of the Saxothuringian mark the major Variscan suture with the hanging-wall (Franke, 1989; Kroner et al., 2007; Schulmann et al., 2014; Willner et al., 1997, 2000; Figure 0.5), marked by occurrences of eclogites, blueschists, coesite- or diamond-bearing paragneisses and granulites (Collett et al., 2017; Faryad & Kachlík, 2013; Klápová et al., 1998; Konopásek & Schulmann, 2005; Kotková & Janák, 2015; Kotková et al., 2011; Massonne, 2005; Massonne et al., 2007; Nasdala & Massonne, 2000; Schmädicke et al., 1992; Schmädicke et al., 1995; Závada et al., 2018; 2021).

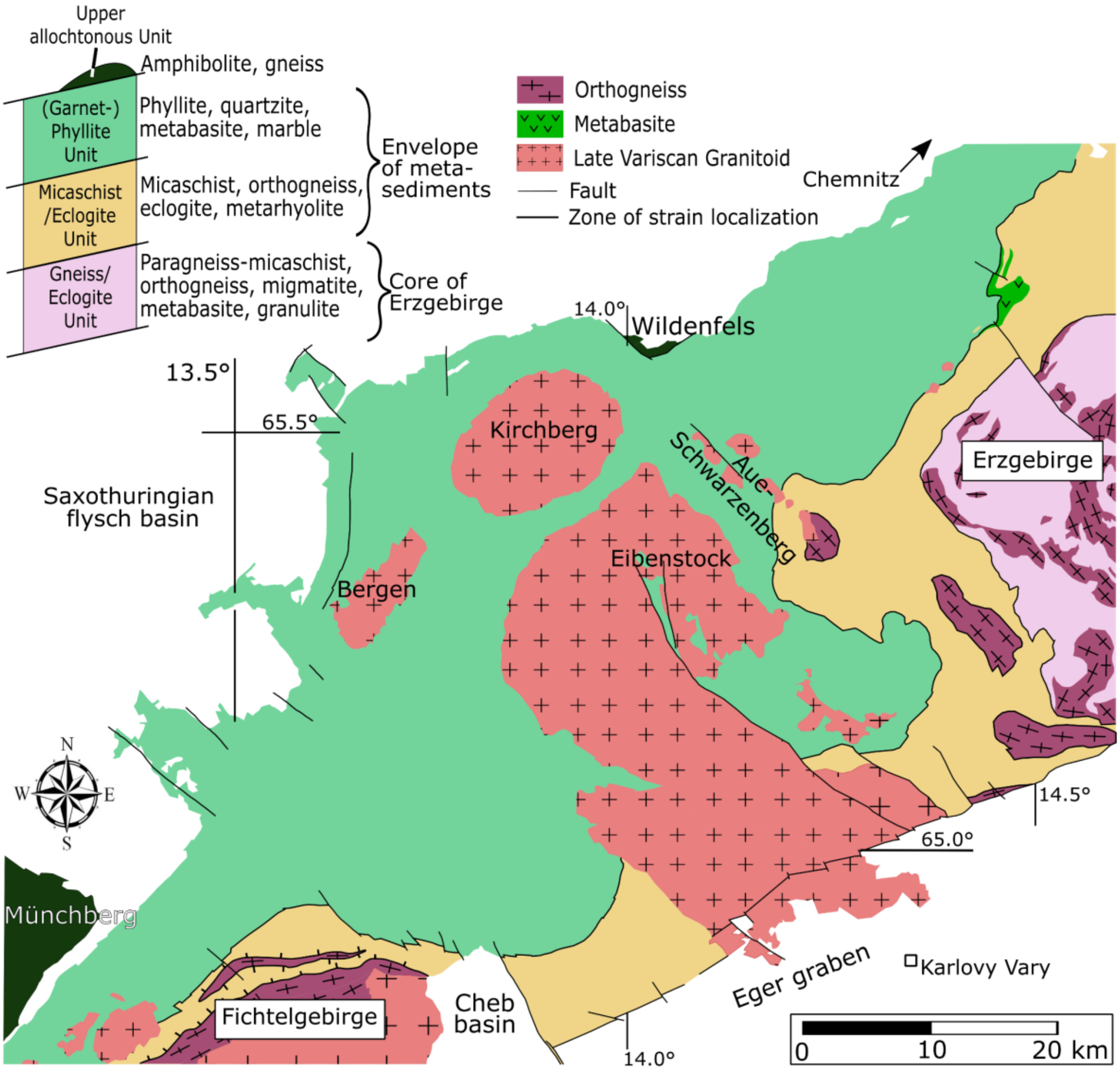

Figure 0.6. Simplified geological map of the Erzgebirge and Fichtelgebirge with structural position of the main units and name of the main granites.

The studied area covers the Erzgebirge (Krušné Hory in Czech), Fichtelgebirge and Elstergebirge in the Saxothuringian Domain (Figures 0.1 and 0.6) and is composed of various orthogneisses and metamorphosed volcano-sedimentary sequence. The protolith age of the orthogneisses in Central Erzgebirge is debated. Like for the micaschists, some authors reported gneisses protolith ages around 480–500 Ma (Collett et al., 2020; Mingram, 1998; Mingram et al., 2004; Kosler et al., 2004; Tichomirowa, 2003) while older ages of ~540–550 Ma were found from the orthogneisses of the Central and Eastern Erzgebirge (Kröner et al., 1995; Mingram et al., 2004; Tichomirowa & Köhler, 2013). The protolith age of the cadomian basement is about 550 Ma (Kröner et al., 1995; Mingram, 1998). The metasediments comprise phyllites, micaschists and paragneisses intercalated by metaconglomerates, quartzites, amphibolites and marbles (Figure 0.6). To the northwest, the Erzgebirge area is flanked by post-Devonian sediments of the Saxothuringian flysch basin (Schäfer et al., 1997) and to the southeast by the Tertiary Eger graben (Figures 0.1 and 0.6). The Erzgebirge forms a large-scale anticlinorium or dome, where the individual units appear as concentric zones (Lorenz & Hoth, 1990; Pietzsch, 1954). The core of the Erzgebirge dome is a medium-grade parautochthonous orthogneiss-dominated unit overlain by medium to high-grade orthogneiss, paragneiss and metabasite bodies of the allochthonous units (Figures 0.1 and 0.6). Based on the metamorphic grade and lithostratigraphy, the Erzgebirge complex was subdivided into several tectonometamorphic units (Rötzler & Plessen, 2010; Schmädicke et al., 1992). From the core to the envelope of the Erzgebirge dome (i.e. from the structurally lower to the upper units), these are (Figures 0.1 and 0.6):

- The Cadomian basement parautochton also called Red-and-Grey Gneiss Unit or Granite-Gneiss Amphibolite Unit (GAU), including the Kateřina-Reitzenhein block. It was metamorphosed at 7–13.5 kbar and ~600–820°C (Kröner et al., 1995; Kryl et al. 2021; Mingram, 1998; Roetzler et al., 1998; Willner et al., 1997).
- The lower allochthon Gneiss/Eclogite Unit (GEU) which comprises the GEU I with *HP* rocks and the GEU II with *UHP* rocks (Rötzler & Plessen, 2010; Schmädicke et al., 1992). The neighboring *UHP* Eger Crystalline Complex (ECC) is part of the GEU II (Konopásek & Schulmann, 2005) and the two complexes – the GEU I and GEU II – alternate in space (Kryl et al., 2021). The GEU I is metamorphosed at *HP* conditions (24–26 kbar and 650–750 ◦C; Hwang et al., 2001; Massonne, 1999; Schmädicke et al., 1992) and the GEU II at *UHP* conditions (~29-60 kbar and ~850-1100°C; Hwang et al., 2006; Kotková et al., 2011; Massonne & Nasdala, 2003; Nasdala & Massonne,

2000; Rötzler et al., 2008; Schmädicke et al., 1992) as highlighted by the presence of diamond and coesite.

- The middle allochthon Micaschist/Eclogite Unit (MEU) metamorphosed up to 26 kbar and 615–700 °C (Collett et al., 2017; Gross et al., 2008; Klápová et al., 1998; Konopásek, 2001; Kulhánek et al., 2021; Rahimi & Massonne, 2018, 2020; Roetzler et al., 1998; Schmädicke et al., 1992).
- The upper allochthon Garnet-Phyllite Unit (GPU) and the Phyllite Unit (PU) metamorphosed at 2–15 kbar and 300–470 °C (Faryad & Kachlík, 2013; Roetzler et al., 1998).
- The uppermost allochthon crystalline complexes of Münchberg or Wildenfels Massifs (Fazlikhani et al., 2022; Stosch & Lugmair, 1990).

Using U-Pb zircon, monazite and rutile, Sm/Nd garnet-whole-rock and Pb-Pb zircon evaporation, many geochronological studies constrained the age of *HP* metamorphism in Erzgebirge to 340 Ma (Kotková et al., 1996; Kröner & Willner, 1998; Kylander-Clark et al., 2013; Massonne et al., 2007; Schmädicke et al., 1995; Tichomirowa et al., 2005, Tichomirowa & Köhler, 2013). This age overlaps partly with ^{40}Ar/^{39}Ar white mica and hornblende cooling ages constrained to 340–330 Ma (Werner & Lippolt, 2000; Hallas et al., 2021). Recent U-Pb zircon and monazite dating of Schmädicke et al. (2018) and Závada et al. (2021) correlated the 345–330 Ma age with the exhumation/retrogression at amphibolite facies conditions, while the pressure peak is constrained to 360-350 Ma. In the Münchberg klippe in the north-west of the studied region, the metamorphic age is at mid-devonian (Fazlikhani et al., 2022; Stosch & Lugmair, 1990).

The studied region was later intruded by large post-kinematic granite intrusions (granites of Eibenstock, Kirchberg, Bergen, magmatic suite of Aue-Schwarzenberg; Figures 0.1 and 0.6) at 325–314 Ma (Förster et al., 1999; Romer et al., 2007; Štemprok et al., 2008; Tichomirowa et al., 2019). Gerstenberger et al. (1982) and Tichomirowa & Leonhardt (2010), using respectively Rb–Sr mica isochrons and zircon evaporation, reported older ages up to 328–329 Ma for the emplacement of the Aue-Schwarzenberg granite suite and the Eibenstock granite. However, further and more precise geochronological investigations on the magmatic activity deny these oldest ages (Gerstenberger, 1989; Velikhin et al., 1994; Werner & Lippolt, 1998, Tichomirowa et al., 2019) and the oldest age of the granites emplacements is set at ~325 Ma. This corresponds to the first major period of Variscan magmatic activity in

Erzgebirge, but younger magmatic intrusions occurred at 280–300 Ma (Carl & Wendt, 1993; Förster et al., 2007; Kempe et al., 2004; Siebel et al., 2010).

3.4 - NOMENCLATURE OF THE STUDIED UNITS

Our study focuses exclusively on the metapelitic rocks occurring along the transitional boundary between the footwall Micaschist/Eclogite Unit and the hanging-wall (Garnet)-Phyllite Unit (Figures 0.1 and 0.6). In this study we refer to phyllites as to the biotite-free fine-grained metapelites of the (Garnet)-Phyllite Unit and to micaschists as to the biotite-garnet-bearing medium-grained metapelites of the Micaschist/Eclogite Unit.

4 - METHODS AND MINERAL ABBREVIATIONS

To understand the polyphase deformation and metamorphism affecting the different lithologies of the Erzgebirge region, a multi-disciplinary approach is essential. To apprehend the complex structural record and variable metamorphic response of the area and to characterize the tectonic evolution, an interconnection between structural geology, metamorphic petrology and geochronology was done in this thesis (Figure 0.7).

The analytical procedures and technical settings are described in detail in each following part to link the methods with sample specificities.

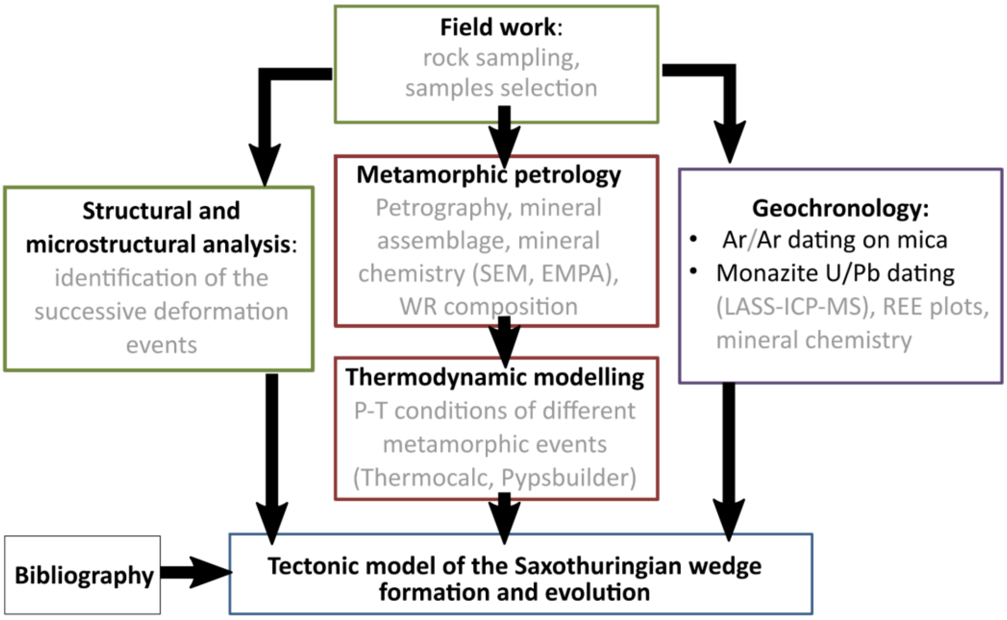

Figure 0.7: Multi-disciplinary methods used during this work

Extensive field work had been performed during four field trip seasons from 2017 to 2020, covering structural mapping and sampling of a large area. The field trips have often been carried out with the supervision of the supervisor Ondrej Lexa and the advisor Petr Jeřábek, and with the cooperation of Vít Peřestý. The field was conducted using the geological maps of Germany (Zitzmann, 1994, 2003; Geologische Übersichtskarte der Bundesrepublik Deutschland 1:250.000 (GÜK250), available at https://geoviewer.bgr.de/mapapps/resources/apps/geoviewer/index.html?lang=de) and Czech Republic (Geological map 1 : 200,000 and 1 : 50,000 [online]. Czech Geological Survey and Geologischer Dienst Freiberg. Available at: https://mapy.geology.cz/geocr50/). A total of 294 outcrops were documented in detail and about 200 rock pieces were sampled for further microstructural, metamorphic and geochronological analysis. It comprises phyllites, micaschists, gneisses, amphibolites and quartzites. These samples represent almost all metasedimentary rock types of Erzgebirge and Fichtelgebirge. The structural description of the area comprises advanced analysis and interpretation of field measurements.

From these numerous samples, the most interesting ones in terms of structures, mineral assemblage, freshness and occurrence of monazite or mica were selected for further studies. Dozens of outcrops and thin-sections were used to understand and characterize the complex polyphase deformation and metamorphism of the studied area. Four representative samples were selected to highlight the tectonometamorphic evolution of the phyllites and micaschists. Eight samples were used for monazite U-Pb geochronology, and fourteen samples were selected for mica ^{40}Ar/^{39}Ar dating.

As much as possible, we tried to select samples suitable for all the methods performed, i.e. presenting different fabric relationships, as well as distinguishable mineral assemblage in the different fabrics, and also with enough, large and fresh monazite and mica to be dated. We did not succeed to find the perfect sample containing this entire criterion and suitable for all the methods, but several of them were studied with a multi-disciplinary approach: ie structures, petrology, phase-equilibria modelling and monazite U-Pb dating (parts I and II), or monazite U-Pb and mica ^{40}Ar/^{39}Ar geochronology (part II). The Table 0.1 shows in which studied samples the different methods overlap is provided, with a summary of the results highlighted by each individual approach.

Mineral abbreviations are as follows (by alphabetical order):

ab: albite, all:allanite, and: andalusite, apa: apatite, bi: biotite, cal: calcite, cd: cordierite, chl: chlorite, cpx: clinopyroxene, ctd: chloritoid, ep: epidote, g: garnet, gl: glaucophane, hem: hematite, ilm: ilmenite, ksp: K-feldspar, ky: kyanite, law: lawsonite, mag: magnetite, ma: margarite, mu: muscovite, mnz: monazite, pa: paragonite, ph: phengite, pl: plagioclase, q: quartz, ru: rutile, sill: sillimanite, sph: sphene, st: staurolite, tur: tourmaline, zr: zircon.

PART I: THE TECTONOMETAMORPHIC EVOLUTION OF THE SAXOTHURINGIAN OROGENIC WEDGE

1- INTRODUCTION

Within the European Variscides, the Saxothuringian Domain preserves numerous occurrences of blueschists, eclogite facies rocks and *UHP* relics clearly pointing to a subduction-related environment (e.g. Collett et al., 2017; Faryad & Kachlík, 2013; Massonne, 2001; Massonne & Nasdala, 2003). Structurally, the high-grade *(U)HP–HT* rocks crop out in the center of a domal structure in the footwall of the lower-grade *HP–LT* metasediments creating apparent normal metamorphic zoning. Such a position is inconsistent with the typical subduction environment, where the sequence of thrust sheets with inverse metamorphic zoning is expected. The existing interpretations of the tectonic evolution of the Erzgebirge and exhumation of *(U)HP* rocks emphasize one of the contrasting mechanisms: i) imbrication of *HP* slices derived from the subducting plate (Schmädicke & Evans, 1997); ii) extrusion from subduction channel (Konopásek & Schulmann, 2005); iii) collapse of the thickened crust and metamorphic core-complex formation (Kröner et al., 1995; Willner et al., 2000).

This part aims to reconcile these contrasting possibilities by linking the evolution of the *(U)HP–HT* core of the Erzgebirge dome with the newly-described record in the hanging wall phyllites and micaschists. Although the tectonometamorphic evolution of the hanging wall is critical in understanding the geodynamic evolution of the Saxothuringian Domain, its role is largely neglected in the literature. The following study is based on the detailed petrography, phase-equilibria modelling, and structural analysis across the phyllite-micaschist transition zone. The polyphase character of the area is emphasized and it is shown that the present-day architecture results from the superposition of the processes associated with the evolution of the orogenic wedge.

2 - ANALYTICAL METHODS

Extensive field work has been conducted for structural analyses and a total of 294 outcrops were documented in detail in Erzgebirge und Fichtelgebirge. About 200 thin-sections with a thickness of 30 µm were done at the thin-section laboratory of the Faculty of Science in Prague. Using a polarizing microscope, the mineral identification and microstructures allowed us to understand the fabric relationships and the mineral assemblages. Some thin-sections were also studied with a Secondary Electron Microscope at the Institute of Petrology and Structural Geology (Charles University, Prague) – to determine the unknown phases.

Microstructural relations and chemical composition of minerals in the studied samples were analyzed using a field emission gun electron probe microanalyzer (FEG-EPMA) JXA-8530F (manufactured by Jeol), equipped with five wave dispersive spectrometers (WDS) at the Institute of Petrology and Structural Geology (Charles University, Prague). Quantitative analyses of all phases were acquired in spot mode with the beam size of 2 µm except for micas and chlorite, for which the beam was defocussed to 5 µm. Garnets were analyzed at 15 kV and 80 nA, other phases at 15 kV and 20 nA. Kα lines were used for detection of all elements except for Y (Lα). The compositional maps of garnet were acquired at 20 kV and 100 nA in spot mode with counting time 80 ms per point. All elements were detected with WDS using the Kα lines. For the data presented below, the mineral compositions were recalculated to standard numbers of oxygen per formula unit, with H2O assumed to be present in stoichiometric amounts. The amount of oxygen used is given in each table of mineral analyses.

The effective bulk rock compositions used in the thermodynamic modelling were calculated on the basis of equilibration volume approach covering the mineral assemblage in question and quantified using the SEM Tescan Vega equipped with EDS (X-Max 50, Oxford Instruments) at the Institute of Petrology and Structural Geology (Charles University, Prague). This approach was chosen in order to estimate the most precisely the effective composition during equilibration of the observed mineral assemblages and at the same time avoids possible sample-scale compositional heterogeneities (Broussolle et al., 2015; Peřestý et al., 2017). Five to twenty-four spectra for each thin-section were acquired in scanning mode of the electron microscope to cover the representative area of the thin-section and to avoid late alteration products. The number of acquired spectra depends on the grain size and banded nature of the sample. The coarse grained samples with few and large porphyroblasts of garnet (MJ6D, MJ58B, and MJ218A) required a larger area coverage than the fine-grained and homogeneous phyllite MJ44. The area analysis used in individual samples thus varies between 31 and 294 mm2. Each of the analyses was acquired at 15 kV and 1.5 nA for 300 s live time. The individual analyzed areas of each sample were averaged. The resulting compositions in molar per cent normalized to 100% are shown in the pseudosections.

The compositional fractions are defined as follows: almandine (Alm) = Fe/(Ca + Fe + Mn + Mg), pyrope (Prp) = Mg/(Ca + Fe + Mn + Mg), grossular (Grs) = Ca/(Ca + Fe + Mn + Mg), spessartine (Sps) = Mn/(Ca + Fe + Mn + Mg), X_{Mg} = Mg /(Fe + Mg), X_{Na} = Na/(Na + K). Atoms per formula unit (a.p.f.u.) are used and the sign "→" indicates compositional trend.

3 - STRUCTURAL RECORD

The studied area was affected by complex polyphase deformation with specific appearance in phyllites and micaschists (Figure I.1). We identified four distinct deformation stages D1-D4 associated with development of four planar fabrics S1-S4.

In phyllites, the dominant planar fabric S2 (Figure I.2b) dips gently to the NW (Figure I.1c). S2 originates from intense transposition of an older metamorphic foliation S1, which appears as intrafolial isoclinal folds or as relics in isolated microlithons (Figures I.1e and I.2a,c,f). Towards the contact with micaschists, the main foliation S2 is affected by asymmetric F3 folds with axial planes S3 dipping gently to moderately to the N-NW (Figures I.1c,e and I.2f).

Micaschists are dominated by a subhorizontal to gently NW-dipping axial planar cleavage S3 associated with closed to isoclinal F3 folds, which heterogeneously overprinted the earlier metamorphic foliation S2 (Figures I.1d,e and I.2d,e). The highest degree of S2 transposition into S3 occurs along the contacts with the hanging wall phyllites and the footwall gneisses, while the central part of micaschists shows relatively well-preserved steeply dipping S2 (Figure I.1d,e). Here, the oldest recognised fabric S1 has been observed in the form of rootless isoclinal folds or locally preserved microlithons.

The whole studied area is heterogeneously affected by the late upright F4 folds with steep NE-SW trending axial planes and subhorizontal axes (Figure I.1b,e). The macroscopic F4 folds in the northernmost phyllites appear as decimetre-scale open folds (Figure I.2b,g) while small-scale crenulations are common in the entire studied region. This late folding was responsible for the development of km-scale open folds and alternation of large-scale antiforms and synforms (Figure I.1b).

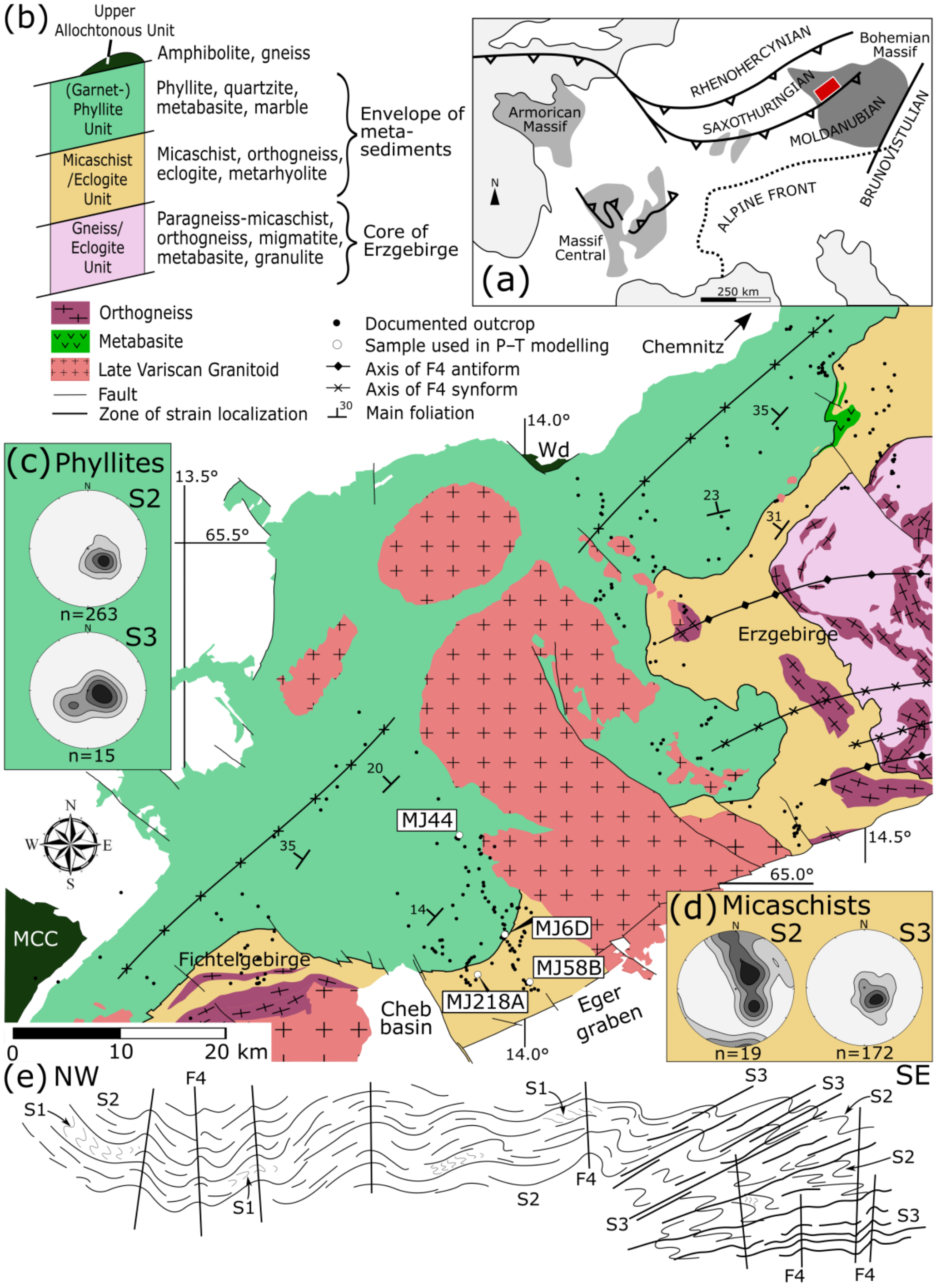

Figure I.1. (a) Simplified tectonic map showing European Variscides (modified after Konopásek et al., 2001). The studied area is shown by the red rectangle. (b) Simplified geological map of the Western part of the Saxothuringian Domain with schematic position of the main lithotectonic units (modified after Rötzler & Plessen, 2010), MCC - Münchberg Crystalline Complex; Wd - Wildenfels Massif. (c,d) Stereonets with equal-area lower hemisphere showing poles of S2 and S3 foliations for phyllites (c) and for micaschists (d). Contours are multiples of mean uniform distribution. (e) Schematic relation of individual fabrics superposition.

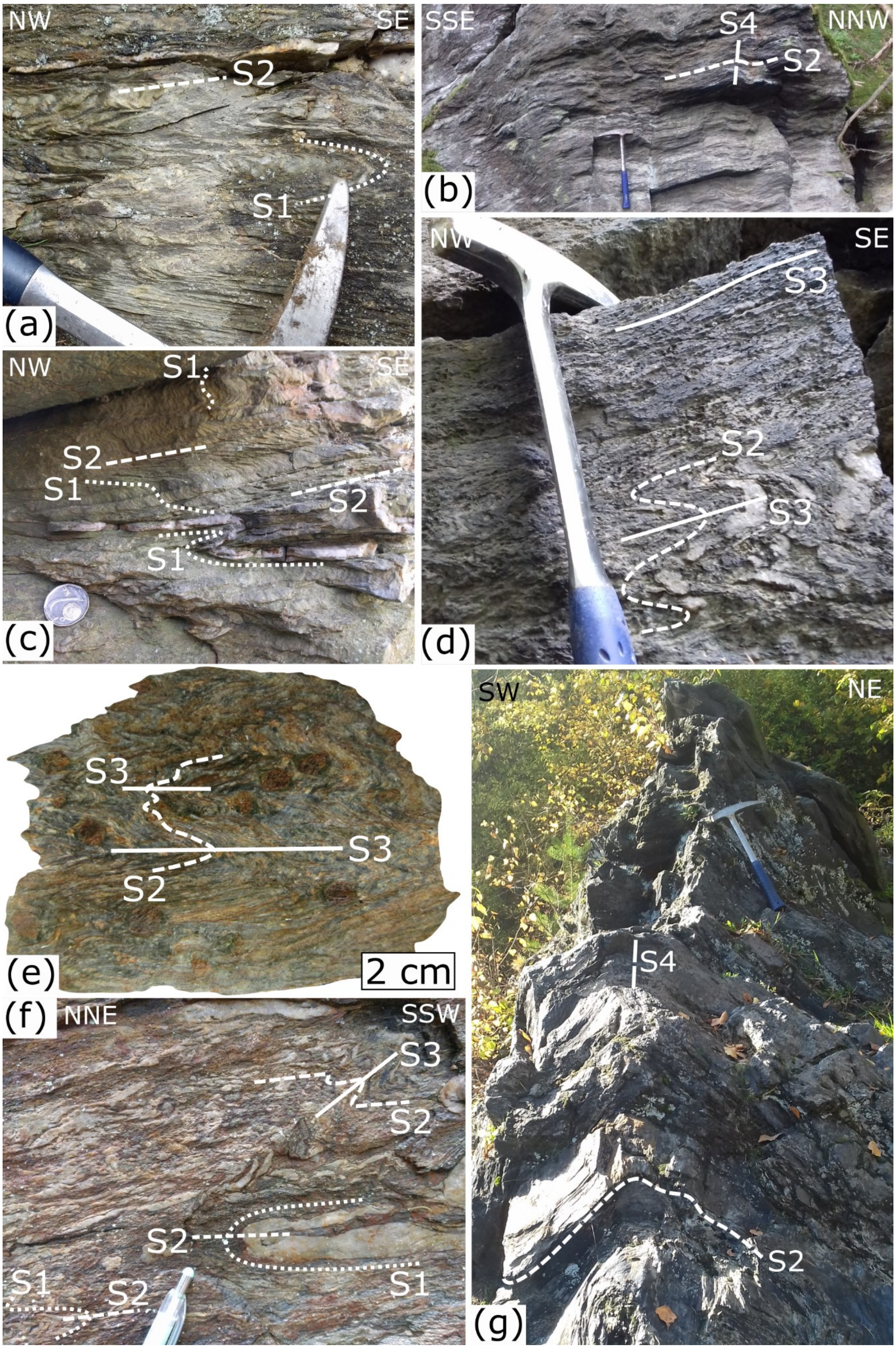

Figure I.2. Field photographs illustrating typical structural relationships. (a) MJ42 phyllite (E 12.486502; N 50.34679): lithons of S1 foliation transposed to S2. (b) MJ129 phyllite (E 12.532851; N 50.241538): sub-horizontal S2 foliation crenulated by S4 cleavage. (c) MJ132 phyllite (E 12.460322; N 50.342645): Preserved S1 foliation transposed to S2. (d) MJ62 micaschist (E 13.040747; N 50.663563): S2 foliation transposed to S3 sub-horizontal fabric. (e) MJ217 micaschist (E 12.504159; N 50.223007): S2 foliation with garnet folded by S3 cleavage. (f) MJ268 phyllite (E 12.7543; N 50.401697): S1 transposed to S2 and folded by F3 folds. (g) MJ109 phyllite (E 12.74818; N 50.614534): S2 foliation folded by open late F4 folds.

4 - PETROGRAPHY AND MINERAL CHEMISTRY

4.1 - DEFORMATION AND METAMORPHISM

About 200 thin-sections from the whole area, cut perpendicular to F2, F3 and F4 fold axes or intersection lineation, were studied to link deformation events with their metamorphic conditions. This investigation revealed four metamorphic assemblages M1, M2, M3 and M4 associated with the four deformation fabrics S1, S2, S3 and S4 respectively.

Phyllites are composed of q-mu-chl-ilm-ru-pa±pl and rarely chloritoid and garnet. Accessory minerals are apatite, zircon, monazite, xenotime and tourmaline. They are characterized by alternating mica rich and quartz rich bands (Figure I.3a). Locally, relic F2 folds and isolated S1 lithons are preserved at a high angle to the enveloping S2 foliation. When the S1 and S2 superposition is missing or when these fabrics are subparallel, it is referred to as composite S2 foliation. Some samples contain chloritoid porphyroblasts up to 4 mm long, forming needles or radial aggregates (Figure I.3b,c). Chloritoid commonly contains inclusion trails of ilmenite or rutile formed in the continuity with the S2 foliation in the matrix. In thin sections with S1 lithons and F2 folds, the trails commonly occur at high angle to the S2 fabric (Figure I.3b,c). This geometry is interpreted as a transversal overgrowth of S1 by needle-shaped chloritoid blasts and their later rotation into the parallelism with S2 suggesting their formation synkinematic with D2. In some cases, the inclusion trails in chloritoid follow the long edge of the chloritoid and thus occur parallel to the composite S2 foliation. As there is no clear difference between the mineral assemblages of the S1 and S2 fabrics in some phyllites, the corresponding metamorphic event is referred to as M1-2 in these samples. The D3 event does not create distinct fabric in most of the phyllites, however it can not be excluded that some of the less-phengitic white micas or randomly oriented chlorite crystals in the matrix or surrounding chloritoid blasts represent static M3 metamorphism. The D4 event is manifested by F4 microcrenulations overprinting the earlier fabrics (Figures I.3a and I.4a). The associated M4 metamorphic overprint occurs only locally and it is represented by chlorite and muscovite aligned parallel to the S4 cleavage in the matrix or by randomly oriented chlorite aggregates in the vicinity of chloritoid grains (Figures I.3b,c and I.4a).

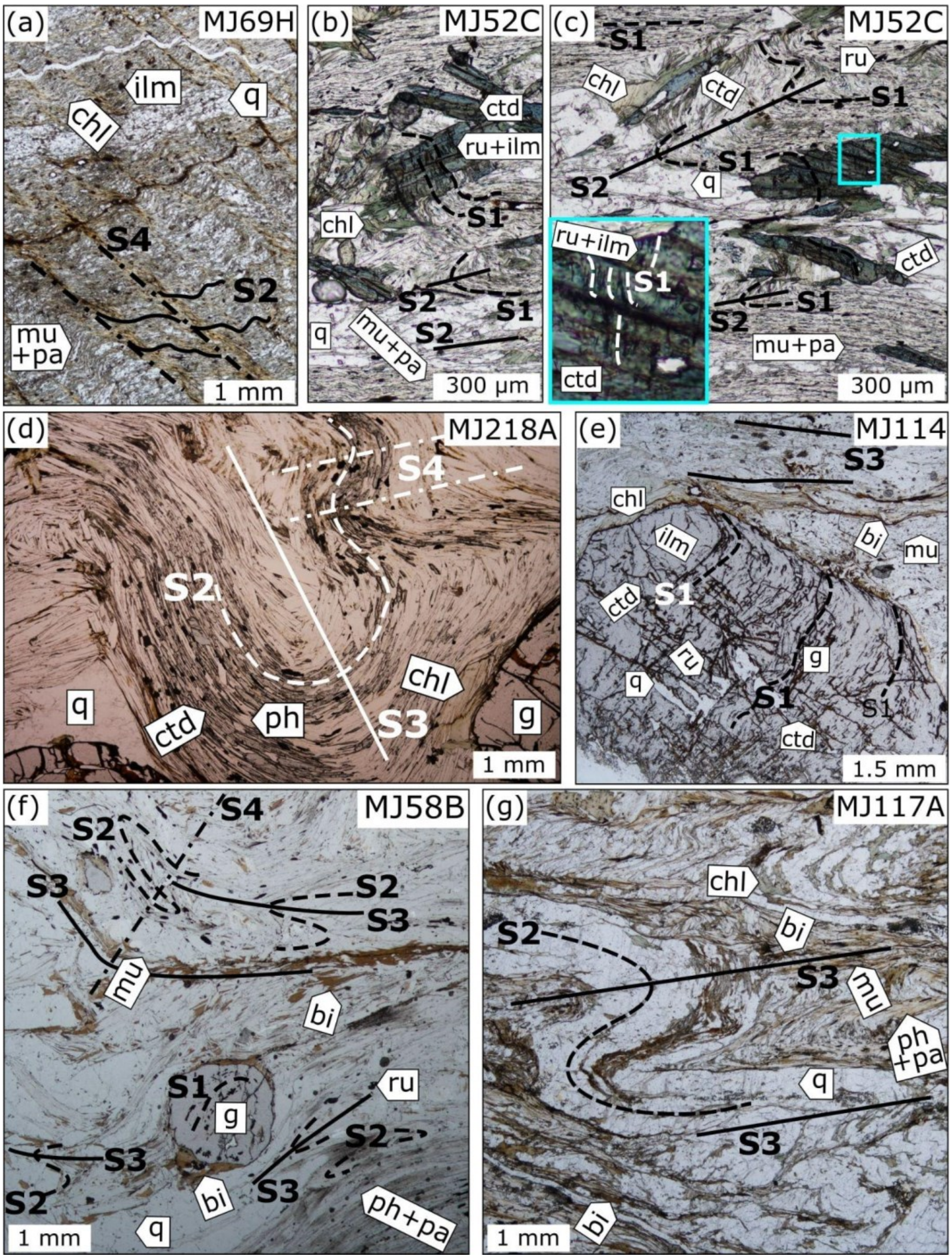

Figure I.3. Microphotographs showing representative mineral assemblages and crystallization-deformation relationships, parallel polars. (a) MJ69H (E 12.979316; N 50.772864): phyllite sample with mu-chl bearing crenulation cleavage S4 at a high angle to the mu-chl-q-ilm bearing S2; (b-c) MJ52C (E 12.467586; N 50.255421): phyllite sample with chloritoid porphyroblasts deformed by the D2 event. Inclusion trails of ilmenite and rutile define the S1 foliation; (d) MJ218A (E 12.514019; N 50.232009): micaschist sample with S2 foliation with garnet and chloritoid-phengite intergrowths is folded by S3 cleavage and later refolded by F4 folds; (e) MJ114 (E 13.031641; N 50.687574): micaschist sample with garnet porphyroblasts. Inclusions trails of S1 foliation in the garnet are at high angle to biotite-bearing S3 fabric; (f) MJ58B (E 12.582822; N 50.225984): micaschist sample with F3 folds refolded by F4 folds. Biotite grows on S3 cleavage domains and around garnet; (g) MJ117A (E 13.050324; N 50.706476): micaschist sample with S2 folded by F3 folds and biotite bearing S3 cleavage.

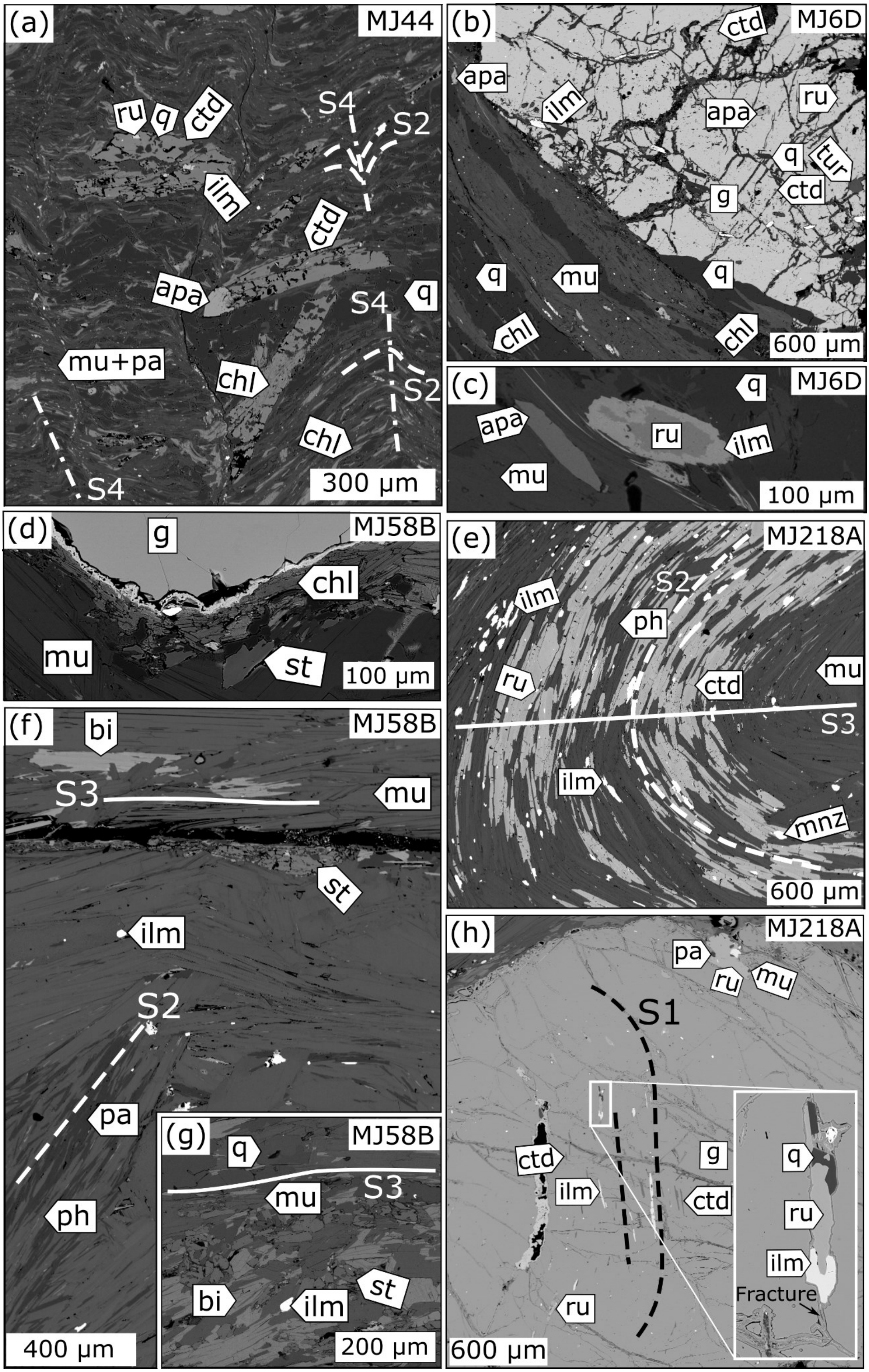
(a)
MJ44
ru
q
ctd
S4
S2
ilm
ctd
apa
q
S4
mu+pa
chl
S2
chl
S4
300 µm
(b)
MJ6D
ctd
apa
ilm
ru
apa
q
tur
ctd
g
q
mu
q
chl
chl
600 µm
(c)
MJ6D
q
apa
ru
ilm
mu
100 µm
(d)
MJ58B
g
chl
mu
st
100 µm
(e)
MJ218A
S2
ilm
ph
ru
ctd
mu
S3
ilm
mnz
600 µm
(f)
MJ58B
bi
S3
mu
st
ilm
S2
pa
ph
400 µm
(g)
MJ58B
q
S3
mu
bi
ilm
st
200 µm
(h)
MJ218A
pa
ru
mu
S1
ctd
ilm
g
ctd
ru
q
ru
ilm
Fracture
600 µm

Figure I.4. Back scattered electron (BSE) images showing representative mineral assemblages and microstructural relationships. (a) ctd-phyllite MJ44 (E 12.490061; N 50.34973): S2 fabric is crenulated by F4 folds. Chloritoid porphyroblasts, sometimes surrounded by chlorite, and mu-pa belong to the S2 foliation; (b) g-phyllite MJ6D (E 12.549922; N 50.2658): Garnet porphyroblast with inclusions of chloritoid in the garnet rim; (c) g-phyllite MJ6D: Rutile grain partly replaced by ilmenite; (d) st-g-micaschist MJ58B (E 12.582822; N 50.225984): Garnet is replaced by M3 chlorite and staurolite; (e) ctd-g-micaschist MJ218A (E 12.514019; N 50.232009): Domain with well-preserved chloritoid-phengite intergrowths, folded by F3 fold. Less phengitic muscovite is present in the right side of the image; (f) st-g-micaschist MJ58B: paragonite and phengite define the S2 mineral assemblage. S3 cleavage domain contains staurolite, biotite and muscovite; (g) st-g-micaschist MJ58B: M3 domain containing staurolite, biotite, muscovite and ilmenite; (h) ctd-g-micaschist MJ218A: Garnet inclusion trails are defined by M1 assemblage of chloritoid, rutile and quartz. Inset shows ilmenite replacing rutile in contact with fractures.

Micaschists are mostly composed of g-mu-q-bi-chl-pa-ilm-ru±pl. Chloritoid is rare in the matrix, but common as inclusions in garnet. Only a few samples contain staurolite. Accessory minerals are apatite, zircon, monazite, xenotime and tourmaline. In most samples, the main foliation is characterized by alternating mica rich and quartz rich bands (Figure I.3g). Micaschists commonly show near complete transposition of S2 by S3 with micro-scale relics of tight and rootless isoclinal F3 folds occurring in almost every sample (Figures I.3d,f,g and I.4e). S2 foliation is defined by the shape preferred orientation of phengitic muscovite sometimes intercalated with chlorite, paragonite (Figures I.3f,g and I.4f), rutile (Figure I.4e) and in a few samples also with chloritoid (Figures I.3d and I.4e) associated with M2 metamorphism. The S3 cleavage domains are associated with distinct metamorphic minerals such as biotite, muscovite, ilmenite and rare staurolite (Figure I.4d,f,g) defining the M3 metamorphic event. Samples with intense D3 transposition contain a higher proportion of biotite than samples with weak overprint. Garnet porphyroblasts are up to 1 cm large and contain inclusion trails of S1 fabric marked by quartz, chloritoid, paragonite, phengite and rutile defining the M1 metamorphic event (Figures I.3e,f and I.4h). The inclusion trails sometimes show complex folded patterns at a high angle to the S2 and/or S3 foliation in the matrix (Figures I.3e,f and I.4h). The garnets are often surrounded by biotite or staurolite, associated with garnet breakdown during the D3 event. The D4 event, associated with open F4 folds and crenulations, overprinted the earlier fabrics and commonly resulted in a superposed interference pattern of F3 and F4 folds (Figure I.3d,f). The metamorphic M4 overprint is weak and locally represented by chlorite aligned parallel to the S4 cleavage in the matrix or around garnet (Figure I.3d,e).

4.2 - MICROSTRUCTURE AND PETROGRAPHY OF THE STUDIED SAMPLES

Four samples with well-defined fabric relations and mineral assemblages were selected for detailed micro-chemical analysis and pseudosection modelling. The selected samples, represented by two phyllites and two micaschists, were collected from the hanging wall phyllites towards the footwall micaschists (for sample locations see Figure I.1b). The structurally highest and lowest grade chloritoid-bearing phyllite sample MJ44 was collected from the central part of the phyllite belt (lat: 50.349730, long: 12.490061). The intermediate grade garnet-bearing quartzitic phyllite sample MJ6D was collected from the boundary between phyllites and micaschists (lat: 50.2658, long: 12.549922). The higher grade micaschists are represented by staurolite-garnet-bearing micaschist sample MJ58B and chloritoid-garnet-bearing micaschist sample MJ218A (lat: 50.225984, long: 12.582822 and lat: 50.232009, long: 12.514019, respectively). The crystallization-deformation sequence for each sample is shown in Figure I.5.

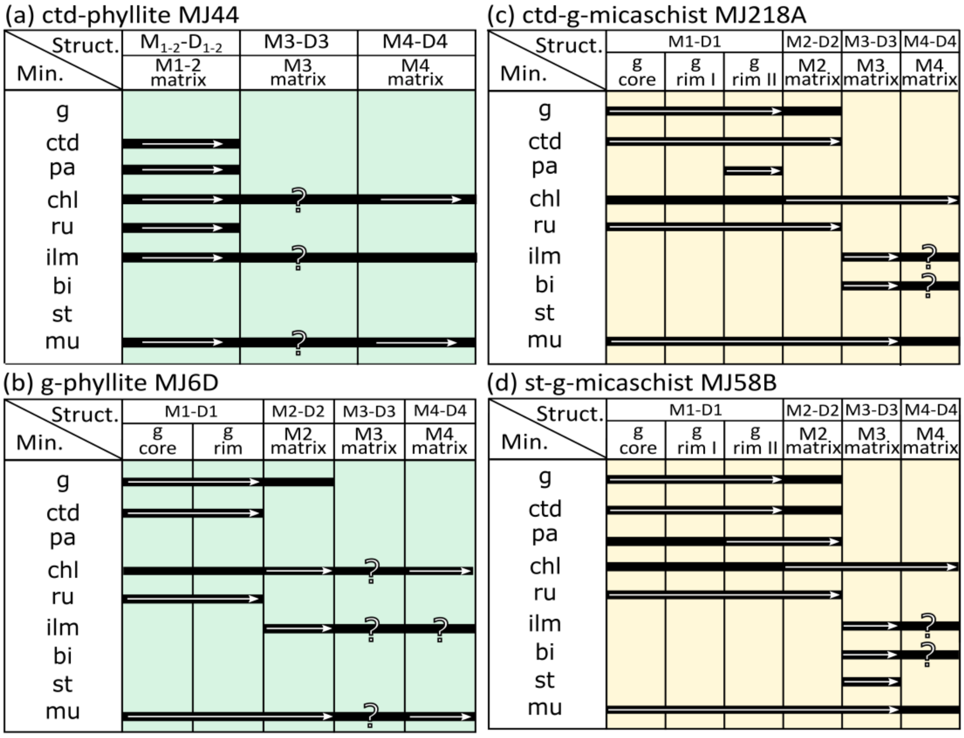

Figure I.5. Crystallization-deformation relationships for phyllites (in green) and for micaschists (in yellow): (a) chloritoid-phyllite MJ44; (b) garnet-phyllite MJ6D; (c) chloritoid-garnet-micaschist MJ218A; (d) staurolite-garnet-micaschist MJ58B. White arrows indicate growth of minerals, black rectangles indicate their stability. Quartz is always present. Min.: minerals; Struct.: structures. See text for details.

The chloritoid-bearing phyllite sample MJ44 (Figures I.1b and I.5a) shows a well-developed muscovite-chlorite bearing composite foliation S2 (Figure I.4a) with an M1-2 assemblage ctd-mu-chl-pa-q-ru-ilm. The needle shaped chloritoid porphyroblasts are partly aligned parallel to S2 (X_{Mg} = 0.09–0.10, Figures I.4a and I.6b; Table I.1) and contain inclusions of quartz, rutile, tiny ilmenite and rarely tiny muscovite (Figure I.4a). The matrix is dominated by fine-grained muscovite (Si = 3.04–3.14 a.p.f.u., X_{Na} = 0.13–0.20 and Ti = 0.00–0.01 a.p.f.u., Figure I.6a; Table I.1) intergrown with tiny paragonite (Figure I.4a). The precise composition of paragonite in the matrix and the muscovite inclusions in chloritoid could not be determined because of their small grain size (<2µm). The other M1-2 minerals include chlorite (X_{Mg} = 0.34–0.38 in Figure I.6d; Table I.1), rutile and ilmenite (Fe^{3+} = 0.06–0.17 a.p.f.u. in Table I.1). Chlorite aligned parallel to the foliation in the mica-rich domains is considered as part of the M1-2 assemblage (Figure I.4a), while the randomly oriented chlorite surrounding chloritoid is considered as a part of either M3 or M4.

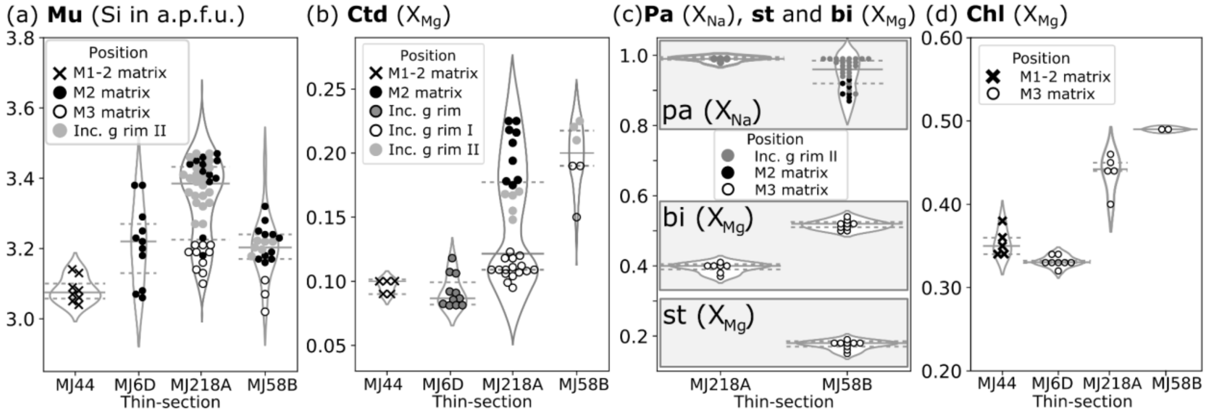

Figure I.6. Compositional variation in: (a) phengitic muscovite (Si in a.p.f.u.); (b) chloritoid (X_{Mg}); (c) paragonite (X_{Na}), staurolite (X_{Mg}) and biotite (X_{Mg}); (d) chlorite (X_{Mg}). The violin plots show the distribution of the data. The central full line shows the median, the dashed lines indicate the 25th and 75th percentiles and circles or crosses show measurements. Inc. = inclusion. Microstructural position of the minerals is indicated by the color and fill of the points.

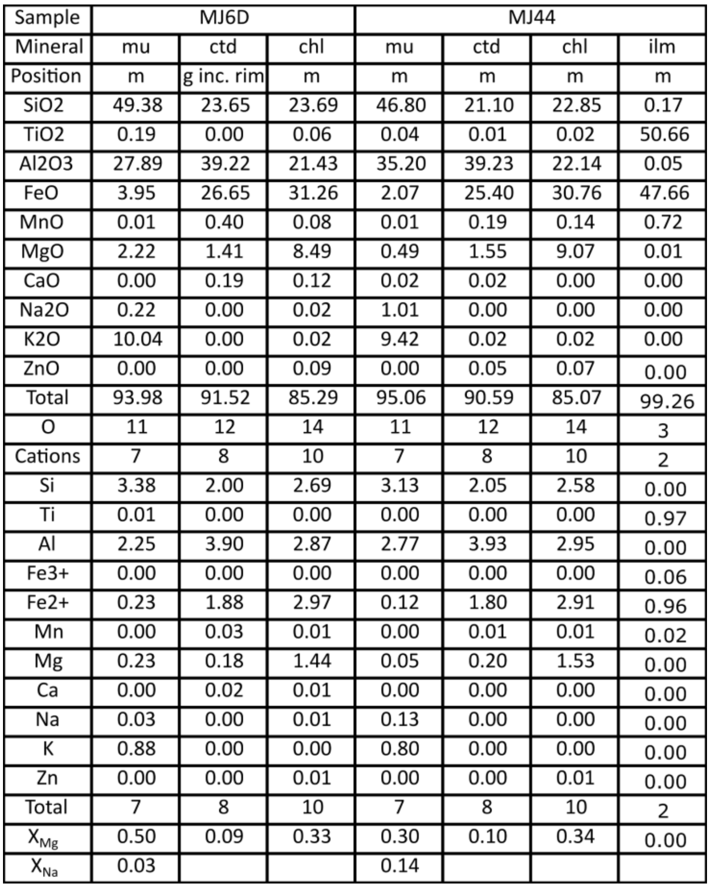

Sample	MJ6D			MJ44			
Mineral	mu	ctd	chl	mu	ctd	chl	ilm
Position	m	g inc. rim	m	m	m	m	m
SiO2	49.38	23.65	23.69	46.80	21.10	22.85	0.17
TiO2	0.19	0.00	0.06	0.04	0.01	0.02	50.66
Al2O3	27.89	39.22	21.43	35.20	39.23	22.14	0.05
FeO	3.95	26.65	31.26	2.07	25.40	30.76	47.66
MnO	0.01	0.40	0.08	0.01	0.19	0.14	0.72
MgO	2.22	1.41	8.49	0.49	1.55	9.07	0.01
CaO	0.00	0.19	0.12	0.02	0.02	0.00	0.00
Na2O	0.22	0.00	0.02	1.01	0.00	0.00	0.00
K2O	10.04	0.00	0.02	9.42	0.02	0.02	0.00
ZnO	0.00	0.00	0.09	0.00	0.05	0.07	0.00
Total	93.98	91.52	85.29	95.06	90.59	85.07	99.26
O	11	12	14	11	12	14	3
Cations	7	8	10	7	8	10	2
Si	3.38	2.00	2.69	3.13	2.05	2.58	0.00
Ti	0.01	0.00	0.00	0.00	0.00	0.00	0.97
Al	2.25	3.90	2.87	2.77	3.93	2.95	0.00
Fe3+	0.00	0.00	0.00	0.00	0.00	0.00	0.06
Fe2+	0.23	1.88	2.97	0.12	1.80	2.91	0.96
Mn	0.00	0.03	0.01	0.00	0.01	0.01	0.02
Mg	0.23	0.18	1.44	0.05	0.20	1.53	0.00
Ca	0.00	0.02	0.01	0.00	0.00	0.00	0.00
Na	0.03	0.00	0.01	0.13	0.00	0.00	0.00
K	0.88	0.00	0.00	0.80	0.00	0.00	0.00
Zn	0.00	0.00	0.01	0.00	0.00	0.01	0.00
Total	7	8	10	7	8	10	2
X_{Mg}	0.50	0.09	0.33	0.30	0.10	0.34	0.00
X_{Na}	0.03			0.14			

Table I.1: Representative mineral analyses of chloritoid-phyllite MJ44 and garnet-phyllite MJ6D. Oxides are in wt%. m = matrix; inc. = inclusion

4.2.2 - GARNETIFEROUS QUARTZITIC PHYLLITE

The garnetiferous quartzitic phyllite sample MJ6D (Figures I.1b and I.5b) was collected from the hinge of a closed decimeter-scale F4 fold. The S1 relics contain garnet, the most phengitic muscovite (Si up to 3.38 a.p.f.u., X_{Na} = 0.03 and Ti = 0.01 a.p.f.u. in Figures I.4b,c and I.6a; Table I.1), quartz, chlorite (X_{Mg} = 0.32–0.34 in Figures I.4b and I.6d; Table I.1), rutile, apatite, ilmenite and chloritoid included in garnet. Garnet porphyroblasts up to 5 mm in diameter contain S1 inclusion trails consisting of chloritoid (Figures I.4b and I.7a), rutile and quartz. Garnet shows pronounced compositional zoning with rimward decrease in Grs and Sps and increase of Prp, Alm and X_{Mg} ($Grs_{0.22\rightarrow0.11}$ $Sps_{0.10\rightarrow0.04}$ $Prp_{0.03\rightarrow0.05}$ $Alm_{0.66\rightarrow0.82}$, X_{Mg} = 0.04→0.06 in Figures I.4b and I.7a,d; Table I.2). The composition of chloritoid inclusions in the garnet rim is X_{Mg} = 0.08–0.12 (Figure I.6b; Table I.1), while the composition of chloritoid inclusions in the garnet core could not be determined because of their small size (<2µm).

Muscovite with low Si content (Si down to 3.06, X_{Na} = 0.07 and Ti = 0.01 a.p.f.u. in Figure I.6a; Table I.1), chlorite and ilmenite surrounding rutile (Figure I.4c) and absence of chloritoid in the matrix are evidence for the M2 stage. Flakes of late chlorite surrounding garnet can be associated with either the M3 or M4 overprint.

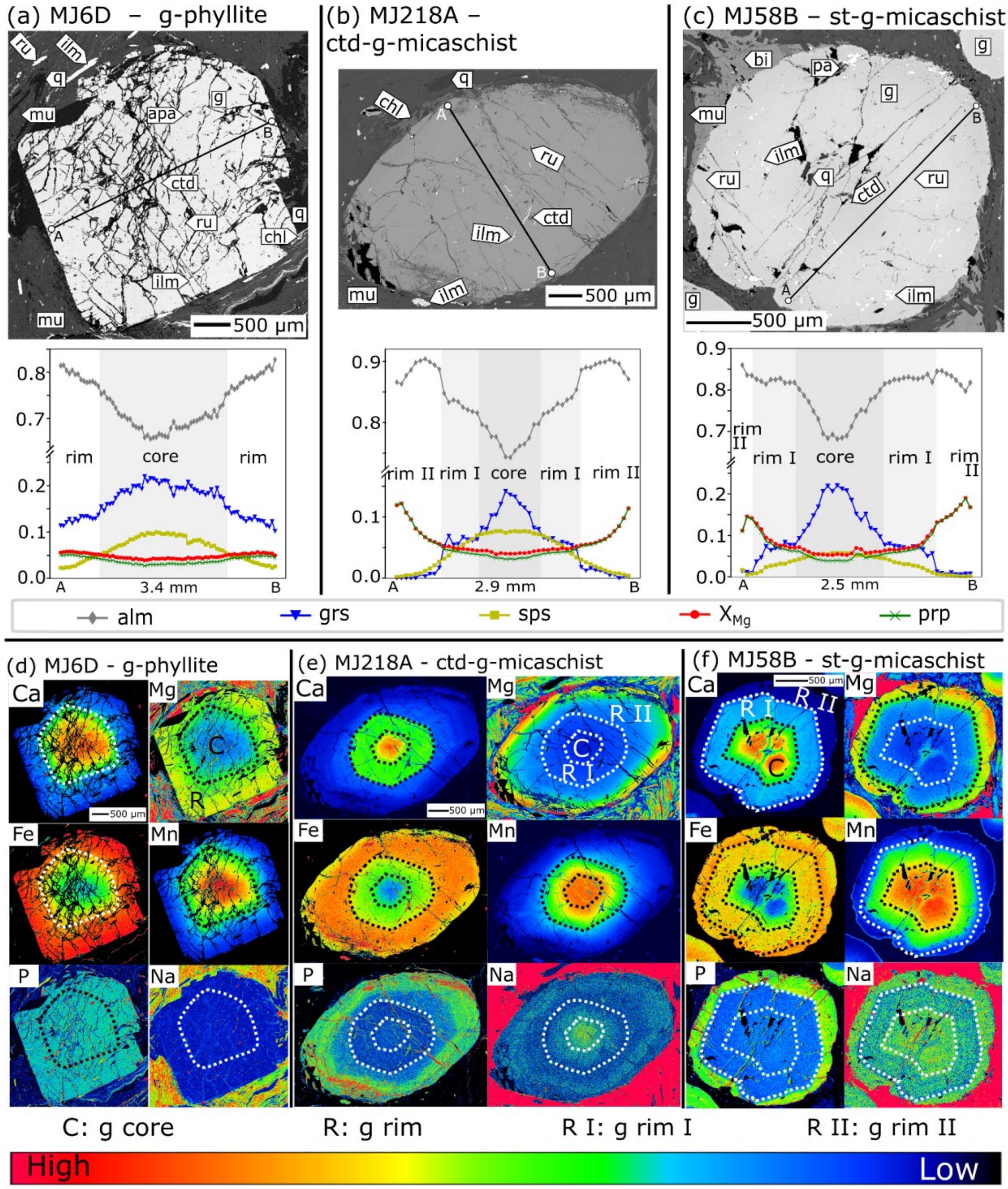

Figure I.7. (a-c) BSE image of garnet with mineral inclusions and compositional profile for garnet from the samples MJ6D (a), MJ218A (b) and MJ58B (c). (d-f) Compositional maps of Ca, Mg, Fe, Mn, P and Na for garnet from the samples MJ6D (d), MJ218A (e) and MJ58B (f).

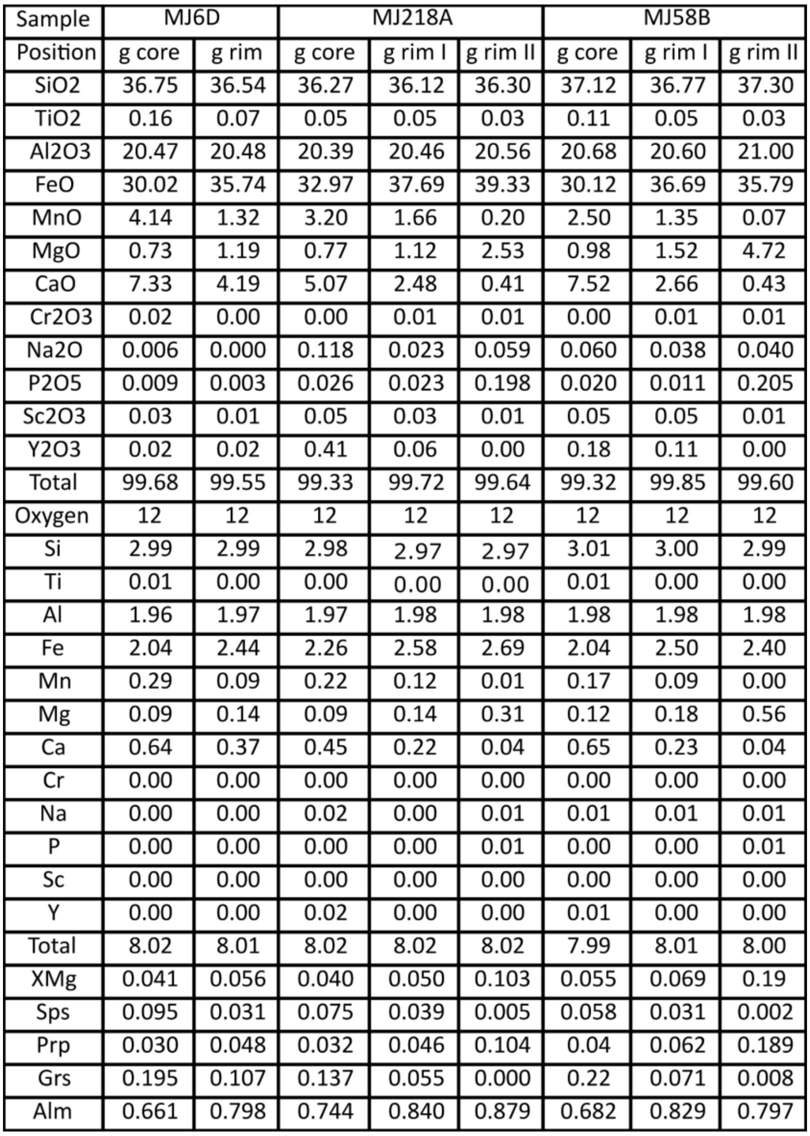

Sample	MJ6D		MJ218A			MJ58B		
Position	g core	g rim	g core	g rim I	g rim II	g core	g rim I	g rim II
SiO2	36.75	36.54	36.27	36.12	36.30	37.12	36.77	37.30
TiO2	0.16	0.07	0.05	0.05	0.03	0.11	0.05	0.03
Al2O3	20.47	20.48	20.39	20.46	20.56	20.68	20.60	21.00
FeO	30.02	35.74	32.97	37.69	39.33	30.12	36.69	35.79
MnO	4.14	1.32	3.20	1.66	0.20	2.50	1.35	0.07
MgO	0.73	1.19	0.77	1.12	2.53	0.98	1.52	4.72
CaO	7.33	4.19	5.07	2.48	0.41	7.52	2.66	0.43
Cr2O3	0.02	0.00	0.00	0.01	0.01	0.00	0.01	0.01
Na2O	0.006	0.000	0.118	0.023	0.059	0.060	0.038	0.040
P2O5	0.009	0.003	0.026	0.023	0.198	0.020	0.011	0.205
Sc2O3	0.03	0.01	0.05	0.03	0.01	0.05	0.05	0.01
Y2O3	0.02	0.02	0.41	0.06	0.00	0.18	0.11	0.00
Total	99.68	99.55	99.33	99.72	99.64	99.32	99.85	99.60
Oxygen	12	12	12	12	12	12	12	12
Si	2.99	2.99	2.98	2.97	2.97	3.01	3.00	2.99
Ti	0.01	0.00	0.00	0.00	0.00	0.01	0.00	0.00
Al	1.96	1.97	1.97	1.98	1.98	1.98	1.98	1.98
Fe	2.04	2.44	2.26	2.58	2.69	2.04	2.50	2.40
Mn	0.29	0.09	0.22	0.12	0.01	0.17	0.09	0.00
Mg	0.09	0.14	0.09	0.14	0.31	0.12	0.18	0.56
Ca	0.64	0.37	0.45	0.22	0.04	0.65	0.23	0.04
Cr	0.00	0.00	0.00	0.00	0.00	0.00	0.00	0.00
Na	0.00	0.00	0.02	0.00	0.01	0.01	0.01	0.01
P	0.00	0.00	0.00	0.00	0.01	0.00	0.00	0.01
Sc	0.00	0.00	0.00	0.00	0.00	0.00	0.00	0.00
Y	0.00	0.00	0.02	0.00	0.00	0.01	0.00	0.00
Total	8.02	8.01	8.02	8.02	8.02	7.99	8.01	8.00
XMg	0.041	0.056	0.040	0.050	0.103	0.055	0.069	0.19
Sps	0.095	0.031	0.075	0.039	0.005	0.058	0.031	0.002
Prp	0.030	0.048	0.032	0.046	0.104	0.04	0.062	0.189
Grs	0.195	0.107	0.137	0.055	0.000	0.22	0.071	0.008
Alm	0.661	0.798	0.744	0.840	0.879	0.682	0.829	0.797

Table I.2: Representative mineral analyses of garnet in the samples MJ6D, MJ218A and MJ58B. Oxides are in wt%.

4.2.3 - CHLORITOID-GARNET MICASCHIST

The chloritoid-garnet micaschist sample MJ218A (Figures I.1b and I.5c) contains relics of isoclinal F3 folds that are overprinted by open F4 folds (Figure I.3d). Domains of the well-preserved M2 assemblage are marked by the phengite-chloritoid intergrowths in the S2 foliation (Figures I.3d and I.4e), while domains of the M3-S3 overprint contain low-Si muscovite, biotite, ilmenite and chlorite. Garnet is part of the M1 assemblage and shows three distinct compositional zones observed mainly in the Alm and Grs components (Figure I.7b,e; Table I.2). The garnet core (Grs$_{0.14\rightarrow0.07}$ Sps$_{0.08\rightarrow0.07}$Prp$_{0.03\rightarrow0.04}$ Alm$_{0.74\rightarrow0.82}$ X_{Mg} =

0.04→0.05) shows a steep increase in Alm and decrease in Grs followed by a gradual change in both components in the rim I ($Grs_{0.07\rightarrow0.04}$ $Sps_{0.07\rightarrow0.02}$ $Prp_{0.04\rightarrow0.06}$ $Alm_{0.82\rightarrow0.84}$ X_{Mg} = 0.04→0.06). The transition to the garnet rim II ($Grs_{<0.01}$ $Sps_{<0.01}$ $Prp_{0.06\rightarrow0.14}$ $Alm_{0.88\rightarrow0.90\rightarrow0.85}$ X_{Mg} = 0.06→0.14) is characterized by a compositional jump in both Grs and Alm followed by a gradual decrease in Grs and gradual increase and then decrease in Alm associated with increase in Prp. Some garnets show a well-defined rim I plateau composition $Grs_{0.07}$ $Sps_{0.03}Prp_{0.05}$ $Alm_{0.84}$ X_{Mg} = 0.06. Garnet inclusions representing M1 assemblage are chloritoid (X_{Mg} = 0.09–0.12 in the rim I, X_{Mg} = 0.15–0.17 in the rim II, Figures I.4h and I.6b; Table I.3), phengitic muscovite (Si = 3.27–3.47 a.p.f.u., Ti = 0.01–0.11 a.p.f.u. in the rim II, Figure I.6a; Table I.3), rutile, paragonite (X_{Na} = 0.98–1.00, Ti = 0.02–0.07 a.p.f.u. in the rim II, Figures I.4h and I.6c; Table I.3), ilmenite (Figure I.4h) and quartz. The chloritoid included in the garnet core could not be analyzed due to its small size (<2µm). Paragonite was found only in the garnet rim II (Figure I.4h).

Minerals defining the M2 assemblage are garnet (Figures I.3d and I.7b,e), quartz, rutile, phengitic muscovite (Si = 3.18–3.47 a.p.f.u. and Ti = 0.01–0.02 a.p.f.u., Figures I.3d, I.4e and I.6a; Table I.3), chloritoid (X_{Mg} = 0.18–0.23, Figures I.3d, I.4e and I.6b; Table I.3) and very fine chlorite.

The M3 mineral assemblage in matrix contains less phengitic muscovite (Si = 3.10–3.23 a.p.f.u. and Ti = 0.01–0.02 a.p.f.u., Figures I.4e and I.6a; Table I.3), biotite (X_{Mg} = 0.37–0.41 and Ti = 0.03–0.08 a.p.f.u., Figure I.6c; Table I.3), ilmenite and chlorite (X_{Mg} = 0.40–0.46, Figure I.6d; Table I.3). Late chlorite flakes are surrounding garnet and may reflect an M4 overprint.

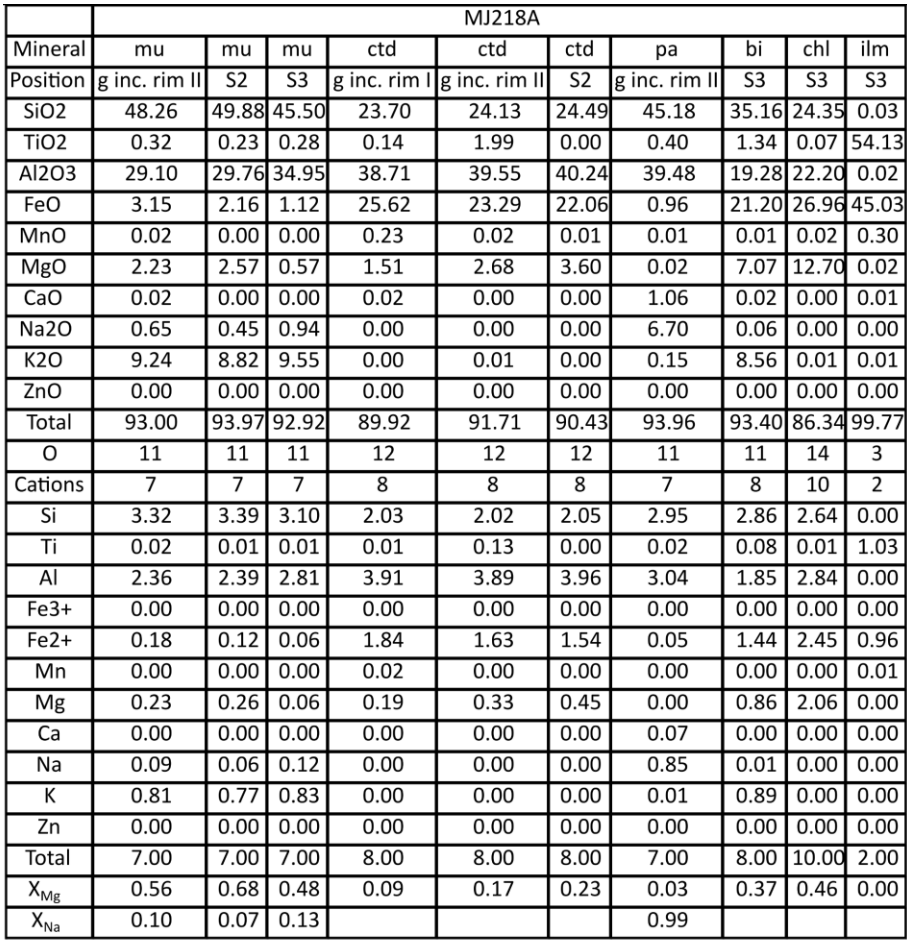

	MJ218A									
Mineral	mu	mu	mu	ctd	ctd	ctd	pa	bi	chl	ilm
Position	g inc. rim II	S2	S3	g inc. rim I	g inc. rim II	S2	g inc. rim II	S3	S3	S3
SiO2	48.26	49.88	45.50	23.70	24.13	24.49	45.18	35.16	24.35	0.03
TiO2	0.32	0.23	0.28	0.14	1.99	0.00	0.40	1.34	0.07	54.13
Al2O3	29.10	29.76	34.95	38.71	39.55	40.24	39.48	19.28	22.20	0.02
FeO	3.15	2.16	1.12	25.62	23.29	22.06	0.96	21.20	26.96	45.03
MnO	0.02	0.00	0.00	0.23	0.02	0.01	0.01	0.01	0.02	0.30
MgO	2.23	2.57	0.57	1.51	2.68	3.60	0.02	7.07	12.70	0.02
CaO	0.02	0.00	0.00	0.02	0.00	0.00	1.06	0.02	0.00	0.01
Na2O	0.65	0.45	0.94	0.00	0.00	0.00	6.70	0.06	0.00	0.00
K2O	9.24	8.82	9.55	0.00	0.01	0.00	0.15	8.56	0.01	0.01
ZnO	0.00	0.00	0.00	0.00	0.00	0.00	0.00	0.00	0.00	0.00
Total	93.00	93.97	92.92	89.92	91.71	90.43	93.96	93.40	86.34	99.77
O	11	11	11	12	12	12	11	11	14	3
Cations	7	7	7	8	8	8	7	8	10	2
Si	3.32	3.39	3.10	2.03	2.02	2.05	2.95	2.86	2.64	0.00
Ti	0.02	0.01	0.01	0.01	0.13	0.00	0.02	0.08	0.01	1.03
Al	2.36	2.39	2.81	3.91	3.89	3.96	3.04	1.85	2.84	0.00
Fe3+	0.00	0.00	0.00	0.00	0.00	0.00	0.00	0.00	0.00	0.00
Fe2+	0.18	0.12	0.06	1.84	1.63	1.54	0.05	1.44	2.45	0.96
Mn	0.00	0.00	0.00	0.02	0.00	0.00	0.00	0.00	0.00	0.01
Mg	0.23	0.26	0.06	0.19	0.33	0.45	0.00	0.86	2.06	0.00
Ca	0.00	0.00	0.00	0.00	0.00	0.00	0.07	0.00	0.00	0.00
Na	0.09	0.06	0.12	0.00	0.00	0.00	0.85	0.01	0.00	0.00
K	0.81	0.77	0.83	0.00	0.00	0.00	0.01	0.89	0.00	0.00
Zn	0.00	0.00	0.00	0.00	0.00	0.00	0.00	0.00	0.00	0.00
Total	7.00	7.00	7.00	8.00	8.00	8.00	7.00	8.00	10.00	2.00
X_{Mg}	0.56	0.68	0.48	0.09	0.17	0.23	0.03	0.37	0.46	0.00
X_{Na}	0.10	0.07	0.13				0.99			

Table I.3: Representative mineral analyses of chloritoid-garnet micaschist sample M218A. Oxides are in wt%. inc. = inclusion.

4.2.4 - STAUROLITE-GARNET MICASCHIST

The staurolite-garnet micaschist sample MJ58B (Figures I.1b and I.5d) shows S2 foliation transposed by heterogeneously developed S3 cleavage and both are folded by open F4 folds (Figure I.3f). Garnet and its inclusions are defining the M1 assemblage (Figures I.3f and I.7c,f; Table I.2). Garnet shows three compositional zones, the core ($Grs_{0.22\rightarrow0.08}$ $Sps_{0.06\rightarrow0.04}$ $Prp_{0.04\rightarrow0.06}$ $Alm_{0.68\rightarrow0.83}$, $X_{Mg}=0.05\rightarrow0.07$), the rim I ($Grs_{0.08\rightarrow0.06}$ $Sps_{0.04\rightarrow0.02}$ $Prp_{0.06\rightarrow0.09}$ $Alm_{0.83\rightarrow0.85}$ $X_{Mg}=0.07\rightarrow0.10$) and the rim II ($Grs_{<0.01}$ $Sps_{<0.01}$ $Prp_{0.09\rightarrow0.19}$ $Alm_{0.85\rightarrow0.80}$ $X_{Mg}=0.10\rightarrow0.19$) with nearly identical compositional characteristics as in the above-described chloritoid-garnet micaschist MJ218A (Figure I.7c,f; Table I.2). Garnet contains inclusions of rutile (Figure I.7c), ilmenite (Figure I.7c) and chloritoid with different composition in rim I and rim II (X_{Mg} = 0.15–0.19 and X_{Mg} = 0.21–0.22, respectively, Figures I.6b and I.7c; Table I.4). Chloritoid inclusions in the garnet core could not be analyzed due to their small size. The garnet rim II contains inclusions of paragonite (X_{Na} = 0.90–1.00 and Ti

= 0.00–0.06 a.p.f.u., Figures I.6c and I.7c; Table I.4) and phengitic muscovite (Si = 3.18–3.22 a.p.f.u., X_{Na} = 0.15–0.17 and Ti = 0.01–0.03 a.p.f.u., Figure I.6a; Table I.4). Chloritoid was only found enclosed in the garnet.

The M2 mineral assemblage consists of rutile, paragonite (X_{Na} = 0.87–0.93 and Ti = 0.00–0.01 a.p.f.u., Figures I.3f, I.4f and I.6c; Table I.4), phengitic muscovite (Si = 3.16–3.32 a.p.f.u., X_{Na} = 0.13–0.19 and Ti = 0.01–0.03 a.p.f.u., Figures I.3f, I.4f and I.6a; Table I.4) and chlorite.

The M3 is associated with narrow S3 cleavage domains (Figures I.3f and I.4f,g) that contain low-Si muscovite (Si = 3.02–3.14 a.p.f.u., X_{Na} = 0.21–0.28 and Ti = 0.01–0.02 a.p.f.u., Figure I.6a; Table I.4), staurolite (X_{Mg} = 0.15–0.19 and Zn = 0.16–0.26 a.p.f.u., Figures I.4d,f,g and I.6c; Table I.4), biotite (X_{Mg} = 0.50–0.54 and Ti = 0.03–0.11 a.p.f.u., Figures I.3f, I.4f,g and I.6c; Table I.4), chlorite (X_{Mg} = 0.49, Figure I.6d; Table I.4) and ilmenite (Figure I.4g; Table I.4). Biotite, staurolite and chlorite commonly surround garnet porphyroblasts (Figures I.3f and I.4d).

Sample	MJ58B										
Mineral	mu	mu	mu	ctd	ctd	pa	pa	st	bi	chl	ilm
Position	g inc. rim II	S2	S3	g inc. rim I	g inc. rim II	g inc. rim II	S2	S3	S3	S3	S3
SiO2	47,74	47,86	45,36	23,97	24,24	45,26	46,88	27,63	35,24	23,79	0,01
TiO2	0,17	0,40	0,40	0,01	0,00	0,23	0,06	0,64	1,62	0,08	54,51
Al2O3	31,79	31,43	37,21	40,31	40,28	39,85	39,75	54,05	19,16	22,65	0,03
FeO	2,05	1,59	0,73	23,87	23,33	0,64	0,69	11,09	17,74	25,10	45,13
MnO	0,00	0,00	0,01	0,12	0,05	0,00	0,02	0,03	0,01	0,04	0,27
MgO	2,10	1,85	0,43	2,30	3,50	0,07	0,39	1,35	10,32	13,75	0,07
CaO	0,02	0,01	0,01	0,02	0,02	0,51	0,13	0,03	0,00	0,00	0,01
Na2O	1,13	1,05	2,02	0,00	0,01	6,95	6,72	0,07	0,40	0,01	0,01
K2O	8,88	8,44	8,17	0,00	0,00	0,66	1,21	0,03	8,40	0,03	0,00
ZnO	0,07	0,00	0,00	0,02	0,04	0,00	0,00	1,92	0,05	0,10	0,00
Total	93,94	92,64	94,33	90,62	91,45	94,17	95,83	96,85	93,00	85,55	100,05
O	11	11	11	12	12	11	11	23	11	14	3
Cations	7	7	7	8	8	7	7	15	8	10	2
Si	3,22	3,28	3,02	2,02	2,01	2,94	2,99	3,96	2,80	2,58	0,00
Ti	0,01	0,02	0,02	0,00	0,00	0,01	0,00	0,07	0,10	0,01	1,04
Al	2,53	2,54	2,92	4,00	3,93	3,05	2,99	9,12	1,79	2,90	0,00
Fe3+	0,00	0,00	0,00	0,00	0,05	0,00	0,00	0,00	0,00	0,00	0,00
Fe2+	0,12	0,09	0,04	1,68	1,57	0,03	0,04	1,33	1,18	2,28	0,95
Mn	0,00	0,00	0,00	0,01	0,00	0,00	0,00	0,00	0,00	0,00	0,01
Mg	0,21	0,19	0,04	0,29	0,43	0,01	0,04	0,29	1,22	2,22	0,00
Ca	0,00	0,00	0,00	0,00	0,00	0,04	0,01	0,00	0,00	0,00	0,00
Na	0,15	0,14	0,26	0,00	0,00	0,87	0,83	0,02	0,06	0,00	0,00
K	0,76	0,74	0,69	0,00	0,00	0,05	0,10	0,01	0,85	0,00	0,00
Zn	0,00	0,00	0,00	0,00	0,00	0,00	0,00	0,20	0,00	0,01	0,00
Total	7,00	7,00	7,00	8,00	8,00	7,00	7,00	15,00	8,00	10,00	2,00
X_{Mg}	0,65	0,67	0,51	0,15	0,22	0,16	0,50	0,18	0,51	0,49	0,00
X_{Na}	0,16	0,16	0,27			0,95	0,89				

Table I.4: Representative mineral analyses of staurolite-garnet micaschist sample MJ58B. Oxides are in wt%. inc. = inclusion.

5 - PHASE-EQUILIBRIA MODELLING

To characterize *P–T* evolution of the above described samples in relation to the deformation fabrics, modelling of phase equilibria has been applied. The presented pseudosections were calculated in THERMOCALC 3.40 (Holland & Powell, 1998, June 2009 update; Powell & Holland, 1988) using thermodynamic data set ds62 of Holland & Powell (2011, updated in July 2016). Calculations were done in the system MnNCKFMASHTO. The calculation for the chloritoid-bearing phyllite MJ44 included Fe^{3+} contents was chosen to obtain the observed assemblage which was not reproduced without inclusion of Fe^{3+} and which also fits with the presence of Fe^{3+} in ilmenite. For the other samples that do not contain any Fe^{3+} rich phases (e.g. magnetite, hematite, epidote) or minerals which may substitute Fe^{3+}, the oxygen content was set to its minimum amount (O = 0.01 mol%). For all the samples, an apatite correction (subtraction of CaO from the bulk-rock composition equivalent to the content bound in apatite) was performed and all calculations were done with H_2O in excess. Correction of the bulk-rock composition due to compositional fractionation of garnet was performed for the three garnet-bearing samples. In each thin-section, the representative area of garnet cores and rims was measured using several garnet maps and profiles. The average composition of the garnet core for MJ6D and core + rim I for MJ58B and MJ218A - multiplied by the modal proportion of garnet core and rim I in each sample - was subtracted from the effective bulk-rock composition.

The activity-composition relations used in calculations included: garnet, chlorite, biotite, staurolite, chloritoid, cordierite, white mica and melt of White et al., 2014; feldspar of Holland & Powell, 2003; ilmenite of White et al., 2000; epidote of Holland & Powell, 2011 and amphibole of Green et al., 2016. The end member phases used in the calculations were quartz, rutile, lawsonite, sphene, kyanite, sillimanite, andalusite and H_2O.

Pseudosection modelling of stable mineral assemblages has been performed using the THERMOCALC front-end program PyPSbuilder, which has been developed by the main supervisor Ondrej Lexa. The program is freely available for other users at https://github.com/ondrolexa/pypsbuilder.

5.1 - P–T EVOLUTION OF THE CHLORITOID PHYLLITE

The observed garnet-free mineral assemblage and composition of phases are not reproduced without calculation with increased oxygen fugacity. The chloritoid-bearing phyllite MJ44 contains ilmenite with significant Fe^{3+} substitution but the sample lacks magnetite. The amount of ferric iron used in the modelling was based on the T-X section, calculated for 480–550 °C at 12 kbar. The T-X section demonstrated that the absence of magnetite and garnet, coexistence of ilmenite and rutile and observed chemical composition of individual phases, is well reproduced for O = 0.2 mol%.

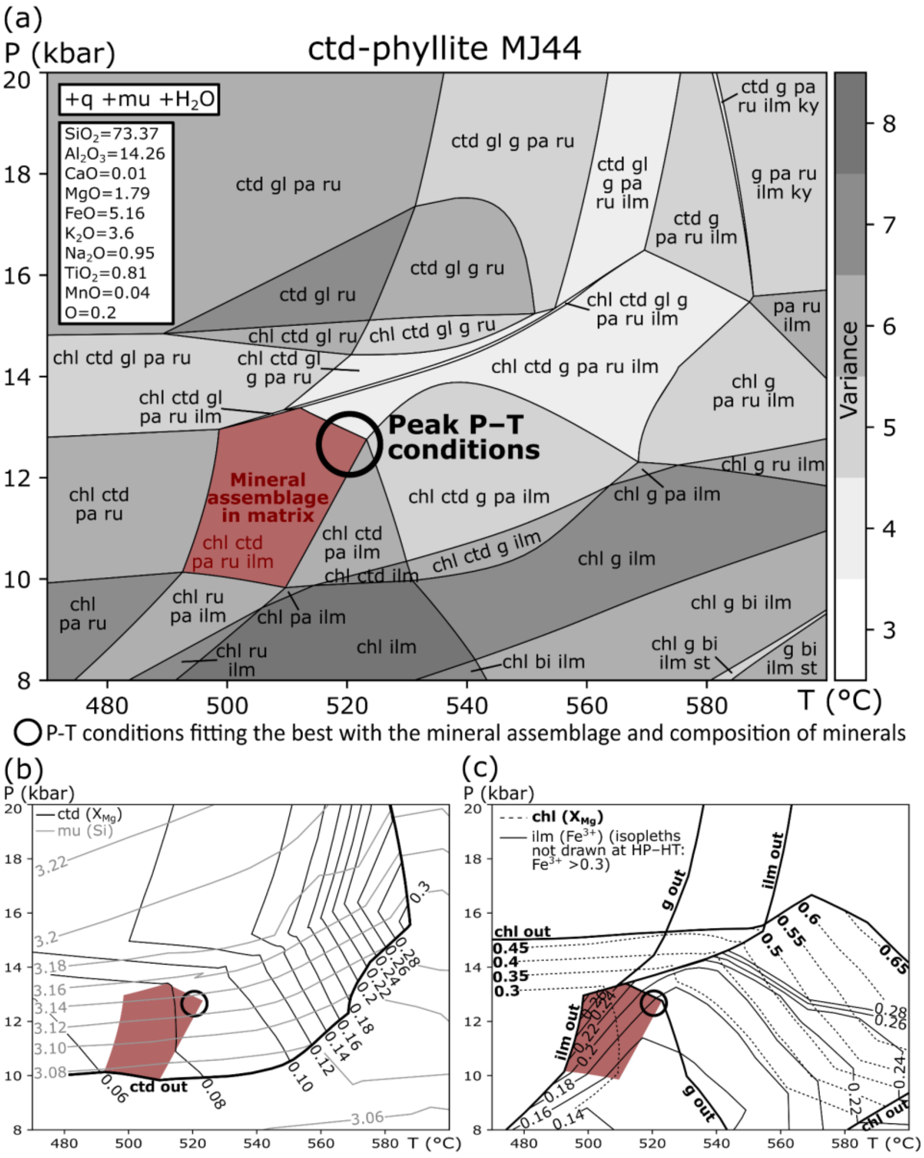

Figure I.8. (a) P–T pseudosection for the chloritoid-phyllite MJ44 (whole rock composition in mol %). In red is shown mineral assemblage in the matrix. The black circle shows the P–T conditions which fit the best with the mineral assemblage, the absence of garnet, coexistence of chloritoid, rutile and ilmenite and isopleth intersection. (b) Isopleths of muscovite (Si in a.p.f.u.) and chloritoid (X_{Mg}). (c) Isopleths of ilmenite (Fe^{3+}) and chlorite (X_{Mg}).

The resulting *P–T* pseudosection is shown in Figure I.8a. The observed M1-2 assemblage ctd-mu-chl-pa-q-ru-ilm corresponds to the equivalent stability field at 10–13 kbar and 490–520 °C. The composition of chloritoid (X_{Mg} = 0.09–0.10, Figure I.6b) and the most phengitic muscovite (Si up to 3.14 a.p.f.u., Figure I.6a) suggests that peak *P–T* M1-2 conditions are around 13 kbar and 520 °C (see the black circle in Figure I.8a) just outside the garnet stability field. These *P–T* conditions are also compatible with the composition of ilmenite (Fe^{3+} up to 0.17 a.p.f.u.) and chlorite (X_{Mg} = 0.34–0.38, Figures I.6d and I.8c). The black circle (Figure I.8) shows the *P–T* conditions which fit the best with the mineral assemblage, the absence of garnet, coexistence of chloritoid, rutile and ilmenite and isopleth intersection. The prograde path to the peak *P–T* conditions can not be constrained due to the lack of change in mineral assemblage and the absence of zoning in minerals. As this sample does not contain garnet, and as the *P–T* conditions calculated here fit with the highest Si content in muscovite, it is likely that this *P–T* estimate corresponds to the peak *P–T* conditions.

Muscovite grains with lower Si content (Si down to 3.04 a.p.f.u.) probably resulted from later re-equilibration of the matrix towards lower pressure, however it is impossible to uniquely assign this re-equilibration to M3 or M4 event.

5.2 - P–T EVOLUTION OF THE GARNETIFEROUS QUARTZITIC PHYLLITE

The *P–T* pseudosection for the garnetiferous quartzitic phyllite MJ6D is shown in Figure I.9a. The effect of garnet fractionation was tested, however due to the low modal proportion of the garnet core, the garnet fractionation did not change the topology and composition of phases of the calculated pseudosection and thus is not shown. The only effect at *HP–LT* conditions is a shift to higher temperature of the garnet-in line by ~40°C and of the garnet Grs and X_{Mg} isopleths by <15°C. The effect on the other chemical variables is negligible.

The M1 mineral assemblage g-ctd-mu-chl-ru-q corresponds to the stability field at 10–17 kbar and 450–550 °C (Figure I.9a). The compositional isopleths of garnet suggest that the garnet core ($Grs_{0.22}$ $Sps_{0.10}$ X_{Mg} = 0.04, Figures I.7a and I.9b) equilibrated at defined range 10–15 kbar and 460–500 °C.

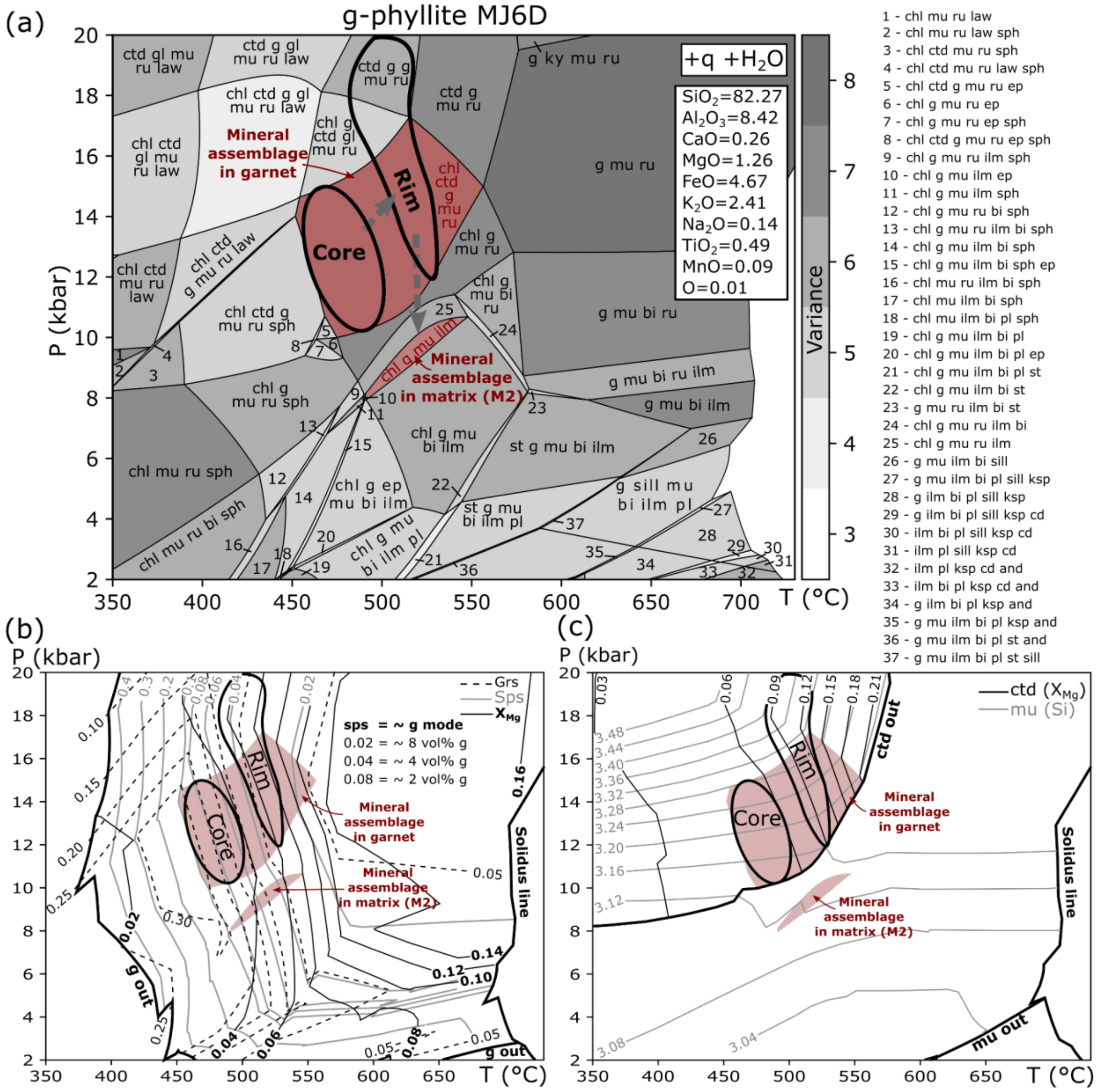

Figure I.9. (a) P–T pseudosection for the garnet-phyllite MJ6D (whole rock composition in mol %). In red are shown mineral assemblages in the garnet and in M2 matrix. Black ellipses show the intersection of isopleths in garnet core and rim. The dashed gray arrow represents a possible P–T path from the garnet core to the rim and then to the M2 mineral assemblage. (b) Isopleths of garnet (X_{Mg}, Grs, Sps) and garnet mode. (c) Isopleths of chloritoid (X_{Mg}) and muscovite (Si in a.p.f.u.).

The garnet rim composition ($Grs_{0.11}$ $Sps_{0.04}$ $X_{Mg} = 0.06$, Figure I.7a) together with composition of chloritoid inclusions ($X_{Mg} = 0.08–0.12$, Figure I.6b) and medium-to-high-Si muscovite (Si = 3.20–3.38 a.p.f.u., Figure I.6a) suggest that the garnet rim equilibrated at 12–20 kbar and 480–530 °C. The higher pressure estimate for the garnet rim reaches the stability field of glaucophane, which was not found in the sample but its mode predicted by the pseudosection is very low (< 1%). Although the lower-pressure estimate is compatible with the lack of glaucophane, the maximum Si content observed in muscovite (up to Si = 3.38 a.p.f.u., Figure I.6a) is reproduced only for the highest pressure estimate, although these isopleths become steeper at *HP*.

The M2 event is characterized by less-phengitic muscovite (Si = 3.06–3.20 a.p.f.u., Figure I.6a), ilmenite, chlorite and the absence of biotite and chloritoid in the matrix. This mineral assemblage q-mu-chl-ilm-g is stable above the biotite-in line at 8–10 kbar and 490–550 °C (Figure I.9a) still within the garnet stability field. The pseudosection shows that during decompression from the peak M1 conditions to the assumed M2 conditions, the garnet mode remains the same and its composition does not significantly change (Figure I.9b). This is compatible with the lack of evidence for garnet growth or its resorption related to M2. Muscovite with lowest Si content (Si = 3.06–3.08 a.p.f.u., Figure I.6a) could be considered as a product of later static re-equilibration during the M3 or M4 event.

5.3 - P–T EVOLUTION OF THE CHLORITOID-GARNET MICASCHIST

P–T pseudosection for the chloritoid-garnet micaschist MJ218A is shown in Figure I.10a. The stable mineral assemblage preserved as inclusions in garnet core and rim I q-g-ctd-ru-mu-chl corresponds to the stability field at 10–17 kbar and 455–560 °C (Figure I.10a). The isopleths for the compositional range of the garnet core ($Grs_{0.14\rightarrow0.07}$ $Sps_{0.08\rightarrow0.07}$ X_{Mg} = 0.04→0.05, Figure I.7b) are subparallel. However, within this field, the observed garnet core compositions restrict the *P–T* conditions to 11–15 kbar and 480–510 °C.

The compositional isopleths for the garnet rim I ($Grs_{0.07}$ $Sps_{0.03}$ X_{Mg} = 0.06, Figure I.7b) together with the composition of chloritoid inclusions in the garnet rim I (X_{Mg} = 0.09–0.12, Figure I.6b) document a slight increase in *P–T* conditions to 12–15 kbar and 500–530 °C in the same stability field.

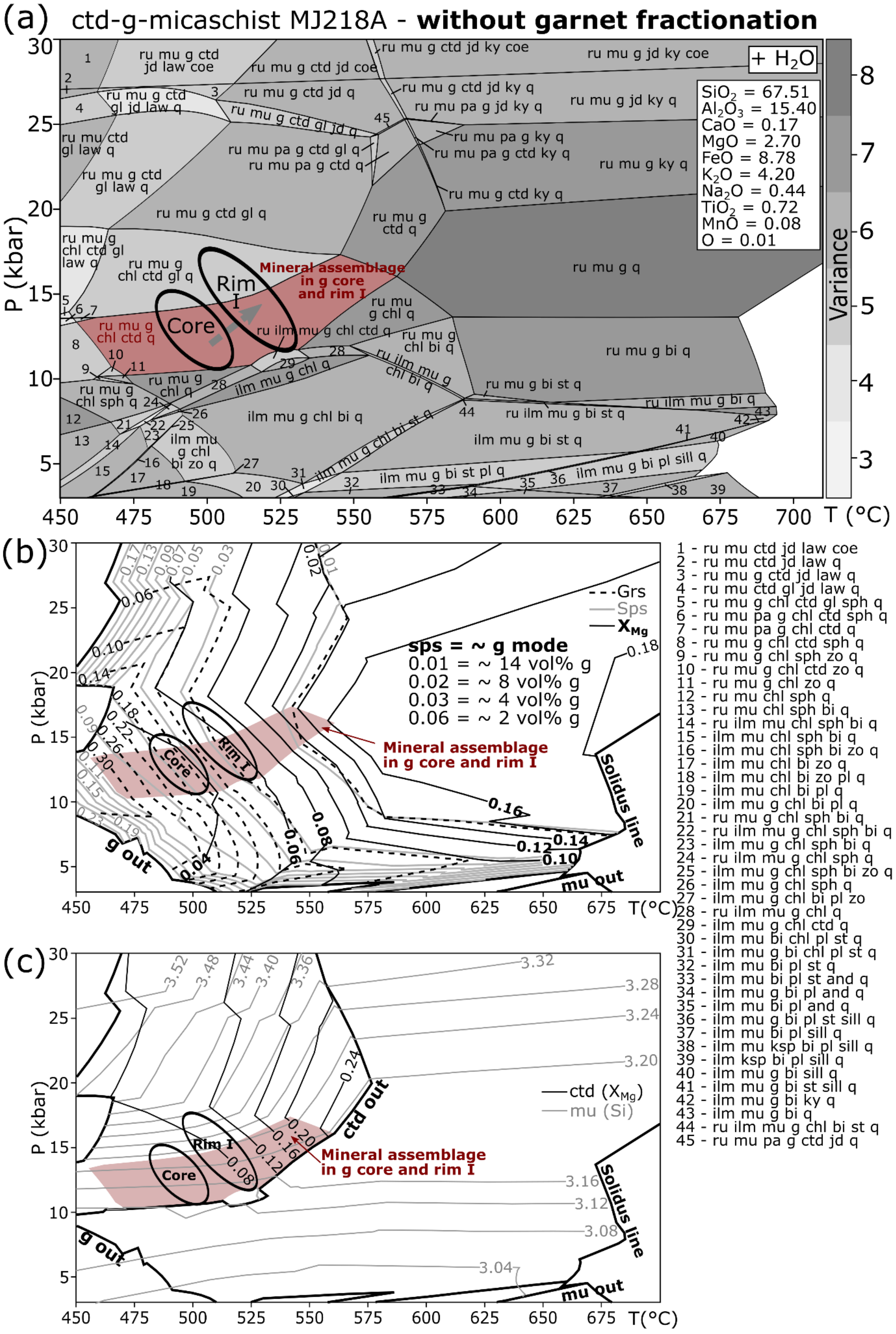

Figure I.10. (a) P–T pseudosection for the chloritoid-garnet micaschist MJ218A without garnet fractionation (whole rock composition in mol %). In red is shown the mineral assemblage in garnet core and rim I. Black ellipses show the intersection of isopleths in garnet core and rim I. The dashed gray line with an arrow presents a possible P–T path from the garnet core to the rim I. (b) Isopleths of garnet (X_{Mg}, Grs, Sps) and garnet mode. (c) Isopleths of chloritoid (X_{Mg}) and muscovite (Si in a.p.f.u.).

Due to the significant amount of garnet in this sample and its pronounced chemical zoning, the garnet core and rim I were fractionated from the bulk rock composition and a new pseudosection was calculated (Figure I.11) to evaluate *P–T* conditions for the garnet rim II. The compositional isopleths of the garnet rim II ($Grs_{<0.01}$ $Sps_{<0.01}$ X_{Mg} = 0.06–0.14, Figure I.7e), inclusions of chloritoid (X_{Mg} = 0.15–0.17, Figure I.6b), phengitic muscovite (Si = 3.27–3.47 a.p.f.u., Figure I.6a) and paragonite (X_{Na}=0.98–1.00, Figure I.6c) intersect at 24–26 kbar and 555–570 °C (Figure I.11a). These *P–T* conditions are in agreement with the garnet rim II inclusions that define the garnet rim II assemblage q-g-ctd-ru-mu-pa corresponding to the relatively small stability field highlighted in red in Figure I.11a. This high pressure *P–T* estimate is in agreement with the increased phosphorus and sodium content in the garnet rim II (Figure I.7e; Table I.2; Brunet et al., 2006; Thompson, 1975). The very high phengite content (up to Si = 3.47 a.p.f.u.) in some muscovite grains in the matrix and garnet rim II is not reproduced by the pseudosection. Such phengite contents occur in the pseudosection at *UHP* conditions, however coesite, jadeite or kyanite were not observed in the sample.

The minerals defining the M2 matrix are g-q-ru-mu-ctd-chl corresponding to the large stability field at 11–18 kbar and 455–570 °C (Figure I.11a). For the M2 matrix, the compositional isopleths of phengitic muscovite (Si = 3.18–3.47 a.p.f.u., Figure I.6a; Table I.3) and chloritoid from the matrix (X_{Mg} = 0.18–0.23, Figure I.6b; Table I.3) narrow this range to 15–18 kbar and 545–565 °C.

The M3 overprint is characterized by less-phengitic muscovite (Si = 3.10–3.23 a.p.f.u., Figure I.6a), biotite (X_{Mg} = 0.37–0.41, Figures I.6c and I.11c), chlorite (X_{Mg} = 0.40–0.46, Figures I.6d and I.11c) and ilmenite. In the pseudosection, the compositional isopleths matching the observed composition of the M3 minerals intersect at 8–13 kbar and 560–580 °C in the garnet stability field (see the M3 black ellipse in Figure I.11a). The mineral assemblage q-mu-chl-ilm-bi-g corresponds to the red stability field at 5–12 kbar and 500–590 °C (Figure I.11a). The composition of the M3 minerals further restricts this *P–T* range to 9 kbar and 580 °C (see the black star in Figure I.11).

Garnet shows no evidence for neither growth nor resorption related to M2 and M3, which is in agreement with the pseudosection which predicts no change in garnet mode during the decompression (Figure I.11). These observations indicate that garnet can be considered as a stable mineral of the M2 and M3 assemblages.

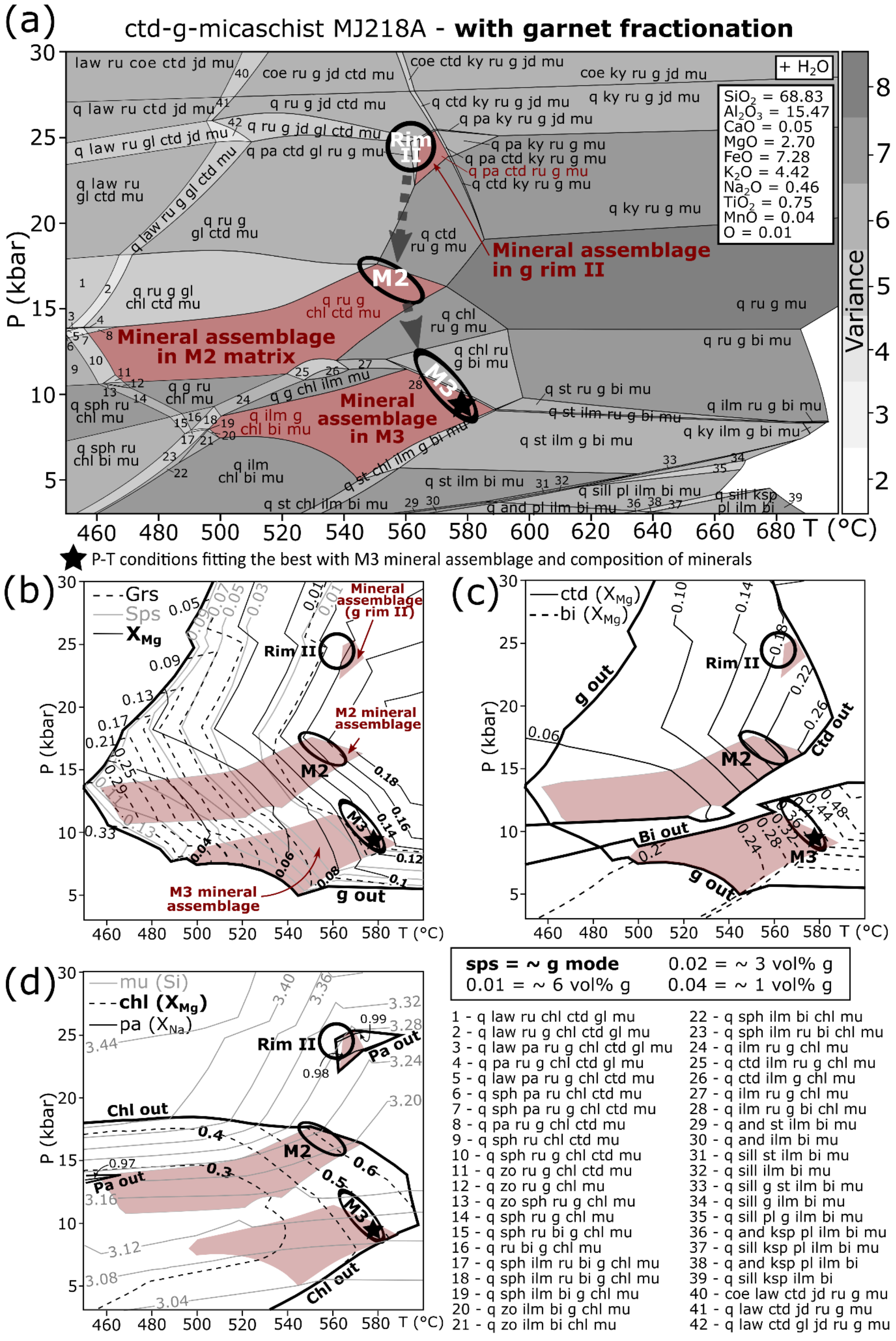

Figure I.11. (a) P–T pseudosection for the micaschist MJ218A with garnet fractionation (whole rock composition in mol %). In red are shown the mineral assemblages in garnet rim I, M2 and M3 matrix. Black ellipses show the intersection of isopleths in garnet rim II, M2 and M3 matrix. The star shows the P–T conditions fitting the best with M3 mineral assemblage and composition of minerals. The dashed grey lines with an arrow present a possible P–T path from the garnet rim II to the M2 and M3 matrix. The garnet mode is shown as inset. (b) Isopleths of garnet (X_{Mg}, Grs, Sps). (c) Isopleths of chloritoid (X_{Mg}) and biotite (X_{Mg}). (d) Isopleths of muscovite (Si in a.p.f.u.), paragonite (X_{Na}) and chlorite (X_{Mg}).

5.4 - P–T EVOLUTION OF THE STAUROLITE-GARNET MICASCHIST

Figure I.12 presents the *P–T* pseudosection for the staurolite-garnet micaschist MJ58B. The stable garnet core and rim I mineral assemblage M1 is q-g-ru-mu-pa-chl-ctd, which corresponds to the large stability field highlighted at 12–18 kbar and 460–580 °C (Figure I.12a). The garnet core composition ($Grs_{0.22\rightarrow0.08}$ $Sps_{0.06\rightarrow0.04}$ $X_{Mg}=0.05\rightarrow0.07$, Figure I.7c) constrains the *P–T* estimate to 12–15 kbar and 480–510 °C within this field.

The intersection of garnet isopleths matching the garnet rim I composition ($Grs_{0.08\rightarrow0.06}$ $Sps_{0.04\rightarrow0.02}$ $X_{Mg}=0.07\rightarrow0.10$, Figure I.7c) shows equilibration at 13–16 kbar and 510–535 °C, still in the same stability field. Composition of chloritoid enclosed in the garnet rim I (X_{Mg} = 0.15–0.19, Figure I.6b) is roughly compatible with this *P–T* estimate.

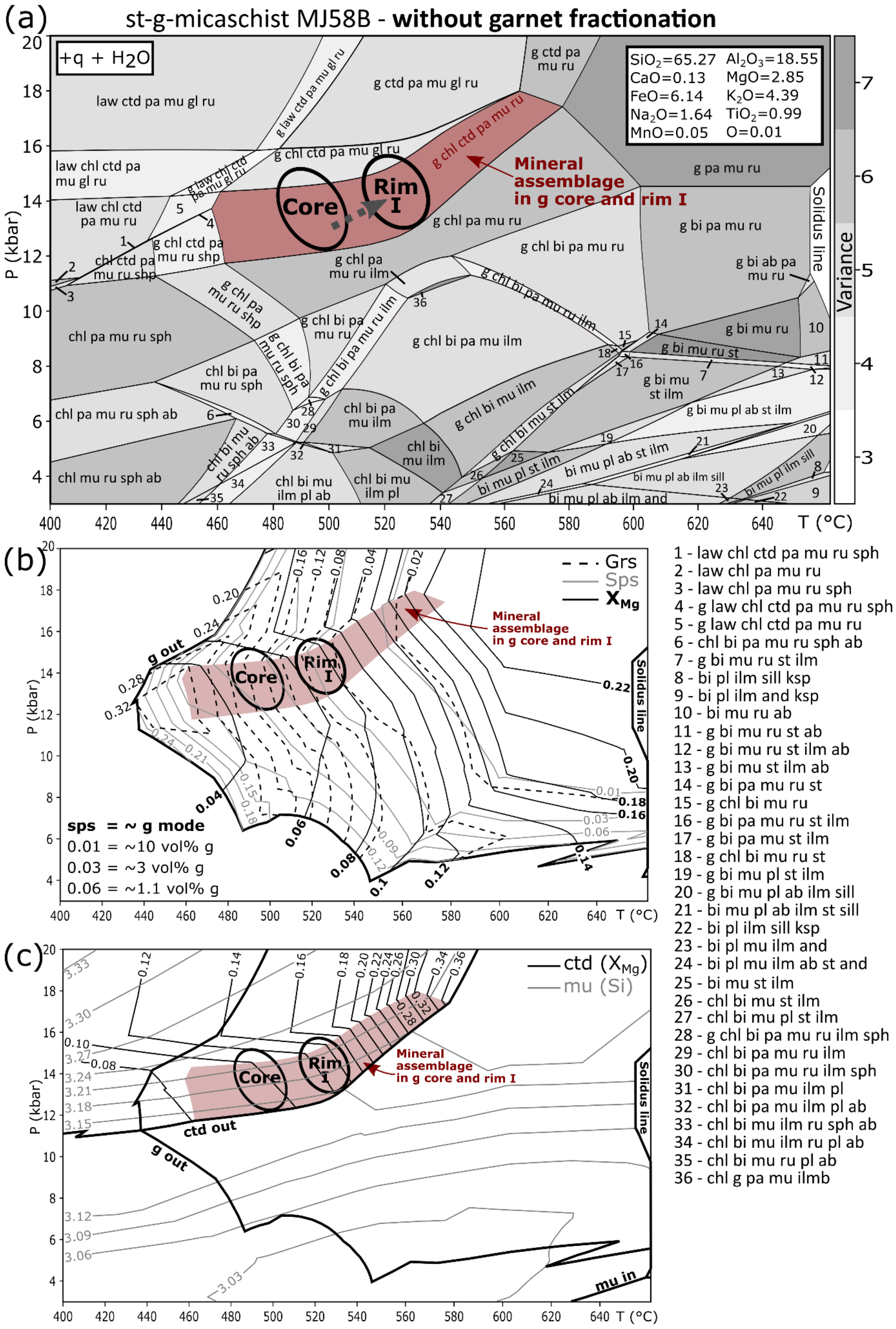

Figure I.12. (a) P–T pseudosection for the staurolite-garnet micaschist MJ58B without garnet fractionation (whole rock composition in mol %). In red is shown the mineral assemblage in garnet core and rim I. Black ellipses show the intersection of isopleths in garnet core and rim I. The dashed gray line presents a possible P–T path from the garnet core to the rim I. (b) Isopleths of garnet (X_{Mg}, Grs, Sps) and garnet mode. (c) Isopleths of chloritoid (X_{Mg}) and muscovite (Si in a.p.f.u.).

To assess the *P–T* conditions of the garnet rim II, fractionation of the garnet core and rim I from the bulk rock composition was performed (Figure I.13a). The composition of the garnet rim II ($Grs_{<0.01}$ $Sps_{<0.01}$ X_{Mg}=0.10→0.19, Figure I.7c) restricts the *P–T* estimate to 18–21 kbar and 565–580 °C (Figure I.13) to the field g-pa-mu-ru-ctd-q, compatible with the composition of the muscovite inclusions (Si=3.18–3.22 a.p.f.u., Figures I.6a and I.13c) in the rim II. However the observed X_{Mg} of chloritoid (X_{Mg}=0.21–0.22, Figures I.6b and I.13c) in the rim II is slightly lower than that predicted by the pseudosection, which may be caused by entrapment of inclusions from the early prograde stage or later diffusion driven re-equilibration with the garnet at high temperature. Such a high pressure estimate is further supported by the elevated sodium and phosphorus in the garnet rim II (Figure I.7f, Table I.2, Brunet et al., 2006; Thompson, 1975) and by high Si in muscovite in matrix (Si up to 3.32 a.p.f.u., Figure I.6a) and overall similarity with the sample MJ218A.

As chloritoid is not present in the matrix, the M2 mineral assemblage q-g-ru-mu-pa-chl corresponds to the large stability field highlighted at 12–17 kbar and 515–605 °C (Figure I.11a). The compositional isopleths of phengitic muscovite in M2 matrix (Si = 3.16–3.32 a.p.f.u., Figure I.6a; Table I.3) narrow this range at 13–17 kbar and 545–605 °C.

Another pseudosection using the effective bulk rock composition covering the minerals of the well-equilibrated M3 domains was calculated to characterize the M3 event (Figure I.4g). The resulting pseudosection (inset in Figure I.13a) shows similar topology to the pseudosection calculated with fractionated garnet core and rim I composition, except the rutile / ilmenite-in lines shifted to lower pressure, the staurolite field is wider in P and T and it has a higher solidus temperature. As garnet is replaced by M3 chlorite, biotite and staurolite, the stable M3 assemblage is defined as q-bi-mu-ilm-st-chl, corresponding to the stability field highlighted at 5–8 kbar and 550–595 °C (inset in Figure I.13a). The compositional isopleths of M3 staurolite (X_{Mg} = 0.15–0.19, Figure I.6c), muscovite (Si = 3.02–3.14 a.p.f.u., Figure I.6a) and chlorite (X_{Mg} = 0.49, Figure I.6d) are compatible in this field (inset in Figure I.13c).

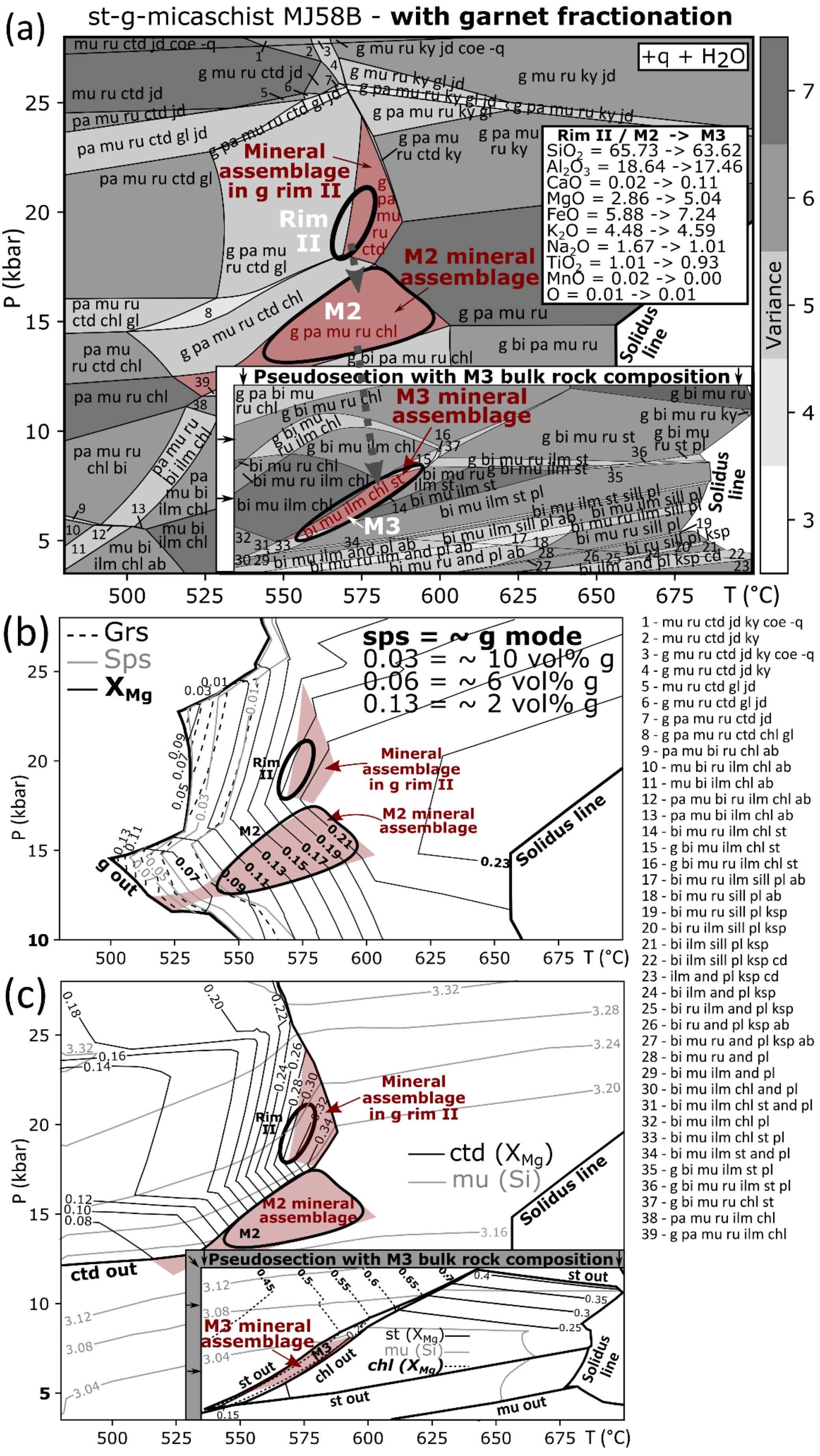

1 - mu ru ctd jd ky coe -q
2 - mu ru ctd jd ky
3 - g mu ru ctd jd ky coe -q
4 - g mu ru ctd jd ky
5 - mu ru ctd gl jd
6 - g mu ru ctd gl jd
7 - g pa mu ru ctd jd
8 - g pa mu ru ctd chl gl
9 - pa mu bi ru chl ab
10 - mu bi ru ilm chl ab
11 - mu bi ilm chl ab
12 - pa mu bi ru ilm chl ab
13 - pa mu bi ilm chl ab
14 - bi mu ru ilm chl st
15 - g bi mu ilm chl st
16 - g bi mu ru ilm chl st
17 - bi mu ru ilm sill pl ab
18 - bi mu ru sill pl ab
19 - bi mu ru sill pl ksp
20 - bi ru ilm sill pl ksp
21 - bi ilm sill pl ksp
22 - bi ilm sill pl ksp cd
23 - ilm and pl ksp cd
24 - bi ilm and pl ksp
25 - bi ru ilm and pl ksp
26 - bi ru and pl ksp ab
27 - bi mu ru and pl ksp ab
28 - bi mu ru and pl
29 - bi mu ilm and pl
30 - bi mu ilm chl and pl
31 - bi mu ilm chl st and pl
32 - bi mu ilm chl pl
33 - bi mu ilm chl st pl
34 - bi mu ilm st and pl
35 - g bi mu ilm st pl
36 - g bi mu ru ilm st pl
37 - g bi mu ru chl st
38 - pa mu ru ilm chl
39 - g pa mu ru ilm chl

Figure I.13. (a) P–T pseudosection for the staurolite-garnet micaschist MJ58B with garnet fractionation (whole rock composition in mol % - average composition of the core and the rim I of the garnets) and pseudosection with M3 bulk rock composition (bulk rock composition measured only in M3 domain) in the inset. In red are shown the mineral assemblages in garnet rim II, M2 and M3 matrix. Black ellipses show the intersection of isopleths in garnet rim II, M2 and M3 matrix. The dashed grey lines with an arrow present a possible P–T path from the garnet rim II to the M2 and M3 matrix. (b) Isopleths of garnet (X_{Mg}, Grs, Sps) and garnet mode. (c) Isopleths of chloritoid (X_{Mg}) and muscovite (Si in a.p.f.u.) in the rim II of the garnet and M2 matrix. In the inset: isopleths of muscovite (Si in a.p.f.u.), staurolite (X_{Mg}) and chlorite (X_{Mg}) for the M3 matrix.

5.5 - RUTILE-ILMENITE OCCURRENCES

Rutile is typically surrounded by an irregular rim of ilmenite with an ameboidal interface between the two minerals (Figure I.4c,h). Calculated *P–T* pseudosections for the M1 and M2 mineral assemblages fit well with the observations, however, differ with respect to the accessory rutile-ilmenite occurrences. Inclusions of ilmenite in garnet (Figures I.3e, I.4b,h and I.7a,b,c) or in chloritoid blasts (Figure I.3b,c) are sometimes present even if the predicted assemblage fields at *HP* conditions lack ilmenite. However, the ilmenite inclusions typically occur in the vicinity of fractures communicating with the M3 matrix and in some cases preserve incomplete replacement of original rutile by ilmenite (Figure I.4b,c,h). Additionally, complex rutile-ilmenite transitions due to interplay of detrital and metamorphic origin were described by Luvizotto et al. (2009) in metasediments in this area. Therefore the discrepancies between predicted and observed rutile-ilmenite stability are not considered as a major constraint for the estimation of *P–T* conditions.

6 - DISCUSSION

Previous research on Erzgebirge *HP* rocks in combination with the results of this study allowed us to characterize geodynamic processes related to the transition from the accretionary prism and subduction phase towards the development of an orogenic wedge. Firstly, we discuss the *P–T* evolution of metamorphic events in context of the individual metamorphic fabrics in each unit. Secondly, the tectonic significance of the metamorphic and deformation events is discussed in the context of structural position, *P–T* evolution and the thermal and tectono-architecture of lithological complexes in the former active margin.

6.1 - BURIAL AND DECOMPRESSION DURING THE SUBDUCTION STAGE

The M1 and M2 events in the studied phyllites and micaschists are associated with the growth of typical *HP–LT* minerals such as chloritoid, phengitic mica (Si up to 3.47 a.p.f.u., Figure I.6a), paragonite, garnet, rutile and chlorite as observed by previous authors (Faryad & Kachlík, 2013; Konopásek, 1998; Rahimi & Massonne, 2018, 2020; Roetzler et al., 1998; Willner et al., 2000).

Most earlier studies suggested that garnet in the micaschists grew during a slight temperature increase along the decompression *P–T* path (e.g. Rahimi & Massonne, 2018, 2020; Roetzler et al., 1998; Willner et al., 2000). This conclusion was drawn based on the garnet chemical composition and folded inclusion trails in garnet combined with the decrease of Si content in the matrix muscovite. The calculated pseudosections show that compositional isopleths of garnet are mostly temperature dependent at *HP* conditions, which prevents unequivocal constraints on the pressure evolution during the garnet growth. However, our study clearly demonstrates that the garnet growth reflects burial *P–T* path because: i) the garnet rim II contains inclusions of *HP* minerals (chloritoid, high Si phengite, paragonite, rutile); ii) the M3 minerals like biotite, chlorite and staurolite were not found as inclusions in garnet, but instead surround and replace garnet; iii) the garnet rim II is enriched in phosphorus and sodium content with P>Na (Figure I.7e,f; Table I.2). The presence of trace amounts of these elements in garnet has been reported to indicate *(U)HP* conditions in other terrains (Schertl et al., 1991; Ye et al., 2000) and experimental work (Brunet et al., 2006; Konzett & Frost, 2009; Thompson, 1975).

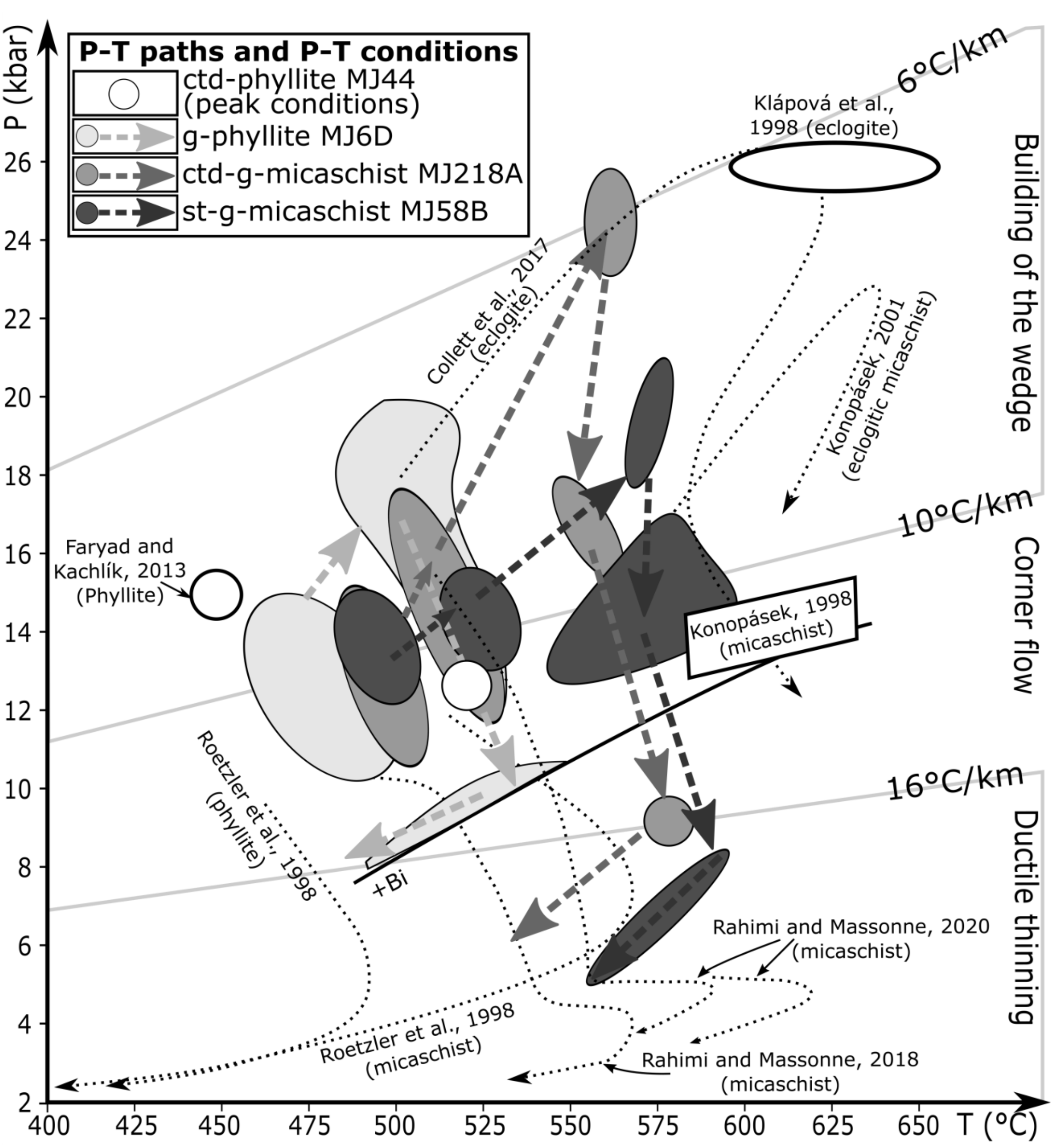

Figure I.14. Summary of P–T conditions for the four studied samples and interpretative P–T paths shown by the thick dashed lines with an arrow. For the chloritoid-phyllite MJ44, the white circle represents the peak conditions. These P–T paths are compared with previous studies. The geothermal gradients visible by the gray lines are associated with prograde subduction (building of the wedge), corner flow and ductile thinning.

In the phyllites, the chloritoid-bearing garnet-free assemblage probably represents the peak pressure conditions of M1-2 metamorphism, while in garnet bearing phyllites and micaschists, M1 and M2 can be distinguished. The early prograde history M1 is recorded by the garnet growth (Figure I.14), while the partial decompression of the matrix is related to M2. The overlap of the maximum *P–T* conditions inferred for phyllites with the *P–T* conditions of the early prograde record in micaschists suggests a common early metamorphic history in similar tectonic setting. This *HP* event showed that from the phyllites in the NW towards the micaschists in the SE, the peak *P–T* conditions continuously increase from 13 kbar and 520 °C up to 25 kbar and 560 °C (Figures I.14 and I.15a), and define a coherent *HP–LT* geothermal gradient ranging from 6 to 11 °C/km (Figure I.14) typical for subduction environment. The new peak pressure estimate for the Erzgebirge micaschists (up to 25 kbar, Figure I.14) is comparable to the previous estimates for eclogite facies rocks (eclogite, marble, eclogitic micaschist) in this region (Collett et al., 2017; Gross et al., 2008; Klápová et al., 1998; Konopásek, 2001; Kulhánek et al., 2021; Massonne, 2012; Massonne & Kopp, 2005; Schmädicke et al., 1992). The estimated peak *P–T* conditions point to a common metamorphic field gradient and thermal structure typical for growth of the accretionary/orogenic wedges above subduction zones (Vanderhaeghe et al., 2003; Vogt & Gerya, 2014).

P–T modelling of the M2 matrix revealed a partial decompression event, which is also supported by the zoning of muscovite with high-Si cores and lower-Si rims (e.g. Konopásek, 1998; Kröner et al., 1995; Rahimi & Massone 2018, 2020; Schmädicke et al., 1995). Such decompression may be linked either to the return flow within the subduction channel or to corner flow in the rear part of the orogenic wedge (Agard et al., 2009; Feehan & Brandon, 1999; Gerya et al., 2002; Platt, 1993, Figure I.15). The lower pressure estimates of phyllites and micaschists reported by Faryad and Kachlík (2013), Konopásek (1998), Rahimi & Massonne (2018, 2020) and Roetzler et al. (1998) summarized in Figure I.14 may reflect the conditions of the M1-2 re-equilibration at lower pressure.

In addition, folded inclusion trails in garnet and in chloritoid porphyroblasts and oscillatory zoning in the garnet rim described by Schumacher et al. (1999) further support a complex structural evolution typical for the subduction channels and orogenic wedges.

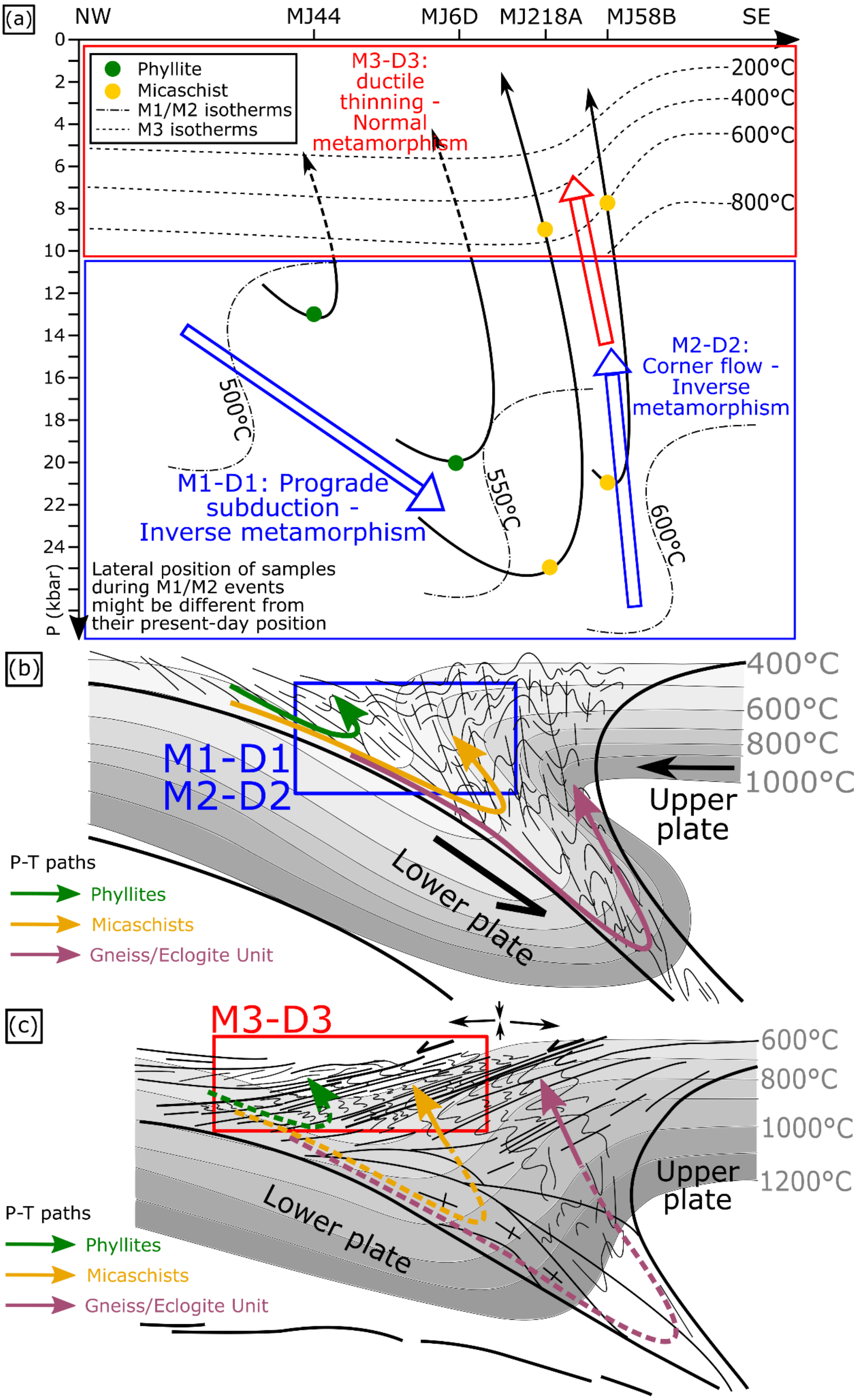

Figure I.15. (a) Summary of P–T position of the samples in the accretionary wedge during convergence and exhumation. The isotherms show a probable inverse metamorphic zoning during M1 and M2 and a normal metamorphism during M3. (b) Idealized thermal and tectono-structures during ongoing subduction and corner flow and (c) subsequent ductile thinning.

6.2 - OROGENIC WEDGE THINNING

Our structural observations indicate that the studied area experienced intense vertical shortening related to the D3 deformation. In the footwall micaschists, this event is associated with the development of axial-planar biotite-staurolite bearing *MP–MT* metamorphic foliation S3. The intriguing feature is the geometrical coherence between this S3 fabric in micaschists and the dominant S2 fabric in phyllites (Figure I.1c,d,e). Based on the crystallization-deformation relationships (Figure I.5) and thermodynamic modelling (Figures I.8 to I.13), the S2 fabric in phyllites was however developed under the *HP–LT* conditions. The distinction of these two fabrics is based not only on the relative structural record, but more importantly on the metamorphic assemblages defining the two individual fabrics. Such contrasting metamorphic field gradients for phyllites S2 and micaschists S3 clearly did not occur simultaneously, and thus the geometrical coherence is explained as a result of a reorientation of the S2 fabric during the vertical shortening D3. Indeed, this re-orientation of the S2 fabric in phyllites is also supported by the occurrence of asymmetric F3 folds in the vicinity of the phyllites-micaschists boundary (Figures I.1e and I.2f), which marks the transition between the limb and hinge domains of the large scale recumbent fold.

The M3 metamorphism in micaschists reflects normal metamorphic zoning and barrovian-type geothermal gradients in the range of 17 to 30 °C/km during the D3 event (Figures I.14 and I.15a,c). Our *P–T* estimates for M3-D3 event in micaschists are 5–9 kbar and 555–595 °C (Figures I.14 and I.15a), which are comparable to the previous estimates by Roetzler et al. (1998) and Rahimi & Massonne (2018, 2020) (Figure I.14). Previous studies in this area proposed a decompression *P–T* path along with a slight heating (Roetzler et al., 1998, Figure I.14) followed by an isobaric heating event (Rahimi & Massonne, 2018, 2020, Figure I.14). In our study, the increase of temperature in micaschists during decompression from M1 (555–580 °C) to M3 (555–595 °C) is not so significant as in the studies of Rahimi & Massonne (2018, 2020), who proposed heating by 50–100 °C, or Roetzler et al. (1998), who proposed heating by 90–130 °C (Figure I.14). Furthermore, the *P–T* path constructed for eclogite in micaschists by Collett et al. (2017) assumes a decrease of pressure and cooling followed by additional pressure decrease and heating to conditions of 620 °C at 12 kbar (Figure I.14).

During the vertical shortening D3, the S2 fabric in phyllites was only heterogeneously reactivated. Nevertheless, the biotite-free assemblages in phyllites contrast with biotite-bearing assemblages in micaschists and implies a significant difference in temperature conditions of the D3 deformation across the phyllite-micaschist boundary. The vertical shortening in micaschists associated with their near-isothermal decompression from ~14 kbar to ~6 kbar reflects their juxtaposition to the hanging wall phyllites along a high-strain shear zone separating these two contrasting structural levels. The possible interpretation of such fabric evolution is shown in Figures I.1e and I.15c.

Our data, together with the previously published *P–T* estimates, show systematic correlation between the peak conditions of the M1 and M3 events, i.e. the higher *P–T* conditions were attained during M1-D1 and the higher temperature peak occurred during M3-D3 in all allochthonous units. This is interpreted as a result of heat advection by the deeply subducted rocks during the exhumation followed by the thermal relaxation and heating of lower pressure rocks (Figure I.15).

7 - CONCLUSIONS AND GEODYNAMIC IMPLICATIONS

The above described M1-D1 evolution is associated with progressive subduction and accretion of the subducted material during transition from the accretionary prism to the orogenic wedge formed above the subducting lithosphere. The differences in the tectonometamorphic evolution of the individual Erzgebirge units allow us to identify their original positions within the orogenic wedge (Figure I.15b): i) the lowest peak pressure conditions during the M1-M2 events and generally gently-inclined S2 foliation place the phyllites to the frontal part of the wedge (the former accretionary prism); ii) the higher-pressure M1-M2 metamorphism and steep S2 fabric place the micaschists to the rear part of the wedge affected by ductile thickening; iii) the ultra-high-pressure and temperature conditions and the presence of mantle fragments place the Gneiss/Eclogite Unit to the subduction channel environment (Schmädicke & Evans, 1997). The current spatial distribution of these crustal segments shows that the frontal part of the orogenic wedge is located in the western part of the Erzgebirge, while the rear and deepest part of the wedge is located mostly to the east. It is suggested that such a distribution of units may reflect the original eastward subduction associated with the D1-D2 stage. Based on the existing geochronological data, this phase occured between c. 350-340 Ma (Kotková et al., 2016; Závada et al., 2021). The E-W convergence has been reported from numerous places in the Bohemian Massif and is restricted to the period 390-340 Ma (Edel et al., 2018; Jeřábek et al., 2016; Konopásek et al., 2019; Peřestý et al., 2017; Racek et al., 2017).

The subsequent D3 event is characterized by the intense vertical shortening and E-W extension of the orogenic wedge (Kryl et al., 2021). The existing $^{40}Ar/^{39}Ar$ data constrain this deformation to 335–330 Ma (Werner & Lippolt, 2000; Willner et al., 2000). The D3 deformation is heterogeneously developed and localized into the high-strain zones which in the present day geometry follow boundaries between the individual Erzgebirge units. Most of these high-strain zones operated as localized shear zones/detachments and were responsible for lateral juxtaposition of the distinct parts of the orogenic wedge (Kryl et al., 2021; Willner et al., 2000). In other words, the Erzgebirge tectonometamorphic units exhibit coherent M1 metamorphic record (reflecting the evolution of the corresponding part of the orogenic wedge), while their spatial arrangement and extent is largely controlled by the D3 detachment zones (Figure I.15b,c).

We are of the opinion that such a dualism in the definition of tectonometamorphic units in Erzgebirge introduces a major obstacle in thoroughly understanding the Erzgebirge tectonic evolution. The multi-stage evolution proposed here untangles the processes of orogenic wedge building and its extensional collapse that can be traced along the entire western margin of the Bohemian Massif (e.g. Jeřábek et al., 2016).

PART II: ASSEMBLY OF THE SAXOTHURINGIAN OROGENIC WEDGE: GEOCHRONOLOGY

1 - INTRODUCTION

Many geochronological studies were performed in the Erzgebirge area of the Saxothuringian Domain, mostly based on zircon, monazite and $^{40}Ar/^{39}Ar$ geochronology, especially in the core of Erzgebirge. However, no attempts have been made to link the published ages with the complex and polyphase tectonic evolution (Jouvent et al., 2022; Kryl et al., 2021) of the Saxothuringian orogenic wedge. Only Hallas et al. (2021) recently linked the $^{40}Ar/^{39}Ar$ ages to the retrograde evolution, but only on the *(U)HP* rocks. The timing of burial, peak *HP* metamorphism and exhumation is a subject of debate and a multidisciplinary study linking the ages to the deformation and metamorphic events is still missing. Most of the studies placed the *(U)HP* peak metamorphism at 340 Ma (Kotková et al., 1996; Kröner & Willner, 1998; Kylander-Clark et al., 2013; Massonne et al., 2007; Schmädicke et al., 1995; Tichomirowa et al., 2005, Tichomirowa & Köhler, 2013), directly followed by the exhumation at 340–330 Ma (Werner & Lippolt, 2000; Hallas et al., 2021). However, recent studies dated the *(U)HP* metamorphism at 360–350 Ma, while the age of 345–330 Ma is correlated with exhumation/retrogression at amphibolite facies conditions (Schmädicke et al., 2018; Závada et al., 2021).

This part II aims to reconcile the contrasting ages and interpretations by coupling the evolution of the *(U)HP–HT* core of the Erzgebirge dome with the newly described age record in the hanging wall phyllites and micaschists. The following study is based on the detailed monazite U-Pb geochronology using laser-ablation split-stream inductively coupled plasma mass spectrometry LASS-ICP-MS, Rare-Earth Elements (REE) geochemistry, *in-situ* and step-heating $^{40}Ar/^{39}Ar$ geochronology on micas, structural and petrographic analysis across the phyllite-micaschist transition zone. In this part, we highlight the tectonic evolution of the units over time and we show that the Saxothuringian orogenic wedge can be subdivided into older outer wedge, and younger transition zone and inner wedge. Additionally, this work documents that younger overprint is in some cases capable of complete or at least partial resetting of monazite, even enclosed in the core of garnet porphyroblasts without obvious REE or textural clues. Thus the best-intended use of *in-situ* geochronology on inclusions in porphyroblasts in order to trace the early metamorphic evolution may commonly be significantly biased.

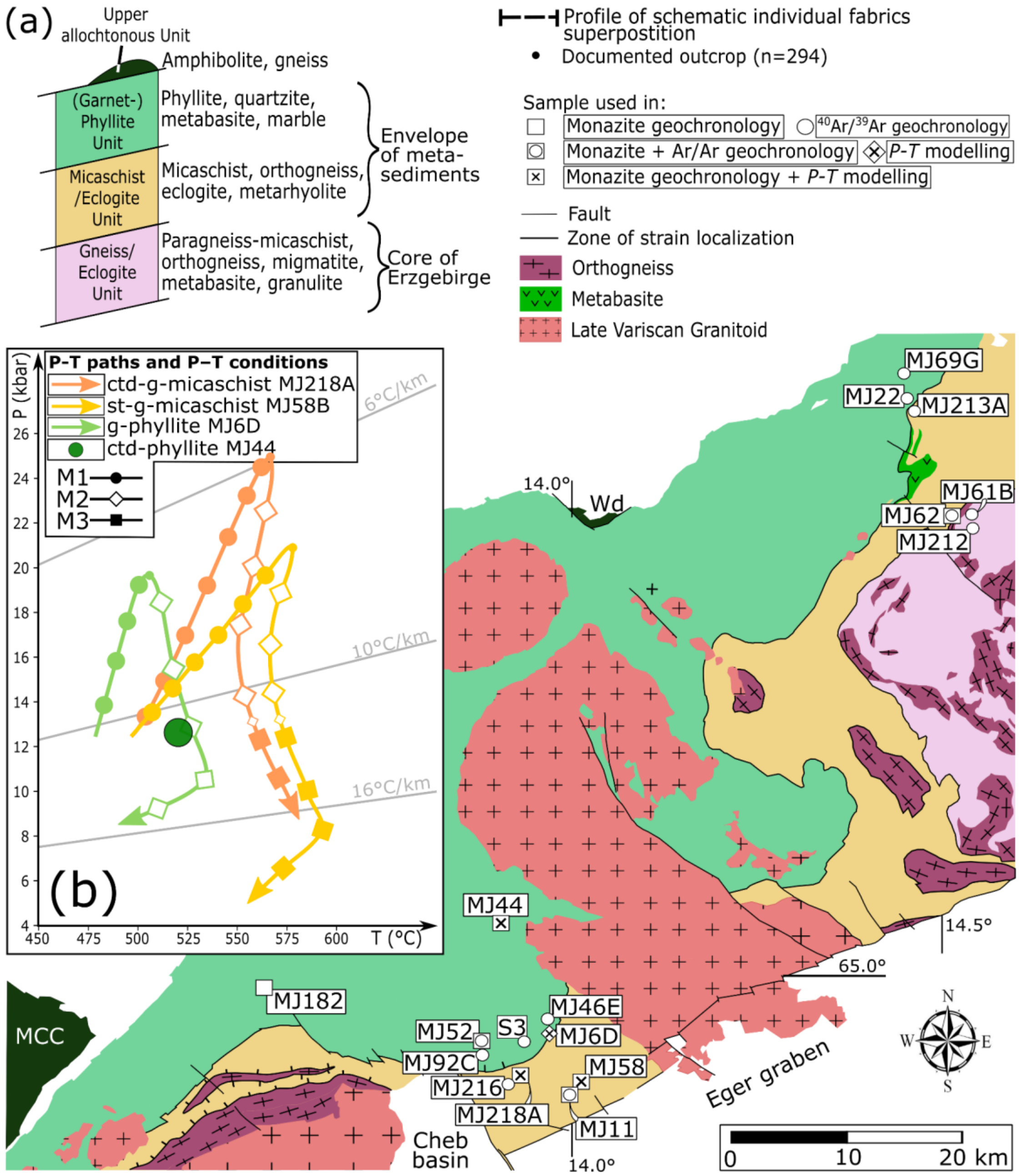

Figure II.1: (a) Simplified geological map of the Erzgebirge and Fichtelgebirge in the Saxothuringian (modified after Jouvent et al., 2022) showing the location of the samples studied by *P–T* modelling, monazite U-Pb dating and mica ^{40}Ar/^{39}Ar dating in this work. MCC: Münchberg Crystalline Complex; Wd: Wildenfels Massif. (b) *P–T* paths of phyllites and micaschists dated in part I (MJ44, MJ6D, MJ218A, MJ58), simplified from the data of Jouvent et al., 2022 with part of the *P–T* path related to M1, M2 or M3 events.

The studied phyllite and micaschist samples have been collected with regard to the previously characterized tectonometamorphic record described by Jouvent et al. (2022). Figure II.1a shows the location of the samples studied in part II by monazite U-Pb and $^{40}Ar/^{39}Ar$ geochronology, and the potential overlap with the samples studied on part I. The studied rocks show a complex polyphase deformation with clear differences between the phyllites and the micaschists. The distinction of four deformation stages D1-D4 associated with four planar fabrics S1-S4 and M1-M4 metamorphic stages proposed in part I (Jouvent et al., 2022) is followed in part II and the P-T conditions are summarized in Figure II.1b. However, because the influence of the retrograde part of M3 (chlorite, biotite) and M4 (chlorite) events on the mineral assemblages is hard to decipher, they are collectively referred as M3-M4 overprint in the following text.

2 - OROGENIC WEDGE FORMATION AND ZONING: EVIDENCE FROM MONAZITE U-PB GEOCHRONOLOGY

2.1 - METHODS

To constrain the age of complex fabric relations and of garnet growth, the micaschists were dated *in-situ* in thin-sections, while the more homogenous garnet-free phyllites were studied from mineral separates mounted in epoxy.

The crushing and separation of the monazite grains and mount preparation of the rock was performed at the Czech Geological Survey in Prague (Czech Republic). Prior to the analyses, the monazite grains were imaged by backscattered electrons (BSE) and secondary electrons (SE) using a field emission gun electron probe microanalyzer (FEG-EPMA) JXA-8530F (manufactured by Jeol), equipped with 5 wave dispersive spectrometers (WDS) at the Institute of Petrology and Structural Geology (Charles University, Prague). The compositional maps of monazite were acquired at 20 kV and 70 nA in spot mode with counting time 50 ms per point. Kα lines were used for detection of Si, Ca and P, Lα lines were used for detection of Sr, La, Nd and Y and Mα lines were used for detection of Th and U.

The monazite U/Th-Pb and Rare Earth Elements (REE) analyses were acquired by laser-ablation split-stream inductively coupled plasma mass spectrometry (LASS-ICP-MS) at the University of California (Santa Barbara, USA) with the cooperation of Andrew Kylander-Clark, expert in monazite U-Pb geochronology. This method allowed us to obtain analyses of isotope ratios and element concentrations from the same volume of analyses (see Kylander-Clark et al., 2013 for a detailed description of the method). Analyses were carried out using a Photon Machines Excite 193 nm laser coupled to a Nu Instruments Plasma HR (U-Pb isotopes) and an Agilent 7700 (element concentration), with an 8 µm spot at 3 Hz for 12 seconds, following a 2-pulse cleaning and 20 second baseline routine. Monazite reference material (RM) 44069 (424 Ma; Aleinikoff et al., 2006) was used as the primary U-Pb standard (every ~10 analyses) and Bananeira (Kylander-Clark et al., 2013) was used as the primary TE RM, assuming 12.9% P in the unknown monazite. Quality control was assessed by repeated measurements of Bananeira (512 Ma; Palin et al., 2013), Trebilcock (272 Ma;

Tomascak et al., 1996), Manangoutry and FC-1 (555 and 55.6 Ma, respectively; Horstwood et al., 2003); secondary RMs were within 2% of their accepted values. Age uncertainties (2σ) expressed in the text are first shown with analytical uncertainties followed by propagated uncertainties (2%) in brackets. Data was processed with Iolite v3.5 (Paton et al., 2011). For each analysis, the ^{238}U/^{206}Pb and ^{207}Pb/^{206}Pb isotopic ratios were plotted on Terra-Wasserburg diagrams using the online version of IsoplotR (Vermeesch, 2018) with anchored isochrons to the Stacey & Kramers (1975) common-Pb model. For discordant U-Pb isotopic ratios we report an intercept age based on a Stacey-Kramers common-Pb value (Stacey & Kramers, 1975).

2.2 - MICROSTRUCTURE AND PETROGRAPHY OF THE DATED SAMPLES

For the present geochronological study, eight samples (three phyllites and five micaschists) with well-defined fabric relations and mineral assemblages were selected for the monazite dating (for sample locations see Figure II.1a and Table II.1). The peak metamorphic grade of the studied samples generally increases from the structural hanging wall towards the footwall. Therefore, the samples are described in the order reflecting their metamorphic grade. The structurally highest chloritoid-phyllite MJ44 was collected from the central part of the phyllite belt, and the phyllite MJ182 and the chloritoid-phyllite MJ52D from its lower part. The micaschists closer to the boundary with the phyllites are represented by the chloritoid-garnet-micaschist MJ218A, followed by the staurolite-garnet-micaschists MJ58D and MJ58G – coming from the same outcrop MJ58 (Figure II.1a) – and the garnet-micaschist MJ11C. The structurally lowest is the garnet-micaschist MJ62B. The samples MJ218A, MJ44, MJ58 and MJ52 have been used for detailed petrographic descriptions and *P–T* estimates in the study of Jouvent et al. (2022). The samples dated here are from the same thin-section (MJ218A), the same rock sample (MJ44) or the same outcrop (MJ58 and MJ52) as in Jouvent et al. (2022). In all samples, accessory minerals are apatite, monazite, zircon, xenotime and tourmaline.

Unit	**Phyllite**			**Micaschist**			
Sample	**MJ182**	**MJ44**	**MJ52D**	**MJ218A**	**MJ58G / MJ58D**	**MJ11C**	**MJ62B**
Latitude	50.299985	50.34973	50.255421	50.232009	50.225984	50.220101	50.663563
Longitude	12.203348	12.490061	12.467586	12.514019	12.582822	12.574597	13.040747

Table II.1: GPS location of the samples used in this work. The samples MJ44, MJ52D, MJ218A, MJ58G, MJ58D2 and MJ62B are also described or shown in Jouvent et al., 2022.

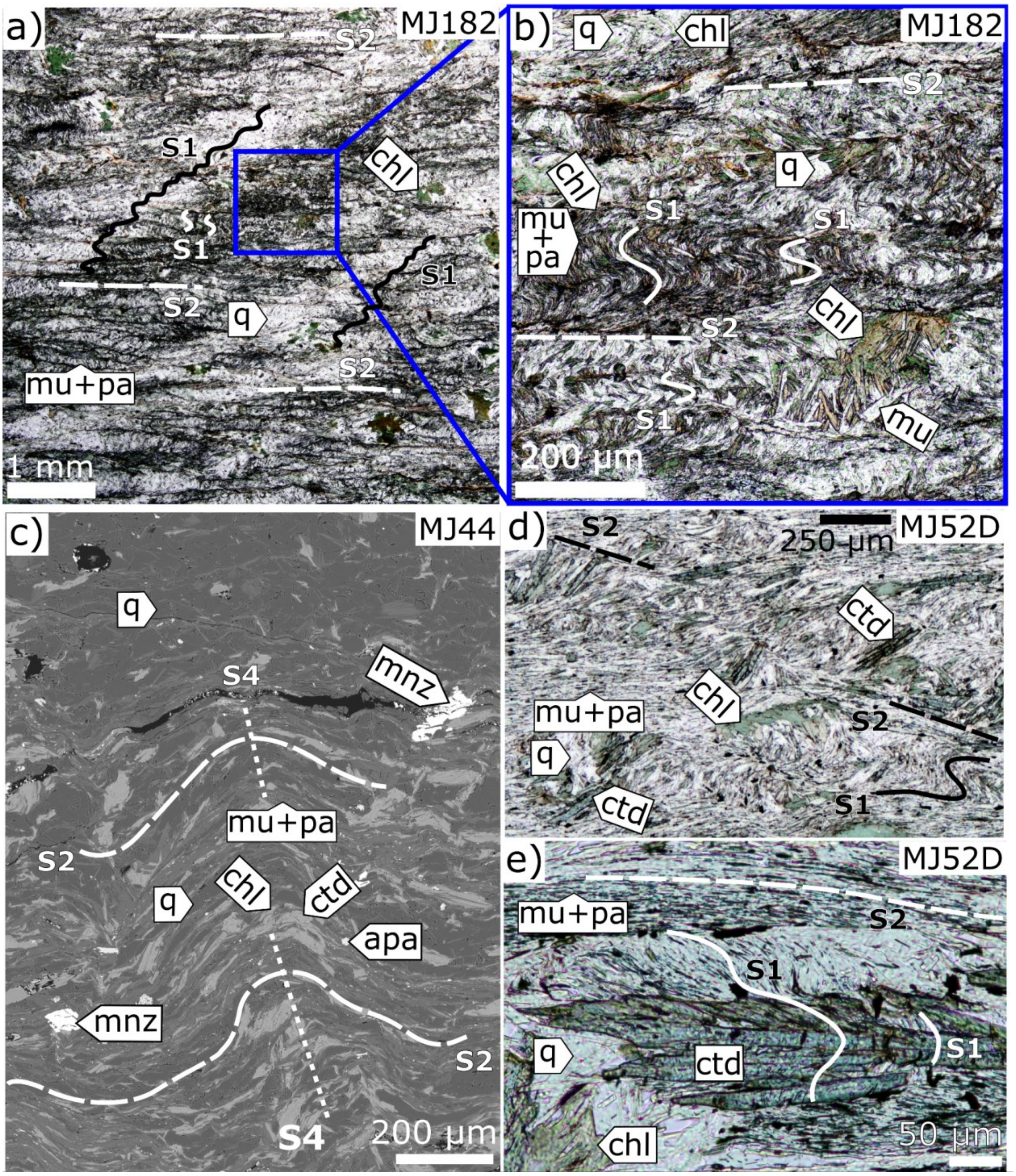

Figure II.2: Microphotographs (parallel polars) and back scattered images showing representative mineral assemblages, crystallization deformation relationships and monazite location in phyllites. More microphotographs and BSE images from the samples MJ44 and MJ52 are visible in Jouvent et al., 2022. (a, b) phyllite MJ182: bedding-parallel foliation S1 transposed to the main sub-horizontal fabric S2 (a). The zoom (b) shows q-mu-chl-pa bearing foliation S1 folded by the S2 fabric containing large chlorite aggregates. (c) ctd-phyllite MJ44: composite S2 foliation is crenulated by F4 folds. Chloritoid porphyroblasts are sometimes surrounded by chlorite. Monazites are visible within the S2 fabric; (d, e) ctd-phyllite MJ52D: S1 foliation (preserved in lithons) is transposed to the main sub-horizontal fabric S2. Chloritoid porphyroblasts surrounded by chlorite are aligned to S2 and inclusion trails of ilmenite and rutile in chloritoids follow the S1 foliation.

2.2.1 - MJ182 PHYLLITE

The sample MJ182 is a very fine grained phyllite that contains chlorite porphyroblasts and aggregates and preserves relics of early muscovite-chlorite bearing foliation S1 in lithons (Figure II.2a,b). The older S1 fabric is transposed into a strong sub-horizontal S2 crenulation cleavage (Figure II.2a). The M1 mineral assemblage is q-mu-chl-pa-ru-ilm and it is indistinguishable from the M2 assemblage in the S2 cleavage domains. The sample does not contain biotite, chloritoid nor garnet. Monazite grains (10–200 µm) occur in the matrix where they are intercalated with fine-grained muscovite, chlorite and paragonite. The monazite grains have anhedral to subhedral crystal shape and contain numerous paragonite, phengite, quartz, rutile, and tourmaline inclusion trails aligned with the S1 foliation.

2.2.2 - MJ52D CHLORITOID PHYLLITE

The chloritoid-phyllite MJ52D (Figure II.2d,e) is a very fine grained phyllite with q-mu-ctd-chl-pa-ru-ilm assemblage. It shows a strong transposition of S1 to S2 foliation with only locally preserved S1 lithons. The main composite foliation S2 is gently folded by S4 cleavage. Chloritoid porphyroblasts are aligned along the S2 foliation and are surrounded by chlorite (Figure II.2e). This sample does not contain garnet nor biotite. Monazite most often appears in the fine-grained matrix and sometimes occurs within chloritoid porphyroblasts along cracks. The monazite grains (10–180 µm) in the matrix are intercalated with muscovite, paragonite and chlorite. They have anhedral to subhedral crystal shape and contain numerous tiny inclusions of apatite, chlorite, paragonite, phengite, quartz, rutile, zircon and tourmaline, randomly aligned.

2.2.3 - MJ44 CHLORITOID PHYLLITE

The very fine grained chloritoid-phyllite MJ44 shows a well-developed muscovite-chlorite-chloritoid bearing composite foliation S2 with the M1-2 assemblage q-mu-ctd-chl-pa-ru-ilm (Figure II.2c). The main foliation is crenulated by S4 cleavage (Figure II.2c). The matrix is dominated by fine-grained muscovite and chlorite intergrowing with tiny paragonite and contains chloritoid porphyroblasts partly aligned to the S2 foliation (Figure II.2c). This sample does not contain garnet nor biotite. The monazite grains (10–150 µm) occur in the matrix intercalated with the muscovite, paragonite and chlorite (Figure II.2c). The monazite grains have anhedral to subhedral crystal shape and contain numerous tiny inclusions of chlorite, phengite, quartz, rutile, paragonite and tourmaline sometimes aligned with the S2 fabric.

2.2.4 - MJ58G / MJ58D2 STAUROLITE-GARNET MICASCHISTS

The staurolite-garnet-micaschists MJ58G and MJ58D2 (Figure II.3a,b,c) show M1-M2 assemblage of q-g-ph-pa-ctd-chl-ru defining S1-S2 foliation, which is heterogeneously transposed by the S3 cleavage, both folded and reactivated by weak D4 deformation. The M3 assemblage occurs in narrow domains of S3 cleavage and domains that contain staurolite, low-Si muscovite, biotite, chlorite and ilmenite (Figure II.3a,b). Biotite, staurolite and chlorite commonly surround garnet porphyroblasts (Figure II.3b,c). The M3 event is characterized by replacement of garnet by biotite and staurolite and the M4 event by chlorite. Anhedral to subhedral monazite grains (10–200 µm) occur in mica-rich domains, intercalated with the minerals in the matrix and they are also preserved in the garnet (Figure II.3c). The monazite grains are aligned along the S2 foliation in the locally well-preserved M1-M2 domains. Monazites were also observed as inclusions in ilmenite, in the garnet rim I and rim II (5–180 µm; Figure II.3c) and in the garnet core (<7 µm). Monazite grains sometimes contain inclusions of muscovite, phengite, rutile, paragonite, quartz, zircon, ilmenite and graphite.

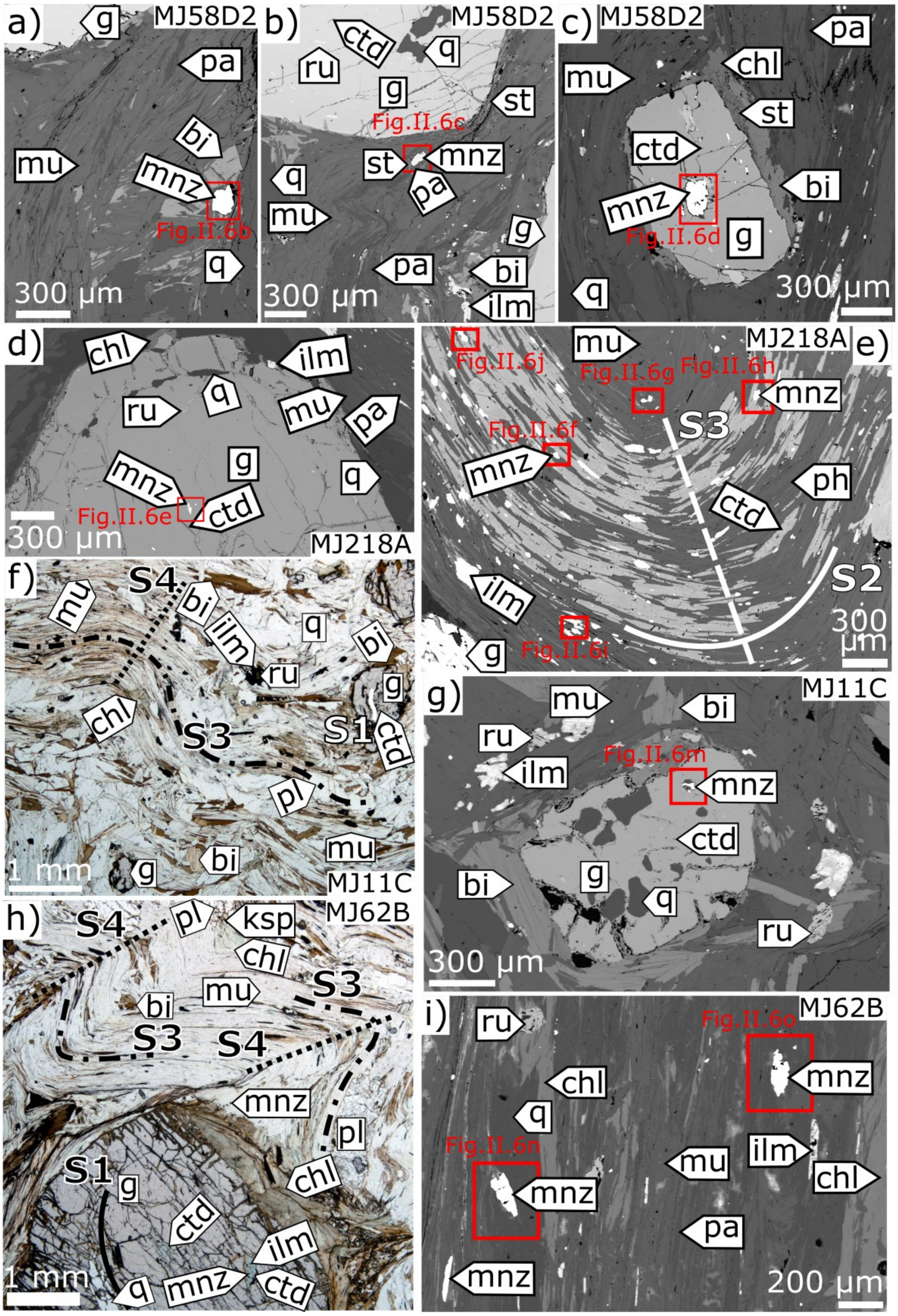

Figure II.3: Microphotographs (parallel polars) and back scattered images showing representative mineral assemblages, crystallization deformation relationships and monazite location in micaschists. More microphotographs and BSE images from the samples MJ58 and MJ218A are visible in Jouvent et al., 2022. (a-c) st-g-micaschist MJ58D2; (d,e) ctd-g-micaschist MJ218A; (f,g) g-micaschist MJ11C with mu-bi-pl-ilm bearing foliation S3 folded by F4 folds. The inclusion trails of ctd-ru-ilm in the garnet define the S1 foliation; (h,i) g-micaschist MJ62B with q-pa-mu-ctd-ilm-ru S1 foliation defined by the garnet inclusion trails. The foliation S3 defined by bi-ilm-pl-ksp is folded by F4 folds. Relics of S2 foliation are still preserved in the limb of the F4 folds with mu-pa intercalation.

2.2.5 - MJ218A CHLORITOID-GARNET MICASCHIST

The chloritoid-garnet-micaschist MJ218A (Figure II.3d,e) contains relics of S2 foliation preserved in isoclinal F3 folds, refolded by open F4 folds. Matrix domains of the well-preserved M1-M2 assemblage contain g-q-ru-ph-ctd-chl±pa with characteristic phengite-chloritoid intergrowths in the S2 foliation (Figure II.3e). Domains of the D3 overprint contain low-Si muscovite, biotite, ilmenite, and chlorite. Chlorite commonly surrounds garnet porphyroblasts and is considered as M4. The garnets are not surrounded by biotite. In the M1-M2 domains, the monazite grains are aligned parallel to the S2 foliation and intergrown with phengite and chloritoid (Figure II.3e). Monazite grains in the matrix (10 to 80 µm) have anhedral to subhedral crystal shape and intercalate with chlorite. Monazite grains inside the garnet are smaller (5–75 µm) and are preserved in the garnet core, rim I and rim II (Figure II.3d). However, the monazite grains in the garnet core are small (<7 µm). Some monazite grains contain inclusions of muscovite, phengite and rutile.

2.2.6 - MJ11C GARNET-MICASCHIST

The garnet-micaschist MJ11C contains relics of isoclinal F2 folds reworked by the main sub-horizontal S3 foliation, which was overprinted by open F4 folds (Figure II.3f). The M1-M2 mineral assemblages preserved in relics of S1 and S2 foliation and as inclusions in garnet correspond to q-ph-pa-g-chl-ru±ctd. The matrix assemblage bi-mu-ilm-pl-chl likely reflects both M3 and M4 metamorphism (Figure II.3f). Garnet is commonly surrounded by biotite and chlorite (Figure II.3f). Monazite grains (10–150 µm) in the matrix are intercalated with muscovite, biotite, chlorite or they are included in the garnet core, rim I and rim II (Figure II.3g). Monazite included in the garnet core have a small size (<7 µm). The monazite grains sometimes contain inclusions of muscovite and rutile and have anhedral to subhedral crystal shape.

2.2.7 - MJ62B GARNET-MICASCHIST

The garnet-micaschist MJ62B contains garnet porphyroblasts, which preserve S1 foliation in the form of inclusion trails consisting of q, ph, pa, ctd, chl, ru and ilm (Figure II.3h). The S2 foliation bearing q-ph-pa-g-chl-ru-ilm is mostly completely transposed by the

S3 fabric, defined by biotite, muscovite, ilmenite, chlorite and plagioclase, which is strongly overprinted and/or reactivated by D4 deformation (Figure II.3h) manifested by a large amount of chlorite surrounding the garnets (Figure II.3h). Large monazite grains (20–200 µm) occur in the matrix (Figure II.3i). Some monazite grains (10–110 µm) were also observed enclosed in the garnet rim I and rim II (Figure II.3h) and some in the garnet core. Monazites included in the garnet core have a very small size (<7 µm). A few monazite grains are enclosed in plagioclase. The monazite grains have a few inclusions of muscovite and rutile.

2.3 - RESULTS: MONAZITE MICROSTRUCTURE, AGES AND REE

2.3.1 - PHYLLITES

The monazite grains in the phyllite samples are zoned with a brighter usually euhedral core and a darker rather anhedral rim in BSE images (Figure II.4). Compared to the rim, the core of the monazite is enriched in Th, U, Y (Figure II.4), Ca, Nd, Si and slightly in Sr, and depleted in La (Tables S.II.1 and S.II.2). The resulting REE patterns and U-Pb isotopic ratios in Figure II.5 are separated according to the location of the analyzed spot inside the monazite. The monazite core is shown in black and the monazite rim in gray. The REE pattern is similar in all three phyllite samples (MJ44, MJ182 and MJ52D*,* respectively in Figure II.5b,d,f) showing a positive slope of the LREE (from La to Sm) in the core domains and a negative slope in the rim domains. Both cores and rims have a negative slope of MREE and HREE (from Sm to Yb), however the cores are slightly enriched in MREE and HREE compared to the rims. The Eu anomaly is not present (Figure II.5b,d,f). All the analyses are discordant but the monazite rims are usually less discordant than the cores (Figure II.5a,c,e).

The phyllite MJ182 has monazites which show a sharp transition between the bright core and dark rim in BSE images (Figure II.4a,b) accompanied by a very slight oscillatory zoning of Th, Ca and Si. Monazite cores have intercept ages of 350.0 ± 1.1 [7.1] Ma and the rims 345.3 ± 1.2 [7.0] Ma (Figure II.5a).

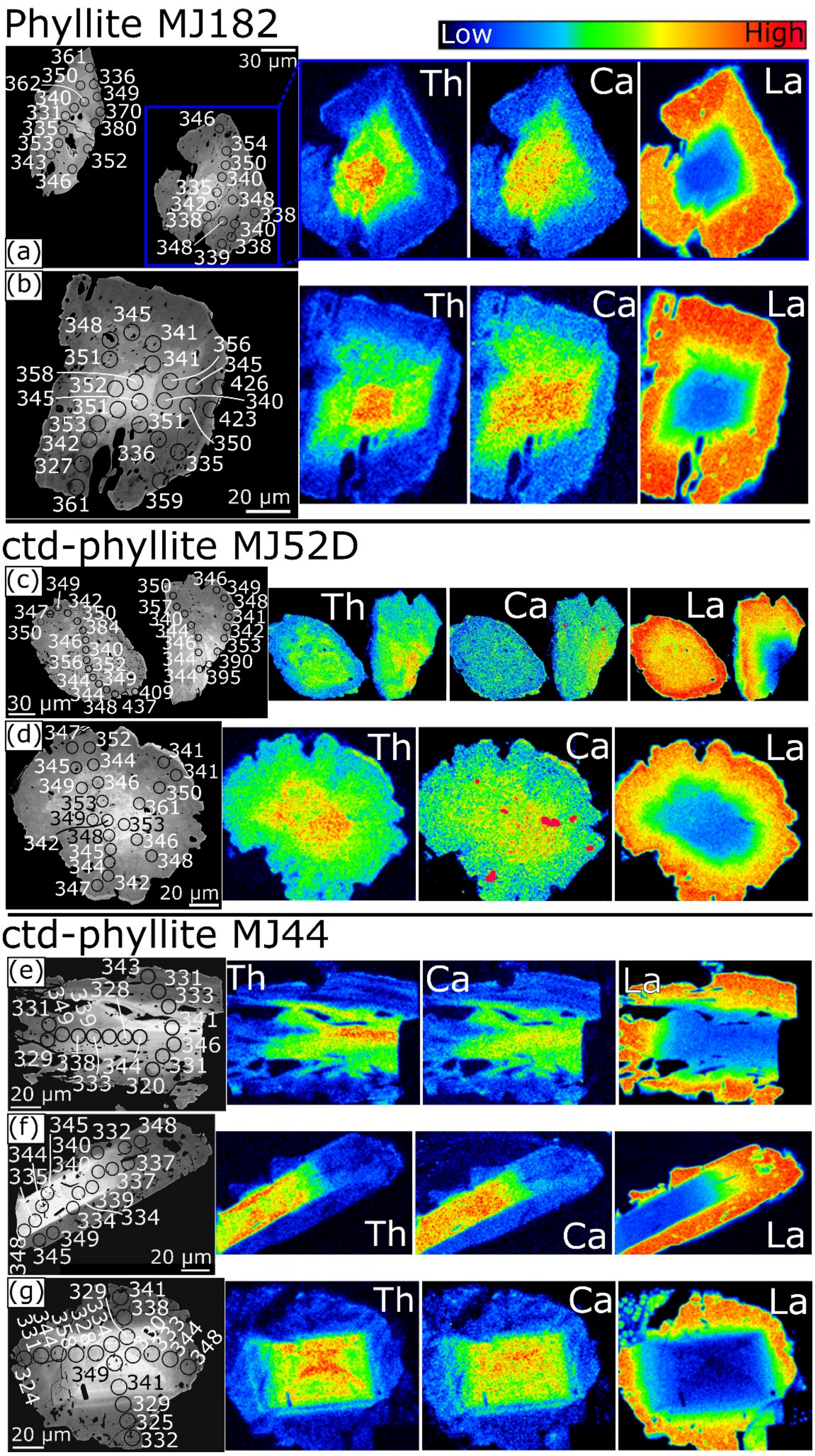

Figure II.4: Back-scattered electron images with analyzed spots (10 µm in diameter) and corresponding ^{207}Pb-corrected ^{238}U/^{206}Pb ages of the phyllites. The red rectangles show Th, U and Y compositional maps of representative monazite grains dated by LA-ICP-MS. Separated monazite grains from: ctd-phyllite MJ44, phyllite MJ182 and ctd-phyllite MJ52D.

Contrary to the monazites in the above described samples, the monazite grains in the chloritoid-phyllite MJ52D show a gradual transition between a bright monazite core and a dark mantle (Figure II.4c,d). In addition, monazites in this sample often show a thin brighter rim in BSE images (Figure II.4d). The intercept ages of the cores are 349.6 ± 2.2 [7.3] Ma and the intercept ages of the rims are 347.7 ± 0.8 [7.0] Ma (Figure II.5c).

The chloritoid-phyllite MJ44 shows a sharp transition between the bright monazite core and the dark monazite rim in the BSE as well as in the Th compositional maps (Figure II.4e,f,g). The monazite sometimes records an oscillatory zoning of thin Th-rich bands in the vicinity of the core-rim boundary (Figure II.4g). The resulting intercept ages in the sample MJ44 show a statistically overlapping age of 340.8 ± 1.1 [6.9] Ma and 339.7 ± 1.0 [6.9] Ma for the core and rim domains, respectively (Figure II.5e).

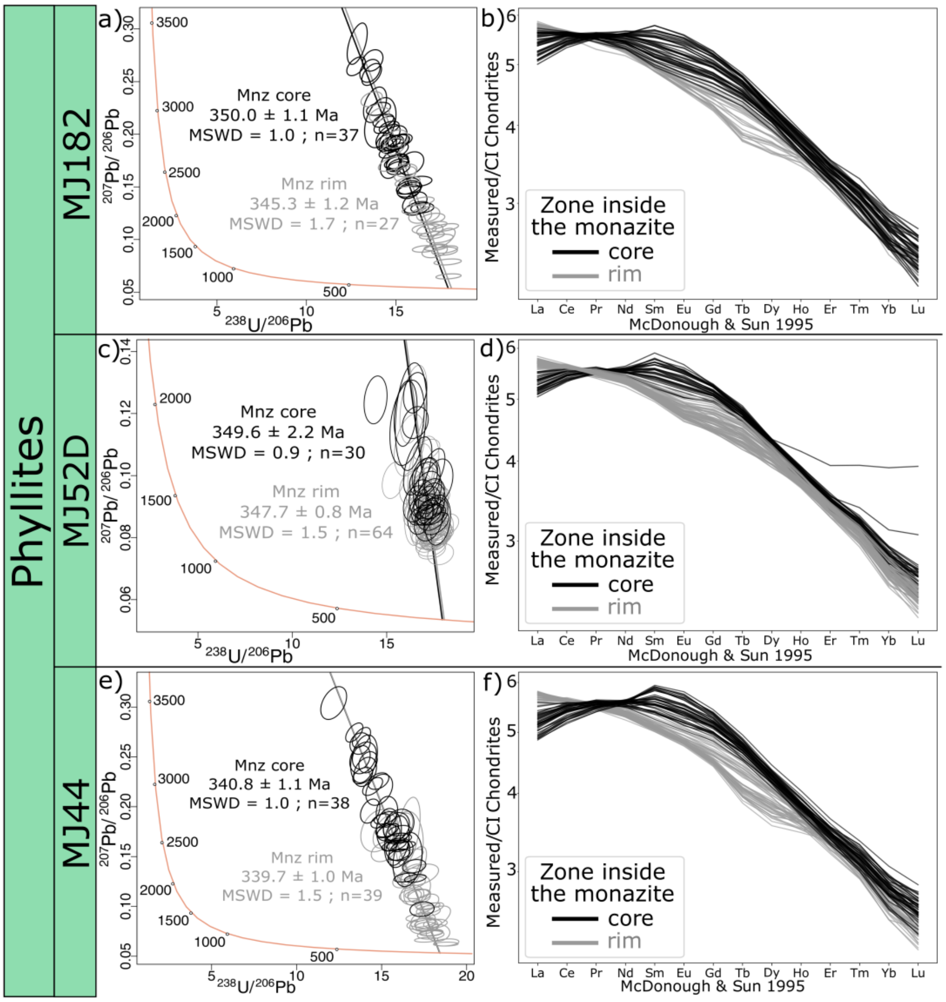

Figure II.5: Monazite geochronology of the phyllites (MJ182, MJ52D and MJ44). The data are grouped according to the position of the analyzed spot inside the monazite. a-c-e: Tera–Wasserburg discordia diagram for the LASS spots in the monazites. Error ellipses 2σ. b-d-f: Chondrite-normalized REE patterns of the monazites. Concentrations are normalized by the chondrite values from McDonough & Sun (1995).

2.3.2 - MICASCHISTS

The monazite grains in the micaschist samples show alternation of brighter and darker zones or a patchy and irregular zoning in BSE images (Figure II.6a,d,e,m,n,o). The brighter zones or bands in monazites are enriched in Th, U (Figure II.6 and Table S.II.3), Ca and Si and the darker zones are slightly depleted in La and sometimes in Nd (Table S.II.4). Nearly all the U-Pb ages are discordant, however monazites in the matrix are usually less discordant than those included in the garnet (Figure II.7a,c,e,g,i). The monazite REE patterns in the micaschists generally show a shallow negative slope of LREE (from La to Sm), which becomes steeper towards the HREE, especially from Tb to Lu (Figure II.7b,d,f,h,j). The monazite grains in the low grade matrix are generally enriched in HREE (from Dy to Lu) compared to those in the M1-M2 matrix or those included in the garnet. A weak Eu anomaly is present in the micaschists MJ11C and MJ62B, which are the only samples containing plagioclase (Figure II.7h,j). For the *in-situ* dating (all the micaschist samples except MJ58G), the intercept ages and REE patterns were grouped and color coded based on their position in the thin-section (Figure II.7). The few monazite grains located in the garnet core could not be analysed by laser-ablation split-stream due to their small size (<7 µm).

The staurolite-garnet-micaschist MJ58G, dated from a mount, shows two distinct REE patterns (Figure II.7b) without any obvious link to the location of the dating spot within the grains. The abnormal REE patterns (the most depleted in HREE) likely represent alteration products of monazite (oxides and hydroxides of REEs) and such spots are not used in the age calculation. The fresh monazites show an intercept age of 338.1 ± 1.4 [6.9] Ma (Figure II.7a).

The monazite intercept ages of the staurolite-garnet-micaschist MJ58D2 are the oldest for the grains in the M1-M2 matrix (334.6 ± 1.1 [6.8] Ma), younger for the grains in the garnet rim (331.0 ± 1.9 [6.9] Ma) and the youngest for the grains in the M3-M4 matrix (329.6 ± 1.4 [6.7] Ma; Figure II.7c). In this sample, the monazite REE patterns show a lower HREE content for the grains in the M1-M2 matrix than for the grains in the M3-M4 matrix, while monazites included in the garnet rim show variable HREE patterns (Figure II.7d).

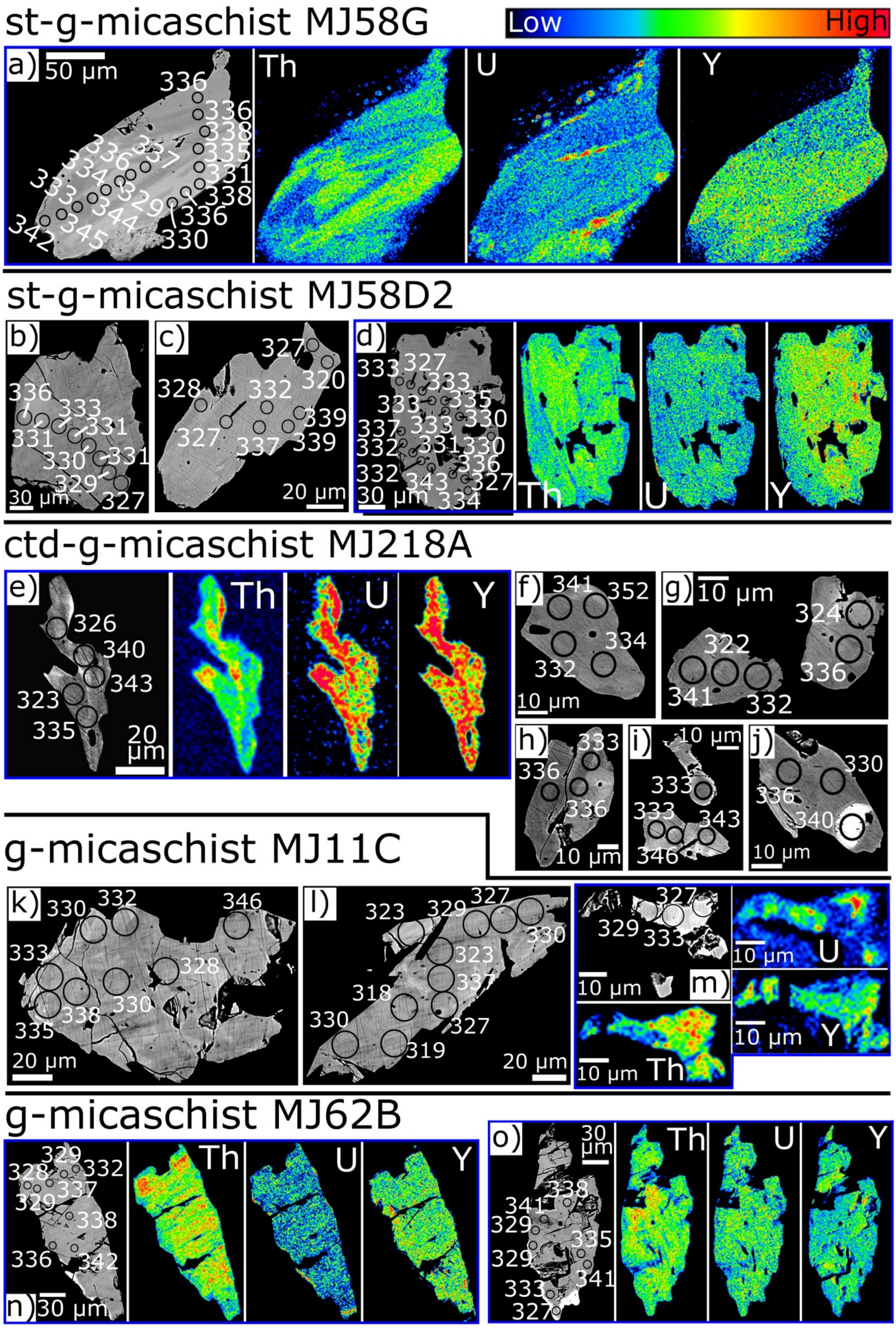

Figure II.6: Back-scattered electron images with analyzed spots (10 µm in diameter) and corresponding ^{207}Pb-corrected ^{238}U/^{206}Pb ages of the micaschists. The red rectangles show detail of monazite grains (location visible in Figure II.3) and Th, U and Y compositional maps of representative monazite grains dated by LA-ICP-MS.

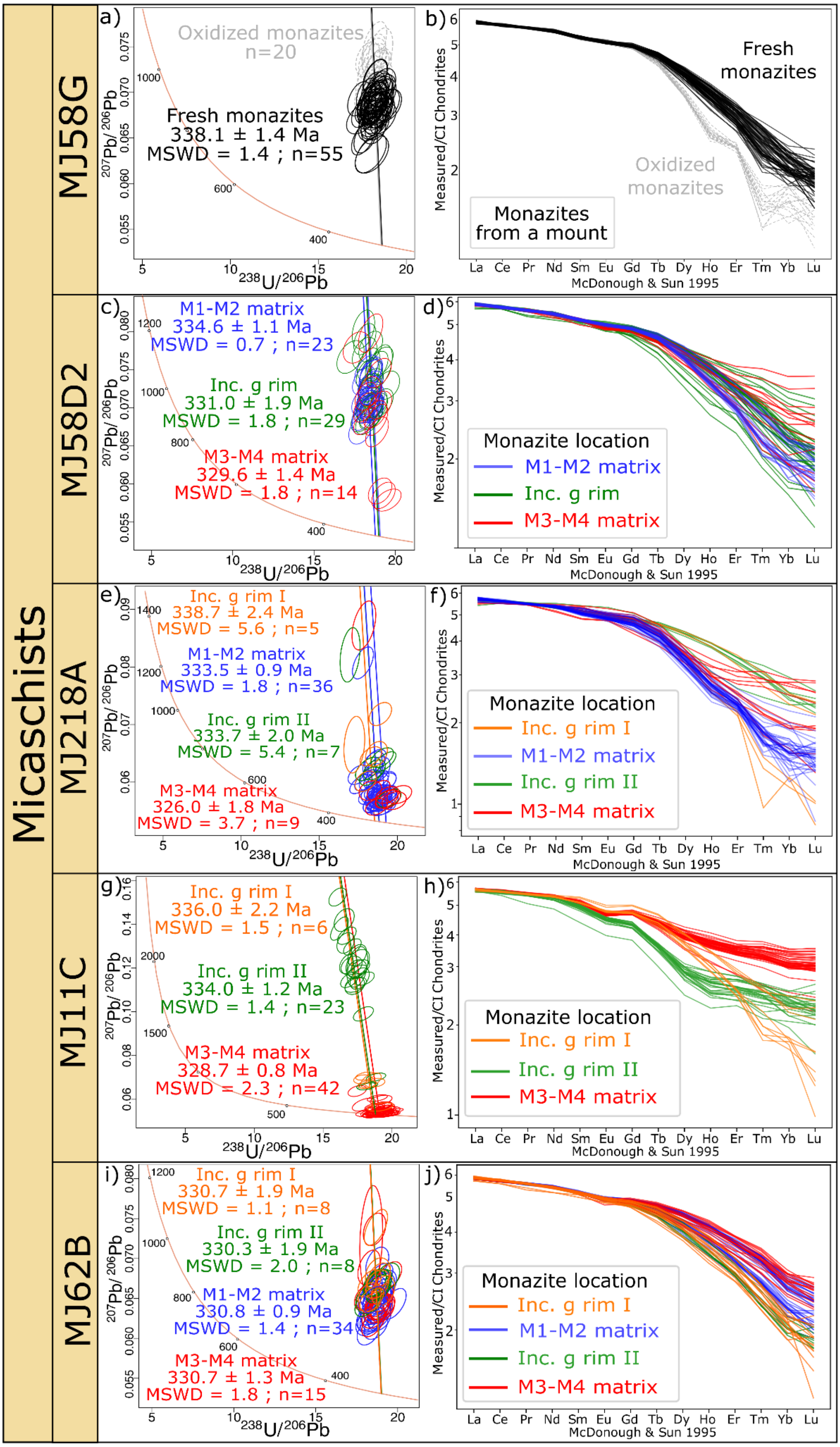
Micaschists
MJ58G
MJ58D2
MJ218A
MJ11C
MJ62B
a)
Oxidized monazites
n=20
Fresh monazites
338.1 ± 1.4 Ma
MSWD = 1.4 ; n=55
1000
600
400
^{207}Pb/^{206}Pb
^{238}U/^{206}Pb
b)
Fresh monazites
Oxidized monazites
Monazites from a mount
Measured/CI Chondrites
La Ce Pr Nd Sm Eu Gd Tb Dy Ho Er Tm Yb Lu
McDonough & Sun 1995
c)
M1-M2 matrix
334.6 ± 1.1 Ma
MSWD = 0.7 ; n=23
Inc. g rim
331.0 ± 1.9 Ma
MSWD = 1.8 ; n=29
M3-M4 matrix
329.6 ± 1.4 Ma
MSWD = 1.8 ; n=14
1200
1000
800
400
d)
Monazite location
M1-M2 matrix
Inc. g rim
M3-M4 matrix
e)
Inc. g rim I
338.7 ± 2.4 Ma
MSWD = 5.6 ; n=5
M1-M2 matrix
333.5 ± 0.9 Ma
MSWD = 1.8 ; n=36
Inc. g rim II
333.7 ± 2.0 Ma
MSWD = 5.4 ; n=7
M3-M4 matrix
326.0 ± 1.8 Ma
MSWD = 3.7 ; n=9
1400
1200
1000
600
400
f)
Monazite location
Inc. g rim I
M1-M2 matrix
Inc. g rim II
M3-M4 matrix
g)
Inc. g rim I
336.0 ± 2.2 Ma
MSWD = 1.5 ; n=6
Inc. g rim II
334.0 ± 1.2 Ma
MSWD = 1.4 ; n=23
M3-M4 matrix
328.7 ± 0.8 Ma
MSWD = 2.3 ; n=42
2000
1500
500
h)
Monazite location
Inc. g rim I
Inc. g rim II
M3-M4 matrix
i)
Inc. g rim I
330.7 ± 1.9 Ma
MSWD = 1.1 ; n=8
Inc. g rim II
330.3 ± 1.9 Ma
MSWD = 2.0 ; n=8
M1-M2 matrix
330.8 ± 0.9 Ma
MSWD = 1.4 ; n=34
M3-M4 matrix
330.7 ± 1.3 Ma
MSWD = 1.8 ; n=15
1200
1000
800
600
400
j)
Monazite location
Inc. g rim I
M1-M2 matrix
Inc. g rim II
M3-M4 matrix

Figure II.7: Monazite geochronology of the micaschists (MJ58G, MJ58D2, MJ218A, MJ11C and MJ62B). The data are grouped according to the position of the monazite in the thin-section. a-c-e-g-i: Tera–Wasserburg discordia diagram for the LASS spots in the monazites. Error ellipses 2σ. b-d-f-h-j: Chondrite-normalized REE patterns of the monazites. Concentrations are normalized by the chondrite values from McDonough & Sun (1995). HP=high-pressure

In the chloritoid-garnet-micaschist MJ218A (Figure II.7e), the oldest intercept age is associated with the monazite grains included in the garnet rim I (338.7 ± 2.4 [7.2] Ma), a younger intercept age is recorded in the monazite grains in the garnet rim II (333.7 ± 2.0 [7.0] Ma) and in the M1-M2 matrix (333.5 ± 0.9 [6.7] Ma) and the youngest age is associated with grains in the M3-M4 matrix (326.0 ± 1.8 [6.8] Ma). The monazite grains in the M1-M2 matrix and in the garnet rim I are depleted in HREEs, contrary to those in the M3-M4 matrix or in the garnet rim II (Figure II.7f).

In the garnet-micaschist MJ11C, the monazite intercept ages are the oldest in the garnet rim I (336.0 ± 2.2 [7.1] Ma), younger in the garnet rim II (334.0 ± 1.2 [6.8] Ma) and the youngest in the M3-M4 matrix (328.7 ± 0.8 [6.6] Ma; Figure II.7g). Similarly to the above-described samples, the REE patterns show three distinct groups, fitting with the position of the monazites in the thin-section (Figure II.7h), with the most depleted HREE in the monazites in the garnet rim I, intermediate HREEs in the monazites included in the garnet rim II and the most enriched HREE in the M3-M4 matrix (Figure II.7h).

In the garnet-micaschist MJ62B, the intercept age is around 331 Ma in all the thin-section domains (Figure II.7i): 1) 330.7 ± 1.9 [6.9] Ma for the monazite grains included in the garnet rim I, 2) 330.3 ± 1.9 [6.9] Ma for the monazite grains in the garnet rim II, 3) 330.8 ± 0.9 [6.7] Ma for the monazite grains in the M1-M2 matrix and 4) 330.7 ± 1.3 [6.7] Ma for the monazite grains in the M3-M4 matrix. In this sample, the REE patterns are less variable compared to the previous samples (Figure II.7j). Monazite grains in the garnet rim I and II are slightly depleted in HREE, the monazite grains in the M1-M2 matrix have slightly more HREE than those in the garnet, and the monazite grains in the M3-M4 matrix are the most enriched in HREE. Although the systematic relationship between REE patterns and location of monazite grains is similar to the above-described micaschist samples, there is no difference in monazite age.

2.3.3 - SUMMARY OF AGES

The individual analyses of monazite grouped by core/rim chemistry in phyllites and by position of grains in micaschists provide relatively large scatter of ages with the mean ages of the individual groups falling between ~350–340 Ma for monazites in the phyllite samples (Figure II.8a-c) and between ~339–326 Ma for monazites in the micaschist samples (Figure II.8d-h). In micaschists, except for the sample MJ62B (Figure II.8h), the older mean ages between ~339–334 Ma occur for the garnet rim I inclusions, for monazites in the M1-M2 matrix or from large monazite grains from a mount (Figure II.8d-g). The garnet rim II inclusions show a slightly younger age between ~334–331 Ma while the M3–M4 matrix monazites show ages of ~331–326 Ma (Figure II.8e-g). Sample MJ62B shows a consistent age of ~330 Ma for all chemically distinct monazite groups (Figure II.8h).

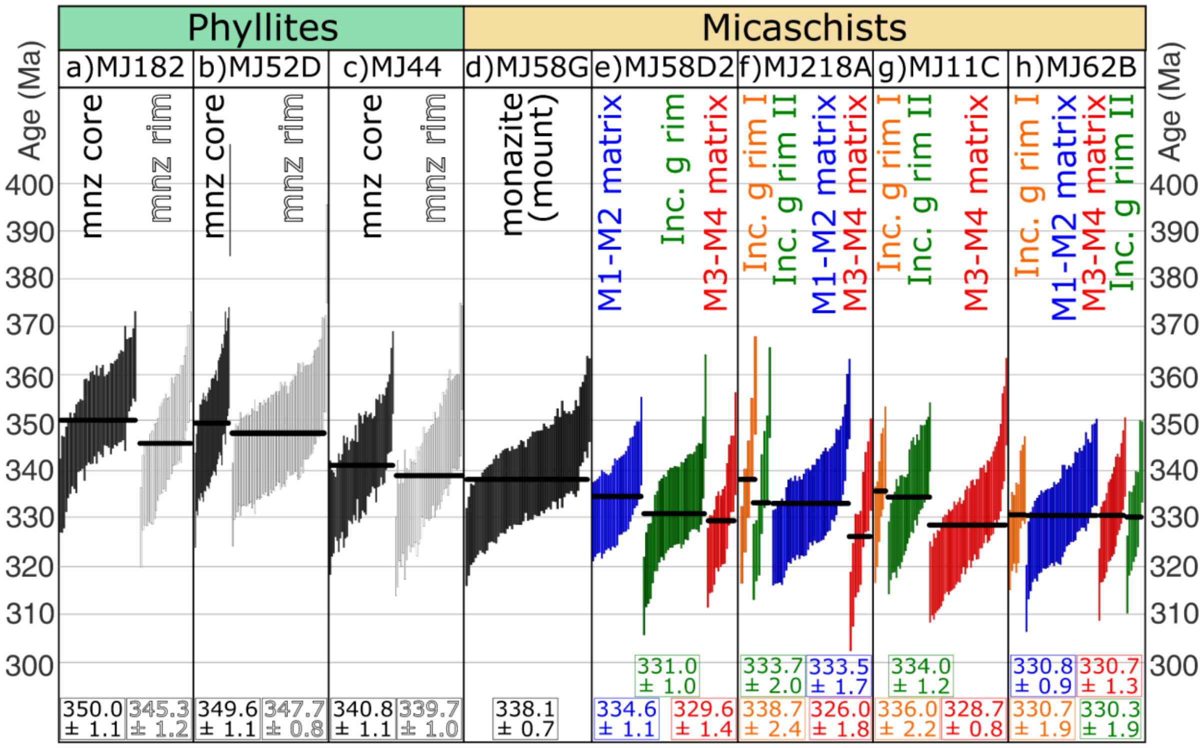

Figure II.8: Summary of the monazite LASS for all the samples. The analyzed domain spots (core/rim of monazite for the phyllites and monazite in thin-section for the micaschists) in selected monazite grains is shown in weighted mean plot of ^{207}Pb corrected ^{238}U/^{206}Pb dates. Error bars are 2σ. mnz: monazite.

2.4 - DISCUSSION OF THE MONAZITE U-PB AGES

The results of this study combined with previous research on Erzgebirge rocks allowed us to reconstruct the development of the orogenic wedge during the transition from the subduction to the collision. We first discuss the significance of the monazite dating, the REE patterns and the monazite inclusions in connection to the individual tectonometamorphic events. Then, the *P–T* paths of individual units are discussed in the context of the Saxothuringian orogenic wedge formation.

2.4.1 - MONAZITE CHEMISTRY IN RELATION TO P–T EVOLUTION AND THE MEANING OF AGES

Since the studied monazite grains in our samples contain inclusions of metamorphic minerals and because they show differences in REE patterns, the resulting monazite ages can be interpreted in relation to the metamorphic evolution of the studied rocks. Following Jouvent et al. (2022), the occurrence of phengite, paragonite and rutile inclusions in both phyllites and micaschists is typical for the peak pressure M1 and partial exhumation M2 stages, while the occurrence of low-Si muscovite and ilmenite inclusions in micaschists are related to lower pressure metamorphic overprint of the M3-M4 matrix (for *P–T* conditions see Figure II.1b and part I).

2.4.1.1 - DISCORDANT AGES AND COMMON LEAD

All the analysed samples showed discordant analyses (Figures II.5 and II.7). The positive correlation between the amount of non-radiogenic ^{204}Pb and the discordance (Figure II.9) indicates that the discordance resulted from the common lead (Holder et al., 2015). A possible cause for the presence of common lead may be the incorporation of Pb-bearing inclusions, which are numerous in some monazite grains, especially in phyllites. However, there is no direct correlation between the amount of inclusions within the samples and the discordance in the Tera-Wasserburg plots. Additionally, monazites in micaschists have a small amount of inclusions, but the discordance is similar.

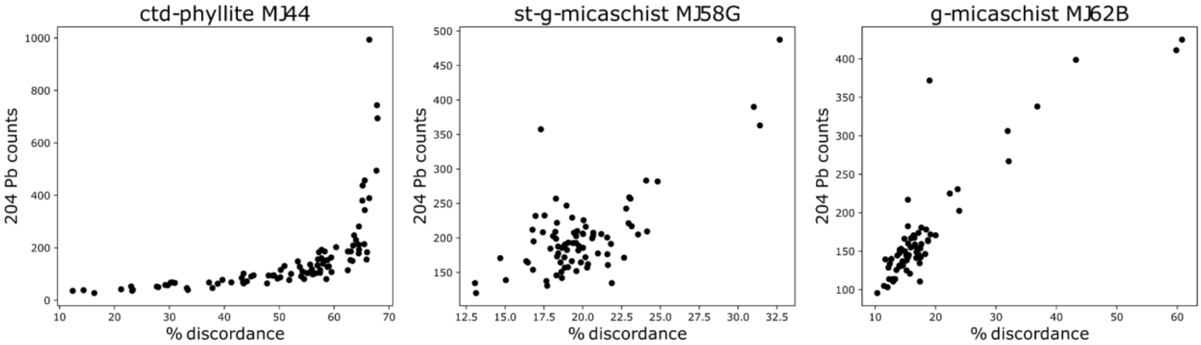

Figure II.9: Percent discordance vs ^{204}Pb counts showing that discordance is the result of non-radiogenic ^{204}Pb in the monazites.

In high-pressure phyllites, the cores are more discordant than rims (Figure II.5). In micaschists, the oldest monazite spots enclosed in the high-pressure garnet are more discordant than the monazites in the lower-pressure M3-M4 matrix, and in the latter case are sometimes nearly concordant (Figure II.7g). Such a general trend can be explained by a presence of common Pb in the original protolith or specific fluid composition which led to the partitioning of Pb to the grains preferentially during the early monazite growth.

However, in high-pressure terrains, Holder et al. (2015) attributed the ^{204}Pb, Sr and Eu enrichment of the monazites to the release of these elements from plagioclase during the plagioclase consuming reaction at eclogite-facies conditions (plagioclase -> clinopyroxene + quartz). Additionally they propose that in the absence of plagioclase, the monazite crystal lattice can, at high pressure, incorporate a significant amount of Pb. Our samples are generally calcium poor and commonly lacking plagioclase everywhere along the calculated *P–T* paths of Jouvent et al. (2022). On the other hand, discordant analyses are observed also in samples containing plagioclase and this suggests that dicordance occurs in various protolith compositions regardless of the mineral assemblage at high-pressure conditions. Although there can be some other causes responsible for the discordance of the *HP* monazites, especially specific protolith and fluid composition during the monazite growth or recrystallization, the link to the properties of monazite crystal lattice at high-pressure can not be ruled out.

2.4.1.2 – REE PATTERNS OF MONAZITES IN PHYLLITES

In phyllites, the monazites show different chemistry in the core and rim. The rims have a negative slope towards HREE typical of metamorphic monazites. On the other hand, the cores show uncommon depletion of LREEs compared to the rims (Figure II.5b,d,f). Such REE patterns are systematically observed in all analyzed phyllite samples, independently of their bulk-rock composition or mineral assemblage. The overall lower abundance of MREE and HREE in the monazite rims compared to the cores can be explained by progressive fractionation of REEs from the original reservoir during the monazite growth. In contrast, the uncommon LREE depletion in the monazite cores is probably bound to their coeval growth with another LREE-bearing phase (Figure II.10a). The typical REE pattern of the monazite with higher LREE content in the rims than in the cores suggests that the LREE-bearing phase was at least partially resorbed during the later phase of the monazite growth (Figure II.10b).

Considering the *P–T* evolution of the studied samples, allanite and apatite are the likely candidates partitioning predominantly LREE's (Hermann, 2002; Janots et al., 2006, 2008; Spandler et al., 2003). Allanite and apatite are both stable at low temperature conditions, suggesting their possible presence during the prograde evolution. In the case of allanite, its earlier presence is supported by the depletion in La in the monazite cores similar to the observation of Janots et al. (2008; Figure II.4 and Table S.II.1). However, no relic allanite was found in our phyllites, consistent with its possible breakdown during the growth of the monazite rim (Figure II.10a,b). On the other hand, apatite is present in the matrix of all the studied samples, and even as inclusions in monazite in the ctd-phyllite sample MJ52D. However, decreasing Ca content from the monazite core towards the rim (Figure II.4) rather suggests depletion of the Ca in the reservoir during the monazite growth, inconsistent with apatite breakdown during the monazite rim formation.

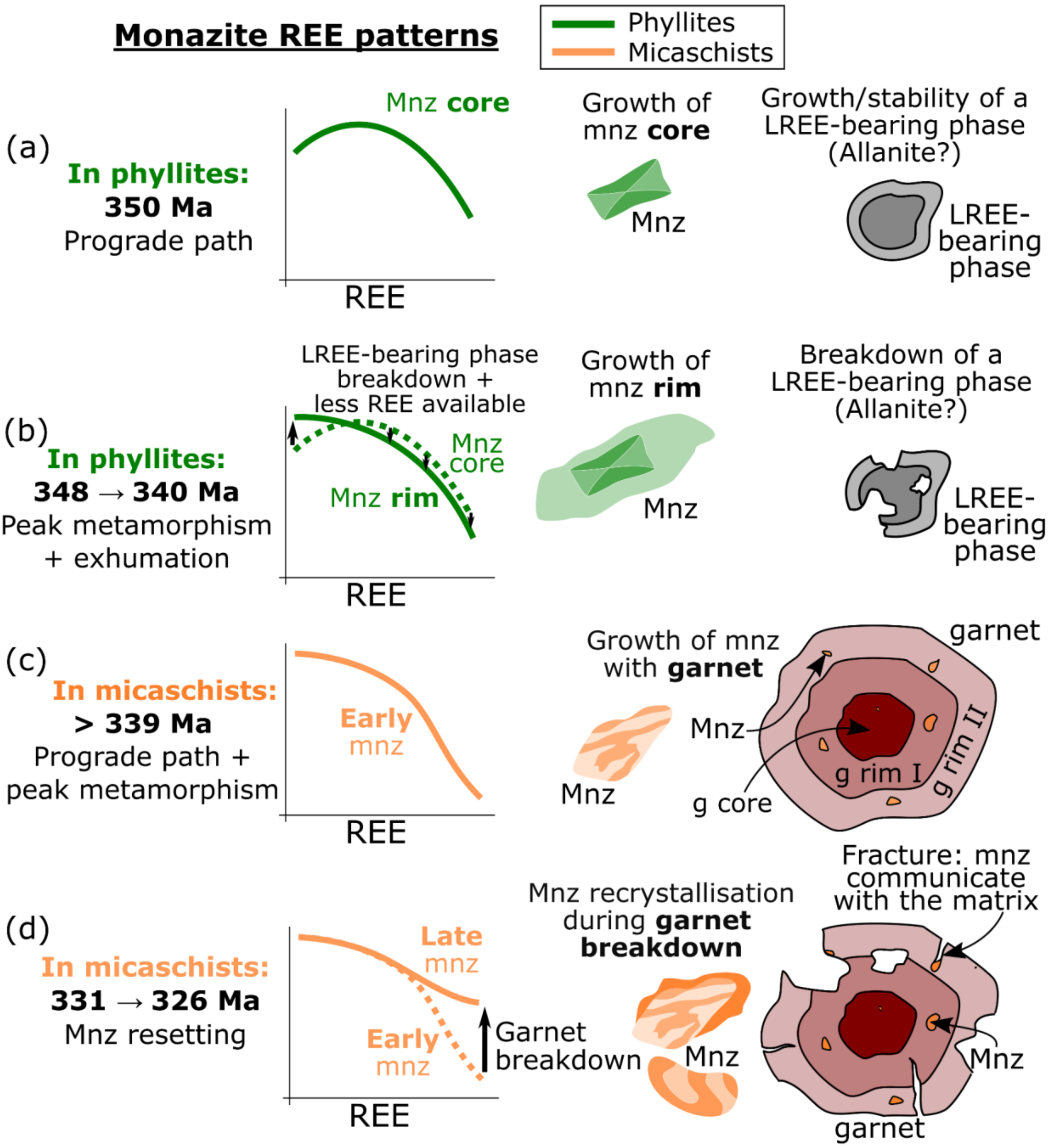

Figure II.10: Monazite Rare Earth Elements (REE) patterns in phyllites (a,b) and in micaschists (c,d), with schematic growth of monazites (mnz) and other minerals affecting monazites composition (Light Rare Earth Elements-bearing phase and garnet) during the different tectonometamorphic events

2.4.1.3 – REE PATTERNS OF MONAZITES IN MICASCHISTS

In micaschists, the monazite grains revealed different chemical compositions based on their location in the studied thin-sections (Figure II.7d,f,h,j). In all the studied micaschist samples, the monazite grains in the M1-M2 matrix and in the garnet rim I have lower HREE compared to those in the M3-M4 matrix. HREE depleted monazite usually grows together with garnet (Figure II.10c), while HREE enriched monazite is usually interpreted as being formed during the garnet breakdown (Figure II.10d; e.g. Gibson et al., 2004; Rubatto et al., 2013). Interestingly, monazite inclusions in the garnet rim II have an intermediate HREE pattern between M3-M4 matrix monazites and inclusions in the garnet rim I (Figure II.7f,h). If monazite inclusions would be growing together with enclosing garnet, monazite inclusions should become more depleted in HREE from the garnet core towards the rim. Because the opposite trend is observed, the REE system of inclusions in the garnet rim II had to be opened to cause its partial re-equilibration with the matrix. Opening of the system could have been facilitated by micro-cracks observed in the garnet in several cases (Figures II.3c,h and II.10d; Jouvent et al., 2022).

2.4.1.4 – PARTIAL RESETTING OF REE PATTERNS AND AGES

The opening of the monazite isotopic system in micaschists is evident also in age data. The best illustration is the garnet-micaschist sample MJ62B, which yields young age (331 Ma) for all the monazites regardless of their position in the thin section, but still keeping REE patterns similar to the other micaschists (Figure II.7i,j). This strongly implies that the ~331 Ma old event is capable of resetting monazite ages, even in the grains enclosed in central parts of ~1 cm garnet porphyroblasts, without complete obliteration of the REE pattern (Figure II.10d). The suggested mechanism is an in-place recrystallization of monazite from a partially opened but local REE reservoir allowing for lead loss but keeping largely unchanged REE content. Additionally the sample MJ11C shows a clear chemically distinct group of ~329 Ma matrix monazites, which are nearly concordant and probably nucleated later as a separate group during the same resetting event.

Many studies showed, by experiments or in nature, a partial or complete resetting of the U-Pb isotope system of monazites due to fluid circulation (Grand'Homme et al., 2016; Kelly et al., 2012; Teufel & Heinrich, 1997; Williams et al., 2011). In the presence of garnet, most of the studies highlighted that monazite included in garnet are protected by the armoring effect of robust garnet, arguing against even partial resetting of monazites in garnet due to an entire disconnection from the matrix (Montel, 2000; Zhu & O'nions, 1999). However, Wang et al. (2020) also reported monazite inclusion in garnet younger than the garnet itself (dated by Lu-Hf geochronology), revealing a possible resetting of monazite, even when this mineral is included in garnet.

The process of partial opening of the isotopic system in monazite can be dated in all the micaschists to ~330 Ma and the relative enrichment of HREE in monazite suggests that this event was associated with significant garnet breakdown (Figure II.10d). Although a minor amount of garnet may be consumed and replaced by biotite and staurolite already during the M3 stage (Jouvent et al., 2022), a significant reduction of the garnet volume occurred after the peak temperature M3 stage during cooling and decompression. Garnet replacement by chlorite occurred also largely during the low-grade M4 reactivation. Similar age associated with reactivation of the Erzgebirge complex during later stages of exhumation (Kryl et al., 2021) had been previously reported from $^{40}Ar/^{39}Ar$ white mica ages (Werner & Lippolt, 2000; Hallas et al., 2021; Figure II.11). Therefore, we interpret the age of ~330 Ma as the very late stage of M3 decompression or the age of D4 reactivation.

2.4.1.5 - AGES AND METAMORPHIC EVENTS

The oldest ages in micaschists around 339 Ma are obtained from the inclusions in garnet rim I (Figure II.7e) and from large monazites in the mount (Figure II.7a). However, due to the resetting event, even these ages may likely be partially biased towards younger ages than the original growth age. Therefore this age is considered as the youngest estimate for the prograde garnet growth towards the peak pressure during the M1 event. The resetting M3-M4 event unfortunately does not allow to directly link the intermediate ages neither to the M2 decompression nor the M3 heating event. It is noteworthy that monazites from the corresponding micaschists in the Krkonoše-Jizera complex, considered as the north-east continuation of the Erzgebirge complex, showed similar scatter of monazite U-Pb ages of 341 Ma and 328 Ma (Žáčková et al. 2010; Konopásek et al., 2019).

In phyllites, the ages are quite homogeneous in two samples, MJ182 and MJ52D, showing the mean ages of ~350 Ma for the monazite cores and ~348–345 Ma for the monazite rims (Figure II.8a-b). The ages of monazite cores are interpreted to reflect the prograde growth associated with the M1 event reflected by the LREE depletion in monazite cores (Figure II.10a) due to stability of allanite. Monazite rim's ages are interpreted here to reflect the partial exhumation during the M2 event (Figure II.11) with typical REE pattern (Figure II.10b). Contrary to the micaschists, partial resetting at ~330 Ma mostly did not affect the phyllites, where monazite core and rim ages are consistently dated at 350 Ma and rims at 348–345 Ma. However, the sample MJ44 have similar REE patterns as the other phyllite samples, but the core and rim show overlapping and younger age around 341 Ma (Figure II.5e,f). This age can be interpreted as either locally younger domain, or as a similar partial resetting process, likely during the exhumation of the phyllites. Therefore in the tectonic interpretation we are using time span for burial and exhumation of phyllites in the range 350–340 Ma. The rarely published $^{40}Ar/^{39}Ar$ cooling ages from the phyllites range from ~356 to ~334 Ma (Faryad & Kachlík, 2013) and support our interpretation of time framework for their burial and exhumation loop.

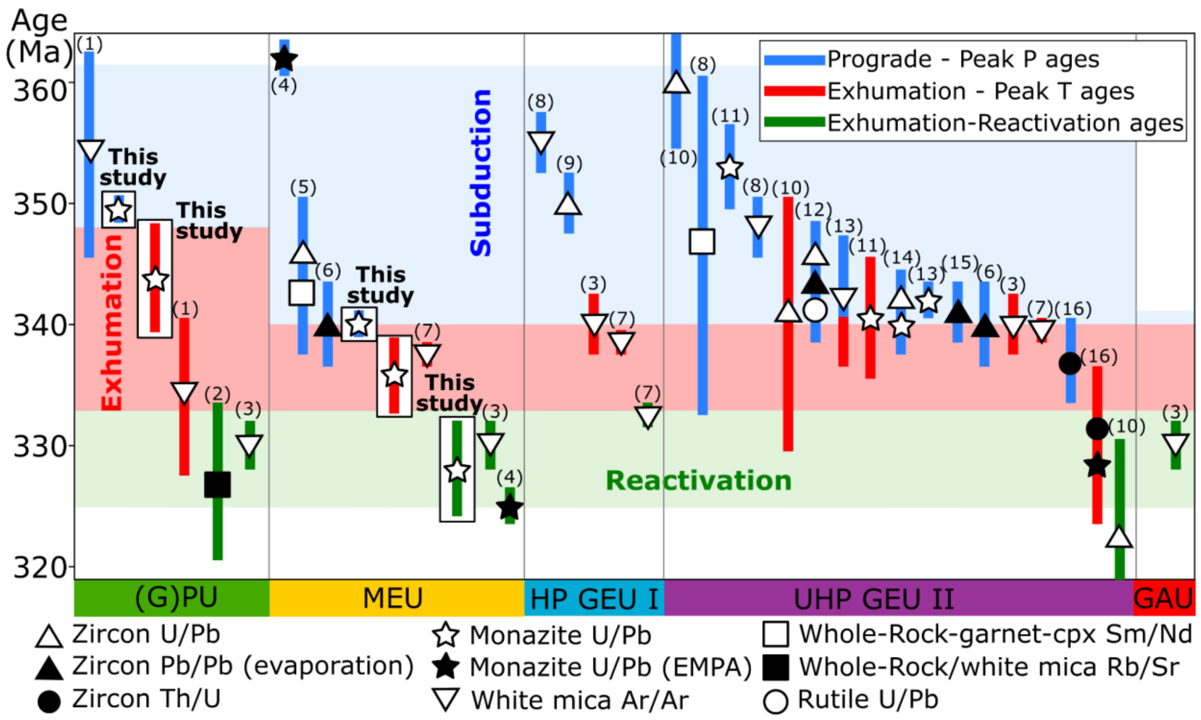

Figure II.11: Summary of ages in the different units of Erzgebirge. Ages are from: (1) Faryad & Kachlík, 2013; (2) Bowes et al., 1999; (3) Werner & Lippolt, 2000; (4) Rahimi & Massonne, 2018; (5) Von Quadt & Günther, 1999; (6) Tichomirowa & Köhler, 2013; (7) Hallas et al., 2021; (8) Schmädicke et al., 1995; (9) Collett et al., 2020; (10) Schmädicke et al., 2018; (11) Závada et al., 2021; (12) Kotková et al., 1996; (13) Zulauf et al., 2002; (14) Kylander-Clark et al., 2013; (15) Kröner & Wilner, 1998; (16) Massonne et al., 2007. Ages are shown taking into account their uncertainty.

Our mean monazite ages from individual groups and samples are in agreement with the previous geochronological studies from the Erzgebirge region. Figure II.11 provides a summary of metamorphic and cooling ages for the Erzgebirge tectonometamorphic evolution. This entire evolution spans from the scarce ages of ~360–355 (Faryad & Kachlík, 2013;

Rahimi & Massonne, 2018; Schmädicke et al., 1995; Schmädicke et al., 2018; Závada et al., 2021) to ages younger than 333 Ma (Werner & Lippolt 2000; Schmädicke et al., 2018; Hallas et al., 2021; Závada et al., 2021) with dominant U-Pb zircon and monazite ages at ~340 Ma (Kotková et al., 1996; Kröner & Willner, 1998; Massonne et al., 2007; Schmädicke et al., 1995; Tichomirowa et al., 2005; Kroner & Romer, 2013). The metamorphic ages plotted separately for the individual Erzgebirge units in Figure II.11 have been color coded following the original author's interpretation. As illustrated also in this study, the distinction between ages reflecting prograde to peak pressure metamorphism and ages reflecting peak temperature and exhumation (Figure II.11) is often debatable.

2.4.2 - ERZGEBIRGE DOME AND ZONING OF THE SAXOTHURINGIAN OROGENIC WEDGE

Spatial arrangement of individual units in the Saxothuringian domain corresponds to an asymmetrical antiformal domal structure (Erzgebirge dome) with successively deeper units exposed towards the east of the dome and separated by extensional shear zones. Recently, Kryl et al. (2021) proposed that the development of the Erzgebirge antiformal dome is associated with the early Carboniferous N-S shortening, while the earlier deformation fabrics originated from progressive evolution of the orogenic wedge. Such an interpretation fits well with our geochronological data showing heterogeneous overprint and reactivation of earlier fabrics at ~331–326 Ma (Figure II.11). Restoration of the wedge geometry in the Erzgebirge (Jouvent et al., 2022; Kryl et al., 2022) reveals early E-W zonation with the eastward increase in *P–T* conditions and complexity of structural record as well as the change in lithology from units dominated by metasediments to units dominated by gneisses.

Orogenic wedges commonly form two contrasting domains, an inner wedge, where deeply subducted crystalline units have been exhumed, and an outer wedge formed by imbricated sedimentary units detached from the subducting plate (Dal Zilio et al., 2020). In our case, the metasediment-dominated units of the Erzgebirge would represent the outer wedge and gneiss dominated units would represent the inner wedge. Indeed, the summary of ages and *P–T* evolution presented separately for individual Erzgebirge units (Figures II.11 and II.12a) show important differences for the (Garnet-)Phyllite Unit, the Micaschist/Eclogite Units and the Gneiss/Eclogite Units (GEU I and II), respectively called (G)PU, MEU and

GEU). The phyllites in the outer shell of the wedge (Figure II.12) show the lowest peak pressure, a relatively cold exhumation gradient and an exhumation age that is older than in the other units. The micaschists towards the inner wedge (Figure II.12) show intermediate pressure, increasing temperature during exhumation, warmer exhumation gradient and exhumation ages similar to the Gneiss/Eclogite Units. The Gneiss/Eclogite Units in the inner part of the wedge show intermediate to ultra-high pressure and warm exhumation gradient. Analysis of deformation structures revealed contrasting structural records in both domains. The outer wedge shows dominance of subhorizontal fabric S2 in phyllites while micaschists and gneisses in the inner wedge are dominated by steeply dipping S2 fabrics reworked by subhorizontal cleavage S3 (Figure I.1e). These differences indicate earlier and colder evolution of (Garnet-)Phyllite Unit in the outer wedge, younger and hotter evolution of the Gneiss/Eclogite Units in the inner wedge, while Micaschist/Eclogite Unit can be understood as a transitional belt between the two. Clearly the structural and metamorphic evolution of the Micaschist/Eclogite Unit is associated with the exhumation and stacking of deep and hot Gneiss/Eclogite Units causing the temporal *MP–MT* metamorphism described in the transitional belt (Konopásek, 1998, 2001; Roetzler et al., 1998; Collett et al., 2017; Rahimi & Massonne, 2018, 2020; Jouvent et al., 2022; Figure II.12a).

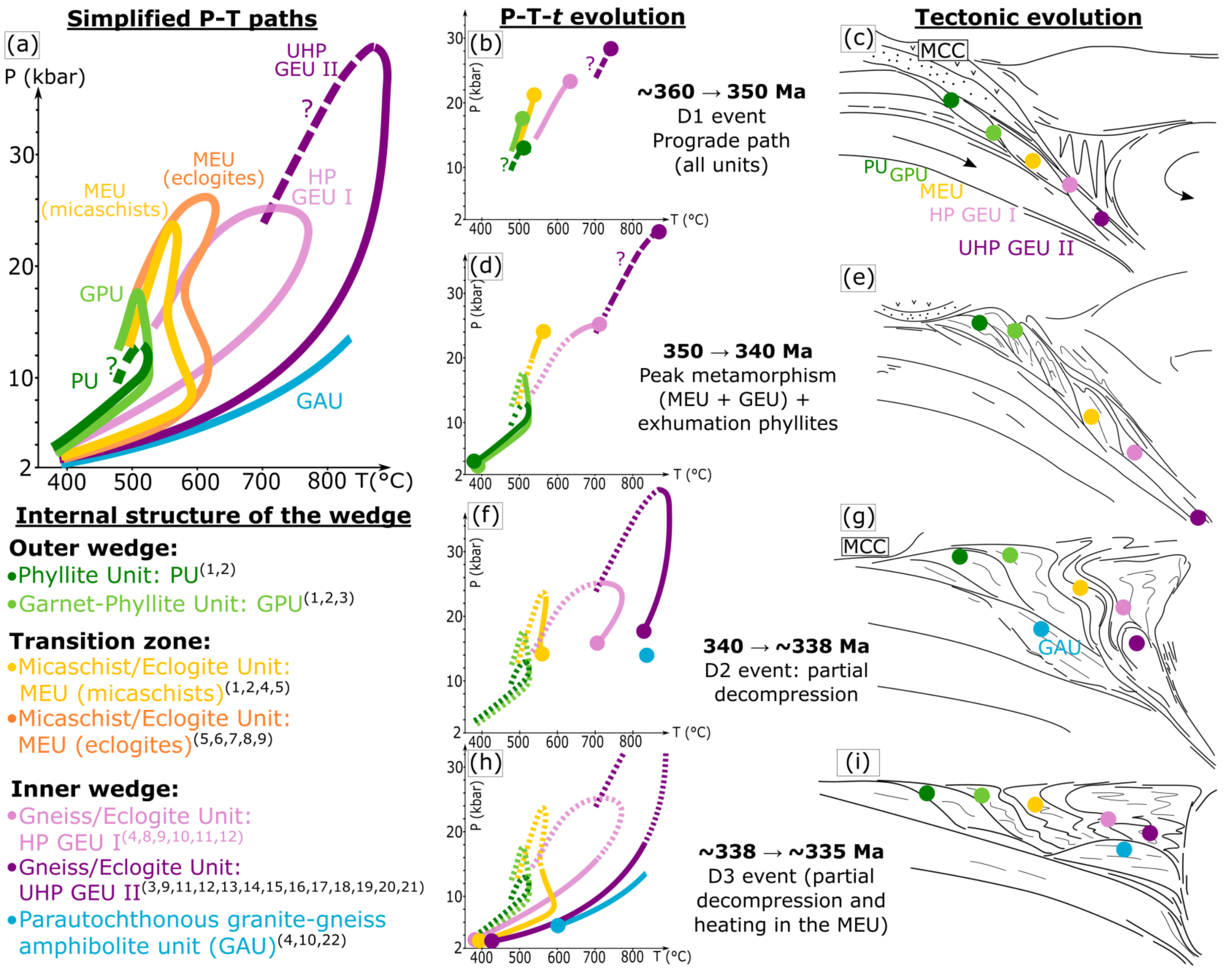

Figure II.12: Timing of the *P*–*T* evolution (a,b,d,f,h) in the different units and schematic tectonic models (c,e,g,i). For the GEU, the *P*–*T* evolution through time is idealized. MCC: Münchberg Crystalline Complex. The *P*–*T* paths are based on: (1) Jouvent et al., 2022; (2) Roetzler et al., 1998; (3) Faryad & Kachlík, 2013; (4) Rötzler, 1995; (5) Konopásek, 2001; (6) Collett et al., 2017; (7) Kulhánek et al., 2021; (8) Klápová et al., 1998; (9) Schmädicke, 1994; (10) Kryl et al., 2021; (11) Rötzler & Plessen, 2010; (12) Mingram & Rötzler, 1999; (13) Schmädicke & Evans, 1997; (14) Hallas, 2020; (15) Hallas et al., 2021; (16) Escudero et al., 2012; (17) Massonne, 1998; (18) Willner et al., 1997; (19) Schmädicke et al., 1992; (20) Zack & Luvizotto, 2006; (21) Massonne & Kopp, 2005; (22) Massonne, 2006.

2.5 - ASSEMBLY OF THE SAXOTHURINGIAN OROGENIC WEDGE

The earliest stages of the Saxothuringian wedge indicate the development of an accretionary wedge during oceanic subduction. Its relics are preserved in the Mariánské Lázně Complex and Münchberg Klippe (Collett et al., 2018, 2022; Deiller et al., 2021; Scherer et al., 2002) located in the hanging wall of the later orogenic wedge (MCC in Figures II.1a and II.12c). The two complexes contain oceanic crust derived fragments that had been subducted to peak pressures at ~390 Ma and later incorporated into the accretionary wedge and exhumed below the blocking temperatures of argon system by ~375 Ma (Dallmeyer & Urban, 1998; Collett et al., 2018). Subsequent stages of the Saxothuringian wedge evolution are recorded in the (Garnet-)Phyllite Unit reaching peak pressure conditions between ~360–345 Ma (Figure II.12b,c). Some of the geochronological data between ~360–355 Ma in the Gneiss/Eclogite Unit II had been interpreted as timing of the *UHP* metamorphism (Figure II.11; Schmädicke et al., 2018; Závada et al., 2021), suggesting that some continental crust had been subducted to the mantle already in the early stages of Variscan evolution (Schulmann et al., 2014; Peřestý et al., 2017).

The principal difference in evolution of the Erzgebirge units is the timing and style of their exhumation. The (Garnet-)Phyllite Unit was exhumed and incorporated into the accretionary wedge between 350–340 Ma, while the other units still experienced subduction (Figure II.12d,e) and were exhumed and incorporated into the wedge between ~340–335 Ma (Figures II.11 and II.12g,i). The earlier exhumed portions of the accretionary wedge occupy outer parts of the orogenic wedge while the later exhumed gneiss dominated units form the inner wedge. The first stage of exhumation of the gneiss dominated units is poorly constrained but is estimated between ~340–338 Ma (Figure II.11) and reflects a return of continental material from the subduction zone. This stage is associated with the formation of a stack of coherent units (nappes) with S2 fabric and M2 assemblages creating an inverted metamorphic gradient (Jouvent et al., 2022; Figure II.12f,g). The continuous return of crustal material from the subduction channel resulted to progressive thickening of the wedge, which started to be compensated by vertical shortening in the upper part of the wedge. This process, known as ductile thinning (e.g. Feehan & Brandon, 1999), was associated with the formation of the subhorizontal S3 fabric which strongly affected the inner wedge units and led to spatial rearrangement of the previous inverse metamorphic zoning. In addition, the thinning led to juxtaposition of the originally deep and hot gneisses to the shallower and colder micaschists resulting in their heating and growth of staurolite and biotite in the S3 cleavage (Jouvent et al., 2022). The main period of ductile thinning is obscured in monazite ages in micaschists, but the intermediate ages between ~338–335 Ma may reflect this event (Figure II.12h,i). This event produced a normal temperature gradient parallel to S3 fabric in the wedge (Kryl at al., 2021; Jouvent et al. 2022) and created a present-day normal metamorphic zoning (Jouvent et al. 2022).

2.6 - CONCLUDING REMARKS ON THE MONAZITE GEOCHRONOLOGY

This study aimed to link the monazite ages with polyphase deformation and metamorphic record of the Saxothuringian orogenic wedge. Our research also focused on the behavior of monazite REE and age systematics during the overprinting events, and the main results are summarized as follows.

- The prograde *HP–LT* evolution in phyllites is well-constrained by monazite to ~350–345 Ma.
- The prograde *HP–LT* evolution in micaschists is constrained by large monazites in the mount and oldest monazites enclosed in the garnet core to be at least 339 Ma old.
- The micaschists are strongly affected by a ~330 Ma old event acting as low-grade overprint during garnet breakdown at the late stage of the ductile thinning of the wedge and its reactivation.
- The Saxothuringian orogenic wedge can thus be subdivided into an older outer wedge formed by phyllites and a younger inner wedge formed by micaschists and gneisses.
- The younger ~330 Ma old event is capable of resetting the oldest monazite ages inside large garnet porphyroblasts, without apparent REE or textural signature.
- High-pressure monazites are prone to incorporate common lead in the crystal structure.

3 - OROGENIC WEDGE EXHUMATION AND REACTIVATION: EVIDENCE FROM MICA ^{40}AR/^{39}AR GEOCHRONOLOGY

3.1 - METHODS AND ANALYTICAL PROTOCOLS

3.1.1 - MICAS CHEMICAL COMPOSITION

Microstructural relations and chemical composition of micas were analyzed using a field emission gun electron probe microanalyzer (FEG-EPMA) JXA-8530F (manufactured by Jeol), equipped with 5 wave dispersive spectrometers (WDS). Quantitative analyses of micas were acquired in spot mode with the beam size of 5 μm. The compositional maps of muscovite were acquired at 20 kV and 100 nA in spot mode with counting time 50 ms per point and step size 1um. Mg, Ti, Mn, Fe, and Na were detected with WDS, Al, Si, K, and Ca with EDS. Kα lines were used for detection of all elements.

The mineral compositions were recalculated to standard numbers of oxygen per formula unit, with H_2O assumed to be present in stoichiometric amounts. The amount of oxygens used is given in each table of mineral analyses. The compositional fractions are defined as follows: X_{Mg} = Mg /(Fe + Mg), X_{Na} = Na/(Na + K). Atoms per formula unit (a.p.f.u.) are used.

3.1.2 - ^{40}AR/^{39}AR GEOCHRONOLOGY

The ^{40}Ar/^{39}Ar geochronometer was used on fourteen samples. The samples were selected in the field with the cooperation of Stéphane Scaillet from the University of Orléans (France), expert in ^{40}Ar/^{39}Ar geochronology. The fundamental criterion for the sample selection was the freshness of the rock and the second criterion was the presence of several fabric relationships. Two samples come from the same outcrops used for monazite U-Pb dating (MJ52 and MJ62). We selected eight phyllites, four micaschists and two gneisses along two cross-sections from the lowest-grade phyllites to higher-grade micaschists and gneisses. ^{40}Ar/^{39}Ar CO$_2$-laser step-heating was applied on single grains and populations handpicked after crushing. The analyses by step-heating were done on 16 samples, with about 36 steps by samples and by *in-situ* laser ablation on two thin-sections. The *in-situ* dating was used to compare step-heating age with spatially controlled data including potential core-rim zoning inside individual mica grains, or across different structures. The samples were prepared differently for dating by step-heating or *in-situ* as following

For the CO$_2$-laser step-heating, the separation of the muscovites and biotites was done by gentle crushing of the whole rock. The dust was removed by decantation after adding de-ionized water, acetone and alcohol in the crushed-rock (ultrasonic bath was not needed), and dried at 50 °C in a vented oven. The best grains of muscovite and biotite were handpicked under a binocular microscope according to their size, freshness and purity. They were weighted, photographed and packed with standard samples into Al foil envelopes.

For spatially resolved UV-laser *in-situ* mapping, thick-sections were carefully selected, cut and polished to 1 µm (adhesive such as superglue was not used) to obtain 300 µm-thick, 10 mm diameter circular sections showing the most interesting structures or the largest micas. These circular sections were photographed (under a binocular microscope and with reflected light) and packed together with standard samples.

The circular sections and the separated grains were irradiated during 10 hours at Corvallis (CLICIT in-core position, Oregon, USA) along with sanidine standard FCT (28.02 ± 0.28 Ma, Renne et al., 1998) and analyzed at the ^{40}Ar/^{39}Ar laboratory (Figure II.13) housed at the Institut des Sciences de la Terre d'Orléans (ISTO, France). After irradiation and return back from the reactor, the micas were carefully unpacked and placed in a stainless steel sample holder and in a laser port pumped to ultra-high vacuum and baked to 195 °C over 48 hours. Extracted gasses were purified using two air-cooled GP50 SAES® getters during 6 minutes before admission into the mass spectrometer. Ar and Cl isotopes were sequentially measured in 20 cycles with an electron multiplier (^{35}Cl, ^{36}Ar ± ^{1}H^{35}Cl, ^{37}Ar ± ^{37}Cl, ^{38}Ar ± ^{1}H^{37}Cl, ^{39}Ar, ^{40}Ar isotopes) and a Faraday cup (^{40}Ar only) by peak-switching on one of the three static noble gas Helix-SFT® (Thermo Fisher Scientific, GmbH) mass-spectrometers operated at ISTO with a mass-resolution in excess of 750. Gas handling and mass-spectrometer operations are fully automated using stand-alone LabView-based software. Procedural blanks were monitored according to their evolution: every third heating step (typically the initial low-*T* heating steps featuring little or no ^{39}Ar) to every sample gas admission (all *in-situ* experiments and mid to high-T extraction steps) in the same conditions as the sample. Typical values were 0.1 fA, 0.001 fA, 0.001 fA, 0.001 fA, and 0.001 fA for m/e = 40, 39, 38, 37, 36, respectively.

Muscovites were step-heated as populations (clusters). For *in-situ* dating, target-matching techniques were employed to allow direct ^{40}Ar/^{39}Ar targeting of mineral zones and structures previously imaged. A high-resolution deep 213-UV laser probe (Photon Machines LXG2+ model) was used to excavate 50 µm–wide square or circular-shaped ablation pits about 30–50 µm–deep at a repetition rate of 20 Hz and 4–5 mJ/pulse. White light interferometry scanning of individual spots revealed steep-walled pits with variable bottom geometry (from nearly flat at integrated pulse counts <600, to progressively cone-shaped due to progressive defocusing and internal reflections past 1000 pulses). Except for a few analyses, ^{37}ArCa and ^{36}ArCl isotopes were all measured close to background values. Overall, they provide no insight on geochemical-age relationships and are not discussed further below.

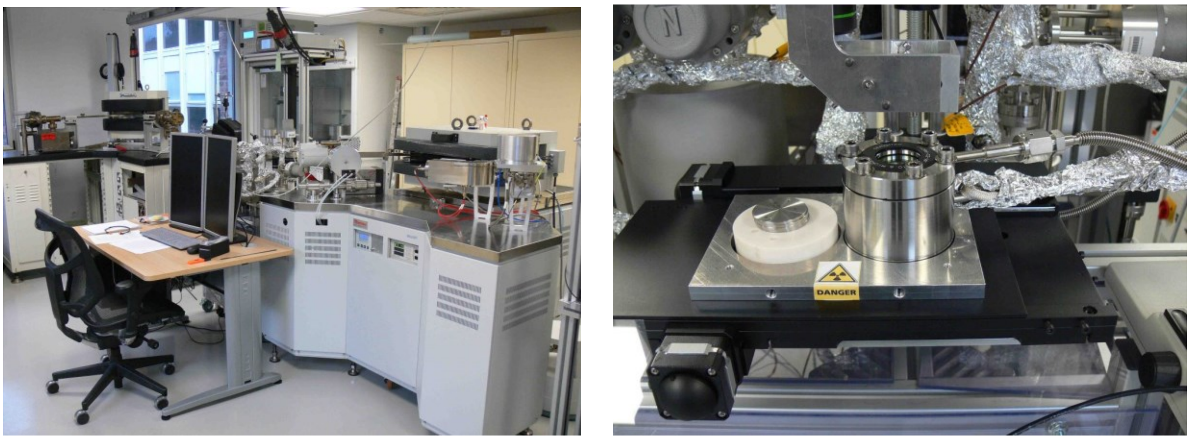

Figure II.13: Measuring equipment of the ^{40}Ar/^{39}Ar laboratory at ISTO (Orléans, France). The samples to be dated are loaded in an ultra-high-vacuum holder (right of the figure) connected to a ^{40}Ar/^{39}Ar mass spectrometer (left of the figure) for noble-gas analysis.

Data regression and age calculations/corrections were made following Scaillet (2000). Regressed ^{40}Ar/^{39}Ar isotopic data are tabulated in the supplementary material (Tables S.II.5–23). Individual age errors include propagation of all instrumental and procedural uncertainties. Plateau ages / Weighted mean ages (WMA) are calculated as integrated (inverse-variance weighted) mean ages over the corresponding steps, and total-gas ages (TGA) by individually summing the Ar isotopes of all steps (equivalent to a K–Ar age). These are quoted at ±1σ.

3.1.2 - PHYLLITE DRILL-CORE STUDY

The phyllites were also studied using the drill-core TIDD003 (PTIS03) reaching a depth of 484 m, drilled close to the city of Olovi (near Studenec: 50.2580950N, 12.5184764E). The drill hole did not reach the micaschists but a difference in grain size is visible from the top to the bottom of the drill core, and interesting folds are preserved. Eight samples were collected along the whole drill core (at a depth of 51 m, 95 m, 128 m, 180 m, 209 m, 225 m, 314 m and 375 m) to make thin-sections. Three of these samples were selected for further dating using the ^{40}Ar/^{39}Ar geochronometer. The samples were named according to the name of the well (S3), followed by their depth of sampling from the surface (e.g. the sample S3-051 was sampled at a depth of 51m; S3-180 at a depth of 180m, etc). The drill core was cut lengthwise and the thin-sections were made perpendicularly to the main sub-horizontal foliation.

3.2 - MICROSTRUCTURE AND PETROGRAPHY OF THE DATED SAMPLES

The samples are ordered in description and age parts from the structurally higher low-grade metasedimentary envelope – ie from the Erzgebirge rim – to the structurally lower high-grade gneisses, belonging to the Erzgebirge core. The position of the samples is visible on the map in Figure II.1a. The GPS location, type of ^{40}Ar/^{39}Ar dating performed (step-heating or *in-situ*) and mineralogy of the samples are given in Table II.2.

Sample	Unit	Lithology	Latitude	Longitude	Dating type		Mineralogy																			Accessory minerals
					Step-heating	In-situ	q	g	mu	bi	pa	ma	ctd	chl	ru	ilm	ab	ksp	cal	ep	all	mag	sph	hem	tur	
MJ69G	Phyllite	chl phyllite	50.772864	12.979316	X		x		x					x	x	x										apatite, zircon, monazite, xenotime
MJ52F		ctd phyllite	50.255421	12.467586	X		x		x		x		x	x	x	x										
MJ22		ab phyllite	50.754045	12.982997	X	X	x		x					x	x	x	x		x						x	
MJ92C		chl phyllite	50.232009	12.514019	X		x		x		x			x	x	x										
S3		chl-ab phyllite	50.258095	12.5184764	X		x		x		x			x	x	x	x								x	
MJ46E		ab-chl phyllite	50.274598	12.547553	X		x		x		x			x	x	x	x									
MJ213A	Micaschist	ep micaschist	50.744004	12.991692	X		x		x		x	x		x	x	x	x			x	x	x				
MJ216		g micaschist	50.225064	12.498943	X		x	x	x	x				x	x	x	x									
MJ11I		quartzitic g micaschist	50.220101	12.574597	X	X	x	x	x	x			x	x	x	x										
MJ62G		g micaschist	50.663563	13.040747	X		x	x	x	x	x		x	x	x	x	x							x	x	
MJ61B	Gneiss	g paragneiss	50.664865	13.061473	X		x	x	x	x				x	x	x	x	x					x			
MJ212		orthogneiss	50.654	13.062439	X		x		x	x	x	x		x	x	x	x	x								

Table II.2: Description of the sample used for $^{40}Ar/^{39}Ar$ geochronology in the part II.

3.2.1 - PHYLLITES

- MJ69G

The sample MJ69G was collected in the Erzgebirge area (Figure II.1a). It is a very fine-grained chloritoid-phyllite with quartz, muscovite (Si = 3.14–3.24 a.p.f.u., Al = 2.48–2.73 a.p.f.u., Figure II.14a; Table II.3), chloritoid, chlorite, ilmenite and rutile M1-2 assemblage (Table II.2). It does not contain biotite nor garnet (Table II.2). The S1 fabric is completely transposed into S2 foliation with rare relics of S1 lithons. Another similar sample (MJ69H) from this outcrop was used to highlight the deformation and metamorphism in the phyllites and is described in part I.4.1. A microphotograph of this sample is visible in Figure I.3a.

- MJ52F

The sample MJ52F is an extremely fine grained chloritoid-phyllite collected from the Fichtelgebirge area (Figure II.1a) containing q-mu-ctd-chl-pa-ru-ilm M1-2 assemblage (Table II.2). Other similar samples (MJ52C and MJ52D) from the same outcrop MJ52 were used to highlight the description of the deformation and metamorphism, and for monazite U-Pb dating. They are described in detail in parts I.4.1 and II.2.2.2. Microphotographs of these samples are visible in Figures I.3b,c and II.2d,e. It does not contain biotite nor garnet. It shows a strong transposition of S1 to S2 foliation with only locally preserved S1 lithons. The main muscovite-chlorite bearing composite foliation S2 is folded by S4 crenulation cleavage. Chloritoid porphyroblasts are aligned along the S2 foliation and are surrounded by chlorite (Figure II.2e). The muscovites are extremely tiny and have a Si content of 3.09–3.28 a.p.f.u. and an Al content of 2.46–2.74 a.p.f.u. (Figure II.14a; Table II.3).

- MJ22

The sample MJ22, collected from the Erzgebirge area (Figure II.1a), is a fine-grained phyllite with q-mu-ph-chl-ab-cal-ilm-ru-tur M1-2 assemblage (Table II.2). It does not contain biotite nor garnet. The phengitic muscovites have a Si content of 3.10–3.37 a.p.f.u. and an Al content of 2.19–2.74 a.p.f.u. (Figure II.14a; Table II.3) with generally slightly more Si in the core of the phengite than in the rim. The S1 fabric is completely transposed into S2 foliation with rare relics of S1 lithons. The albite porphyroblasts have folded inclusion trails with ilmenite and rutile at high angle to the S2 fabric. This sample was selected for *in-situ* dating as it contains relatively large white mica grains (~1–2 mm) contrary to the other phyllites.

However, the phengites from the circular sections were too small and too thin to be individually dated and the *in-situ* ages are likely a mix of 2-3 white micas belonging to the same fabric.

Sample	MJ69G	MJ52F	MJ22	MJ92C	MJ46E	MJ213A		MJ11I		MJ62G		MJ61B	MJ212
Mineral	mu	mu	mu	mu	mu	mu	mu	mu	mu	mu	mu	mu	mu
Position	S1-2	S1-2	S1-2	S1-2	S1-2	S2	S3	S2	S3	S2	S3	S2	S2
SiO2	47,75	47,27	47,72	46,78	46,45	49,38	46,19	47,88	47,74	47,78	46,37	50,08	49,83
TiO2	0,22	0,49	0,37	0,11	0,34	0,21	0,20	0,21	0,14	0,30	0,32	0,79	0,65
Al2O3	34,29	30,94	29,04	33,64	34,90	27,84	35,66	31,27	35,80	28,61	33,67	26,56	30,48
FeO	2,19	4,76	4,21	2,93	2,15	3,40	2,62	2,67	1,29	4,33	2,41	3,51	2,89
MnO	0,02	0,00	0,02	0,02		0,02	0,01	0,00	0,01	0,00	0,01	0,05	0,03
MgO	1,06	1,92	2,14	0,84	0,70	2,72	0,70	1,47	1,02	2,08	0,70	2,93	2,67
CaO	0,00	0,00	0,00	0,02		0,05	0,01	0,00	0,02	0,01	0,02	0,00	0,02
Na2O	0,71	0,60	0,45	1,22	0,77	0,40	0,92	0,54	1,58	0,59	0,73	0,10	0,14
K2O	8,80	9,05	10,54	9,00	10,07	10,11	9,23	10,07	8,76	10,09	10,31	11,01	9,60
Total	95,09	95,03	94,48	94,62	95,37	94,17	95,54	94,19	96,36	93,80	94,55	95,08	96,43
O	11	11	11	11	11	11	11	11	11	11	11	11	11
Cations	7	7	7	7	7	7	7	7	7	7	7	7	7
Si	3,20	3,19	3,24	3,14	3,10	3,36	3,07	3,25	3,13	3,26	3,12	3,38	3,32
Ti	0,01	0,03	0,02	0,01	0,02	0,01	0,01	0,01	0,01	0,02	0,02	0,04	0,03
Al	2,71	2,46	2,32	2,67	2,74	2,23	2,80	2,50	2,76	2,30	2,67	2,12	2,39
Fe3+	0,00	0,00	0,00	0,00	0,00	0,00	0,00	0,00	0,00	0,00	0,00	0,00	0,00
Fe2+	0,12	0,27	0,24	0,16	0,12	0,19	0,15	0,15	0,07	0,25	0,14	0,20	0,16
Mn	0,00	0,00	0,00	0,00	0,00	0,00	0,00	0,00	0,00	0,00	0,00	0,00	0,00
Mg	0,11	0,19	0,22	0,08	0,07	0,28	0,07	0,15	0,10	0,21	0,07	0,30	0,26
Ca	0,00	0,00	0,00	0,00	0,00	0,00	0,00	0,00	0,00	0,00	0,00	0,00	0,00
Na	0,09	0,08	0,06	0,16	0,10	0,05	0,12	0,07	0,20	0,08	0,10	0,01	0,02
K	0,75	0,78	0,91	0,77	0,86	0,88	0,78	0,87	0,73	0,88	0,89	0,95	0,81
Total	7,00	7,00	7,00	7,00	7,00	7,00	7,00	7,00	7,00	7,00	7,00	7,00	7,00
XMg	0,46	0,42	0,47	0,34	0,37	0,59	0,32	0,49	0,58	0,46	0,34	0,60	0,62
XNa	0,11	0,09	0,06	0,17	0,10	0,06	0,13	0,07	0,22	0,08	0,10	0,01	0,02

Table II.3: Representative muscovite analyses of the samples used for $^{40}Ar/^{39}Ar$ dating. Oxides are in wt%.

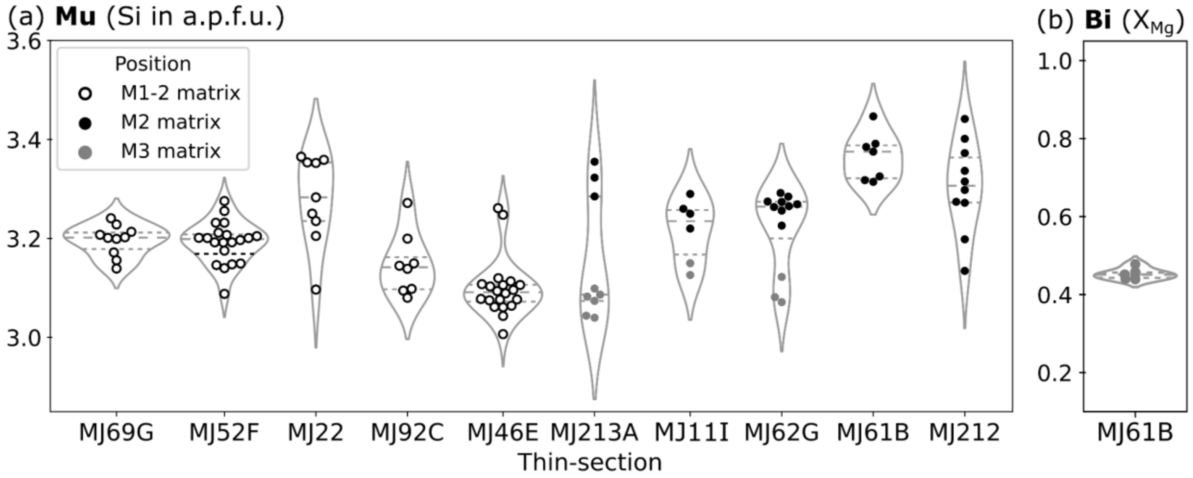

Figure II.14. Compositional variation in: (a) White mica (Si in a.p.f.u.); (b) biotite (X_{Mg}). The violin plots show the distribution of the data. The central full line shows the median, the dashed lines indicate the 25th and 75th percentiles and circles show measurements. Microstructural position of the micas is indicated by the color and fill of the points.

- MJ92C

The sample MJ92C (Figure II.1a) is a very fine-grained phyllite with q-mu-chl-pa-ilm-ru M1-2 assemblage (Table II.2). It was collected from the Fichtelgebirge area (Figure II.1a). It does not contain biotite nor garnet. The muscovites have a Si content of 3.08–3.27 a.p.f.u. and an Al content of 2.46–2.78 a.p.f.u. (Figure II.14a; Table II.3). The S1 fabric is completely transposed into S2 foliation and thick layers of quartz and muscovite/chlorite are visible.

- S3-051

The phyllite sample S3-051 was collected from the Fichtelgebirge area (Figure II.1a), from the drill core at a depth of 51m from the surface. It is a fine-grained phyllite with q-mu-chl-ab-ru-ilm M1-2 assemblage (Table II.2). The sample contains large chlorite flakes in the matrix, intercalating with tiny muscovites. The albite porphyroblasts contain folded inclusion trails of rutile and ilmenite. The composite S1-S2 foliation is crenulated by F4 folds.

- S3-180

The phyllite sample S3-180 (Figure II.1a) was collected from the Fichtelgebirge area, from the drill core at a depth of 180m. It is a fine-grained phyllite with q-mu-chl-ab-ru-ilm-tur M1-2 assemblage (Table II.2). The S1 foliation is almost completely transposed into S2 foliation, rarely preserving lithons with S1 relics

- S3-375

The phyllite sample S3-375 was collected from the drill core at a depth of 375m, in the Fichtelgebirge area (Figure II.1a). It is a fine-grained phyllite with q-mu-chl-ab-ru-ilm-tur M1-2 assemblage (Table II.2). The albite porphyroblasts are numerous and preserve folded inclusion trails of rutile and ilmenite. The composite S1 foliation, marked by alternation of quartz and muscovite bands, is strongly transposed in S2 foliation.

- MJ46E

The sample MJ46E, collected from the Fichtelgebirge area (Figure II.1a), is a very fine-grained phyllite containing quartz, muscovite (Si = 3.01–3.26 a.p.f.u., Al = 2.46–2.85 a.p.f.u.; Figure II.14a; Table II.3), chlorite, albite, paragonite, ilmenite and rutile (Table II.2). The S1 fabric is folded and crenulated by the S2 foliation alternating muscovite-chlorite and quartz.

3.2.2 - MICASCHISTS

- MJ213A

The sample MJ213A, collected from the Erzgebirge area (Figure II.1a), is an epidote-micaschist bearing quartz, phengitic muscovite (Si = 3.04–3.36 a.p.f.u., Al = 2.23–2.82 a.p.f.u.; Figure II.14a; Table II.3), chlorite, epidote, allanite, magnetite, margarite, paragonite, albite, apatite, ilmenite and rutile (Table II.2). The phengitic muscovite in the S2 foliation have a higher Si content (Si = 3.28–3.36 a.p.f.u., Al = 2.23–2.30 a.p.f.u.; Figure II.14a; Table II.3) than the muscovites in the M3 fabric (Si = 3.04–3.10 a.p.f.u., Al = 2.73–2.82 a.p.f.u.; Figure II.14a; Table II.3). The epidotes and phengitic muscovite are elongated along the S2 foliation and the epidotes often have an allanite core. The sample does not contain biotite nor garnet.

- MJ216

The sample MJ216 (Figure II.1a) is a garnet-micaschist bearing q-mu-ab-g-chl-bi-ilm-ru (Table II.2). It was collected from the Fichtelgebirge area (Figure II.1a). The garnets are small and strongly replaced by chlorite and biotite. The albite porphyroblasts contain folded inclusion trails of ilmenite and rutile. The main S3 foliation is strongly folded by F4 folds.

- MJ11I

The sample MJ11I (Figure II.1a) is a quartzitic garnet-micaschist with q-mu-g-bi-chl-ilm-ru (Table II.2). It was collected from the Fichtelgebirge area (Figure II.1a). Another similar sample from this outcrop (MJ11C) was used for monazite U-Pb dating and is described in detail in part II.2.2.6. Microphotographs of this sample are visible in Figure II.3f,g. It contains relics of isoclinal F2 folds reworked by the main sub-horizontal S3 foliation, which was overprinted by open F4 folds (Figure II.3f). The M1-M2 mineral assemblages preserved in relics of S1-S2 foliations and as inclusions in garnet correspond to q-ph-pa-g-chl-ru±ctd. The matrix assemblage bi-mu-ilm-pl-chl likely reflects both M3 and M4 metamorphism (Figure II.3f). Garnet is commonly surrounded by biotite and chlorite (Figure II.3f). Very few grains of phengitic muscovite (in M2 matrix: Si = 3.22–3.29 a.p.f.u., Al = 2.25–2.39 a.p.f.u. and in M3 matrix: Si = 3.13–3.15 a.p.f.u., Al = 2.67–2.76 a.p.f.u.; Figure II.14a; Table II.3) are present in the sample. This quartzite sample does not present significant microstructures. However, it was selected for *in-situ* dating as it contains very fresh white mica, contrary to the other micaschists, and large white mica grains (~1–2 mm).

- MJ62G

The sample MJ62G, collected from the Fichtelgebirge area (Figure II.1a), is a garnet-micaschist bearing q-mu-g-bi-chl-ab-ilm-ru-tur-hem (Table II.2). Another similar sample from this outcrop (MJ62C) was used for monazite U-Pb dating and is described in detail in part II.2.2.7. Microphotograph of this sample and photograph of the outcrop are visible in Figures II.3h,i and I.2d. The S2 foliation bearing q-ph-pa-g-chl-ru-ilm is mostly completely transposed by the S3 fabric, defined by biotite, muscovite, ilmenite, chlorite and plagioclase, which is strongly overprinted and/or reactivated by D4 deformation (Figure II.3h). The phengitic muscovite in the S2 foliation have a higher Si content (Si = 3.23–3.29 a.p.f.u., Al = 2.24–2.40 a.p.f.u.; Figure II.14a; Table II.3) than the muscovites in the M3 fabric (Si = 3.07–3.13 a.p.f.u., Al = 2.67–2.71 a.p.f.u.; Figure II.14a; Table II.3) and the phengitic muscovites generally have slightly more Si in their core than in their rim. The garnets are replaced by chlorite around the garnets or in large quantities inside some garnets. The main S3 foliation is folded by F4 folds (Figure II.3h).

3.2.3 - GNEISSES

- MJ61B

The sample MJ61B (Figure II.1a), collected from the Erzgebirge area, is a paragneiss bearing q-bi-g-chl-mu-ab-ksp-ilm-ru-sph-apa (Table II.2). The matrix contains a lot of biotites (X_{Mg} = 0.44–0.48, Figure II.14b; Table II.3), sometimes fresh but often retrograded and very few phengites (Si = 3.31–3.45 a.p.f.u., Al = 2.09–2.22 a.p.f.u.; Figure II.14a; Table II.3). The sample is lacking microstructures and the minerals do not have a systematic orientation in the matrix.

- MJ212

The sample MJ212 (Figure II.1a), collected from the Erzgebirge area, is an orthogneiss with q-pl-ab-mu-bi-chl-ilm-ma-pa-ksp-ru-apa (Table II.2). Biotites and phengitic muscovites (Si = 3.13–3.44 a.p.f.u., Al = 2.23–2.65 a.p.f.u.; Figure II.14a; Table II.3) are aligned along the main subhorizontal foliation S3. The muscovites are often surrounded by chlorite. The sample has thick quartz-rich and mica-rich layers.

White micas show a compositional variability from muscovite to almost pure phengite (Figures II.14a and II.15), with a Si content between 3.01–3.37 a.p.f.u. in the phyllites, 3.04–3.36 a.p.f.u. in the micaschists and 3.13–3.45 a.p.f.u. in the gneisses. In the micaschists, the highest values are observed for the phengite grains in the M2 matrix (Si = 3.22–3.36 a.p.f.u.; Figure II.14a), while the M3 matrix contains grains that are significantly poorer in Si (3.04–3.15 a.p.f.u.; Figure II.14a). Thus, there is a clear trend during the polyphase metamorphism with the Si-richest white micas in the HP matrix (Si up to 3.45 a.p.f.u.) and the Si-poorest white micas in the *LP* matrix (Si down to 3.01 a.p.f.u.).

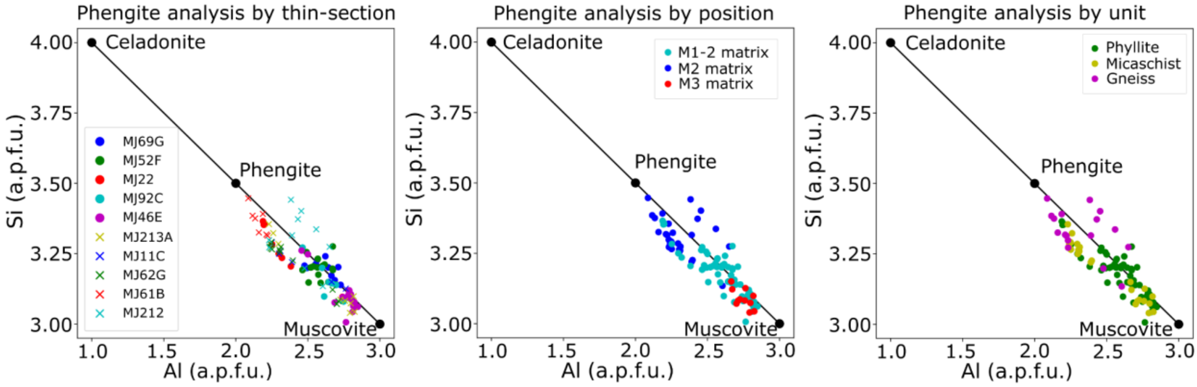

Figure II.15. Plots showing Si versus Al (in a.p.f.u.) for white mica compositions. The line of ideal Tschermak substitution is indicated. The poles of muscovite, phengite and celadonite are shown by the black dots. The data points are shown by color and shape by: (a) thin-section, (b) position of the mineral in the thin-section, (c) unit and rock type.

The figure II.15 shows the chemical variations due to Tschermak substitution in each sample by thin-section, by position of the white mica in the thin-section or by unit (rock type). The most phengitic grains were found in the gneisses, in the M2 matrix of the micaschists and in rare phyllites, while the less phengitic white micas were found in the M3 matrix of the micaschists, or in the phyllite samples.

Some white mica grains record a slight compositional zoning of Si, Al, Mg and Fe (Figure II.16c,d), while other white mica do not show any zoning (Figure II.16a), or present an alternation of low and high content of Mg, Fe and Al (Figure II.16b,d). Other authors reported the presence of zoned phengites with a core rich in Si and a Si-poor rim (Faryad & Kachlík, 2013 and Rahimi & Massonne, 2018, 2020).

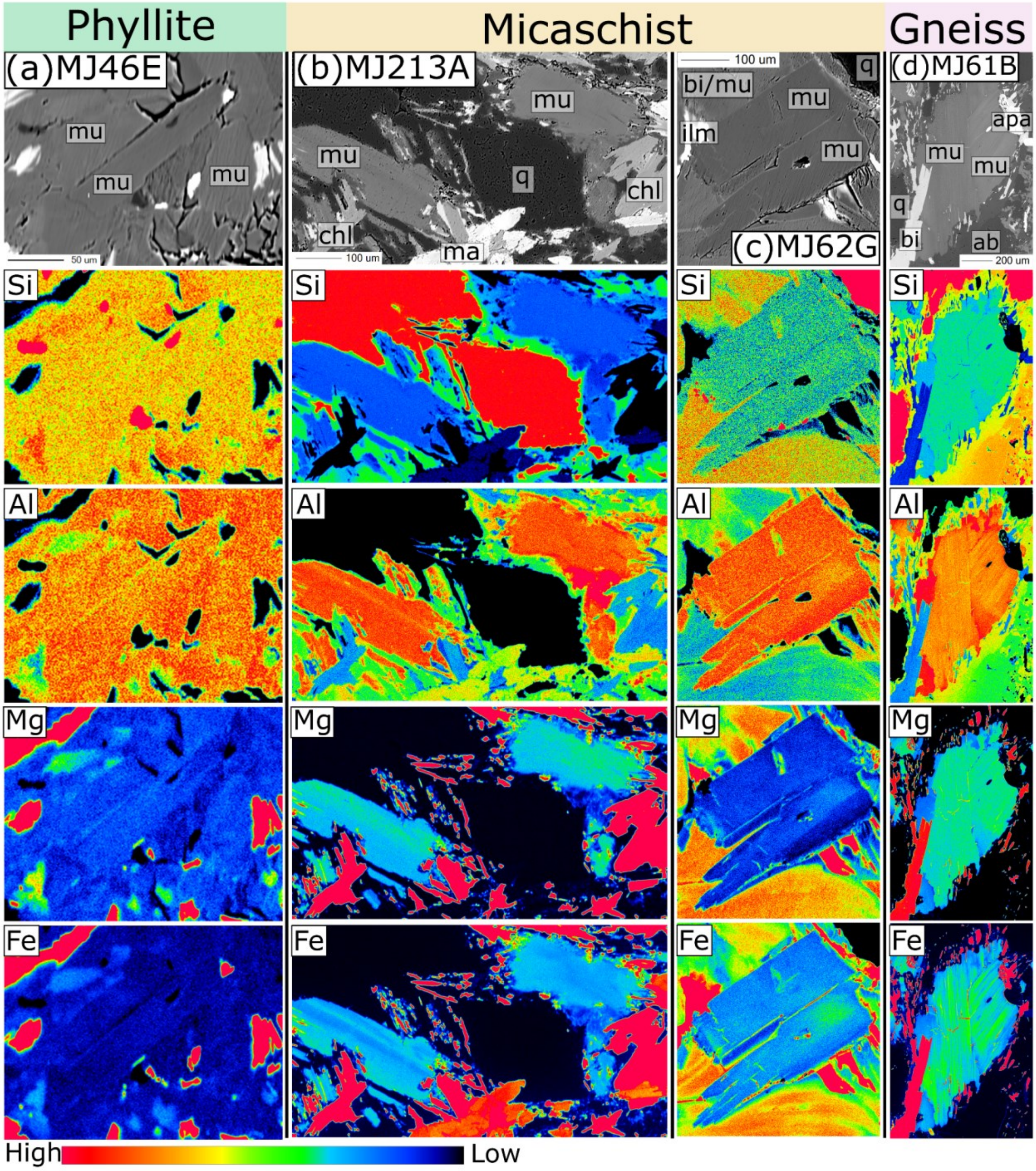

Figure II.16. Compositional maps of Si, Al, Mg and Fe for white mica of the samples MJ46E (a), MJ213A (b), MJ62G (c) and MJ61B (d).

3.3 - RESULTS

All the samples were dated by CO_2-laser step-heating, and two samples (MJ22 and MJ11I) were in addition analyzed by UV-laser *in-situ* mapping. All the dating was performed on muscovites, except on one biotite in the sample MJ61B. The age errors are quoted at 1σ level.

3.3.1 - PHYLLITES GEOCHRONOLOGY

- MJ69G

For the chloritoid-phyllite MJ69G, the age spectrum (Figure II.17 and Table S.II.5) measured on a very fine-grained white mica population is characterized by a sharp increase of apparent $^{40}Ar/^{39}Ar$ ages over the first three degassing steps, followed by consistent apparent ages at 343 Ma. The end of the spectrum shows a decrease of apparent $^{40}Ar/^{39}Ar$ ages over the last six degassing steps. The WMA and TGA are calculated at 343.1 ± 1.1 Ma (MSWD = 1.55) and 338.2 ± 3.5 Ma, respectively.

- MJ52F

In the chloritoid-phyllite MJ52F, an extremely fine-grained white mica population was analyzed and gave the least flat spectrum of all the acquired spectra. The spectrum is characterized by a progressive increase of the apparent $^{40}Ar/^{39}Ar$ ages followed by a plateau at 340 (blue spectrum in Figure II.17 and Table S.II.6). The WMA is calculated at 340.0 ± 0.9 Ma (MSWD = 1.11) and the TGA at 332.7 ± 3.3 Ma. We decided to duplicate the measure to ensure the age and the spectrum shape. The second dating produced similar age and spectrum shape (black spectrum in Figure II.17 and Table S.II.7). The WMA is 343.4 ± 1.3 Ma (MSWD = 1.41) and the TGA 334.2 ± 3.4 Ma.

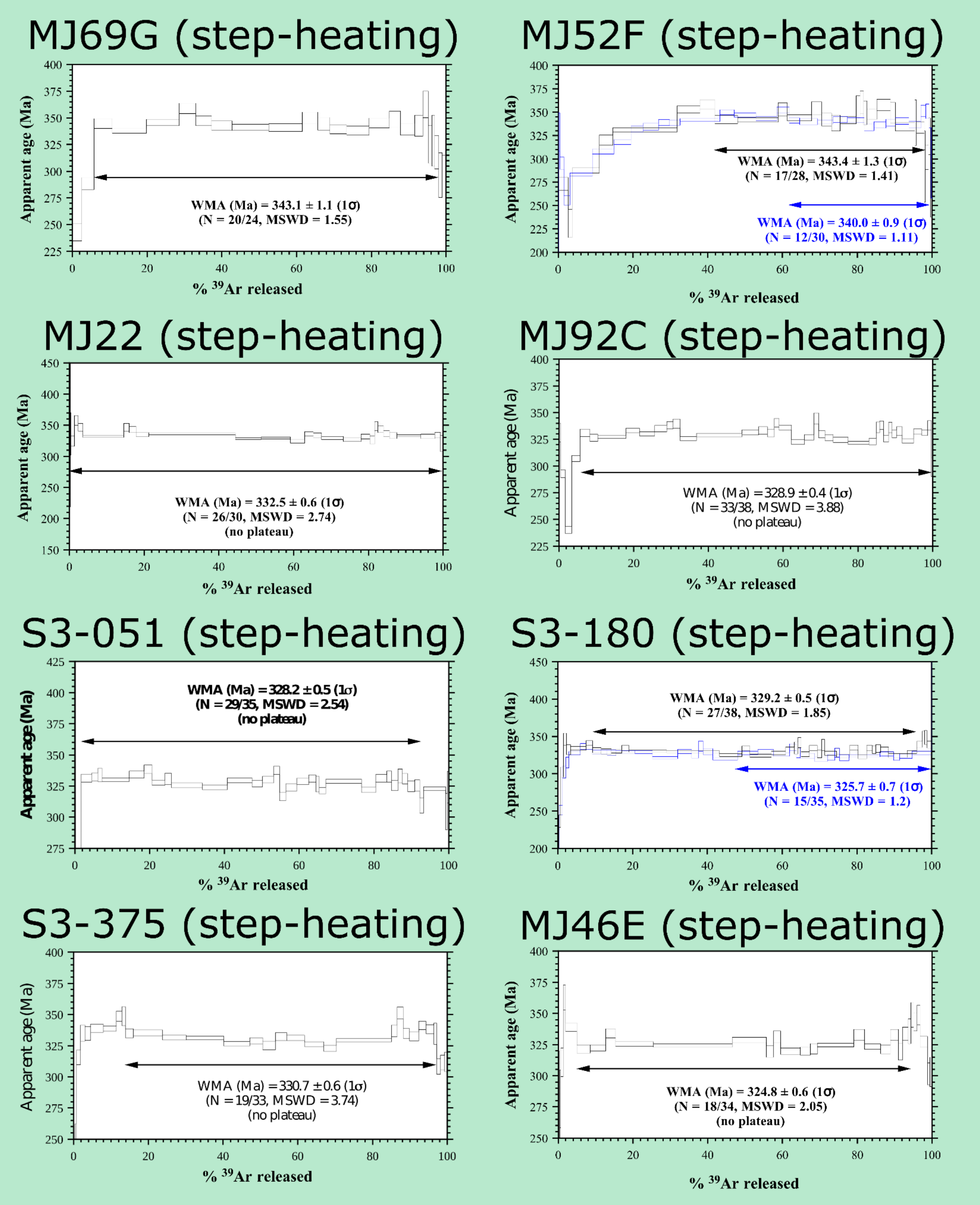

Figure II.17. Step-heating ^{40}Ar/^{39}Ar age spectra of phengites from the phyllites. WMA: Weighted Mean Age. Error boxes and WMA are ± 1σ. Note that the scale of the vertical axis is different for all the samples.

- MJ22

For the phyllite MJ22, a fine-grained white mica population was analyzed and the age spectrum is overall flat with an apparent $^{40}Ar/^{39}Ar$ age of ~333 Ma (no plateau; Figure II.17 and Table S.II.8). The WMA is calculated at 332.5 ± 0.6 Ma (MSWD = 2.74), and the TGA at 333.2 ± 3.3 Ma.

Additionally, larger white mica grains were dated with *in-situ* UV-laser by 33 points across the minerals (Figure II.18 and Table S.II.9). The crystals yield consistent apparent ages between 324 and 353 Ma (except one analysis with an age of 598 Ma which was excluded) with a WMA calculated at 335.8 ± 0.6 Ma (MSWD = 2.67) and a TGA at 336.5 ± 3.3 Ma. The position of the *in-situ* ages in the circular section is visible on Figure II.18e. The spectra of the *in-situ* dating and of the ordered ages obtained by step-heating are shown in the same graph, for comparison (Figure II.18f). In addition, the probability density plot of the *in-situ* ages is presented in Figure II.18g and shows two age peaks at 328.7 and 334.2 Ma for the *in-situ* dating.

- MJ92C

For the phyllite MJ92C, a very fine-grained white mica population yields a slightly discordant age spectrum with apparent $^{40}Ar/^{39}Ar$ ages varying between 322 and 345 Ma (no plateau; Figure II.17 and Table S.II.10). The WMA and TGA are calculated at 328.9 ± 0.4 Ma (MSWD = 3.88) and 327.2 ± 3.2 Ma, respectively.

- S3-051

The age spectrum of the fine-grained white mica population of the phyllite S3-051 is slightly discordant with apparent $^{40}Ar/^{39}Ar$ ages varying between 317 and 339 Ma (no plateau; Figure II.17 and Table S.II.11). The WMA and TGA are calculated at 328.2 ± 0.5 Ma (MSWD = 2.54) and 326.0 ± 3.2 Ma, respectively.

- S3-180

The phyllite S3-180 was dated two times by step-heating. The fine-grained white mica population is characterized by a sharp increase of the apparent $^{40}Ar/^{39}Ar$ ages up to 328 and 332 Ma, respectively, followed by plateaux at ~326 Ma and ~329 Ma (Figure II.17 and Tables S.II.12 and S.II.13). The WMA are calculated at 325.7 ± 0.7 Ma and 329.2 ± 0.5 Ma (MSWD = 1.2 and 1.85), respectively, and the TGA at 325.1 ± 3.2 Ma and 329.5 ± 3.3 Ma, respectively.

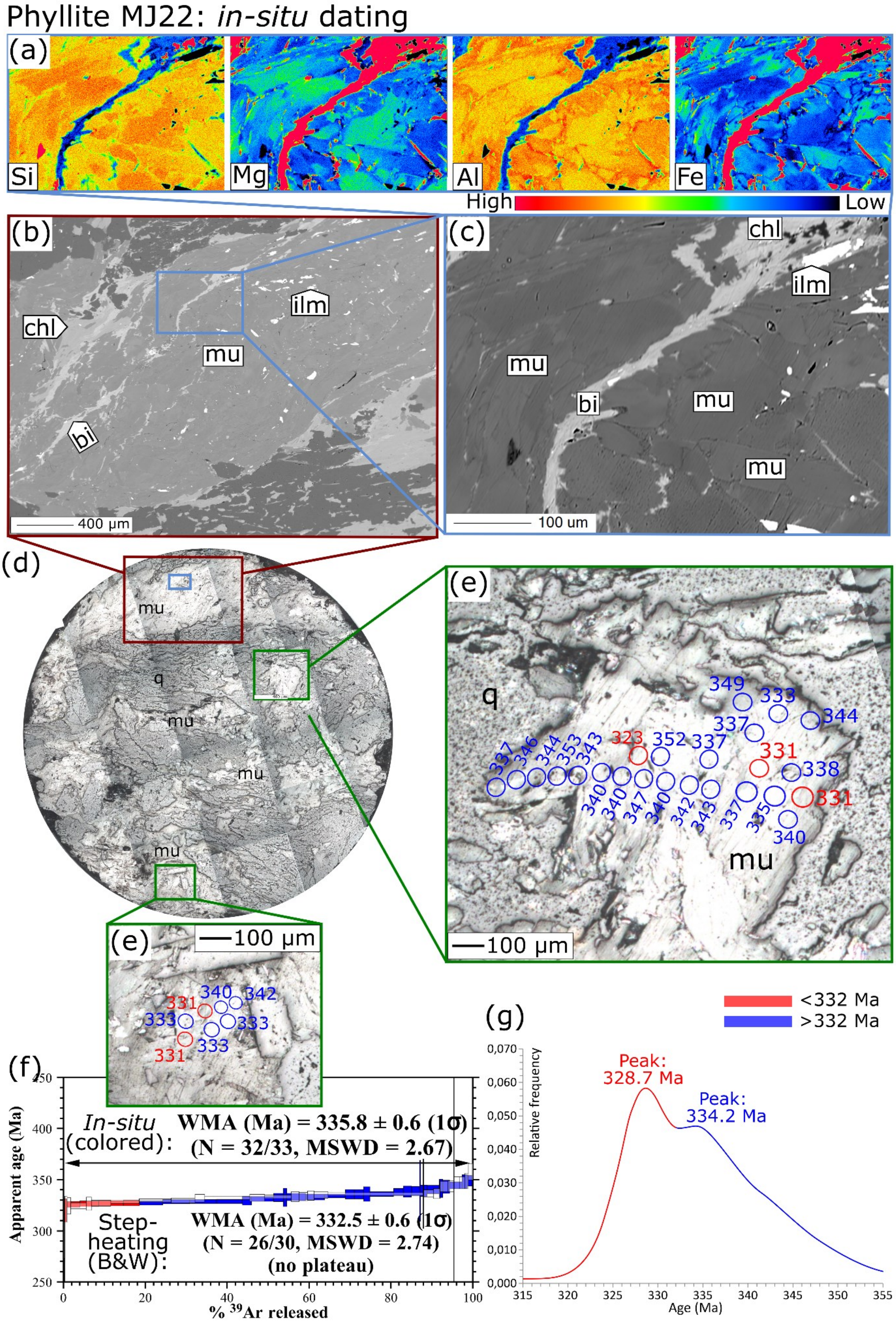

Figure II.18. In-situ ^{40}Ar/^{39}Ar age spectra of phengites from the phyllite MJ22. (d) Circular sections (reflected light microscope) with BSE images (b,c) and compositional maps (a,c). (e) Location of the in-situ dating with rounded weighted mean age for each measure. (f) Age spectra of the in-situ dating (in red and blue) and of the ordered ages obtained by step-heating (in black and white) for comparison. (g) Probability density plot showing two peak ages at 328.7 and 334.2 Ma for the in-situ dating.

- S3-375

The age spectrum of the fine-grained white mica population of the phyllite S3-375 is slightly discordant with apparent $^{40}Ar/^{39}Ar$ ages varying between 323 and 341 Ma (no plateau; Figure II.17 and Table S.II.14). The WMA and TGA are calculated at 330.7 ± 0.6 Ma (MSWD = 3.74) and 330.8 ± 3.3 Ma, respectively.

- MJ46E

For the phyllite MJ46E, a very fine-grained white mica population yields a slightly discordant age spectrum with apparent $^{40}Ar/^{39}Ar$ ages varying between 320 and 334 Ma (no plateau; Figure II.17 and Table S.II.15). The WMA and TGA are calculated at 324.8 ± 0.6 Ma (MSWD = 2.05) and 329.8 ± 3.3 Ma, respectively.

3.3.2 - MICASCHISTS AND GNEISSES GEOCHRONOLOGY

- MJ213A

The age spectrum of the epidote-micaschist MJ213A is overall flat with a plateau at ~333 Ma (Figure II.19 and Table S.II.16). The step #13 was excluded from the calculation. The WMA is calculated at 332.8 ± 0.5 Ma (MSWD = 1.46), and the TGA at 334.5 ± 3.3 Ma.

- MJ216

$^{40}Ar/^{39}Ar$ step-heating of the garnet-micaschist MJ216 yielded a globally decreasing age spectrum with apparent ages ranging from 323 to 349 Ma with a plateau at ~328 Ma (Figure II.19 and Table S.II.17). The WMA is calculated at 327.8 ± 0.5 Ma (MSWD = 1.57) and the TGA at 329.4 ± 3.2 Ma.

- MJ11I

For the quartzitic garnet-micaschist MJ11I, white mica population yields a slightly discordant age spectrum with apparent $^{40}Ar/^{39}Ar$ ages varying between 324 and 346 Ma (no plateau). The WMA and TGA are calculated at 329.9 ± 0.5 Ma (MSWD = 3.295) and 328.8 ± 3.3 Ma, respectively (Figure II.19 and Table S.II.18).

This sample presents large fresh white mica grains and was chosen for additional *in-situ* dating. Five single white mica grains of different size were dated *in-situ* by 44 points across the minerals (Figure II.20 and Table S.II.19). The crystals yield consistent apparent ages between 337 and 351 Ma with a WMA calculated at 334.8 ± 0.3 Ma (MSWD = 4.60) and a TGA at 335.3 ± 3.3 Ma. The location of the *in-situ* ages in the phengites is visible on Figure II.20c,d. The spectra of the *in-situ* dating and of the ordered ages obtained by step-heating are shown in the same graph, for comparison (Figure II.20e). In addition, the probability density plot of the *in-situ* ages is presented in Figure II.20f and shows only one age peak at 334.3 Ma for the *in-situ* dating.

- MJ62G

The age spectrum of the garnet-micaschist MJ62G is overall flat with a plateau at ~328 Ma (Figure II.19 and Table S.II.20). The step #18 was excluded from the calculation. The WMA is calculated at 327.6 ± 0.6 Ma (MSWD = 0.86), and the TGA at 332.1 ± 3.3 Ma.

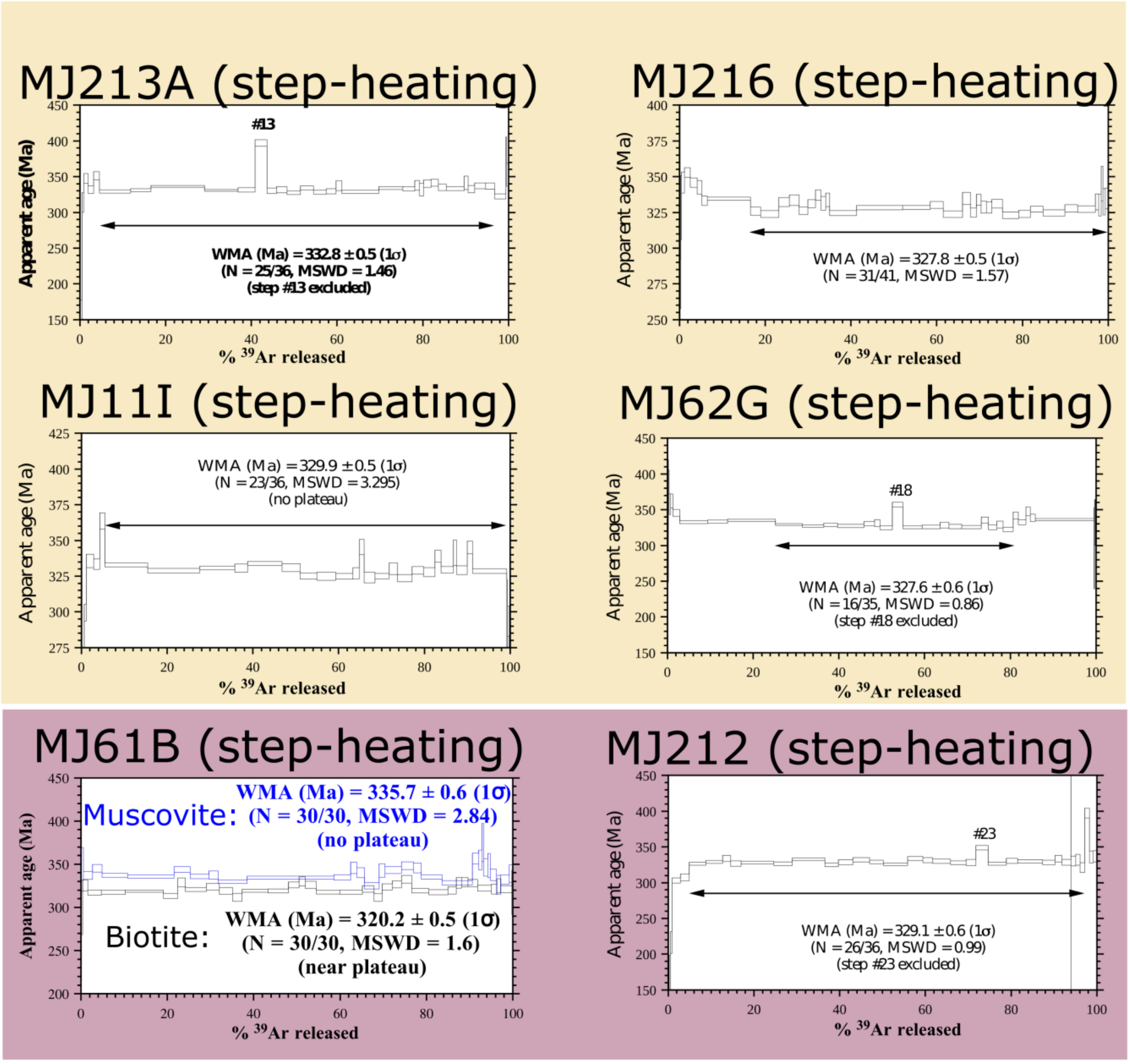

Figure II.19. Step-heating ^{40}Ar/^{39}Ar age spectra of white micas and one biotite from micaschists and gneisses. WMA: Weighted Mean Age. Error boxes and WMA are ± 1σ. Note that the scale of the vertical axis is different for all the samples.

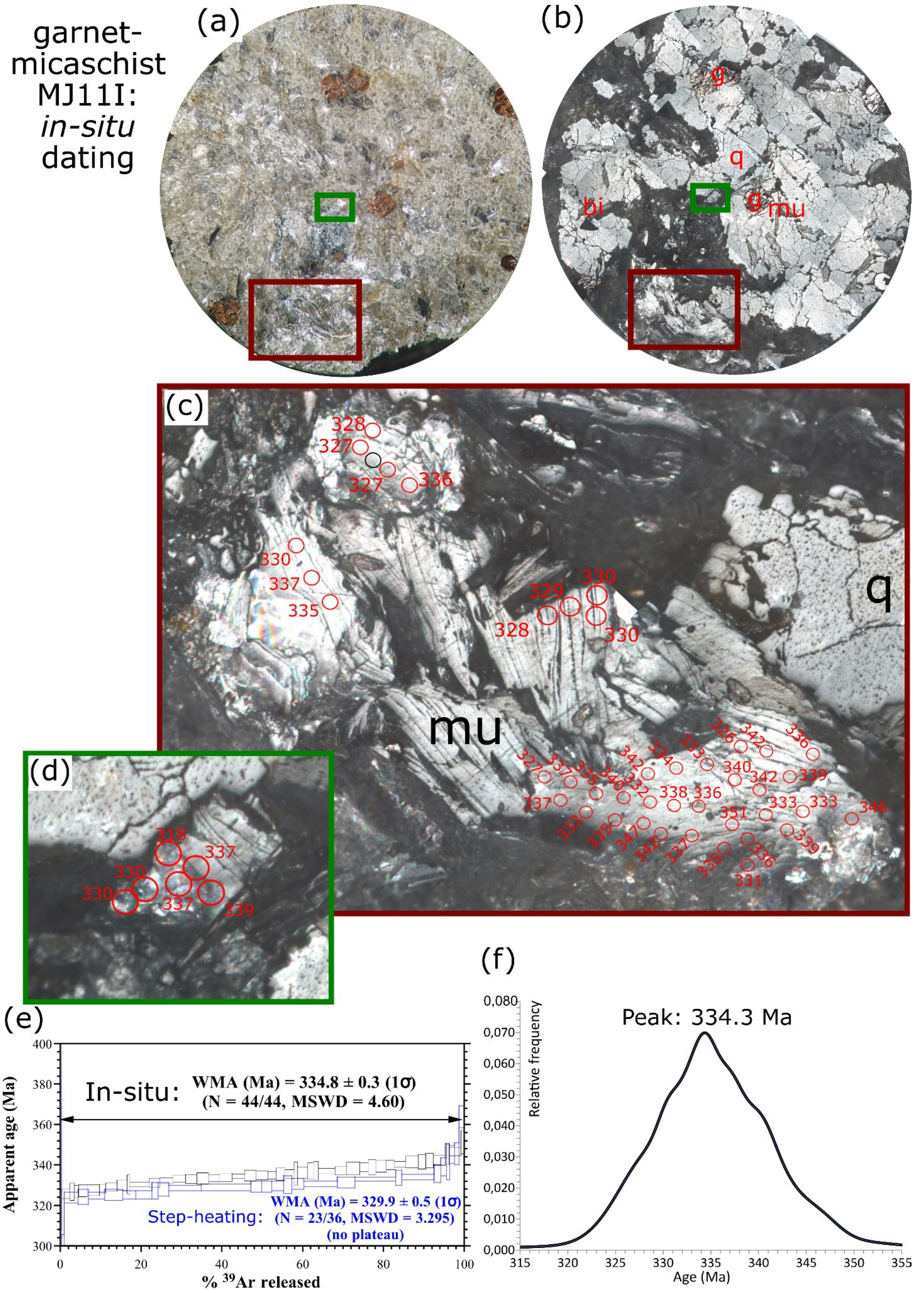

Figure II.20. *In-situ* ^{40}Ar/^{39}Ar age spectra of white micas from the g-micaschist MJ11I. Circular sections: (a) optical microscope, (b) reflected light microscope with (c,d) location of the *in-situ* mapping with rounded weighted mean age for each measure, (e) age spectra of the in-situ dating (in black) and of the ordered ages obtained by step-heating (in blue) for comparison, (f) probability density plot showing a peak age at 334.3 Ma for the *in-situ* dating.

- MJ61B

The age spectrum of white mica population in the paragneiss MJ61B is slightly discordant with apparent $^{40}Ar/^{39}Ar$ ages varying between 296 and 355 Ma (no plateau; blue spectrum in Figure II.19 and Table S.II.21). The WMA and TGA are calculated at 335.7 ± 0.6 Ma (MSWD = 2.84) and 336.8 ± 3.4 Ma, respectively.

This sample presents large fresh biotite grains and was chosen for additional biotite dating by step-heating. The age spectrum of biotite population is overall flat with a near plateau at 320.2 Ma (black spectrum in Figure II.19 and Table S.II.22). The WMA is calculated at 320.2 ± 0.5 Ma (MSWD = 1.6), and the TGA at 320.7 ± 3.2 Ma.

- MJ212

In the orthogneiss MJ212, the age spectrum (Figure II.19 and Table S.II.23) is characterized by an increase of apparent $^{40}Ar/^{39}Ar$ ages over the first three degassing steps, followed by a plateau at ~329 Ma. The step #23 was excluded from the calculation. The WMA and TGA are calculated at 329.1 ± 0.6 Ma (MSWD = 0.99) and 328.6 ± 3.3 Ma, respectively.

3.3.3 - SUMMARY OF AGES

The individual $^{40}Ar/^{39}Ar$ analyses of white mica grouped by unit (phyllites, micaschists and gneisses) provide a relatively large scatter of ages with ages falling between ~343–325 Ma in the phyllite samples (Figures II.17, II.18f and II.21), between ~333–328 Ma (and even up to 335 Ma for the *in-situ* dating) in the micaschist samples (Figures II.19, II.20e and II.21), and between ~336–329 Ma in the gneiss samples (Figures II.19 and II.21). The spatial age disposition of the ages is visible in Figure II.21.

The micaschists have relatively homogeneous $^{40}Ar/^{39}Ar$ ages, with a mean age around 330 Ma, while the phyllites show two age groups. The three oldest ages of 343–340 Ma in phyllites are about 10 Ma older than the rest of the phyllite ages and occurred in the two phyllites located the most far away from the high-grade Erzgebirge core (Figure II.21). The rest of the ages is quite homogeneous, around 330 Ma, like in the micaschists. Similarly, the paragneiss MJ61B also presents an old age of 336 Ma while the orthogneiss MJ212 records a younger age of 329 Ma (Figure II.21a,c).

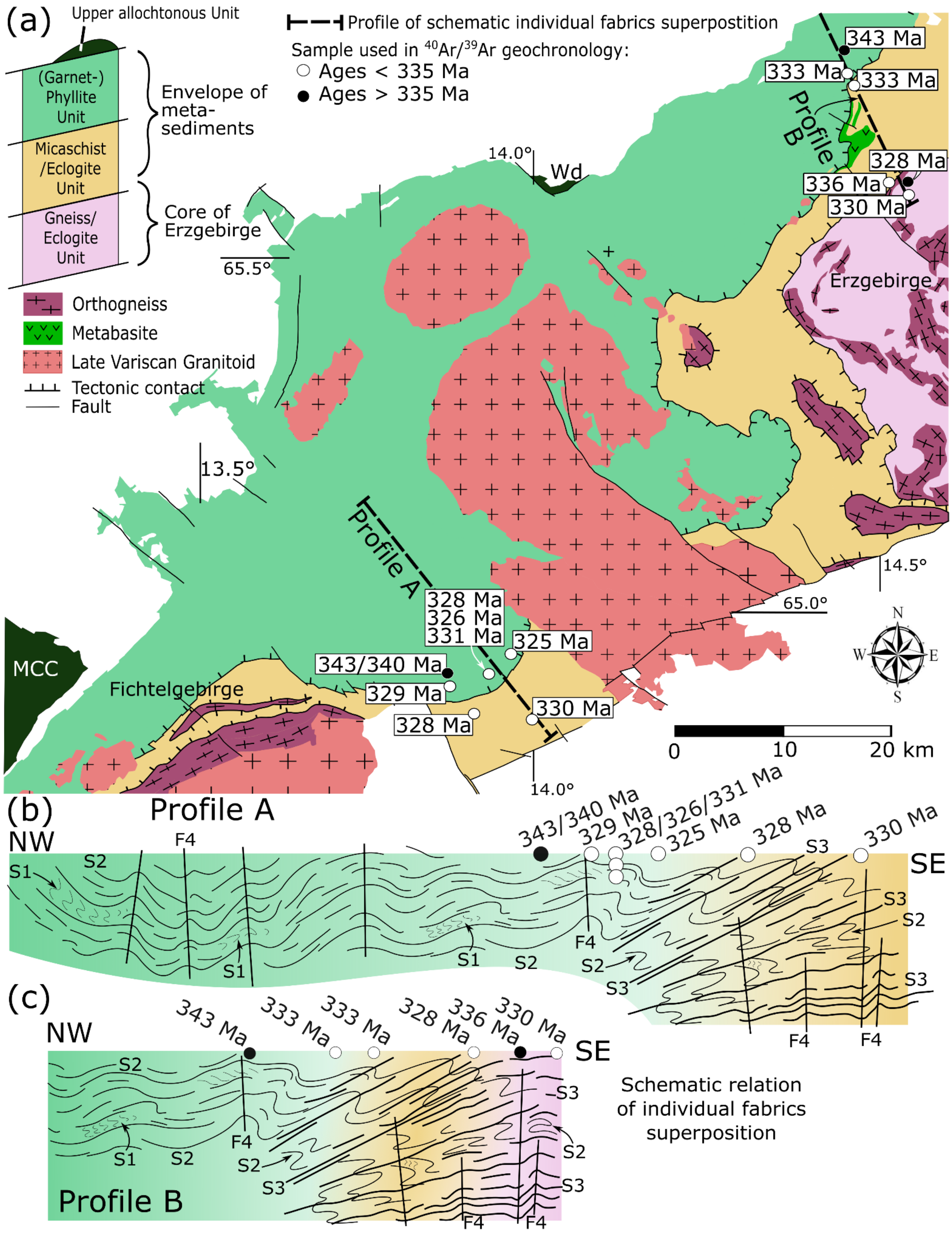

Figure II.21. (a) Location of the samples dated by mica ^{40}Ar/^{39}Ar geochronology with rounded WMA ages and approximate location of the two profiles visible by the dashed lines. (c-d) Schematic profiles from the phyllites to the micaschists and gneisses with approximate position of the outcrops and their rounded WMA ages.

The ages obtained by *in-situ* dating (Figures II.17, II.18f, II.19 and II.20e) systematically gave slightly older ages than the step-heating analyses of the same sample, for the phyllite MJ22 (step-heating: 332.5 ± 0.6 Ma and *in-situ*: 335.8 ± 0.6 Ma) and for the micaschist MJ11I (step-heating: 329.9 ± 0.5 Ma and *in-situ*: 334.8 ± 0.3 Ma).

Collected on a drill core, the phyllite samples S3-051, S3-180 and S3-375, sampled at a depth of 51, 180 and 375 m, respectively, provided ^{40}Ar/^{39}Ar ages of 328 Ma, 326/329 Ma (two measures for the same sample) and 330 Ma, respectively (Figures II.17 and 21a,b).

The only biotite was measured in the paragneiss MJ61B and was dated at 320 Ma (Figure II.19).

3.4 - DISCUSSION OF THE ^{40}AR/^{39}AR AGES

The results of this study, combined with the literature on Erzgebirge rocks, allowed us to reconstruct the exhumation process of the orogenic wedge. We first discuss some advantages and limits of ^{40}Ar/^{39}Ar dating. Then, the significance of the new ages is investigated in relation with the monazite ages and other available geochronology to highlight the timing of the individual events. Finally, the timing of these events is discussed for each unit in the context of the Saxothuringian orogenic wedge exhumation.

3.4.1 - ADVANTAGES AND LIMITS OF ^{40}AR/^{39}AR DATING METHOD FOR THIS STUDY

This study used cutting-edge geochronology with the step-heating and *in-situ* ^{40}Ar/^{39}Ar dating of a large collection of samples from phyllites to micaschists and gneisses. An important limitation to a well-conducted ^{40}Ar/^{39}Ar study is the necessity of collecting very fresh samples in the field, with preferably large mica grains. However, the micas in phyllitic rocks are usually very fine-grained, and more generally, the metasediments of the Bohemian Massif are often rapidly altered by the climate, lichen and mosses. This was a limitation to get samples suitable for the ^{40}Ar/^{39}Ar dating from all the wanted outcrops, i.e. from the samples already studied by monazite U-Pb dating and phase-equilibria modelling.

In addition to step-heating measurements, a very precise *in-situ* dating was performed on two white micas from one phyllite and one micaschist, both previously dated by step-heating. The apparent ages obtained by *in-situ* dating are systematically older than the ones obtained by step-heating, for both rock types (Figures II.18f and II.20e). Indeed, the dating of a white mica population by step-heating can lead to a mix with younger white micas, decreasing the measured age, contrary to the *in-situ* dating of bigger grains or of similar grain size but at least from the same foliation.

The phyllite MJ52F presents the least flat spectrum (Figure II.17) from all the spectra, with an important increase of ages up to 341 Ma. This measurement was duplicated to ensure the age and spectrum shape. In both cases, a very similar shape of spectrum was obtained, and the ages are quite similar (343.4 ± 1.3 Ma and 340.0 ± 0.9 Ma; Figure II.17). The phyllite S3-180 was also duplicated and also gave similar spectra and about the same ages (325.7 ± 0.7 Ma and 329.2 ± 0.5 Ma; Figure II.17). Despite slightly different ages in both samples, the age variability is less than 1% and can be due to the internal variability of the sample as a population of white mica was dated, and not only a single white mica grain in the case of step-heating dating.

3.4.2 - MEANING OF AGES IN RELATION TO MONAZITE U-PB AGES, METAMORPHISM, DEFORMATION AND MAGMATISM

All the previous studies that calculated the *P–T* conditions of Erzgebirge metasediments agreed that, even affected by successive metamorphic events, the phyllites and micaschists always experienced temperatures of minimum 450°C (Roetzler et al., 1998; Konopásek, 2001; Faryad & Kachlík, 2013; Rahimi & Massonne, 2018, 2020; Jouvent et al., 2022), above the white mica closure temperature, assumed to be 350–425°C for white micas (Dodson, 1973; Harrison et al., 2009; Hodges, 1991; Lister & Baldwin, 1996; Purdy, 1975; Robbins, 1972). Thus, the $^{40}Ar/^{39}Ar$ ages measured by this study cannot be interpreted as crystallization ages, but as cooling ages or perhaps as recrystallization ages below the closure temperature.

3.4.2.1 - MEANING OF AGES IN THE PHYLLITES

The comparison of monazite U-Pb and white mica $^{40}Ar/^{39}Ar$ ages highlights different responses of the rocks and units during the polyphase deformation and metamorphism experienced by the metasediments.

In the phyllites, two groups of $^{40}Ar/^{39}Ar$ ages are obtained (~340–343 Ma and ~330 Ma), depending on their distance to the Erzgebirge core. This tendency of two age groups is also recorded by the *in-situ* dating in the phyllite MJ22. Indeed, the probability density plot (Figure II.18g) shows an asymmetric distribution of ages, with two age peaks, at 328.7 and 334.2 Ma. Moreover, the monazite ages in the phyllites are systematically older than the $^{40}Ar/^{39}Ar$ ages. This can be shown by the comparison of monazite and $^{40}Ar/^{39}Ar$ ages in one outcrop (ctd-phyllite MJ52) which was studied using both geochronological methods. U-Pb ages of 350 and 348 Ma were obtained from this outcrop by the dating of the monazite cores and rims, respectively (part II.2, Figures II.5c and II.22), while the $^{40}Ar/^{39}Ar$ ages are 343 and 340 Ma (Figures II.17 and II.22). In this phyllite, even considering the uncertainty of the measurement, the ages obtained by both methods are never overlapping (Figure II.22), and show that the youngest monazite ages (~348 Ma) and the oldest $^{40}Ar/^{39}Ar$ ages (~343 Ma) obtained for the chloritoid-phyllites indicate cooling and exhumation soon after the prograde path directly following the prograde path of the phyllites dated at ~350–345 Ma (Figure II.23; part II.2).

Outcrop	ctd-phyllite MJ52
Sample	MJ52D (mnz) and MJ52F (white mica)
Monazite U-Pb age	349.6 ± 1.1 Ma (mnz core), 347.7 ± 0.8 Ma (mnz rim)
White mica Ar/Ar age	343.4 ± 1.3 Ma (step-heating) 340.0 ± 0.9 Ma (step-heating)

Outcrop	g-micaschist MJ11
Sample	MJ11C (mnz) and MJ11I (white mica)
Monazite U-Pb age	336.0 ± 2.2 Ma (mnz in the g rim I) 334.0 ± 1.2 Ma (mnz in the g rim II) 328.7 ± 0.8 Ma (mnz in the M3-M4 matrix)
White mica Ar/Ar age	334.8 ± 0.3 Ma (in-situ) 329.9 ± 0.5 Ma (step-heating)

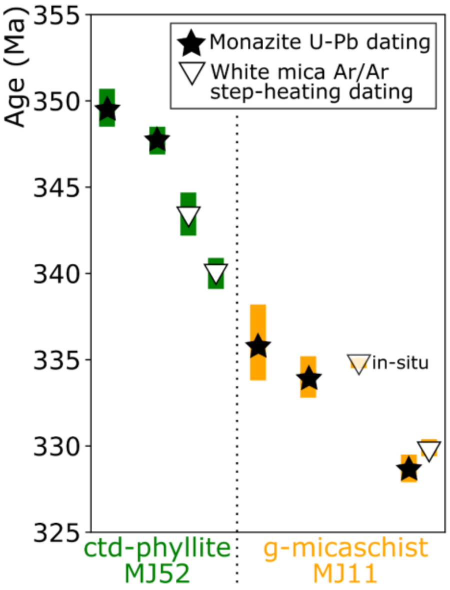

Figure II.22: Comparison of ages obtained using two geochronological methods: monazite U-Pb (black stars) and white mica $^{40}Ar/^{39}Ar$ ages (white triangles) on the same outcrop (ctd-phyllite MJ52 and g-micaschist MJ11). The $^{40}Ar/^{39}Ar$ ages are obtained by step-heating, except for one age done by in-situ dating, and indicated in the graph. All the ages are plotted by adding the uncertainty of the measure.

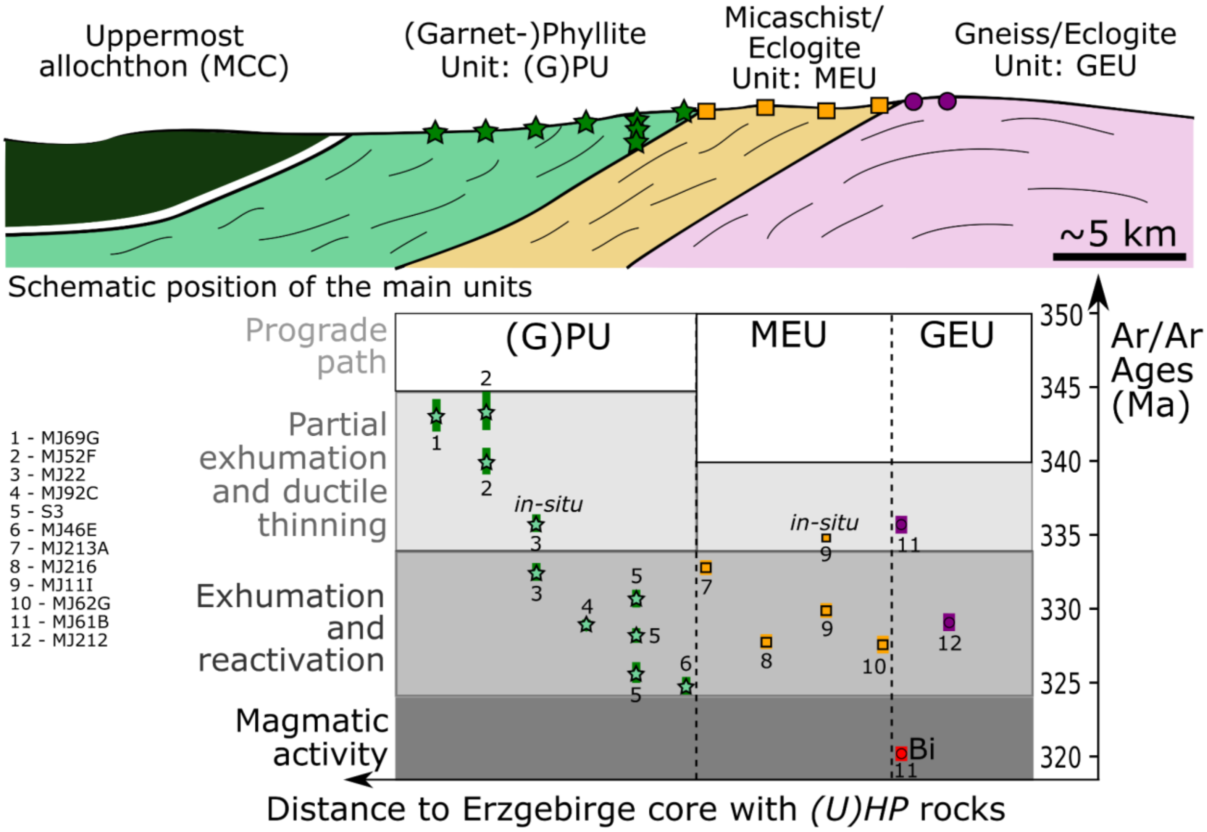

Figure II.23: Projected distribution of $^{40}Ar/^{39}Ar$ ages (Weighted Mean Ages ± 1σ) over the distance to (U)HP rocks of Erzgebirge core (in kilometer-scale) and distribution of the dated samples on a schematic cross-section showing the position of the main units. The background gray scale indicates the tectonic event associated with the ages.

Except in the structurally higher phyllites which are dated at 340–343 Ma, the $^{40}Ar/^{39}Ar$ ages in the structurally lowermost phyllites are relatively homogeneous and young (~330 Ma; Figure II.23) compared to the corresponding monazite U-Pb ages (350–340 Ma). This indicates a strong event happening at ~330 Ma compatible with the U-Pb monazite event of the same age recognized in micaschists. However, only the phyllites close to the high-grade Micaschist/Eclogite Unit, i.e. with the shortest distance to the Erzgebirge high-grade core (Figures II.21 and II.23), were affected by this 330 Ma event (Figure II.23).

We can also note that the oldest $^{40}Ar/^{39}Ar$ ages of 340–343 Ma obtained in the ctd-phyllites overlap with the youngest monazite age measured in the ctd-phyllite MJ44 (part II.2) with an age of ~340 Ma for the monazite core and rim (Figure II.5e). This monazite age was interpreted as either locally younger domain, or as a similar partial resetting of age, likely during the exhumation of the phyllites. This new $^{40}Ar/^{39}Ar$ ages of 340–343 Ma rather favor the second scenario with a time span for burial and exhumation of phyllites in the range 350–340 Ma (Figure II.23), also supported by Faryad & Kachlík (2013) who published the only $^{40}Ar/^{39}Ar$ ages known from literature for phyllites, ranging from ~356 to ~334 Ma and supporting the proposed time scale for the burial and exhumation loop of the phyllites.

3.4.2.2 - MEANING OF AGES IN THE MICASCHISTS AND GNEISSES

In this study, except for one slightly older $^{40}Ar/^{39}Ar$ *in-situ* age, all the $^{40}Ar/^{39}Ar$ step-heating ages of the micaschists range between 325 and 333 Ma, overlapping with the monazite U-Pb ages of the micaschists in the M3-M4 matrix (326–331 Ma; part II.2; Figure II.8). Furthermore, considering the age uncertainties, an overlap of the monazite U-Pb and white mica $^{40}Ar/^{39}Ar$ ages occurs. This is well-shown by the g-micaschist MJ11 (Figure II.22). From this outcrop MJ11, the monazite U-Pb ages are 336 Ma for monazite in the g rim I, 334 Ma for monazite in the g rim II and 329 Ma for monazite in the M3-M4 matrix, while the $^{40}Ar/^{39}Ar$ *in-situ* age is 335 Ma and the $^{40}Ar/^{39}Ar$ step heating age is 330 Ma (Figure II.22). The monazites included in the garnets gave similar ages than the phengite dated by *in-situ* $^{40}Ar/^{39}Ar$ dating (~335 Ma), and the monazites in the M3-M4 matrix also gave an age overlapping with the $^{40}Ar/^{39}Ar$ step-heating (~329 Ma). Finding in the same sample the same age of *in-situ* $^{40}Ar/^{39}Ar$ dating and monazite included in garnets emphasizes that some micas could have been protected in the matrix and not re-equilibrated by later metamorphic stages, indicating a potential cooling age. However, similarly as we showed that even monazite inclusion in garnet can be reset, the $^{40}Ar/^{39}Ar$ isotopic system could potentially be open and the $^{40}Ar/^{39}Ar$ age could also be younger than originally. Another hypothesis would be the mixing of originally old and young micas, producing a mean age. In addition, the study of the monazite U-Pb ages showed a strong reset of the monazites occurring at ~330 Ma. Obtaining the same age of ~330 Ma in the same sample by both monazite and $^{40}Ar/^{39}Ar$ dating, and, more importantly, in most of the other micaschists by $^{40}Ar/^{39}Ar$ step-heating dating, highlights that most of the white micas were also likely recrystallized or cooled down around 325–331 Ma by this 330 Ma old event.

A relatively old age of ~336 Ma was acquired for the paragneiss MJ61B, contrasting with younger ages around 330 Ma found in the other gneiss dated in this study and in the rest of the micaschists. This highlights that the strong event happening at 330 Ma did not affect all the units homogeneously, but was the most pronounced in the Micaschist/Eclogite Unite, while gneisses stayed relatively protected.

Finally, the biotite dated in the paragneiss provided an age of ~320 Ma, fitting with the timing of the large post-kinematic granite intrusions in the area, dated between 323–314 Ma (Figure II.23; Štemprok et al., 2008; Tichomirowa et al., 2019). Gerstenberger et al.

(1982) and Tichomirowa & Leonhardt (2010), using respectively Rb–Sr mica isochrons and zircon evaporation, reported older ages up to 328–329 Ma for the emplacement of the Aue-Schwarzenberg granite suite and the Eibenstock granite (see Figures 0.6 and I.1b for the location of the granites). This early age of the granitic intrusions could lead to interpret our white mica $^{40}Ar/^{39}Ar$ ages as dating the magmatic activity in the Western Erzgebirge. However, further and more precise geochronological investigations on the magmatic activity deny these oldest ages (Gerstenberger, 1989; Velikhin et al., 1994; Werner & Lippolt, 1998, Tichomirowa et al., 2019), and the oldest age of the granites emplacements is set at ~325 Ma.

3.4.2.3 - THE 330 MA OLD EVENT: END OF D3 OR BEGINNING OF D4 DEFORMATION?

One important question resulting from the monazite and $^{40}Ar/^{39}Ar$ geochronology is to which event is the ~330 Ma old event related to? Two hypotheses can be considered. The 330 Ma event can fit either to the end of the D3 event, or to the beginning of the D4 reactivation. Although they can be temporarily relatively close, they represent an orthogonal kinematic framework. Moreover, as the post-kinematic granite intrusions in the area occurred already from ~325 Ma (Tichomirowa et al., 2019), and as the D2 or D3 event probably took place until ~335 Ma as shown by monazite ages and *in-situ* $^{40}Ar/^{39}Ar$ ages, a relatively short time period of ~10 Ma remains for the last thermal event and final exhumation. We can also notice the misalignment between the boundary phyllites/micaschists and the location of the phyllite samples where the $^{40}Ar/^{39}Ar$ ages of 330 Ma spatially appear for the first time, which is a little bit northwards to this boundary phyllites/micaschists (Figure II.24). As shown in part I, the S3 fabric is strongly developed in the micaschists, but also starts to be weakly developed in the phyllites close to the micaschists (Figure II.21b,c). The spatial occurence of the 330 Ma event more or less corresponds with the localized high-strain domains of the S3 fabric (Figures II.21b,c and II.24), favoring that the D3 event lasted until 330 Ma. Indeed, the D4 upright folding is homogeneously developed in the phyllites and micaschists. We would then expect to record the age of 330 Ma in the northern phyllites as well, which is not the case. Based on these observations, we more likely interpret the age of 330 Ma as the end of the D3 ductile thinning and exhumation during extension, rather than the D4 event. However, this interpretation can still be debated.

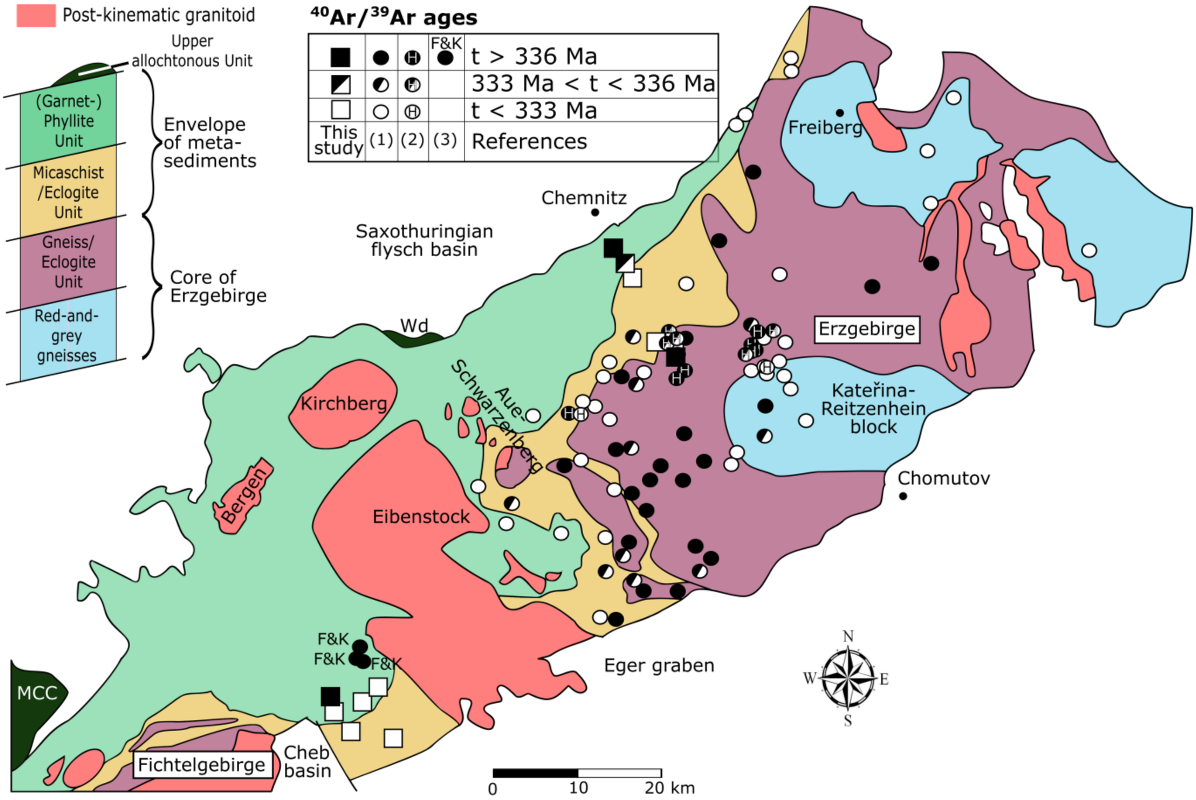

Figure II.24: Location of the outcrop dated by $^{40}Ar/^{39}Ar$ geochronology (Weighted Mean Ages) in this study (in rectangles) and other studies (in circles): (1) Werner & Lippolt, 2000; (2) Hallas et al., 2021; (3) Faryad & Kachlík, 2013. $^{40}Ar/^{39}Ar$ ages younger than 333 Ma are in white, ages older than 336 Ma are in black and intermediate ages older than 333 Ma and younger than 336 Ma are in black and white. MCC: Münchberg Crystalline Complex; Wd: Wildenfels Massif. Modified after Werner & Lippolt, 2000.

3.4.3 - WEDGE ASSEMBLY AND EXHUMATION

The $^{40}Ar/^{39}Ar$ ages resulting from this study, in link with the monazite U-Pb ages and with the other geochronological studies of the area allowed us to constrain the timing of wedge exhumation and reactivation, and the kinematics of the successive deformations affecting the units.

A simple model to explain why the structurally upper phyllites are older than the deeper phyllites and micaschists could simply be by crustal cooling. Indeed, the rocks would first get cold on the top of the pile and later on the bottom, as the structurally lower rocks are initially hotter. However, this hypothesis is invalidated by the GEU, which also records old ages of >336 Ma (this study; Hallas et al., 2021; Werner & Lippolt, 2000), similar to the northern phyllites. Indeed, this alternation of old and young ages was also reported in deeper units of Erzgebirge by other authors. Hallas et al., 2021 did a similar study using ^{40}Ar/^{39}Ar dating, but on the high-grade core of Erzgebirge. Their results show ages ranging from ~340 to 328 Ma with two age groups (Figures II.11 and II.24). The oldest age group at ~339 Ma is interpreted as the formation of the main foliation during west-directed emplacement of the *UHP* rocks in mid-crustal levels, and the youngest age at ~333 Ma is associated with the final transport of the units in the upper crust. Werner & Lippolt, 2000 also did an extensive ^{40}Ar/^{39}Ar dating of various units in the Erzgebirge. Similarly, they obtained two age groups (~340 and ~330 Ma; Figures II.11 and II.24). The youngest ages are in the Garnet-Phyllite Unit, Micaschist/Eclogite Unit and parautochthonous unit (Red-and-Grey Gneiss), while the oldest ages are recorded in the *UHP* Gneiss/Eclogite Unit. Including the ^{40}Ar/^{39}Ar ages of this study, this complicated age pattern of young, old and again young ages (from the uppermost phyllites to the deepest parautochthon unit, Figure II.24) cannot be explained as a simple uplift and exhumation. Using thermal models, Werner & Lippolt, 2000 explained this spatial age pattern by Variscan crustal imbrication of a cold unit into a hotter environment during the mineral cooling phase.

Our age results globally fits with the ages of these studies showing two age groups. The oldest ages of 343–340 Ma recorded in the upper phyllites are simply interpreted by crustal cooling as the upper phyllites are first exhumed and cooled down, and then were not affected by the 330 Ma old event. However, similarly to Hallas et al. (2021) but contrary to Werner & Lippolt (2000), we interpret the complex spatial age pattern as the result of a two stages exhumation with first the exhumation of the rocks to mid-crustal levels, followed by a wedge reactivation forming the Erzgebirge dome due the orthogonal shortening with imbrication of the parautochthonous unit creating detachment zones in the micaschists and in the parautochthonous unit.

Based on our ^{40}Ar/^{39}Ar and monazite U-Pb ages, and previous studies performed in Erzgebirge, we can propose the following timing for the wedge assembly and exhumation. The phyllites entered the wedge at ~360–350 Ma, recorded a prograde evolution until ~345 Ma, and were rapidly exhumed at ~340 Ma, soon after their peak metamorphism. The micaschists might have entered the wedge slightly later, at ~340 Ma, but could also have followed the same timing of wedge building than the gneisses, despite no age older than 339 Ma was recorded in micaschists. Their peak of metamorphism at ~339 Ma was followed by partial exhumation and slight heating during ductile thinning from 339 Ma until 330 Ma. At the phyllites/micaschists boundary, in the micaschists and in the parautochthonous unit, the rocks record from a strong thermal event at 330 Ma, resetting most of the monazites in micaschists and maybe white mica isotopic system during the final exhumation stage. In the gneisses, a similar timing of prograde history was recorded, entering the wedge at ~360–355 Ma (Figure II.12b,c), as shown by the ^{40}Ar/^{39}Ar ages of Schmädicke et al. (1995) in Figure II.11 and followed by prograde path and peak metamorphism until ~340 Ma (Figures II.11 and II.12d,e). However, after its exhumation at ~340–338 Ma (Figure II.12f,g), the GEU was not affected by the 330 Ma old event, as shown by the ^{40}Ar/^{39}Ar ages almost always older than 336 Ma in this unit (Figure II.24; Hallas et al., 2021; Werner & Lippolt, 2000).

In the previous parts with the tectonometamorphic study and the monazite dating, we highlight that the D1-D2 events correspond to the wedge assembly with an E-W convergence and a vergence towards the east, also reported from several places in the Bohemian Massif (Edel et al., 2018; Hallas et al., 2021; Jeřábek et al., 2016; Konopásek et al., 2019; Peřestý et al., 2017; Racek et al., 2017; Schmädicke et al., 1992; Schmädicke et al., 1995), followed by a ductile thinning D3, which still keeps with the same orientation (Figure II.25a). However, a very significant change in the geometry happened quite quickly after the E-W convergence and D3 extension. It reactivated the units, creating the antiform and synforms of Erzgebirge (Figures II.24 and II.25b). This change of kinematics in the wedge corresponds to a N-S shortening of the entire Erzgebirge region during this last exhumation stage (Kryl et al., 2021; Figure II.25b) and corresponds to a major event occurring in the whole Variscan belt as shown also in the West Sudetes, in Krkonoše-Jizera Massif (Konopásek et al., 2019; Žáčková et al., 2010; Žáčková, 2011) and more globally at the Rheno-Hercynian–Saxo-Thuringian boundary zone (Stephan et al., 2016). It may reflect the relocation of the subduction zones from the internal Variscan zone to the Paleotethys boundary as proposed by Edel et al. (2018) due to the closure of the Rheno-Hercynian Ocean.

A potential candidate for this change in geodynamics is the indentation of the parautochthonous unit Kateřina-Reitzenhein block (Figure II.25b), imbricating the area during post-collisional collapse at 330 Ma, while the compressional D4 event was later responsible for large-scale folding, creating the antiform and synform, typical for Erzgebirge geometry.

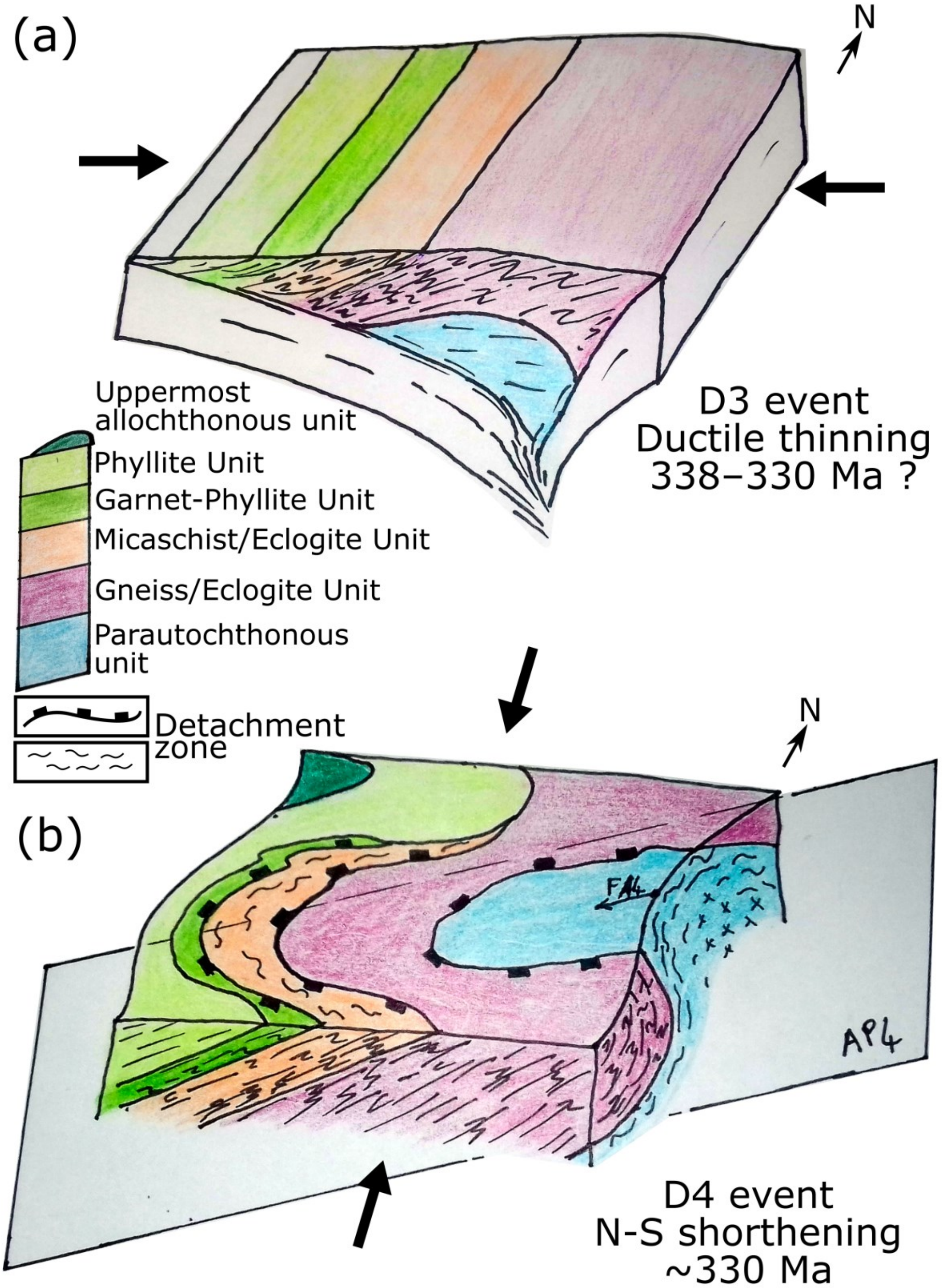

Figure II.25: 3D tectonic model showing: (a) the arrangement of the units during the E-W convergence during the D3 event, followed by (b) N-S orthogonal shortening with upright folding and wedge reactivation D4, creating the structures of the antiformal dome of Erzgebirge. The F4 axial plane orientation is schematized by the vertical grey plane and the subhorizontal F4 fold axis orientation is shown on the parautochthonous unit. The uppermost allochthonous unit could correspond here to the Wildenfels Massif.

3.5 - CONCLUDING REMARKS ON THE ^{40}AR/^{39}AR GEOCHRONOLOGY

This study aimed to link the ^{40}Ar/^{39}Ar ages with polyphase deformation and exhumation record of the Saxothuringian orogenic wedge. This research also focused on the comparison with *in-situ*, step-heating ^{40}Ar/^{39}Ar ages and monazite U-Pb ages. The main conclusions are summarized below.

- The exhumation of the phyllites is well-constrained by ^{40}Ar/^{39}Ar ages to be at 343–340 Ma.
- The micaschists and the deepest phyllites are strongly affected by a ~330 Ma old event associated with white mica recrystallization or cooling during low-grade overprint in the late stage of the ductile thinning D3 or due to wedge reactivation during the D4 event.
- Younger ages of ~330 Ma are recorded in the micaschists and in the parautochthonous unit, while older ages of ~340 Ma are found in the upper phyllites and in the gneisses.
- The spatial alternation of old and young ages in the units cannot be explained by a simple crustal cooling and can be explained by the imbrication of the Kateřina-Reitzenhein parautochthonous unit, creating two detachment zones, in the micaschists and in the parautochthonous unit.
- A change of wedge geodynamics occurred from E-W subduction, collision and ductile thinning to N-S compression and wedge reactivation during final exhumation and following upright folding. This created the present-day antiformal and synformal structures of Erzgebirge.

4 - IMPLICATIONS FOR THE WEDGE DYNAMICS

The *P–T–t* and structural evolution of the studied units in Erzgebirge suggest their progressive mechanical decoupling from the subducting plate and their subcretion to the overriding continental margin. The mechanical decoupling took place in different depths and different times that is typical for continuous basal traction caused by lithospheric subduction (e.g. Burov et al., 2001; Yamato et al., 2007). Such a process commonly leads to thickening of the wedge where the thermal budget is controlled by advecting heat related to continuous return of hot crustal material from the subduction channel (Vanderhaeghe et al., 2003; Vanderhaeghe, 2012). Thus while the early stages of wedge formation (accretionary wedge stage) indicate overall low thermal gradients and *HP–LT* metamorphism, the later stages (orogenic wedge stage) indicate progressive thermal maturation and increasing thermal gradient in the inner part of the orogenic wedge.

In the classical triangular wedge models, the rocks are brought down by basal traction and scraped off from the downgoing slab near the singularity point defined as a point where the subducting slab meets the rigid buttress upper plate (Platt, 1986). Here, the offscraped material is compressed against the buttress which results in a development of vertical fabric and fast exhumation. Closer to the surface, the exhumation decelerates and a horizontal fabric related to ductile thinning is formed (Feehan & Brandon, 1999; Ring & Brandon, 1999). This simple model is probably relevant for the accretionary wedge stage even when the subducting slab changes from oceanic to continental. However, later when the deep subducted continental crust starts to be exhumed from the subduction channel due to its buoyancy, the wedge dynamics changes dramatically and the orogenic wedge is formed. Subcretion of the relatively hot crust at the base of the former accretionary wedge causes its thickening and subsequent collapse allowing for exhumation of the deep inner wedge. The inner wedge is exhumed through the hanging wall accretionary wedge leading to its erosion and dismembering into extensional allochthons that are pushed into the outer wedge position. It is important to note that in the Saxothuringian wedge the transition from subvertical channel fabric S2, reflecting wedge thickening, to subhorizontal fabric S3, reflecting wedge thinning, occurred for all inner wedge units and transitional michaschists in similar depth corresponding to pressures of 8–12 kbar (Kryl et al., 2021; Jouvent et al., 2022). Such depths of transition from vertical to horizontal fabrics reflecting decelerating exhumation are extremely similar to other exhumed orogenic domains (Schulmann et al., 2008). The collapse of the Saxothuringian wedge thus very much resembles to the collapse of a thickened orogenic root in typical collisional orogens, where the exhumation is controlled by the gravitational force.

CONCLUDING SUMMARY

1 - TECTONIC MODEL OF THE SAXOTHURINGIAN OROGENIC WEDGE

This study aimed to determine the polyphase deformation and metamorphic record of the Saxothuringian orogenic wedge. The *P–T* path of the metasediments of Erzgebirge, in link with the monazite U-Pb and mica ^{40}Ar/^{39}Ar ages provided an important knowledge about the wedge formation and its geodynamics and our research provided a tectonic model of the whole wedge evolution. The complex deformation and metamorphic phases, typical for the orogenic wedge building, is summarized as follows.

- **D1-M1 event** is the oldest stage identified in Erzgebirge. It is characterized by *HP–LT* prograde metamorphism of the rock in the wedge up to the peak pressure, calculated from 13 kbar and 520°C in phyllites, up to 25 kbar and 560°C in micaschists with a geothermal gradient of 6–11°C/km typical of a subduction zone. The M1 event is associated with the prograde growth of the garnet and growth of phengite, chloritoid, paragonite and rutile in a steep S1 foliation.
- **D2-M2 event** corresponds to the partial decompression of the rocks with deformation and metamorphic overprint of the previous fabric. This event is associated with a S2 fabric, sub-horizontal in the phyllites and steep towards the micaschists. The newly formed S2 foliation is associated with *HP–LT* minerals similar to the M1 metamorphism, but with lower pressure conditions (8–10 kbar and 490–550 °C in the garnetiferous phyllite and 13–18 kbar and 545–595 °C in micaschists) and is linked to the return flow in the subduction channel or corner flow in the rear part of the wedge.
- **D3-M3 event** is the major tectonomotemorphic event in the micaschists. It highlights the internal extensional collapse of the wedge via ductile thinning and *MP–MT* assemblage containing biotite, staurolite, muscovite and ilmenite. The M3 overprint intensifies towards the micaschists with the development of the main sub-horizontal S3 fabric resulting from a significant vertical shortening associated with slight heating up to 5–9 kbar and 600°C and a barrovian-type geothermal gradient of 17–30°C/km. The end of this event records cooling and decompression in the same kinematic framework.

- **D4-M4 event** is the latest deformation stage identified in Erzgebirge, responsible for N-S orthogonal shortening. It is manifested by the low-grade reactivation of earlier fabrics developed during ductile thinning and upright folding.

The study shows the importance of combining structures, petrology, geochemistry, phase-equilibria modelling (part I) with geochronological data (part II) to better understand the tectonometamorphic history. However, even if the association of different geochronological methods (*in-situ* monazite U-Pb and mica step-heating and *in-situ* ^{40}Ar/^{39}Ar dating) brings complementary information about the timing of individual tectonic events, it is sometimes not enough to accurately interpret the obtained ages. Indeed, we faced the problem of partial monazite resetting (even for monazite included in garnet) by late thermal event occurring at low-grade conditions at ~330 Ma. The consequence of this resetting is the impossibility to precisely date the M2 and M3 events. Only a range of ages can be provided, between the end of the prograde M1 evolution (~339 Ma), and the beginning of the final rock exhumation (~331 Ma). Moreover, a similar question happens for the signification of the age of 330 Ma which can fit to the end of D3 event or the beginning of D4 deformation.

The present work aimed to reconstruct the original position of the units within the orogenic wedge, and their evolution over time. For the first time, we show that the Saxothuringian wedge can be subdivided into two parts comprising an older outer wedge formed by low-grade phyllites, a younger inner wedge with high-grade gneisses and in-between a transition zone with medium-to-high-grade micaschists, similarly to the other orogenic wedges worldwide. The phyllites are placed in the frontal part of the wedge (former accretionary prism) in the western part of the wedge. The micaschists are in the rear part of the wedge and the *UHP–HT* gneisses in the subduction channel, both in the East. The restoration of the wedge geometry in the Erzgebirge reveals early E-W zonation with the eastward increase in *P–T* conditions and complexity of structural record as well as the change in lithology from units dominated by metasediments to units dominated by gneisses. The D1-D2 stage corresponds to an E-W convergence with a subduction towards the east, also known from other places on Bohemian Massif at the similar times. The D1-M1 and D2-M2 events might have resulted in an inverse metamorphic zoning, typical for a subduction environment. The phyllites likely entered first the wedge and experienced prograde metamorphism at ~350–345 Ma Ma, followed by an exhumation at 343–340 Ma, while the micaschists possibly entered the wedge slightly later than the phyllites, at least at ~339 Ma as shown by the oldest monazite in garnet and in mount. In the gneisses, many studies also show that the rocks probably entered the wedge from ~360 Ma with peak conditions until ~340 Ma. This study highlights the tectonic evolution marked by the transition from the accretion of the subducted continental material to building of the Saxothuringian orogenic wedge from ~360 to ~340 Ma. This is followed by a partial exhumation and extensional collapse with ductile thinning D3-M3 happening, safely dated between 339–331 Ma, and probably at ~335 Ma. During the D3-M3 event, an intense vertical shortening occurred with an E-W extension of the orogenic wedge. D3 deformation is localized in high-strain zones following the boundaries between the units, and operating as localized shear zones or detachments, responsible for lateral juxtaposition of the distinct parts of the orogenic wedge. This deformation is also responsible for the present-day architecture of the units in Erzgebirge with a normal metamorphic zoning. The lower-grade phase of this event can either be assigned to the age of 330 Ma, but could also have taken place earlier, between ~335–331 Ma. Due to major reorientation of convergence direction in Variscan belt (Edel et al., 2018), this process is followed by intracontinental deformation D4 responsible for N-S orthogonal shortening, heterogeneous reactivation and final exhumation, possibly happening at ~330 Ma. However, it remains unclear whether this final D4 event can be attributed to the age of 330 Ma, or if this stage occurred later at lower *P–T* conditions of the D3 ductile thinning and is thus not recorded by our geochronological study. Finally, the whole area is intruded by post-kinematic granites from 325 Ma.

2 - GENERAL CONCLUSION

We have used a multidisciplinary approach to reconstruct the Variscan *P–T–t* evolution of the Saxothuringian Domain. Field and structural geology, associated with petrology, mineral chemistry and phase-equilibria modelling brought new constraints on the tectonic evolution of the metasediments surrounding the Erzgebirge *UHP* rocks. In addition, the monazite U-Pb and mica ^{40}Ar/^{39}Ar geochronometers were used to date the individual deformation and metamorphic stages.

During this study, we also highlighted that even a study combining metamorphism, monazite *in-situ* LASS geochronology coupled with REE geochemistry and ^{40}Ar/^{39}Ar geochronology did not succeed to figure out the precise age of all the individual tectonometamorphic stages and only time interval can sometimes be provided.

We propose a tectonic model of the Saxothuringian orogenic wedge over time from the accretion of the subducted continental material and building of the Saxothuringian wedge from ~360 to ~340 Ma, to its partial exhumation, extensional collapse and ductile thinning at 339–331 Ma. This event is followed by a heterogeneous wedge reactivation during orthogonal N-S shortening and final exhumation, possibily at ~330 Ma, before magmatic activity at ~325 Ma. The spatial arrangement of lithologies from phyllites to gneisses revealed early internal structures resulting from E-W convergence with *P–T* conditions increasing towards the east, while the present-day architecture of the wedge results from reactivation and final exhumation during late N-S shortening.

This thesis brings new knowledge on the active margin evolution and shows the assembly and evolvement of the Variscan collisional orogen in the Saxothuringian Domain, similar to other orogens from all over the world.

REFERENCES

- Agard, P., Yamato, P., Jolivet, L., & Burov, E. (2009). Exhumation of oceanic blueschists and eclogites in subduction zones: timing and mechanisms. Earth-Science Reviews, 92(1-2), 53-79.
- Agard, P., & Vitale-Brovarone, A. (2013). Thermal regime of continental subduction: the record from exhumed HP–LT terranes (New Caledonia, Oman, Corsica). *Tectonophysics*, *601*, 206-215.
- Aleinikoff, J. N., Schenck, W. S., Plank, M. O., Srogi, L., Fanning, C. M., Kamo, S. L., & Bosbyshell, H. (2006). Deciphering igneous and metamorphic events in high-grade rocks of the Wilmington Complex, Delaware: Morphology, cathodoluminescence and backscattered electron zoning, and SHRIMP U-Pb geochronology of zircon and monazite. *Geological Society of America Bulletin*, *118*(1-2), 39-64.
- Beaumont, C., Ellis, S., Hamilton, J., & Fullsack, P. (1996). Mechanical model for subduction-collision tectonics of Alpine-type compressional orogens. *Geology*, *24*(8), 675-678.
- Beaumont, C., Jamieson, R. A., Nguyen, M. H., & Lee, B. (2001). Himalayan tectonics explained by extrusion of a low-viscosity crustal channel coupled to focused surface denudation. *Nature*, *414*(6865), 738-742.
- Bowes, D. R., Farrow, C. M., Hopgood, A. M., Jelínek, E., Košler, J., & Rogers, G. (1999). Early Carboniferous Rb-Sr mica-whole-rock ages of phases of medium-and low-pressure metamorphism in the Saxothuringian zone, western Bohemia. *Neues Jahrbuch für Mineralogie-Abhandlungen*, 83-103.
- Broussolle, A., Štípská, P., Lehmann, J., Schulmann, K., Hacker, B. R., Holder, R., ... & Buriánek, D. (2015). P–T–t–D record of crustal-scale horizontal flow and magma-assisted doming in the SW Mongolian Altai. Journal of Metamorphic Geology, 33(4), 359-383.
- Brovarone, A. V., Beyssac, O., Malavieille, J., Molli, G., Beltrando, M., & Compagnoni, R. (2013). Stacking and metamorphism of continuous segments of subducted lithosphere in a high-pressure wedge: the example of Alpine Corsica (France). *Earth-Science Reviews*, *116*, 35-56.
- Brunet, F., Bonneau, V., & Irifune, T. (2006). Complete solid-solution between Na3Al2 (PO4) 3 and Mg3Al2 (SiO4) 3 garnets at high pressure. American Mineralogist, 91(1), 211-215.
- Burov, E., Jolivet, L., Le Pourhiet, L., & Poliakov, A. (2001). A thermomechanical model of exhumation of high pressure (HP) and ultra-high pressure (UHP) metamorphic rocks in Alpine-type collision belts. *Tectonophysics*, *342*(1-2), 113-136.
- Burov, E., François, T., Agard, P., Le Pourhiet, L., Meyer, B., Tirel, C., ... & Brun, J. P. (2014). Rheological and geodynamic controls on the mechanisms of subduction and HP/UHP exhumation of crustal rocks during continental collision: Insights from numerical models. *Tectonophysics*, *631*, 212-250.

- Carl, C., & Wendt, I. (1993). Radiometrische Datierung der Fichtelgebirgsgranite. *Zeitschrift fur Geologische Wissenschaften*, *21*, 49-49.
- Collett, S., Štípská, P., Kusbach, V., Schulmann, K., & Marciniak, G. (2017). Dynamics of Saxothuringian subduction channel/wedge constrained by phase-equilibria modelling and micro-fabric analysis. Journal of Metamorphic Geology, 35(3), 253-280.
- Collett, S., Štípská, P., Schulmann, K., Peřestý, V., Soldner, J., Anczkiewicz, R., ... & Kylander-Clark, A. (2018). Combined Lu-Hf and Sm-Nd geochronology of the Mariánské Lázně Complex: New constraints on the timing of eclogite-and granulite-facies metamorphism. *Lithos*, *304*, 74-94.
- Collett, S., Schulmann, K., Štípská, P., & Míková, J. (2020). Chronological and geochemical constraints on the pre-variscan tectonic history of the Erzgebirge, Saxothuringian Zone. Gondwana Research, 79, 27-48.
- Collett, S., Schulmann, K., Deiller, P., Štípská, P., Peřestý, V., Ulrich, M., ... & Míková, J. (2022). Reconstruction of the mid-Devonian HP-HT metamorphic event in the Bohemian Massif (European Variscan belt). *Geoscience Frontiers*, *13*(3), 101374.
- Dahlen, F. A., Suppe, J., & Davis, D. (1984). Mechanics of fold-and-thrust belts and accretionary wedges: Cohesive Coulomb theory. *Journal of Geophysical Research: Solid Earth*, *89*(B12), 10087-10101.
- Dallmeyer, R. D., & Urban, M. (1998). Variscan vs Cadomian tectonothermal activity in northwestern sectors of the Teplá-Barrandian zone, Czech Republic: constraints from 40Ar/39Ar ages. *Geologische Rundschau*, *87*(1), 94-106.
- Dal Zilio, L., Ruh, J., & Avouac, J. P. (2020). Structural evolution of orogenic wedges: interplay between erosion and weak décollements. *Tectonics*, *39*(10), e2020TC006210.
- Deiller, P., Štípská, P., Ulrich, M., Schulmann, K., Collett, S., Peřestý, V., ... & Míková, J. (2021). Eclogite subduction wedge intruded by arc-type magma: the earliest record of Variscan arc in the Bohemian Massif. *Gondwana Research*, *99*, 220-246.
- Dodson, M. H. (1973). Closure temperature in cooling geochronological and petrological systems. *Contributions to Mineralogy and Petrology*, *40*(3), 259-274.
- Edel, J. B., Schulmann, K., Lexa, O., & Lardeaux, J. M. (2018). Late Palaeozoic palaeomagnetic and tectonic constraints for amalgamation of Pangea supercontinent in the European Variscan belt. Earth-science reviews, 177, 589-612.
- Escudero, A., Miyajima, N., & Langenhorst, F. (2012). Microstructure, composition and P–T conditions of rutile from diamondiferous gneiss of the Saxonian Erzgebirge, Germany. *Geochemistry*, *72*(1), 25-30.
- Faryad, S. W., & Kachlík, V. (2013). New evidence of blueschist facies rocks and their geotectonic implication for Variscan suture (s) in the Bohemian Massif. Journal of Metamorphic Geology, 31(1), 63-82.
- Fazlikhani, H., Bauer, W., & Stollhofen, H. (2022). Variscan structures and their control on latest to post-Variscan basin architecture: insights from the westernmost Bohemian Massif and southeastern Germany. *Solid Earth*, *13*(2), 393-416.

- Feehan, J. G., & Brandon, M. T. (1999). Contribution of ductile flow to exhumation of low-temperature, high-pressure metamorphic rocks: San Juan-Cascade nappes, NW Washington State. Journal of Geophysical Research: Solid Earth, 104(B5), 10883-10902.
- Förster, H. J., Tischendorf, G., Trumbull, R. B., & Gottesmann, B. (1999). Late-collisional granites in the Variscan Erzgebirge, Germany. Journal of Petrology, 40(11), 1613-1645.
- Förster, H. J., Gottesmann, B., Tischendorf, G., Siebel, W., Rhede, D., Seltmann, R., & Wasternack, J. (2007). Permo-Carboniferous subvolcanic rhyolitic dikes in the western Erzgebirge/Vogtland, Germany: a record of source heterogeneity of post-collisional felsic magmatism. *NEUES JAHRBUCH FUR MINERALOGIE*, *183*(3), 123.
- Franke, W. (1989). Tectonostratigraphic units in the Variscan belt of central Europe. Geol Soc Am Spec Pap, 230, 67-90.
- Franke, W. (2000). The mid-European segment of the Variscides: tectonostratigraphic units, terrane boundaries and plate tectonic evolution. *Geological Society, London, Special Publications*, *179*(1), 35-61.
- Franke, W. (2006). The Variscan orogen in Central Europe: construction and collapse. *Geological Society, London, Memoirs*, *32*(1), 333-343.
- Franke, W., & Stein, E. (2000). Exhumation of high-grade rocks in the Saxo-Thuringian Belt: geological constraints and geodynamic concepts. *Geological Society, London, Special Publications*, *179*(1), 337-354.
- Geologische Übersichtskarte der Bundesrepublik Deutschland 1:250.000 (GÜK250), available at https://geoviewer.bgr.de/mapapps/resources/apps/geoviewer/index.html?lang=de
- Geological map 1 : 200,000. In: Geological map 1 : 50,000 [online]. Praha: Czech Geological Survey and Geologischer Dienst Freiberg [cit. 1961-09-06]. Available at: https://mapy.geology.cz/geocr50/
- Gerstenberger, H., Kaemmel, T., Haase, G., Geisler, M., 1982. Zur Charakterisierung der Granite im Westerzgebirge: Rb/Sr-radiogeochronologische Untersuchungen und Spurenelementkonzentrationen. Freib. Forsch. C 389, 220–246.
- Gerstenberger, H. (1989): Autometasomatic Rb enrichments in highly evolved granites causing lowered Rb-Sr isochron intercepts. Earth Planet. Sci. Lett., 93, 65-75.
- Gerya, T. V., Stöckhert, B., & Perchuck, A. L. (2002). Exhumation of high pressure metamorphic rocks in a subduction channel: A numerical simulation. Tectonics, 21(6), 1056.
- Gibson, H. D., Carr, S. D., Brown, R. L., & Hamilton, M. A. (2004). Correlations between chemical and age domains in monazite, and metamorphic reactions involving major pelitic phases: an integration of ID-TIMS and SHRIMP geochronology with Y–Th–U X-ray mapping. *Chemical Geology*, *211*(3-4), 237-260.
- Godin, L., Grujic, D., Law, R. D., & Searle, M. P. (2006). Channel flow, ductile extrusion and exhumation in continental collision zones: an introduction. *Geological Society, London, Special Publications*, *268*(1), 1-23.

- Grand'Homme, A., Janots, E., Seydoux-Guillaume, A. M., Guillaume, D., Bosse, V., & Magnin, V. (2016). Partial resetting of the U-Th-Pb systems in experimentally altered monazite: Nanoscale evidence of incomplete replacement. *Geology*, *44*(6), 431-434.
- Green, E. C. R., White, R. W., Diener, J. F. A., Powell, R., Holland, T. J. B., & Palin, R. M. (2016). Activity–composition relations for the calculation of partial melting equilibria in metabasic rocks. Journal of Metamorphic Geology, 34(9), 845-869.
- Gross, J., Burchard, M., Schertl, H. P., & Maresch, W. V. (2008). Common high-pressure metamorphic history of eclogite lenses and surrounding metasediments: a case study of calc–silicate reaction zones (Erzgebirge, Germany). European Journal of Mineralogy, 20(5), 757-775.
- Grujic, D. (2006). Channel flow and continental collision tectonics: an overview. *Geological Society, London, Special Publications*, *268*(1), 25-37.
- Hallas, P. (2020). *Tectonics of an intracontinental exhumation channel in the Erzgebirge, Central Europe* (Doctoral dissertation, TU Bergakademie Freiberg).
- Hallas, P., Pfänder, J. A., Kroner, U., & Sperner, B. (2021). Microtectonic control of 40Ar/39Ar white mica age distributions in metamorphic rocks (Erzgebirge, N-Bohemian Massif): Constraints from combined step heating and multiple single grain total fusion experiments. *Geochimica et Cosmochimica Acta*, *314*, 178-208.
- Harrison, T. M., Célérier, J., Aikman, A. B., Hermann, J., & Heizler, M. T. (2009). Diffusion of 40Ar in muscovite. *Geochimica et Cosmochimica Acta*, *73*(4), 1039-1051.
- Hermann, J. (2002). Allanite: thorium and light rare earth element carrier in subducted crust. *Chemical geology*, *192*(3-4), 289-306.
- Hodges, K. V. (1991). Pressure-temperature paths. *Annual Review of Earth and Planetary Sciences*, *19*, 207.
- Holder, R. M., Hacker, B. R., Kylander-Clark, A. R., & Cottle, J. M. (2015). Monazite trace-element and isotopic signatures of (ultra) high-pressure metamorphism: Examples from the Western Gneiss Region, Norway. *Chemical Geology*, *409*, 99-111.
- Holland, T. J. B., & Powell, R. T. J. B. (1998). An internally consistent thermodynamic data set for phases of petrological interest. Journal of metamorphic Geology, 16(3), 309-343.
- Holland, T., & Powell, R. (2003). Activity–composition relations for phases in petrological calculations: an asymmetric multicomponent formulation. Contributions to Mineralogy and Petrology, 145(4), 492-501.
- Holland, T. J. B., & Powell, R. (2011). An improved and extended internally consistent thermodynamic dataset for phases of petrological interest, involving a new equation of state for solids. Journal of Metamorphic Geology, 29(3), 333-383.
- Horstwood, M. S., Foster, G. L., Parrish, R. R., Noble, S. R., & Nowell, G. M. (2003). Common-Pb corrected in situ U–Pb accessory mineral geochronology by LA-MC-ICP-MS. *Journal of Analytical Atomic Spectrometry*, *18*(8), 837-846.
- Hwang, S. L., Shen, P., Chu, H. T., Yui, T. F., & Lin, C. C. (2001). Genesis of microdiamonds from melt and associated multiphase inclusions in garnet of ultrahigh-pressure gneiss from Erzgebirge, Germany. *Earth and Planetary Science Letters*, *188*(1-2), 9-15.

- Hwang, S. L., Chu, H. T., Yui, T. F., Shen, P., Schertl, H. P., Liou, J. G., & Sobolev, N. V. (2006). Nanometer-size P/K-rich silica glass (former melt) inclusions in microdiamond from the gneisses of Kokchetav and Erzgebirge massifs: Diversified characteristics of the formation media of metamorphic microdiamond in UHP rocks due to host-rock buffering. *Earth and Planetary Science Letters*, *243*(1-2), 94-106.
- Jamieson, R. A., Beaumont, C., Nguyen, M. H., & Lee, B. (2002). Interaction of metamorphism, deformation and exhumation in large convergent orogens. *Journal of Metamorphic Geology*, *20*(1), 9-24.
- Janots, E., Negro, F., Brunet, F., Goffé, B., Engi, M., & Bouybaouène, M. L. (2006). Evolution of the REE mineralogy in HP–LT metapelites of the Sebtide complex, Rif, Morocco: monazite stability and geochronology. *Lithos*, *87*(3-4), 214-234.
- Janots, E., Engi, M., Berger, A., Allaz, J., Schwarz, J. O., & Spandler, C. (2008). Prograde metamorphic sequence of REE minerals in pelitic rocks of the Central Alps: implications for allanite–monazite–xenotime phase relations from 250 to 610 C. *Journal of Metamorphic Geology*, *26*(5), 509-526.
- Jouvent, M., Lexa, O., Peřestý, V., & Jeřábek, P. (2022). New constraints on the tectonometamorphic evolution of the Erzgebirge orogenic wedge (Saxothuringian Domain, Bohemian Massif). *Journal of Metamorphic Geology*, *40*(4), 687-715.
- Jeřábek, P., Konopásek, J., & Žáčková, E. (2016). Two-stage exhumation of subducted Saxothuringian continental crust records underplating in the subduction channel and collisional forced folding (Krkonoše-Jizera Mts., Bohemian Massif). Journal of Structural Geology, 89, 214-229.
- Kelly, N. M., Harley, S. L., & Möller, A. (2012). Complexity in the behavior and recrystallization of monazite during high-T metamorphism and fluid infiltration. *Chemical geology*, *322*, 192-208.
- Kempe, U., Bombach, K., Matukov, D., Schlothauer, T., Hutschenreuter, J., Wolf, D., & Sergeev, S. (2004). Pb/Pb and U/Pb zircon dating of subvolcanic rhyolite as a time marker for Hercynian granite magmatism and Sn mineralisation in the Eibenstock granite, Erzgebirge, Germany: Considering effects of zircon alteration. *Mineralium Deposita*, *39*(5), 646-669.
- Klápová, H., Konopásek, J., & Schulmann, K. (1998). Eclogites from the Czech part of the Erzgebirge: multi-stage metamorphic and structural evolution. Journal of the Geological Society, 155(3), 567-583.
- Konopásek, J. (1998). Formation and destabilization of the high pressure assemblage garnet-phengite-paragonite (Krušné hory Mountains, Bohemian Massif): The significance of the Tschermak substitution in the metamorphism of pelitic rocks. Lithos, 42(3-4), 269-284.
- Konopásek, J. (2001). Eclogitic micaschists in the central part of the Krusne hory Mountains (Bohemian Massif). European Journal of Mineralogy, 13(1), 87-100.
- Konopásek, J., Schulmann, K., & Lexa, O. (2001). Structural evolution of the central part of the Krušné hory (Erzgebirge) Mountains in the Czech Republic—evidence for changing stress regime during Variscan compression. Journal of Structural Geology, 23(9), 1373-1392.

- Konopásek, J., & Schulmann, K. (2005). Contrasting Early Carboniferous field geotherms: evidence for accretion of a thickened orogenic root and subducted Saxothuringian crust (Central European Variscides). Journal of the Geological Society, 162(3), 463-470.
- Konopásek, J., Anczkiewicz, R., Jeřábek, P., Corfu, F., & Žáčková, E. (2019). Chronology of the Saxothuringian subduction in the West Sudetes (Bohemian Massif, Czech Republic and Poland). Journal of the Geological Society, 176(3), 492-504.
- Konzett, J., & Frost, D. J. (2009). The high P–T stability of hydroxyl-apatite in natural and simplified MORB—an experimental study to 15 GPa with implications for transport and storage of phosphorus and halogens in subduction zones. Journal of Petrology, 50(11), 2043-2062.
- Košler, J., Bowes, D. R., & Konopásek, J. M. (2004). Laser ablation ICPMS dating of zircons in Erzgebirge orthogneisses: evidence for Early Cambrian and Early Ordovician granitic plutonism in the western Bohemian Massif. European Journal of Mineralogy, 15-22.
- Kossmat, F. (1927). *Gliederung des varistischen Gebirgsbaues*. GA Kaufmann's Buchh., Amtl. Hauptvertriebsstelle d. Sächs. Geolog. Landesamts.
- Kotková, J., Kröner, A., Todt, W., & Fiala, J. (1996). Zircon dating of North Bohemian granulites, Czech Republic: further evidence for the Lower Carboniferous high-pressure event in the Bohemian Massif. Geologische Rundschau, 85(1), 154-161.
- Kotková, J., O'Brien, P. J., & Ziemann, M. A. (2011). Diamond and coesite discovered in Saxony-type granulite: Solution to the Variscan garnet peridotite enigma. Geology, 39(7), 667-670.
- Kotková, J., & Janák, M. (2015). UHP kyanite eclogite associated with garnet peridotite and diamond-bearing granulite, northern Bohemian Massif. Lithos, 226, 255-264.
- Kotková, J., Whitehouse, M., Schaltegger, U., & D'Abzac, F. X. (2016). The fate of zircon during UHT–UHP metamorphism: isotopic (U/Pb, δ18O, Hf) and trace element constraints. Journal of Metamorphic Geology, 34(7), 719-739.
- Kröner, A., Willner, A. P., Hegner, E., Frischbutter, A., Hofmann, J., & Bergner, R. (1995). Latest Precambrian (Cadomian) zircon ages, Nd isotopic systematics and PT evolution of granitoid orthogneisses of the Erzgebirge, Saxony and Czech Republic. Geologische Rundschau, 84(3), 437-456.
- Kröner, A., & Willner, A. P. (1998). Time of formation and peak of Variscan HP-HT metamorphism of quartz-feldspar rocks in the central Erzgebirge, Saxony, Germany. Contributions to Mineralogy and Petrology, 132(1), 1-20.
- Kroner, U., Hahn, T., Romer, R. L., & Linnemann, U. (2007). The Variscan orogeny in the Saxo-Thuringian zone-heterogenous overprint of Cadomian/Paleozoic Peri-Gondwana crust. Special Papers-Geological Society of America, 423, 153.
- Kroner, U., & Romer, R. L. (2013). Two plates—many subduction zones: the Variscan orogeny reconsidered. *Gondwana Research*, *24*(1), 298-329.
- Kryl, J., Jeřábek, P., & Lexa, O. (2021). From subduction channel to orogenic wedge: Exhumation recorded by orthogneiss microstructures in Erzgebirge, Bohemian Massif. *Tectonophysics*, *820*, 229096.

- Kulhánek, J., Faryad, S. W., Jedlicka, R., & Svojtka, M. (2021). Dissolution and reprecipitation of garnet during eclogite-facies metamorphism; major and trace element transfer during atoll garnet formation. *Journal of Petrology*, *62*(11), egab077.
- Kylander-Clark, A. R., Hacker, B. R., & Cottle, J. M. (2013). Laser-ablation split-stream ICP petrochronology. *Chemical Geology*, *345*, 99-112.
- Li, Z. C., Pei, X. Z., Bons, P. D., Li, R. B., Pei, L., Chen, G. C., ... & Gao, F. (2022). Petrogenesis and tectonic setting of the early-middle triassic subduction-related granite in the eastern segment of East Kunlun: evidences from petrology, geochemistry, and zircon U-Pb-Hf isotopes. International Geology Review, 64(5), 698-721.
- Linnemann, U., Pereira, F., Jeffries, T. E., Drost, K., & Gerdes, A. (2008). The Cadomian Orogeny and the opening of the Rheic Ocean: the diacrony of geotectonic processes constrained by LA-ICP-MS U–Pb zircon dating (Ossa-Morena and Saxo-Thuringian Zones, Iberian and Bohemian Massifs). *Tectonophysics*, *461*(1-4), 21-43.
- Lister, G. S., & Baldwin, S. L. (1996). Modelling the effect of arbitrary PTt histories on argon diffusion in minerals using the MacArgon program for the Apple Macintosh. *Tectonophysics*, *253*(1-2), 83-109.
- Lorenz, W., & Hoth, K. (1990). Lithostratigraphie im Erzgebirge-Konzeption, Entwicklung, Probleme und Perspektiven. Abhandlungen des Staatlichen Museums für Mineralogie und Geologie zu Dresden, 37, 7-35.
- Luvizotto, G. L., Zack, T., Triebold, S., & Von Eynatten, H. (2009). Rutile occurrence and trace element behavior in medium-grade metasedimentary rocks: example from the Erzgebirge, Germany. Mineralogy and Petrology, 97(3-4), 233.
- Maierová, P., Schulmann, K., Lexa, O., Guillot, S., Štípská, P., Janoušek, V., & Čadek, O. (2016). European Variscan orogenic evolution as an analogue of Tibetan-Himalayan orogen: Insights from petrology and numerical modeling. *Tectonics*, *35*(7), 1760-1780.
- Malavieille, J. (2010). Impact of erosion, sedimentation, and structural heritage on the structure and kinematics of orogenic wedges: Analog models and case studies. *GSA today*, *20*(1), 4-10.
- Massonne, H. J. (1998, April). A new occurrence of microdiamonds in quartzofeldspathic rocks of the Saxonian Erzgebirge, Germany, and their metamorphic evolution. In *International Kimberlite Conference: Extended Abstracts* (Vol. 7, pp. 552-554).
- Massonne, H. J. (1999). Experimental aspects of UHP metamorphism in pelitic systems. *International geology review*, *41*(7), 623-638.
- Massonne, H. J. (2001). First find of coesite in the ultrahigh-pressure metamorphic area of the central Erzgebirge, Germany. European Journal of Mineralogy, 13(3), 565-570.
- Massonne, H. J. (2005). Involvement of crustal material in delamination of the lithosphere after continent-continent collision. International Geology Review, 47(8), 792-804.
- Massonne, H. J. (2006). Early metamorphic evolution and exhumation of felsic high-pressure granulites from the north-western Bohemian Massif. *Mineralogy and Petrology*, *86*(3), 177-202.

- Massonne, H. J. (2012). Formation of amphibole and clinozoisite–epidote in eclogite owing to fluid infiltration during exhumation in a subduction channel. Journal of Petrology, 53(10), 1969-1998.
- Massonne, H. J., & Nasdala, L. (2003). Characterization of an early metamorphic stage through inclusions in zircon of a diamondiferous quartzofeldspathic rock from the Erzgebirge, Germany. American Mineralogist, 88(5-6), 883-889.
- Massonne, H. J., & Kopp, J. (2005). A low-variance mineral assemblage with talc and phengite in an eclogite from the Saxonian Erzgebirge, central Europe, and its P–T evolution. Journal of Petrology, 46(2), 355-375.
- Massonne, H. J., Kennedy, A., Nasdala, L., & Theye, T. (2007). Dating of zircon and monazite from diamondiferous quartzofeldspathic rocks of the Saxonian Erzgebirge–hints at burial and exhumation velocities. Mineralogical Magazine, 71(4), 407-425.
- Matte, P. (1986). Tectonics and plate tectonics model for the Variscan belt of Europe. *Tectonophysics*, *126*(2-4), 329-374.
- McDonough, W. F., & Sun, S. S. (1995). The composition of the Earth. *Chemical geology*, *120*(3-4), 223-253
- Mingram, B. (1998). The Erzgebirge, Germany, a subducted part of northern Gondwana: geochemical evidence for repetition of early Palaeozoic metasedimentary sequences in metamorphic thrust units. Geological Magazine, 135(6), 785-801.
- Mingram, B., & Rötzler, K. (1999). *Geochemische, petrologische und geochronologische Untersuchungen im Ergebirgskristallin: Rekonstruktion eines Krustenstapels*. Verlag der Gesellschaft für Geowissenschaften.
- Mingram, B., Kröner, A., Hegner, E., & Krentz, O. (2004). Zircon ages, geochemistry, and Nd isotopic systematics of pre-Variscan orthogneisses from the Erzgebirge, Saxony (Germany), and geodynamic interpretation. International Journal of Earth Sciences, 93(5), 706-727.
- Montel, J. M. (2000). Preservation of old U-Th-Pb ages in shielded monazite; example from the Beni Bousera Hercynian kinzigites (Morocco). *J. metamorphic Geol.*, *18*, 335-342.
- Muttoni, G., Kent, D. V., Garzanti, E., Brack, P., Abrahamsen, N., & Gaetani, M. (2003). Early permian pangea 'B'to late permian pangea 'A'. *Earth and Planetary Science Letters*, *215*(3-4), 379-394.
- Nance, R. D. (2022). The supercontinent cycle and Earth's long-term climate. *Annals of the New York Academy of Sciences*.
- Nance, R. D., & Murphy, J. B. (1994). Contrasting basement isotopic signatures and the palinspastic restoration of peripheral orogens: Example from the Neoproterozoic Avalonian-Cadomian belt. *Geology*, *22*(7), 617-620.
- Nance, R. D., Gutiérrez-Alonso, G., Keppie, J. D., Linnemann, U., Murphy, J. B., Quesada, C., ... & Woodcock, N. H. (2010). Evolution of the Rheic ocean. *Gondwana Research*, *17*(2-3), 194-222.
- Nance, R. D., Gutiérrez-Alonso, G., Keppie, J. D., Linnemann, U., Murphy, J. B., Quesada, C., ... & Woodcock, N. H. (2012). A brief history of the Rheic Ocean. *Geoscience Frontiers*, *3*(2), 125-135.

- Nasdala, L., & Massonne, H. J. (2000). Microdiamonds from the Saxonian Erzgebirge, Germany: in situ micro-Raman characterisation. European Journal of Mineralogy, 12(2), 495-498.
- O'Brien, P. J. (2000). The fundamental Variscan problem: high-temperature metamorphism at different depths and high-pressure metamorphism at different temperatures. *Geological Society, London, Special Publications*, *179*(1), 369-386.
- Palin, R. M., Searle, M. P., Waters, D. J., Parrish, R. R., Roberts, N. M. W., Horstwood, M. S. A., ... & Anh, T. T. (2013). A geochronological and petrological study of anatectic paragneiss and associated granite dykes from the D ay N ui C on V oi metamorphic core complex, N orth V ietnam: constraints on the timing of metamorphism within the R ed R iver shear zone. *Journal of Metamorphic Geology*, *31*(4), 359-387.
- Paton, C., Hellstrom, J., Paul, B., Woodhead, J., & Hergt, J. (2011). Iolite: Freeware for the visualisation and processing of mass spectrometric data. *Journal of Analytical Atomic Spectrometry*, *26*(12), 2508-2518.
- Peacock, S. M. (1987). Creation and preservation of subduction-related inverted metamorphic gradients. *Journal of Geophysical Research: Solid Earth*, *92*(B12), 12763-12781.
- Peřestý, V., Lexa, O., Holder, R., Jeřábek, P., Racek, M., Štípská, P., ... & Hacker, B. (2017). Metamorphic inheritance of Rheic passive margin evolution and its early-Variscan overprint in the Teplá-Barrandian Unit, Bohemian Massif. Journal of Metamorphic Geology, 35(3), 327-355.
- Pietzsch, K. (1954). Die Gneise des Sächsischen Erzgebirges. Geologie, 3(4), 391-412.
- Platt, J. P. (1986). Dynamics of orogenic wedges and the uplift of high-pressure metamorphic rocks. *Geological society of America bulletin*, *97*(9), 1037-1053.
- Platt, J. P. (1993). Exhumation of high-pressure rocks: A review of concepts and processes. Terra nova, 5(2), 119-133.
- Plunder, A., Agard, P., Dubacq, B., Chopin, C., & Bellanger, M. (2012). How continuous and precise is the record of P–T paths? Insights from combined thermobarometry and thermodynamic modelling into subduction dynamics (Schistes Lustrés, W. Alps). *Journal of Metamorphic Geology*, *30*(3), 323-346.
- Powell, R., & Holland, T. J. B. (1988). An internally consistent dataset with uncertainties and correlations: 3. Applications to geobarometry, worked examples and a computer program. Journal of metamorphic Geology, 6(2), 173-204.
- Purdy, J. W. (1975). K-Ar ages on rock-forming minerals from the Central Alps.
- Racek, M., Lexa, O., Schulmann, K., Corsini, M., Štípská, P., & Maierová, P. (2017). Re-evaluation of polyphase kinematic and 40 Ar/39 Ar cooling history of Moldanubian hot nappe at the eastern margin of the Bohemian Massif. International Journal of Earth Sciences, 106(2), 397-420.
- Rahimi, G., & Massonne, H. J. (2018). Pressure-temperature-time evolution of a Variscan garnet-bearing micaschist from the northeastern Fichtelgebirge, NW Bohemian Massif in central Europe. Lithos, 316, 366-384.
- Rahimi, G., & Massonne, H. J. (2020). Metamorphic Evolution of Chloritoid-Bearing Micaschist from the Variscan Elstergebirge: Evidences for Stacking of High-Pressure

Rocks in the Saxothuringian Zone of Central Europe. Journal of Earth Science, 31(3), 425-446.

- Renne, P. R., Swisher, C. C., Deino, A. L., Karner, D. B., Owens, T. L., & DePaolo, D. J. (1998). Intercalibration of standards, absolute ages and uncertainties in 40Ar/39Ar dating. *Chemical Geology*, *145*(1-2), 117-152.
- Ring, U., & Brandon, M. T. (1999). Ductile deformation and mass loss in the Franciscan subduction complex: implications for exhumation processes in accretionary wedges. *Geological Society, London, Special Publications*, *154*(1), 55-86.
- Robbins, C. S. (1972). Radiogenic argon diffusion in muscovite under hydrothermal conditions. *M. Sc. Thesis, Brown Univ., Providence, RI*, *88*.
- Rötzler, K. (1995). Die PT-Entwicklung der Metamorphite des Mittel-und Westerzgebirges.
- Roetzler, K., Schumacher, R., Maresch, W. V., & Willner, A. P. (1998). Characterization and geodynamic implications of contrasting metamorphic evolution in juxtaposed high-pressure units of the Western Erzgebirge (Saxony, Germany). European Journal of Mineralogy, 10(2), 261-280.
- Rötzler, K., & Plessen, B. (2010). The Erzgebirge: a pile of ultrahigh-to low-pressure nappes of Early Palaeozoic rocks and their Cadomian basement. In Pre-Mesozoic Geology of Saxo-Thuringia-From the Cadomian Active Margin to the Variscan Orogen (pp. 253-270). Schweizerbart.
- Rötzler, J., Hagen, B., & Hoernes, S. (2008). Geothermometry of the ultrahigh-temperature Saxon granulites revisited. Part I: New evidence from key mineral assemblages and reaction textures. European Journal of Mineralogy, 20(6), 1097-1115.
- Romer, R. L., Thomas, R., Stein, H. J., & Rhede, D. (2007). Dating multiply overprinted Sn-mineralized granites—examples from the Erzgebirge, Germany. Mineralium Deposita, 42(4), 337-359.
- Rubatto, D., Chakraborty, S., & Dasgupta, S. (2013). Timescales of crustal melting in the Higher Himalayan Crystallines (Sikkim, Eastern Himalaya) inferred from trace element-constrained monazite and zircon chronology. *Contributions to Mineralogy and Petrology*, *165*(2), 349-372.
- Scaillet, S. (2000). Numerical error analysis in 40Ar/39Ar dating. *Chemical Geology*, *162*(3-4), 269-298.
- Schäfer, J., Neuroth, H., Ahrendt, H., Dörr, W., & Franke, W. (1997). Accretion and exhumation at a Variscan active margin, recorded in the Saxothuringian flysch. Geologische Rundschau, 86(3), 599-611.
- Scherer, E. E., Mezger, K., & Munker, C. (2002, August). Lu-Hf ages of high pressure metamorphism in the Variscan fold belt of southern Germany. In *Geochimica et Cosmochimica Acta* (Vol. 66, No. 15 A, pp. A677-A677). THE BOULEVARD, LANGFORD LANE, KIDLINGTON, OXFORD OX5 1GB, ENGLAND: PERGAMON-ELSEVIER SCIENCE LTD.
- Schertl, H. P., Schreyer, W., & Chopin, C. (1991). The pyrope-coesite rocks and their country rocks at Parigi, Dora Maira Massif, Western Alps: detailed petrography, mineral chemistry and PT-path. Contributions to Mineralogy and Petrology, 108(1-2), 1-21.

- Schmädicke, E., Okrusch, M., & Schmidt, W. (1992). Eclogite-facies rocks in the Saxonian Erzgebirge, Germany: high pressure metamorphism under contrasting PT conditions. Contributions to Mineralogy and Petrology, 110(2), 226-241.
- Schmädicke, E. (1994). *Die Eklogite des Erzgebirges* (Vol. 456). Deutscher Verlag für Grundstoffindustrie.
- Schmädicke, E., Mezger, K., Cosca, M. A., & Okrusch, M. (1995). Variscan Sm-Nd and Ar-Ar ages of eclogite facies rocks from the Erzgebirge, Bohemian Massif. Journal of Metamorphic Geology, 13(5), 537-552.
- Schmädicke, E., & Evans, B. W. (1997). Garnet-bearing ultramafic rocks from the Erzgebirge, and their relation to other settings in the Bohemian Massif. Contributions to Mineralogy and Petrology, 127(1), 57-74.
- Schmädicke, E., Will, T. M., Ling, X., Li, X. H., & Li, Q. L. (2018). Rare peak and ubiquitous post-peak zircon in eclogite: Constraints for the timing of UHP and HP metamorphism in Erzgebirge, Germany. Lithos, 322, 250-267.
- Schulmann, K., Lexa, O., Štípská, P., Racek, M., Tajčmanová, L., Konopásek, J., ... & Lehmann, J. (2008). Vertical extrusion and horizontal channel flow of orogenic lower crust: key exhumation mechanisms in large hot orogens?. *Journal of metamorphic Geology*, *26*(2), 273-297.
- Schulmann, K., Lexa, O., Janoušek, V., Lardeaux, J. M., & Edel, J. B. (2014). Anatomy of a diffuse cryptic suture zone: an example from the Bohemian Massif, European Variscides. Geology, 42(4), 275-278.
- Schumacher, R., Rötzler, K., & Maresch, W. V. (1999). Subtle oscillatory zoning in garnet from regional metamorphic phyllites and mica schists, western Erzgebirge, Germany. The Canadian Mineralogist, 37(2), 381-403.
- Seifert, T., & Sandmann, D. (2006). Mineralogy and geochemistry of indium-bearing polymetallic vein-type deposits: Implications for host minerals from the Freiberg district, Eastern Erzgebirge, Germany. *Ore Geology Reviews*, *28*(1), 1-31.
- Siebel, W., Shang, C. K., & Presser, V. (2010). Permo-Carboniferous magmatism in the Fichtelgebirge: dating the youngest intrusive pulse by U-Pb, 207Pb/206Pb and 40Ar/39Ar geochronology. *Z geol Wiss*, *38*(2-3), 85-98.
- Sizova, E., Gerya, T., & Brown, M. (2014). Contrasting styles of Phanerozoic and Precambrian continental collision. *Gondwana Research*, *25*(2), 522-545.
- Spear, F. S. (1993). Metamorphic phase equilibria and pressure-temperature-time paths. *Mineralogical Society of America Monograph*, 352-356.
- Spandler, C., Hermann, J., Arculus, R., & Mavrogenes, J. (2003). Redistribution of trace elements during prograde metamorphism from lawsonite blueschist to eclogite facies; implications for deep subduction-zone processes. *Contributions to Mineralogy and Petrology*, *146*(2), 205-222.
- Stacey, J. T., & Kramers, 1. (1975). Approximation of terrestrial lead isotope evolution by a two-stage model. *Earth and planetary science letters*, *26*(2), 207-221
- Štemprok, M., Dolejš, D., Müller, A., & Seltmann, R. (2008). Textural evidence of magma decompression, devolatilization and disequilibrium quenching: an example from

the Western Krušné hory/Erzgebirge granite pluton. *Contributions to Mineralogy and Petrology*, *155*(1), 93-109.

- Stephan, T., Kroner, U., Hahn, T., Hallas, P., & Heuse, T. (2016). Fold/cleavage relationships as indicator for late Variscan sinistral transpression at the Rheno-Hercynian–Saxo-Thuringian boundary zone, Central European Variscides. *Tectonophysics*, *681*, 250-262.
- Stosch, H. G., & Lugmair, G. W. (1990). Geochemistry and evolution of MORB-type eclogites from the Münchberg Massif, southern Germany. *Earth and Planetary Science Letters*, *99*(3), 230-249.
- Teufel, S., & Heinrich, W. (1997). Partial resetting of the U Pb isotope system in monazite through hydrothermal experiments: An SEM and U Pb isotope study. *Chemical Geology*, *137*(3-4), 273-281.
- Tichomirowa, M. (2003). Die Gneise des Erzgebirges-hochmetamorphe Äquivalente von neoproterozoisch-frühpaläozoischen Grauwacken und Granitoiden der Cadomiden.
- Tichomirowa, M., Whitehouse, M. J., & Nasdala, L. (2005). Resorption, growth, solid state recrystallisation, and annealing of granulite facies zircon—a case study from the Central Erzgebirge, Bohemian Massif. Lithos, 82(1-2), 25-50.
- Tichomirowa, M., & Leonhardt, D. (2010). New age determinations (Pb/Pb zircon evaporation, Rb/Sr) on the granites from Aue-Schwarzenberg and Eibenstock, western Erzgebirge, Germany. *Z geol Wiss*, *38*(2–3), 99-123.
- Tichomirowa, M., & Köhler, R. (2013). Discrimination of protolithic versus metamorphic zircon ages in eclogites: Constraints from the Erzgebirge metamorphic core complex (Germany). *Lithos*, *177*, 436-450.
- Tichomirowa, M., Kässner, A., Sperner, B., Lapp, M., Leonhardt, D., Linnemann, U., ... & Whitehouse, M. (2019). Dating multiply overprinted granites: The effect of protracted magmatism and fluid flow on dating systems (zircon U-Pb: SHRIMP/SIMS, LA-ICP-MS, CA-ID-TIMS; and Rb–Sr, Ar–Ar)–Granites from the Western Erzgebirge (Bohemian Massif, Germany). Chemical Geology, 519, 11-38.
- Thompson, R. N. (1975). Is upper-mantle phosphorus contained in sodic garnet?. Earth and Planetary Science Letters, 26(3), 417-424.
- Tomascak, P. B., Krogstad, E. J., & Walker, R. J. (1996). U-Pb monazite geochronology of granitic rocks from Maine: implications for late Paleozoic tectonics in the Northern Appalachians. *The Journal of Geology*, *104*(2), 185-195.
- Vanderhaeghe, O. (2012). The thermal–mechanical evolution of crustal orogenic belts at convergent plate boundaries: A reappraisal of the orogenic cycle. *Journal of Geodynamics*, *56*, 124-145.
- Vanderhaeghe, O., Medvedev, S., Fullsack, P., Beaumont, C., & Jamieson, R. A. (2003). Evolution of orogenic wedges and continental plateaux: insights from crustal thermal–mechanical models overlying subducting mantle lithosphere. Geophysical Journal International, 153(1), 27-51.
- Velikhin, V. I., Chernyshov, I. V., Simonova, L. I., & Yudintsev, S. V. (1994). Geotectonic position, petrochemical and geochronological features of the Younger

Granite Complex in the Krusne hory (Erzgebirge) of the Bohemian Massif. *J Czech Geol Soc*, *39*(1), 116.

- Vermeesch, P. (2018). IsoplotR: A free and open toolbox for geochronology. *Geoscience Frontiers*, *9*(5), 1479-1493.
- Vogt, K., & Gerya, T. V. (2014). From oceanic plateaus to allochthonous terranes: numerical modelling. Gondwana Research, 25(2), 494-508.
- Von Quadt, A., & Günther, D. (1999). Evolution of Cambrian eclogitic rocks in the Erzgebirge: a conventional and LA-ICP-MS U–Pb zircon and Sm–Nd study. *Terra Nostra*, *99*(1), 164.
- Wang, D., Fisher, C. M., Vervoort, J. D., & Cao, H. (2020). Nd isotope re-equilibration during high temperature metamorphism across an orogenic belt: Evidence from monazite and garnet. *Chemical Geology*, *551*, 119751.
- Werner, O., & Lippolt, H. J. (1998). Datierung von postkinematischen magmatischen Intrusionsphasen des Erzgebirges: Thermische und hydrothermale Überprägung der Nebengesteine. *Terra Nostra*, *98*(2), 160-163.
- Werner, O., & Lippolt, H. J. (2000). White mica 40Ar/39Ar ages of Erzgebirge metamorphic rocks: simulating the chronological results by a model of Variscan crustal imbrication. Geological Society, London, Special Publications, 179(1), 323-336.
- White, R. W., Powell, R., Holland, T. J. B., & Worley, B. A. (2000). The effect of TiO2 and Fe2O3 on metapelitic assemblages at greenschist and amphibolite facies conditions: mineral equilibria calculations in the system K2O-FeO-MgO-Al2O3-SiO2-H2O-TiO2-Fe2O3. Journal of Metamorphic Geology, 18(5), 497-511.
- White, R. W., Powell, R., & Johnson, T. E. (2014). The effect of Mn on mineral stability in metapelites revisited: New a–x relations for manganese-bearing minerals. Journal of Metamorphic Geology, 32(8), 809-828.
- Williams, M. L., Jercinovic, M. J., Harlov, D. E., Budzyń, B., & Hetherington, C. J. (2011). Resetting monazite ages during fluid-related alteration. *Chemical Geology*, *283*(3-4), 218-225.
- Willett, S., Beaumont, C., & Fullsack, P. (1993). Mechanical model for the tectonics of doubly vergent compressional orogens. *Geology*, *21*(4), 371-374.
- Willner, A. P., Rötzler, K., & Maresch, W. V. (1997). Pressure-temperature and fluid evolution of quartzo-feldspathic metamorphic rocks with a relic high-pressure, granulite-facies history from the Central Erzgebirge (Saxony, Germany). Journal of Petrology, 38(3), 307-336.
- Willner, A. P., Krohe, A., & Maresch, W. V. (2000). Interrelated PTtd paths in the Variscan Erzgebirge dome (Saxony, Germany): Constraints on the rapid exhumation of high-pressure rocks from the root zone of a collisional orogen. International Geology Review, 42(1), 64-85.
- Yamato, P., Agard, P., Burov, E., Le Pourhiet, L., Jolivet, L., & Tiberi, C. (2007). Burial and exhumation in a subduction wedge: Mutual constraints from thermomechanical modeling and natural P-T-t data (Schistes Lustrés, western Alps). *Journal of Geophysical Research: Solid Earth*, *112*(B7).

- Ye, K., Cong, B., & Ye, D. (2000). The possible subduction of continental material to depths greater than 200 km. Nature, 407(6805), 734-736.
- Zack, T., & Luvizotto, G. L. (2006). Application of rutile thermometry to eclogites. *Mineralogy and Petrology*, *88*(1), 69-85.
- Žáčková, E., Konopásek, J., Jeřábek, P., Finger, F., & Košler, J. (2010). Early Carboniferous blueschist facies metamorphism in metapelites of the West Sudetes (northern Saxothuringian Domain, Bohemian Massif). *Journal of Metamorphic Geology*, *28*(4), 361-379.
- Žáčková, E. (2011). Variscan and pre-Variscan tectonometamorphic processes in external zones of the Bohemian Massif-examples from the Krkonoše-Jizera Massif and the Letovice Complex.
- Závada, P., Schulmann, K., Racek, M., Hasalová, P., Jeřábek, P., Weinberg, R. F., ... & Roberts, A. (2018). Role of strain localization and melt flow on exhumation of deeply subducted continental crust. Lithosphere, 10(2), 217-238.
- Závada, P., Štípská, P., Hasalová, P., Racek, M., Jeřábek, P., Schulmann, K., ... & Holder, R. (2021). Monazite geochronology in melt-percolated UHP meta-granitoids: An example from the Erzgebirge continental subduction wedge, Bohemian Massif. Chemical Geology, 559, 119919.
- Zeh, A., & Gerdes, A. (2010). Baltica-and Gondwana-derived sediments in the Mid-German Crystalline Rise (Central Europe): implications for the closure of the Rheic ocean. *Gondwana Research*, *17*(2-3), 254-263.
- Zhao, Z., Bons, P. D., Wang, G., Liu, Y., & Zheng, Y. (2014). Origin and pre-Cenozoic evolution of the south Qiangtang basement, Central Tibet. *Tectonophysics*, *623*, 52-66.
- Zhao, Z., Bons, P. D., Wang, G., Soesoo, A., & Liu, Y. (2015). Tectonic evolution and high-pressure rock exhumation in the Qiangtang terrane, central Tibet. *Solid Earth*, *6*(2), 457-473.
- Zhao, Z., Bons, P. D., Stübner, K., Wang, G. H., & Ehlers, T. A. (2017). Early cretaceous exhumation of the Qiangtang Terrane during collision with the Lhasa Terrane, Central Tibet. *Terra Nova*, *29*(6), 382-391.
- Zhao, Z. B., Bons, P. D., Li, C., Wang, G. H., Ma, X. X., & Li, G. W. (2020). The Cretaceous crustal shortening and thickening of the South Qiangtang Terrane and implications for proto-Tibetan Plateau formation. *Gondwana Research*, *78*, 141-155.
- Zhu, X. K., & O'nions, R. K. (1999). Zonation of monazite in metamorphic rocks and its implications for high temperature thermochronology: a case study from the Lewisian terrain. *Earth and Planetary Science Letters*, *171*(2), 209-220.
- Zitzmann, Arnold (1994): Geowissenschaftliche Karten in der Bundesrepublik Deutschland. In: Zeitschrift der Deutschen Geologischen Gesellschaft, Band 145, E. Schweizerbart´sche Verlagsbuchhandlung Stuttgart, 38-87.
- Zitzmann, Arnold (2003): Die Geologische Übersichtskarte 1 : 200 000 – von der Karte bis zur Sachdatenbank. Zeitschrift der Deutschen Geologischen Gesellschaft, Band 154/1, E. Schweizerbart´sche Verlagsbuchhandlung Stuttgart, 121-139.

- Zulauf, G., Dörr, W., Fiala, J., Kotková, J., Maluski, H., & Valverde-Vaquero, P. (2002). Evidence for high-temperature diffusional creep preserved by rapid cooling of lower crust (North Bohemian shear zone, Czech Republic). *Terra Nova*, *14*(5), 343-354.

APPENDIX

Table S.II.1: Monazite U-Pb MC-ICP-MS data of the phyllite samples (MJ44, MJ182 and MJ52D). **Intercept ages calculated using $^{207}Pb/^{206}Pb$ values from the Stacey & Kramers (1975) lead isotopic evolution model. (The table continues next pages)

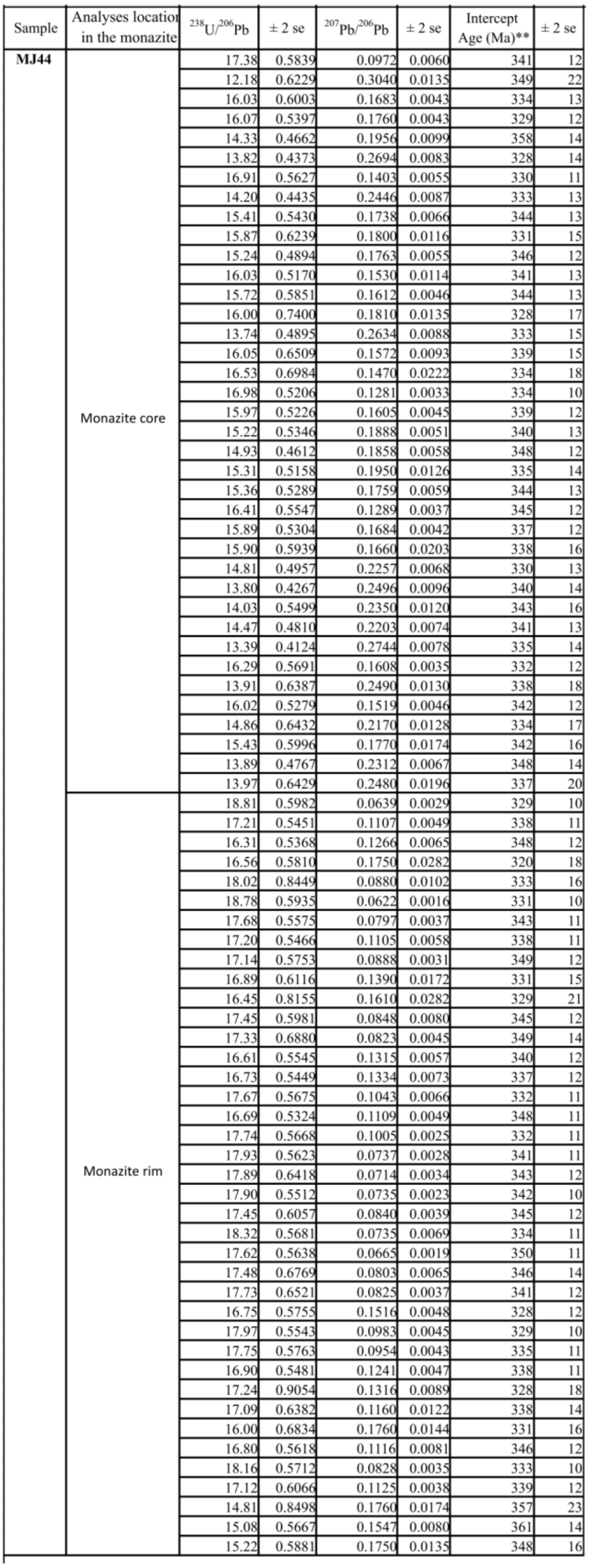

Sample	Analyses location in the monazite	$^{238}U/^{206}Pb$	± 2 se	$^{207}Pb/^{206}Pb$	± 2 se	Intercept Age (Ma)**	± 2 se
MJ44	Monazite core	17.38	0.5839	0.0972	0.0060	341	12
		12.18	0.6229	0.3040	0.0135	349	22
		16.03	0.6003	0.1683	0.0043	334	13
		16.07	0.5397	0.1760	0.0043	329	12
		14.33	0.4662	0.1956	0.0099	358	14
		13.82	0.4373	0.2694	0.0083	328	14
		16.91	0.5627	0.1403	0.0055	330	11
		14.20	0.4435	0.2446	0.0087	333	13
		15.41	0.5430	0.1738	0.0066	344	13
		15.87	0.6239	0.1800	0.0116	331	15
		15.24	0.4894	0.1763	0.0055	346	12
		16.03	0.5170	0.1530	0.0114	341	13
		15.72	0.5851	0.1612	0.0046	344	13
		16.00	0.7400	0.1810	0.0135	328	17
		13.74	0.4895	0.2634	0.0088	333	15
		16.05	0.6509	0.1572	0.0093	339	15
		16.53	0.6984	0.1470	0.0222	334	18
		16.98	0.5206	0.1281	0.0033	334	10
		15.97	0.5226	0.1605	0.0045	339	12
		15.22	0.5346	0.1888	0.0051	340	13
		14.93	0.4612	0.1858	0.0058	348	12
		15.31	0.5158	0.1950	0.0126	335	14
		15.36	0.5289	0.1759	0.0059	344	13
		16.41	0.5547	0.1289	0.0037	345	12
		15.89	0.5304	0.1684	0.0042	337	12
		15.90	0.5939	0.1660	0.0203	338	16
		14.81	0.4957	0.2257	0.0068	330	13
		13.80	0.4267	0.2496	0.0096	340	14
		14.03	0.5499	0.2350	0.0120	343	16
		14.47	0.4810	0.2203	0.0074	341	13
		13.39	0.4124	0.2744	0.0078	335	14
		16.29	0.5691	0.1608	0.0035	332	12
		13.91	0.6387	0.2490	0.0130	338	18
		16.02	0.5279	0.1519	0.0046	342	12
		14.86	0.6432	0.2170	0.0128	334	17
		15.43	0.5996	0.1770	0.0174	342	16
		13.89	0.4767	0.2312	0.0067	348	14
		13.97	0.6429	0.2480	0.0196	337	20
	Monazite rim	18.81	0.5982	0.0639	0.0029	329	10
		17.21	0.5451	0.1107	0.0049	338	11
		16.31	0.5368	0.1266	0.0065	348	12
		16.56	0.5810	0.1750	0.0282	320	18
		18.02	0.8449	0.0880	0.0102	333	16
		18.78	0.5935	0.0622	0.0016	331	10
		17.68	0.5575	0.0797	0.0037	343	11
		17.20	0.5466	0.1105	0.0058	338	11
		17.14	0.5753	0.0888	0.0031	349	12
		16.89	0.6116	0.1390	0.0172	331	15
		16.45	0.8155	0.1610	0.0282	329	21
		17.45	0.5981	0.0848	0.0080	345	12
		17.33	0.6880	0.0823	0.0045	349	14
		16.61	0.5545	0.1315	0.0057	340	12
		16.73	0.5449	0.1334	0.0073	337	12
		17.67	0.5675	0.1043	0.0066	332	11
		16.69	0.5324	0.1109	0.0049	348	11
		17.74	0.5668	0.1005	0.0025	332	11
		17.93	0.5623	0.0737	0.0028	341	11
		17.89	0.6418	0.0714	0.0034	343	12
		17.90	0.5512	0.0735	0.0023	342	10
		17.45	0.6057	0.0840	0.0039	345	12
		18.32	0.5681	0.0735	0.0069	334	11
		17.62	0.5638	0.0665	0.0019	350	11
		17.48	0.6769	0.0803	0.0065	346	14
		17.73	0.6521	0.0825	0.0037	341	12
		16.75	0.5755	0.1516	0.0048	328	12
		17.97	0.5543	0.0983	0.0045	329	10
		17.75	0.5763	0.0954	0.0043	335	11
		16.90	0.5481	0.1241	0.0047	338	11
		17.24	0.9054	0.1316	0.0089	328	18
		17.09	0.6382	0.1160	0.0122	338	14
		16.00	0.6834	0.1760	0.0144	331	16
		16.80	0.5618	0.1116	0.0081	346	12
		18.16	0.5712	0.0828	0.0035	333	10
		17.12	0.6066	0.1125	0.0038	339	12
		14.81	0.8498	0.1760	0.0174	357	23
		15.08	0.5667	0.1547	0.0080	361	14
		15.22	0.5881	0.1750	0.0135	348	16

Table S.II.1 (continued)

Sample	Analyses location in the monazite	$^{238}U/^{206}Pb$	± 2 se	$^{207}Pb/^{206}Pb$	± 2 se	Intercept Age (Ma)**	± 2 se
MJ182	Monazite core	15.01502	0.53741	0.1731	0.00485	353	13.34
		14.55604	0.55283	0.1981	0.00929	351	14.94
		15.1263	0.4612	0.1849	0.0056	345	11.63
		15.14693	0.4797	0.1935	0.00496	340	11.89
		14.47387	0.45764	0.1918	0.00654	356	12.62
		12.77139	0.42307	0.2645	0.00728	358	15.08
		15.10574	0.52947	0.1924	0.00615	341	13.08
		15.72327	0.53256	0.1462	0.00487	351	12.33
		15.08296	0.50646	0.1729	0.00693	352	12.84
		16.05136	0.55875	0.1351	0.00816	350	12.9
		14.61988	0.45299	0.2066	0.00468	345	12.06
		15.07386	0.49915	0.1732	0.00633	352	12.61
		15.67398	0.53053	0.1495	0.00524	351	12.38
		14.02525	0.54991	0.2241	0.00504	349	15.1
		14.29593	0.47163	0.2129	0.00504	349	12.98
		15.79529	0.53322	0.1487	0.00452	348	12.19
		14.60707	0.44686	0.1833	0.00487	358	11.97
		15.72327	0.55723	0.1487	0.00807	350	13.23
		14.12429	0.71711	0.211	0.01946	354	21.56
		14.35544	0.47222	0.209	0.00667	349	13.12
		14.81481	0.51662	0.1902	0.00445	349	13.08
		15.1653	0.46608	0.1719	0.00403	351	11.52
		14.8368	0.64173	0.195	0.01073	346	16.54
		13.83126	0.5272	0.228	0.01378	352	16.67
		16.47446	0.52663	0.13	0.0039	343	11.22
		15.12859	0.53049	0.168	0.00515	353	13.07
		16.26016	0.61234	0.1552	0.00399	335	12.99
		13.69863	0.46861	0.2701	0.0083	331	14.59
		13.64256	0.44961	0.2568	0.00852	340	14.29
		14.7167	0.48709	0.171	0.01057	362	13.69
		16.18123	0.57825	0.1296	0.00528	350	12.79
		15.2207	0.56009	0.194	0.00523	338	13.4
		12.83697	0.45761	0.286	0.01605	342	18.14
		15.84786	0.57675	0.1723	0.00899	335	13.4
		13.55014	0.46237	0.2602	0.00888	340	14.78
		14.83459	0.48623	0.1917	0.00599	348	12.6
		14.71454	0.44944	0.1926	0.00476	350	11.85
	Monazite rim	14.70588	0.56068	0.1717	0.00566	361	14.48
		17.75568	0.60652	0.1114	0.00299	327	11.22
		15.01502	0.53741	0.1954	0.00708	342	13.5
		16.35323	0.5251	0.1224	0.00566	350	11.58
		16.89189	0.59608	0.1089	0.00473	345	12.3
		16.44737	0.56271	0.1363	0.00332	341	11.87
		15.57147	0.49149	0.1657	0.00497	345	11.6
		17.60253	0.57695	0.1013	0.00767	335	11.43
		17.7683	0.55593	0.0905	0.00293	336	10.5
		14.07261	0.4545	0.2188	0.00531	351	13.01
		15.52072	0.49772	0.1622	0.00588	348	11.92
		17.93722	0.57733	0.065	0.00199	345	10.95
		17.16444	0.57919	0.0889	0.00503	349	11.86
		16.592	0.55238	0.0911	0.00256	360	11.89
		17.01259	0.5704	0.104	0.00296	345	11.56
		16.581	0.55195	0.1099	0.00356	351	11.74
		13.64256	0.48518	0.2333	0.00577	353	14.47
		17.1969	0.53919	0.1137	0.00284	337	10.63
		15.64945	0.56726	0.1548	0.00404	349	13.02
		17.06193	0.54571	0.1202	0.00384	336	10.92
		15.26019	0.48754	0.1484	0.00342	361	11.9
		17.88909	0.62484	0.0787	0.00232	339	11.73
		17.71793	0.58523	0.089	0.00315	338	11.13
		16.79825	0.52899	0.1241	0.00585	340	11.1
		14.88095	0.50856	0.1882	0.00667	348	13.09
		17.45201	0.60571	0.1009	0.00337	338	11.72
		16.00256	0.53705	0.1288	0.00352	354	12.05
		17.2206	0.52941	0.0926	0.00251	346	10.59

Table S.II.1 (continued)

Sample	Analyses locatio in the monazite	$^{238}U/^{206}Pb$	± 2 se	$^{207}Pb/^{206}Pb$	± 2 se	Intercept Age (Ma)**	± 2 se
MJ52D	Monazite core	17.00391	0.56252	0.0888	0.00393	352	11.65
		17.30104	0.61466	0.0934	0.0046	344	12.27
		17.75884	0.61123	0.0981	0.00593	333	11.67
		17.69912	0.55823	0.0857	0.00663	340	11
		17.2117	0.61058	0.0855	0.00538	349	12.48
		17.36111	0.55646	0.0894	0.00268	345	10.99
		17.1409	0.57823	0.0911	0.00449	348	11.8
		17.62425	0.54458	0.0845	0.00294	342	10.52
		17.02417	0.55171	0.1	0.00465	346	11.34
		16.87194	0.55739	0.0924	0.00514	353	11.78
		16.53439	0.53467	0.0909	0.00476	361	11.76
		16.63894	0.61539	0.1031	0.00768	353	13.44
		17.15266	0.60789	0.0952	0.00507	346	12.36
		17.07942	0.55157	0.0913	0.00224	349	11.21
		17.18804	0.56007	0.0874	0.00281	349	11.31
		17.13502	0.56276	0.0987	0.00584	345	11.55
		15.99744	0.49735	0.12	0.00864	358	11.95
		16.85204	0.53821	0.0873	0.00266	356	11.29
		14.40922	0.49894	0.1244	0.00631	395	14.08
		16.28664	0.68315	0.119	0.0142	353	16.24
		17.4216	0.67358	0.0877	0.00437	344	13.29
		17.43983	0.55512	0.0875	0.00273	344	10.89
		17.34906	0.56732	0.0873	0.00266	346	11.24
		16.94915	0.59867	0.099	0.00437	348	12.36
		17.38224	0.57733	0.0918	0.00477	343	11.48
		16.07717	0.74565	0.117	0.01125	358	17.37
		16.49893	0.50211	0.1267	0.00534	344	10.87
		16.51528	0.56167	0.1171	0.00421	349	12
		16.77571	0.54906	0.0874	0.0052	357	11.81
		17.38224	0.57225	0.1012	0.00614	339	11.42
		16.3372	0.53676	0.096	0.00453	363	11.99
	Monazite rim	17.53771	0.58614	0.08	0.0034	346	11.49
		18.13894	0.55085	0.0842	0.00285	332	10.05
		17.4703	0.5532	0.0904	0.00421	342	10.88
		17.40644	0.53748	0.0813	0.00282	348	10.66
		17.33102	0.6687	0.0855	0.00228	347	13.25
		17.51313	0.62439	0.0821	0.00216	345	12.17
		17.39736	0.59588	0.083	0.00276	347	11.79
		17.66784	0.63154	0.0822	0.00267	342	12.12
		17.54078	0.56743	0.0842	0.00388	344	11.11
		17.23544	0.56661	0.0885	0.00232	348	11.34
		17.2117	0.70092	0.0848	0.00286	350	14.1
		17.7305	0.65211	0.0821	0.00488	341	12.56
		17.71479	0.54754	0.0815	0.00324	341	10.52
		17.34906	0.58675	0.0909	0.00368	344	11.63
		17.20578	0.54985	0.0809	0.00281	352	11.16
		17.4216	0.62018	0.0823	0.00283	347	12.24
		17.2117	0.61058	0.0948	0.00338	345	12.21
		17.45505	0.58555	0.0885	0.0022	343	11.42
		17.63047	0.57553	0.0925	0.00295	338	11
		17.85077	0.56249	0.0747	0.00283	342	10.69
		17.4216	0.67358	0.0921	0.00524	342	13.29
		17.53156	0.57425	0.0892	0.00358	341	11.17
		17.40947	0.54643	0.0794	0.00271	348	10.85
		17.36111	0.67032	0.0794	0.00255	349	13.34
		17.53156	0.54306	0.0785	0.00217	346	10.62
		17.38224	0.56387	0.0906	0.0027	344	11.09
		17.65537	0.56821	0.0878	0.00244	340	10.86
		16.8976	0.5307	0.0832	0.00527	357	11.33
		17.36111	0.67032	0.0778	0.00312	350	13.39
		16.42036	0.58937	0.123	0.0103	348	13.43
		17.57469	0.56754	0.0811	0.0035	344	11.08
		17.23544	0.55299	0.0851	0.00319	349	11.16
		17.52234	0.56675	0.0834	0.0026	344	11.05
		17.03868	0.51953	0.0873	0.00339	352	10.72
		16.98947	0.53384	0.0812	0.00258	356	11.09
		17.81578	0.59871	0.0813	0.0025	340	11.32
		17.31302	0.55063	0.0885	0.00331	346	10.98
		15.35155	0.48389	0.0985	0.00482	384	12.24
		16.97793	0.66811	0.0937	0.00725	350	14.03
		17.63047	0.57311	0.084	0.00212	342	11.01
		17.27116	0.57816	0.0838	0.00462	349	11.72
		17.25328	0.53857	0.0884	0.0054	347	11
		17.39736	0.58055	0.0757	0.00213	350	11.56
		17.07067	0.56888	0.1047	0.00654	343	11.76
		17.58087	0.58121	0.0805	0.00376	344	11.36
		17.09402	0.52869	0.0839	0.00261	353	10.83
		16.72241	0.56898	0.0952	0.00339	355	12.05
		17.1409	0.53095	0.0953	0.0062	346	11.01
		16.77852	0.54585	0.1005	0.00796	351	11.94
		16.20746	0.66017	0.1098	0.0082	359	15.03
		17.46115	0.56007	0.0918	0.00495	342	11.07
		16.69728	0.53861	0.0933	0.00441	356	11.56
		17.25328	0.57483	0.0786	0.0027	352	11.62
		17.7683	0.57233	0.0805	0.00281	341	10.91
		17.68347	0.54966	0.0801	0.00323	343	10.61
		17.33102	0.60046	0.0909	0.00293	345	11.87
		17.74623	0.55343	0.0802	0.00234	341	10.56
		16.81803	0.51646	0.094	0.00553	353	11.06
		16.8691	0.52493	0.0892	0.00429	355	11.09
		16.58925	0.52181	0.0869	0.0077	362	11.82
		16.83218	0.5535	0.0977	0.00509	351	11.69
		17.1145	0.5719	0.1083	0.00282	341	11.4
		16.55903	0.55227	0.0888	0.00429	361	12.08
		17.24138	0.68291	0.0904	0.00333	347	13.64

Table S.II.2: Monazite REE MC-ICP-MS data of the phyllite samples: MJ44, MJ182 and MJ52D. (The table continues next pages)

Sample	Analyses location in the monazite	Number of analysis	U ppm	Th ppm	La ppm	Ce ppm	Pr ppm	Nd ppm	Sm ppm	Eu ppm	Gd ppm	Tb ppm	Dy ppm	Ho ppm	Er ppm	Tm ppm	Yb ppm	Lu ppm
MJ44	Monazite core	4	504	34900	49900	199000	37300	174000	44500	10300	25500	1860	4510	356	450	37	112	9
		5	528	58000	18700	103700	27400	183000	108000	25400	44700	2350	5320	408	531	43	121	12
		6	535	81800	18000	88800	22700	162000	117000	30100	45900	2690	5030	444	555	51	145	15
		7	544	74600	21500	124000	28500	181000	103900	24000	40800	2400	5510	460	531	45	133	13
		13	282	56200	32900	148500	32400	192000	64000	16200	30700	1940	4690	347	464	35	106	11
		14	322	62800	26100	115000	27900	187000	98400	26200	42000	2240	4600	384	528	43	126	15
		15	528	86600	17200	94800	22700	166000	119000	31700	43600	2570	5340	470	538	48	144	14
		16	325	61700	23100	113000	26900	189000	98000	26200	36500	2030	4950	392	520	43	140	12
		17	317	46400	42900	184000	36400	167000	48900	11700	22900	1740	4050	379	459	36	111	11
		21	465	41600	74700	231000	32000	139000	25800	6060	13900	1160	3000	282	337	25	66	6
		22	504	45500	47000	192000	35200	144000	37900	9170	20100	1570	3650	291	351	29	79	9
		23	441	77100	36400	177000	32700	180000	50300	12000	25500	1790	4270	358	438	36	100	9
		27	414	71100	28000	152000	29100	175000	51600	13900	24600	1700	3780	333	400	29	90	7
		28	419	72900	32000	161000	32200	177000	57600	14200	28700	2000	4060	362	419	34	89	11
		29	318	46800	36800	163000	31500	163000	48500	12000	24700	1670	4420	359	480	34	120	10
		30	394	36800	54600	227000	35400	187000	42200	9290	19300	1670	3910	364	460	35	108	11
		38	638	46400	90000	215000	29200	143000	52100	11100	20400	1260	3540	326	426	38	108	12
		39	545	98000	20800	106200	26800	181000	120100	29500	46200	2590	5190	446	552	51	141	14
		40	498	77400	34200	155000	31200	169000	74500	18800	36800	2180	4910	405	504	42	123	11
		41	401	76200	25300	132000	29200	173000	80300	19300	32100	2380	4820	381	465	41	114	11
		43	388	68100	25700	122800	28700	171000	73600	19540	34700	2160	4600	381	442	35	108	9
		44	546	72600	19800	105000	24000	178000	112000	27600	47900	2810	5640	508	607	45	150	13
		45	627	78000	18400	104000	25900	180000	128000	35400	53600	3230	6680	592	703	57	186	18
		46	514	81400	35000	148000	31500	158000	65300	18300	32100	2100	4780	368	499	41	133	13
		47	440	51100	48800	206000	36600	147100	32600	8650	18300	1540	3580	308	380	30	92	9
		51	416	48500	44200	196000	36900	188000	52200	12700	26500	1900	4070	342	428	31	94	10
		52	295	57900	34100	166300	34600	182000	68800	15800	29800	2020	4110	388	474	37	118	9
		53	375	65400	30700	145000	31700	175000	73300	17700	32600	2160	4620	347	454	39	117	11
		54	406	70500	33000	169000	36200	182000	58100	15400	28900	2010	4620	367	478	33	96	10
		55	462	31900	52800	198000	35200	137000	34800	7650	16700	1230	3470	272	384	25	71	6
		61	272	69400	42100	197000	39500	189000	48500	12940	25100	1730	4070	328	406	30	91	10
		62	491	63300	61400	205000	34800	152000	36400	7460	19100	1540	3640	323	434	29	93	9
		75	366	56000	45800	202000	34400	156000	35800	8620	17900	1400	3380	258	325	27	68	7
		77	442	93800	19800	115000	29600	195000	107000	23500	38400	2280	5330	376	539	39	115	11
		78	434	79300	32900	160000	30800	168000	66400	15500	30600	2180	4610	392	449	35	105	10
		87	419	84100	30200	161000	32100	197000	64700	16000	30200	2220	4420	387	474	35	107	11
		88	313	65400	38500	176000	33100	179000	50300	12800	23900	1930	3960	309	451	35	107	10
		89	516	55300	51000	198000	39100	168000	34900	8570	19400	1540	3910	336	385	26	92	8
	Monazite rim	3	984	5320	103000	291000	33100	118000	23900	5610	12200	1217	3460	301	362	33	77	5
		8	635	11400	92000	240000	33900	118300	20800	4920	11100	980	2810	270	340	25	71	5
		18	436	21500	77700	226000	33300	139000	32200	6560	15700	1400	3550	312	413	32	88	9
		20	453	17500	114000	261000	31000	98000	19400	3670	7610	727	2310	275	284	24	60	5
		24	612	20900	101000	240000	33500	117000	20500	4900	9290	780	2680	257	364	28	66	6
		25	1278	5510	137000	272000	31100	126000	18900	4110	8030	626	2530	280	413	33	101	10
		26	608	11190	132000	258000	27600	94900	16900	3640	5860	387	1450	204	270	21	59	5
		31	369	20600	78300	237000	32000	128000	22300	5540	11400	1196	2920	283	336	27	78	6
		32	479	10840	126300	281000	30200	111000	17800	3890	7730	705	2580	260	343	26	76	7
		33	486	14300	140000	262000	26700	89000	17800	3850	6000	390	1660	221	403	33	94	9
		34	497	7230	126000	240000	28700	90400	16100	3380	6000	345	1310	200	375	31	99	8
		35	744	7500	153000	253000	30000	102500	18600	3870	5970	321	1186	221	456	45	138	13
		36	682	9140	144300	270000	29600	96700	17700	3480	5800	324	1180	173	378	35	100	7
		42	448	40300	86000	220000	33300	140000	31700	7000	13500	1070	2640	269	362	28	85	9
		48	574	23900	92400	262000	32200	131000	23500	5730	12900	1140	3220	300	380	29	77	8
		49	528	13700	115000	250000	29400	112000	18000	4180	8850	861	2780	257	363	27	75	7
		50	546	9720	129000	256000	28000	102000	16900	3670	5970	493	1870	258	348	31	89	8
		56	835	8230	113000	269000	34400	117000	20600	4350	9200	940	2570	274	318	23	69	5
		57	677	6990	130000	268000	27700	108600	18500	3600	6400	421	1900	221	354	28	73	6
		58	671	6070	144000	261000	28300	104600	17300	3780	6310	366	1360	216	453	41	126	13
		59	993	9850	137000	254000	26700	92600	17200	3560	6260	430	1620	244	347	30	80	7
		60	674	20000	100300	244000	29300	112000	22400	4400	9400	863	2700	269	346	25	61	6
		63	706	6130	112200	262000	31400	117000	20000	4060	8220	730	2600	252	365	26	74	7
		64	983	8720	116000	258000	31300	106000	21900	4480	9200	882	2580	274	367	25	82	8
		65	699	4550	129000	261000	26700	100800	18800	3850	5920	435	1500	222	352	30	87	8
		66	868	8010	130000	259000	28800	98000	18100	3820	6720	331	1287	231	404	35	127	12
		67	460	16100	124000	255000	25000	88400	16400	3550	5380	329	1300	203	355	30	81	10
		68	646	8880	130000	243000	28700	97000	16700	3530	5880	321	1170	220	412	44	122	13
		69	591	10050	123900	252000	27600	97500	16100	3740	6020	377	1530	267	424	34	110	10
		70	493	14900	150000	255000	29000	100100	18100	3660	6130	361	1440	231	406	38	109	12
		71	490	16600	123000	241000	30100	87000	15300	3250	5580	417	1430	188	257	21	54	4
		72	701	4010	146400	254000	28100	92700	16100	3780	6180	491	1840	197	313	21	53	7
		73	877	3960	131000	280000	28200	96400	16500	3910	6600	408	1690	228	281	29	73	6
		74	476	14900	141000	273000	28700	97200	16700	3870	6350	422	1470	212	398	35	99	10
		79	1029	9800	132000	262000	32700	108000	17600	4100	7710	755	2350	275	332	31	73	11
		81	454	10270	107100	251000	29600	109900	17100	3740	7020	659	2140	227	317	25	64	8
		83	447	11360	115000	229000	26200	89500	15300	3510	5750	483	1750	204	326	22	64	7
		84	346	17800	114400	270000	30500	113000	18100	3560	7690	688	2200	196	296	22	53	5
		85	384	26800	72000	234000	34700	137000	27700	6470	14700	1320	3100	279	350	23	71	6

Table S.II.2 (continued)

Sample	Analyses location in the monazite	Number of analysis	U ppm	Th ppm	La ppm	Ce ppm	Pr ppm	Nd ppm	Sm ppm	Eu ppm	Gd ppm	Tb ppm	Dy ppm	Ho ppm	Er ppm	Tm ppm	Yb ppm	Lu ppm
MJ182	Monazite core	4	356	52000	88800	263000	31900	119000	21100	5150	11500	1019	3200	257	317	21	61	6
		5	277	70100	38100	165000	31900	164000	42000	11790	20900	1650	3640	306	369	30	90	9
		6	370	95500	34200	172000	39200	204000	71000	18200	32300	2160	4660	423	533	39	125	11
		7	495	65800	59300	222000	33800	147000	28900	7470	18200	1620	3750	320	401	32	81	6
		12	453	61700	55000	203000	37000	171000	36700	8900	21100	1770	3950	339	396	28	82	9
		13	242	64100	41600	184000	35500	181000	50500	13200	22900	1760	3910	295	402	31	86	8
		14	336	46200	86500	235000	31600	123000	20300	4950	11800	1060	3080	258	305	21	67	7
		21	406	58100	73700	224000	32800	133000	27600	5540	13980	1329	3460	285	335	26	74	6
		22	316	68500	27600	143000	30200	165000	52400	14000	28200	1870	4220	341	426	31	103	9
		28	514	33900	93100	270000	35500	130000	26200	6470	14000	1210	3270	289	367	31	93	9
		29	304	49800	40800	175000	34300	188000	54800	15500	26900	2150	4340	381	456	35	106	11
		30	347	64900	29600	155000	34600	187000	59700	16000	30500	2110	4610	399	433	39	95	10
		31	382	62900	29800	159000	32600	190000	71600	18800	35100	2510	5770	453	529	48	135	13
		32	239	47500	36000	174000	35300	210000	61900	17100	31200	2300	4900	386	479	37	115	11
		35	262	34600	65800	253000	35000	141000	27700	6570	14300	1200	3030	261	325	24	70	6
		37	367	40500	59300	240000	38000	180000	39400	9770	20500	1760	4340	350	462	36	106	10
		42	401	34700	98600	232000	25200	89800	14800	3500	7890	833	2470	210	264	18	56	4
		43	431	35800	102500	249000	29600	94000	16900	3930	9300	960	2700	225	301	22	63	5
		44	354	42400	100700	267000	32400	126000	20200	4920	11440	1090	3210	255	321	26	71	7
		45	328	39000	101500	269000	28600	114000	17900	4500	10900	954	2740	210	302	19	55	7
		46	368	42500	97000	245000	37000	119000	20200	4840	10900	1110	2960	259	329	24	69	6
		47	489	49600	84300	239000	31600	129000	23900	5960	12780	1270	3260	280	342	25	63	7
		50	408	54600	63400	236000	36600	162000	33300	8600	17700	1560	4330	365	449	33	108	8
		51	313	42500	56100	217000	34200	149000	34700	8350	17300	1450	3600	284	373	29	95	7
		57	634	34700	111800	259000	29300	102600	16800	3870	9120	914	2820	231	292	23	58	6
		58	446	45100	80500	252000	32900	133000	23400	5770	13300	1230	3110	276	327	25	66	5
		59	460	49400	61700	235000	35900	152000	33000	7270	17800	1490	4180	325	425	32	91	7
		60	362	51200	41900	195000	33400	162000	41200	11500	21500	1880	4520	375	446	36	109	9
		61	218	40200	29300	148000	31900	183000	89000	20800	31800	2250	4700	416	467	39	133	11
		62	226	27100	29100	149000	32900	180000	88600	21500	36000	2140	4980	422	507	37	120	10
		63	365	39100	63400	244000	39600	170000	36100	8610	19900	1660	4170	357	392	29	88	8
		69	521	53300	103600	257000	34500	122000	21200	5410	11500	1140	3270	279	357	26	68	7
		70	201	57000	43200	197000	35800	179000	53900	12700	24100	1800	3740	293	406	33	85	7
		71	290	67500	24200	130000	30100	187000	67400	18500	29700	2140	4280	391	463	37	104	11
		72	227	44800	36000	172000	31500	177000	49700	14700	27900	2090	4420	362	442	35	98	9
		75	340	32200	124000	273000	28900	91500	13500	3140	6690	701	2100	208	250	17	59	4
		78	366	49100	71300	219000	29400	113300	22600	5370	12600	1110	2850	225	291	22	62	6
	Monazite rim	1	1131	6740	149000	274000	27600	75600	11200	2120	3580	225	977	166	272	27	75	7
		2	1054	10680	154000	283000	25400	80800	11400	2130	3410	258	1390	196	299	26	65	7
		3	568	32400	144000	263000	26100	83000	12600	2550	5570	657	2210	206	275	22	59	5
		8	887	43800	129000	258000	28500	98500	15400	3040	6240	717	2220	234	276	22	65	5
		11	1109	39800	123000	265000	29100	101500	14400	3220	6200	714	2410	236	296	25	63	6
		15	510	33000	124000	249000	25900	92700	11100	2650	5780	598	1990	206	279	19	59	6
		16	506	33500	136000	276000	24700	79000	12600	2660	4940	544	1980	200	254	23	58	7
		19	1363	11960	154000	263000	27700	91100	13900	2500	4010	280	1370	198	316	29	87	8
		20	1000	20500	131000	236000	24500	78500	13000	2340	4360	432	1670	209	295	24	65	7
		23	569	43600	105200	251000	28900	106700	17700	3880	9300	1000	2910	283	318	24	67	6
		24	531	40100	118300	247000	26700	93800	14700	2970	7320	824	2450	259	296	23	60	7
		26	1360	8450	152000	271000	27100	84000	13100	2580	4030	263	1320	194	339	26	63	5
		27	1047	14500	139000	253000	27900	95800	13300	2710	5160	403	1650	189	299	20	59	5
		38	764	16100	155000	289000	31100	100000	14100	2790	5900	632	2060	222	288	24	63	7
		39	647	18200	133000	267000	28400	91200	13400	2700	5740	570	2170	208	258	22	56	7
		40	630	22700	147000	276000	28000	92900	13500	3070	6540	692	2220	226	286	24	69	6
		41	1090	7820	118000	210000	18200	67200	11700	2220	3600	269	1070	165	224	17	58	6
		48	841	26700	119300	262000	30200	97500	15400	3040	6710	763	2460	233	291	22	56	5
		55	586	29000	111000	232000	26800	107000	15400	3730	8100	810	2240	211	273	19	56	5
		56	685	33100	105000	250000	31400	120000	20000	4700	9400	963	2880	264	335	24	60	7
		64	416	37900	81600	216000	34900	119000	20800	5260	11700	1060	2820	263	292	23	71	5
		65	1039	6190	157000	255000	27400	92000	12500	2080	3920	212	1000	193	318	28	85	7
		66	824	7820	155000	256000	25500	85000	11380	1970	3290	218	1050	150	260	25	77	6
		67	697	13760	160000	246000	28800	84800	11130	2030	3810	313	1430	170	253	21	55	7
		68	354	30800	124000	264000	27600	91800	13400	3000	6610	711	2030	196	256	22	49	5
		74	762	9980	173000	270000	26800	82400	11100	2000	3890	242	1260	181	289	23	62	6
		79	710	35200	142000	256000	26700	94800	13800	3130	6680	709	2420	228	307	23	58	5
		80	973	11980	159000	278000	27100	91000	12800	2390	4410	372	1740	225	364	30	75	7

Table S.II.2 (continued)

Sample	Analyses location in the monazite	Number of analysis	U ppm	Th ppm	La ppm	Ce ppm	Pr ppm	Nd ppm	Sm ppm	Eu ppm	Gd ppm	Tb ppm	Dy ppm	Ho ppm	Er ppm	Tm ppm	Yb ppm	Lu ppm
MJ52D	Monazite core	6	420	59200	53200	209000	34000	149000	37400	9450	23700	1890	4370	385	461	40	107	11
		7	451	55300	36700	165000	30900	160000	66600	17100	35300	2350	5240	425	552	48	141	13
		12	484	63400	52500	216000	33300	159000	43700	11600	25500	1990	4890	411	495	42	113	13
		13	423	61500	28700	139000	29900	163000	92000	19300	36900	2380	4690	404	508	37	117	10
		14	506	69900	49000	205000	35200	162000	47600	12500	27500	2120	4770	337	465	38	106	10
		21	460	64000	53900	214000	31700	146000	37800	9540	22800	1760	4380	396	448	40	108	11
		22	418	69300	34000	143000	30000	167000	68200	17300	33000	2020	4620	393	487	38	125	10
		23	540	89500	29200	133000	27900	168000	88200	19700	33700	2240	4990	416	491	42	137	11
		26	417	61900	43300	180000	30600	140000	53000	12800	28100	2140	4610	389	497	43	120	13
		27	468	74100	39200	174000	29600	165000	75800	16500	33400	2390	5120	411	548	46	136	12
		28	500	58300	77900	242000	32500	129000	24300	5970	17400	1540	3870	362	471	34	106	11
		32	355	56700	31200	149000	27000	145600	47000	11730	24800	1740	3970	338	367	31	90	9
		33	447	66000	54200	214000	35100	162000	45500	11300	25100	1940	4530	407	483	38	96	9
		38	488	75900	51400	207000	33900	171000	57200	14360	29300	2280	5140	435	509	40	116	12
		39	419	70400	29700	139000	29200	165000	75100	19100	33400	2130	4900	375	458	44	110	9
		43	418	64800	64100	214000	33000	142000	34500	8720	22500	1770	4060	349	475	35	95	11
		44	412	72800	33800	165000	31900	169000	76500	18300	34300	2560	4940	421	522	43	128	13
		45	442	60800	76500	221000	31500	120700	25700	6020	17300	1470	3680	287	396	31	84	7
		48	547	67400	35000	169000	33200	175000	76700	20400	32600	2330	5090	443	488	41	122	11
		50	433	53800	54900	214000	31900	151000	39500	10030	24700	1920	4550	377	515	42	118	11
		57	521	70700	43300	194000	34200	168000	55800	13900	29500	2080	4920	422	479	38	108	9
		58	459	66100	46000	189000	32500	165000	53900	11860	27000	1890	4330	351	416	33	92	8
		59	494	60800	63700	232000	36800	145000	32200	8260	20800	1740	4350	344	441	35	102	9
		85	339	58800	37500	170000	33100	158000	53400	13700	27100	2090	4620	374	485	39	114	10
		86	572	88400	26100	129400	31800	194000	118000	25700	36100	2740	5240	463	559	45	138	12
		93	338	54800	55700	207000	31600	153000	35400	9180	22700	1730	3960	336	366	31	84	8
		94	378	55100	38500	172000	31000	164000	55200	15200	28300	2040	4480	354	478	34	113	12
		95	420	63500	59500	211000	38000	144000	38800	9900	23300	1770	4470	447	530	60	215	29
		96	400	62900	35200	174000	33000	176000	67500	18200	35700	2230	4850	386	476	37	94	12
		109	543	55100	77100	228000	31200	129000	23300	5950	18600	1780	5250	760	1390	216	1300	208
		110	380	49600	72900	217000	31800	131000	28300	7410	18100	1500	3630	308	386	29	89	8
	Monazite rim	3	492	34100	123700	252000	26600	106600	16800	3320	8420	886	3010	297	409	31	80	7
		4	571	45500	105500	251000	31400	106600	19100	4130	11700	1370	4020	352	450	37	110	10
		5	461	49600	85700	241000	33400	120700	24800	6300	16800	1640	3960	350	436	35	109	9
		10	534	37200	121000	236000	28300	101400	15900	3080	8020	960	2990	303	387	29	81	7
		11	497	43900	96100	240000	27200	114400	20000	4400	12300	1250	3530	321	422	32	91	8
		15	514	35500	116000	242000	31600	109000	17300	3500	8600	1110	3360	310	398	34	85	7
		18	736	39200	145000	261000	27800	106500	15600	2740	5590	535	2270	262	382	33	83	8
		19	671	42200	115700	245000	27000	106500	15600	2640	5960	698	2570	257	378	30	79	8
		20	483	46100	106000	232000	29200	111000	17000	3940	10600	1240	3570	322	398	30	84	9
		25	438	49200	96900	254000	31400	125000	22800	4790	14700	1560	3880	343	448	32	100	9
		29	537	46000	116000	258000	33500	107000	17700	3570	9470	1130	3300	286	386	33	79	9
		30	632	39200	135000	256000	31400	94700	17100	2690	5840	630	2520	274	377	28	81	7
		31	635	38200	144000	254000	26100	97200	14700	2670	5970	602	2270	275	325	33	77	7
		34	479	57500	90000	255000	33400	130000	26200	6410	17800	1640	4290	366	413	35	106	8
		35	553	46500	118000	270000	31900	115000	18800	3390	8710	1100	3230	319	401	32	85	8
		36	517	41800	124000	247000	30000	114000	17000	3210	8220	953	2880	294	350	29	76	8
		37	409	55800	69000	217000	34400	134000	29100	6810	19800	1610	3990	342	425	35	98	10
		42	445	35400	113700	246000	26000	97000	14700	2730	5590	687	2210	240	298	23	60	7
		46	530	53900	105300	278000	30400	109700	18600	3940	11550	1246	3450	308	399	33	87	9
		47	595	44700	132000	268000	30900	109200	17600	3000	7370	797	2890	294	367	31	71	8
		51	519	43600	96000	249000	30500	118000	20500	4790	12700	1470	3760	345	413	33	84	8
		52	622	45600	111000	247000	28700	111400	17500	3510	10550	1124	3240	315	384	32	88	7
		53	695	38100	118000	251000	28200	103000	15500	2790	6370	707	2480	285	383	28	80	8
		54	712	40600	127000	256000	28600	106000	16100	2780	6050	668	2500	274	398	29	88	8
		55	670	40900	130000	259000	30100	104100	16400	2920	6220	764	2880	298	428	32	90	9
		60	504	46200	89700	238000	29700	101700	19600	4440	13200	1420	3700	313	385	31	89	8
		61	525	44600	106000	260000	31200	109000	16900	3460	8970	1110	3510	318	368	33	86	7
		62	552	38000	127000	245000	28800	93900	15400	2830	6350	825	2910	317	398	31	90	7
		63	744	41600	132800	271000	29200	102700	15830	2660	5950	684	2480	311	427	33	89	9
		66	577	31700	125000	229000	24200	87500	16800	4050	8900	859	2420	271	351	28	73	7
		67	621	31000	160000	286000	30200	92100	15800	2690	5870	576	2210	265	388	38	79	7
		68	632	46800	119000	245000	29700	101400	15800	2840	5760	718	2690	257	327	28	71	7
		69	636	55900	122000	262000	29800	106000	15100	3080	7550	846	2840	269	338	24	58	7
		70	601	55000	129000	263000	30100	103400	16200	2930	7370	863	2610	280	302	26	70	6
		71	541	52500	116000	265000	27700	105000	15000	3140	8100	879	2560	263	322	23	62	5
		72	568	59600	122000	267000	30400	110700	15900	3400	8750	997	2950	266	325	26	66	7
		73	505	56100	112700	251000	31100	115000	19400	3640	9640	1100	3280	306	382	28	69	6
		74	479	49800	102000	242000	30400	114000	19200	3540	9150	1030	3290	298	342	25	73	6
		75	455	37700	121000	243000	27700	99700	15700	3060	7650	904	2890	292	372	29	76	6
		76	522	42200	119600	277000	28200	115400	17200	2970	6760	866	3020	285	371	29	75	6
		77	562	31600	134000	256000	28300	98000	14900	2780	5860	607	2470	279	352	29	75	6
		78	657	34600	142000	245000	28700	93100	14200	2590	5850	614	2430	276	418	35	84	8
		79	641	32500	145000	266000	26300	95700	15300	2550	5340	579	2010	261	376	27	67	6
		81	564	33200	144000	246000	25900	86400	14300	2700	5820	597	2030	247	322	25	69	6
		82	508	34000	129100	240000	27300	89300	14800	2850	6350	770	2660	252	343	28	79	7
		83	487	45300	115000	260000	28700	101500	17000	3410	8730	1155	3120	291	387	30	74	7
		84	437	54300	104000	257000	32700	116700	22600	5060	14100	1570	3580	380	437	32	85	7
		87	394	47900	95000	258000	32700	120000	22300	5590	15700	1520	4020	331	434	36	92	7
		88	439	32800	96500	211000	22700	75700	13300	2300	5670	672	2180	234	300	22	56	5
		89	601	41300	120000	234000	28900	91700	15500	3090	6790	806	2820	280	364	29	79	7
		90	621	35900	143000	248000	29100	101500	15900	2790	6350	653	2510	279	367	31	74	9
		92	432	47400	98200	258000	30400	105900	18200	4220	11590	1230	3610	308	389	33	88	7
		99	577	26200	141000	251000	24900	90000	14310	2390	5490	535	2180	252	343	26	79	7
		100	822	42800	124300	273000	30100	104000	15000	2660	5540	657	2560	292	377	32	87	6
		101	501	35800	118000	281000	28700	114800	15600	3020	7430	920	3110	260	383	30	75	7
		102	638	46500	107100	236000	26900	101700	16500	3190	8220	1050	3390	282	349	28	74	7
		103	553	35500	120000	270000	28600	110000	18300	3820	9110	1030	3310	351	425	35	91	10
		104	543	36600	120000	243000	30600	103300	15800	3080	6690	899	3000	288	319	29	80	6
		105	575	35300	118000	233000	28600	93000	14600	2550	6030	690	2710	300	458	34	125	13
		106	585	41600	128000	274000	29300	108000	17700	3070	7380	893	3070	300	376	31	97	9
		107	510	42100	113800	263000	32300	110700	17300	3100	8590	1140	3340	319	394	36	83	7
		108	464	43900	103100	259000	30500	112000	17800	4320	11100	1320	3410	349	441	35	117	10
		111	436	44400	113000	255000	31600	107100	19300	4260	13000	1340	3580	296	397	31	84	8
		112	471	34400	113000	228000	28000	95100	14720	2570	6710	761	2480	240	334	28	78	8

Table S.II.3: Monazite U-Pb MC-ICP-MS data of the micaschist samples (MJ218A, MJ58D2, MJ58G, MJ11C and MJ62B). **Intercept ages calculated using $^{207}Pb/^{206}Pb$ values from the Stacey & Kramers (1975) lead isotopic evolution model. (The table continues next pages)

Sample	Analysis from thin-section or mount	Analysis location in the thin-section or in the monazite	$^{238}U/^{206}Pb$	± 2 se	$^{207}Pb/^{206}Pb$	± 2 se	Intercept Age (Ma)**	± 2 se
MJ218A	Thin-section	Inc. g rim I	18.30	0.5645	0.0645	0.0014	338	10
			17.24	0.5444	0.0665	0.0040	358	11
			17.96	0.5527	0.0602	0.0014	346	11
			18.66	0.5708	0.0649	0.0018	332	10
			18.91	0.5835	0.0718	0.0016	324	10
		Inc. g rim II	18.53	0.5744	0.0621	0.0014	335	10
			19.19	0.5876	0.0635	0.0014	323	10
			18.12	0.6525	0.0623	0.0017	343	12
			18.27	0.5702	0.0611	0.0013	340	10
			19.03	0.5848	0.0643	0.0014	326	10
			19.49	0.6182	0.0572	0.0013	321	10
			16.97	0.5233	0.0821	0.0039	356	11
		M1-M2 matrix	18.71	0.5769	0.0599	0.0014	333	10
			18.49	0.5641	0.0616	0.0013	336	10
			18.48	0.5663	0.0632	0.0017	336	10
			18.60	0.5657	0.0637	0.0016	333	10
			18.80	0.5694	0.0568	0.0013	333	10
			17.99	0.5878	0.0603	0.0015	346	11
			18.20	0.5554	0.0576	0.0012	343	10
			17.66	0.5845	0.0597	0.0014	352	11
			18.25	0.5676	0.0604	0.0015	341	10
			18.79	0.6010	0.0587	0.0013	332	10
			18.68	0.5644	0.0573	0.0013	334	10
			18.37	0.5610	0.0579	0.0013	340	10
			18.96	0.5748	0.0575	0.0014	330	10
			18.60	0.5821	0.0581	0.0012	336	10
			18.92	0.6020	0.0574	0.0012	330	10
			19.18	0.6074	0.0600	0.0015	325	10
			18.81	0.5904	0.0623	0.0017	330	10
			18.95	0.6404	0.0579	0.0014	329	11
			18.74	0.6005	0.0564	0.0012	334	11
			18.54	0.5931	0.0564	0.0013	337	11
			19.26	0.5872	0.0580	0.0012	324	10
			19.20	0.5902	0.0573	0.0012	326	10
			18.93	0.5923	0.0573	0.0015	330	10
			19.10	0.6551	0.0557	0.0011	328	11
			18.67	0.5837	0.0568	0.0014	335	10
			18.99	0.6032	0.0556	0.0012	330	10
			19.32	0.6076	0.0566	0.0012	324	10
			18.88	0.6160	0.0580	0.0012	331	11
			18.95	0.6146	0.0563	0.0012	330	11
			19.21	0.6188	0.0578	0.0013	325	10
			17.79	0.5465	0.0807	0.0023	341	10
			19.19	0.6044	0.0601	0.0013	325	10
			18.86	0.5890	0.0573	0.0014	331	10
			18.53	0.5827	0.0565	0.0015	338	10
			17.50	0.5340	0.0613	0.0014	355	11
			18.65	0.6570	0.0605	0.0013	334	12
		M3 matrix	17.86	0.6234	0.0872	0.0035	337	12
			19.31	0.5963	0.0571	0.0013	324	10
			18.66	0.5707	0.0557	0.0012	336	10
			18.80	0.5988	0.0586	0.0014	332	10
			19.41	0.6438	0.0571	0.0013	322	11
			18.27	0.5920	0.0585	0.0014	341	11
			19.79	0.6331	0.0568	0.0013	316	10
			19.36	0.6059	0.0578	0.0012	323	10
			20.13	0.6451	0.0578	0.0013	311	10

Table S.II.3 (continued)

Sample	Analysis from thin-section or mount	Analysis location in the thin-section or in the monazite	$^{238}U/^{206}Pb$	± 2 se	$^{207}Pb/^{206}Pb$	± 2 se	Intercept Age (Ma)**	± 2 se
MJ58D2	Thin-section	Inc. g rim II	18.51	0.5863	0.0688	0.0014	333	10
			18.53	0.5780	0.0702	0.0015	332	10
			18.59	0.5649	0.0701	0.0015	331	10
			18.51	0.5660	0.0700	0.0015	332	10
			17.97	0.5718	0.0685	0.0014	343	11
			18.30	0.5933	0.0701	0.0015	336	11
			18.81	0.5817	0.0701	0.0015	327	10
			18.37	0.5782	0.0710	0.0016	334	10
			18.78	0.5924	0.0705	0.0015	327	10
			18.85	0.5692	0.0755	0.0016	324	10
			19.12	0.6114	0.0761	0.0015	319	10
			18.43	0.5611	0.0719	0.0016	333	10
			18.40	0.5625	0.0726	0.0015	333	10
			18.13	0.5579	0.0790	0.0017	335	10
			18.50	0.5665	0.0690	0.0015	333	10
			18.48	0.5973	0.0780	0.0017	329	11
			18.55	0.5867	0.0733	0.0015	330	10
			19.14	0.5944	0.0707	0.0015	321	10
			19.53	0.5970	0.0730	0.0015	314	9
			18.53	0.5741	0.0742	0.0019	330	10
			18.28	0.5948	0.0682	0.0014	337	11
			19.06	0.6172	0.0754	0.0023	320	10
			18.32	0.5614	0.0700	0.0014	335	10
			18.04	0.5632	0.0803	0.0021	336	10
			18.30	0.5781	0.0744	0.0016	334	10
			18.35	0.5621	0.0757	0.0017	333	10
			18.11	0.6136	0.0771	0.0017	336	11
			18.45	0.5683	0.0726	0.0015	332	10
			17.24	0.6829	0.0767	0.0018	353	14
		M1-M2 matrix	18.59	0.5870	0.0699	0.0015	331	10
			18.27	0.5665	0.0704	0.0015	336	10
			18.35	0.5660	0.0705	0.0014	335	10
			18.38	0.5601	0.0698	0.0015	334	10
			18.49	0.5765	0.0701	0.0014	332	10
			18.52	0.5602	0.0716	0.0015	331	10
			18.40	0.5745	0.0724	0.0017	333	10
			18.02	0.5737	0.0708	0.0015	341	11
			17.83	0.5657	0.0670	0.0014	346	11
			18.00	0.5450	0.0690	0.0016	342	10
			18.50	0.5752	0.0745	0.0015	330	10
			18.19	0.5703	0.0698	0.0015	338	10
			18.06	0.5668	0.0736	0.0015	339	10
			18.23	0.5930	0.0749	0.0016	335	11
			18.43	0.5805	0.0708	0.0016	333	10
			18.04	0.5680	0.0684	0.0016	341	11
			18.29	0.5580	0.0710	0.0015	336	10
			18.59	0.5789	0.0700	0.0016	331	10
			18.50	0.5607	0.0723	0.0015	331	10
			18.53	0.5681	0.0746	0.0016	330	10
			18.46	0.5637	0.0742	0.0016	331	10
			18.50	0.6130	0.0729	0.0015	331	11
			18.65	0.5691	0.0710	0.0016	329	10
		M3 matrix	19.27	0.5909	0.0585	0.0014	324	10
			17.61	0.6643	0.0779	0.0017	345	13
			18.96	0.6376	0.0745	0.0016	322	11
			18.48	0.6136	0.0798	0.0021	328	11
			19.06	0.5822	0.0703	0.0015	323	10
			18.76	0.5827	0.0691	0.0015	328	10
			18.83	0.5807	0.0684	0.0017	327	10
			18.21	0.5615	0.0715	0.0015	337	10
			18.12	0.5688	0.0700	0.0016	339	11
			18.16	0.5904	0.0682	0.0014	339	11
			19.54	0.6683	0.0579	0.0012	320	11
			18.88	0.5776	0.0668	0.0016	327	10
			18.44	0.5666	0.0721	0.0016	332	10
			19.05	0.5898	0.0591	0.0014	327	10

Table S.II.3 (continued)

Sample	Analysis from thin-section or mount	Analysis location in the thin-section or in the monazite	$^{238}U/^{206}Pb$	± 2 se	$^{207}Pb/^{206}Pb$	± 2 se	Intercept Age (Ma)**	± 2 se
MJ58G	Mount	Monazite core	17.90	0.5425	0.0688	0.0015	344	10
			18.38	0.5797	0.0704	0.0016	334	10
			18.68	0.5871	0.0708	0.0015	329	10
			18.29	0.5536	0.0698	0.0016	336	10
			18.27	0.5606	0.0686	0.0015	337	10
			18.63	0.6068	0.0702	0.0015	330	11
			18.34	0.5687	0.0691	0.0016	336	10
			18.18	0.6017	0.0695	0.0015	338	11
			18.56	0.5711	0.0703	0.0015	331	10
			18.35	0.5585	0.0695	0.0016	335	10
			18.20	0.5677	0.0694	0.0014	338	10
			17.91	0.5754	0.0684	0.0014	344	11
			17.45	0.6949	0.0671	0.0014	353	14
			18.05	0.7746	0.0632	0.0017	343	15
			17.99	0.7257	0.0633	0.0017	345	14
			17.70	0.5511	0.0652	0.0015	349	11
			17.90	0.5603	0.0691	0.0015	344	11
			18.36	0.6388	0.0683	0.0014	336	12
			18.23	0.5605	0.0682	0.0016	338	10
			18.14	0.5935	0.0699	0.0019	339	11
			17.33	0.5447	0.0693	0.0015	355	11
			17.60	0.5742	0.0679	0.0014	350	11
			18.13	0.6041	0.0691	0.0016	339	11
			17.99	0.7257	0.0683	0.0014	342	14
			17.91	0.5609	0.0688	0.0020	343	11
			17.57	0.5527	0.0650	0.0015	352	11
			18.25	0.5517	0.0676	0.0014	338	10
			18.02	0.5560	0.0668	0.0014	342	10
			18.88	0.5972	0.0686	0.0014	326	10
			18.28	0.5630	0.0671	0.0015	337	10
			18.35	0.5578	0.0664	0.0014	337	10
			18.50	0.5725	0.0678	0.0014	333	10
			18.44	0.5689	0.0686	0.0015	334	10
			18.14	0.5598	0.0689	0.0015	339	10
			18.12	0.5520	0.0682	0.0014	340	10
			17.84	0.5467	0.0697	0.0016	345	10
			18.47	0.6146	0.0682	0.0015	334	11
			18.56	0.5891	0.0685	0.0016	332	10
			18.08	0.5723	0.0684	0.0016	341	11
			18.13	0.5579	0.0666	0.0014	341	10
			17.98	0.5753	0.0664	0.0014	343	11
			18.70	0.5952	0.0671	0.0014	330	10
			18.32	0.5666	0.0680	0.0015	336	10
			18.17	0.5541	0.0673	0.0015	339	10
			18.63	0.5735	0.0677	0.0014	331	10
			19.02	0.5835	0.0686	0.0014	324	10
			18.14	0.5757	0.0662	0.0015	340	11
			18.04	0.6034	0.0680	0.0016	341	11
			18.46	0.6044	0.0700	0.0014	333	11
			18.56	0.5894	0.0696	0.0016	331	10
			18.08	0.5596	0.0685	0.0016	340	10
			18.23	0.5584	0.0715	0.0017	337	10
			18.71	0.5848	0.0697	0.0015	329	10
			17.98	0.5463	0.0682	0.0014	343	10
			18.24	0.5665	0.0718	0.0015	336	10
		Monazite rim	17.90	0.5390	0.0721	0.0016	342	10
			17.78	0.5356	0.0705	0.0017	345	10
			18.45	0.5770	0.0695	0.0016	333	10
			18.18	0.5613	0.0739	0.0017	336	10
			18.20	0.5634	0.0734	0.0016	336	10
			17.97	0.5618	0.0733	0.0016	341	11
			18.18	0.5548	0.0709	0.0015	338	10
			18.26	0.5856	0.0700	0.0015	337	11
			18.50	0.5779	0.0693	0.0014	333	10
			18.06	0.5441	0.0700	0.0014	340	10
			18.27	0.5769	0.0715	0.0016	336	10
			18.52	0.5826	0.0743	0.0023	330	10
			17.82	0.5666	0.0736	0.0016	343	11
			18.45	0.5685	0.0730	0.0015	332	10
			18.35	0.5621	0.0728	0.0015	334	10
			18.53	0.5679	0.0714	0.0015	331	10
			18.30	0.5792	0.0727	0.0015	335	10
			18.20	0.5570	0.0754	0.0019	335	10
			18.15	0.5559	0.0745	0.0015	337	10
			17.74	0.5447	0.0698	0.0015	346	10

Table S.II.3 (continued)

Sample	Analysis from thin-section or mount	Analysis location in the thin-section or in the monazite	$^{238}U/^{206}Pb$	± 2 se	$^{207}Pb/^{206}Pb$	± 2 se	Intercept Age (Ma)**	± 2 se
MJ11C	Thin-section	Inc. g rim I	17.88	0.5418	0.0692	0.0017	344	10
			18.05	0.5618	0.0706	0.0015	340	10
			18.20	0.5498	0.0668	0.0015	339	10
			19.16	0.7469	0.0565	0.0016	327	13
			18.47	0.6047	0.0686	0.0029	333	11
			18.76	0.5930	0.0676	0.0016	329	10
			18.14	0.5745	0.0660	0.0013	340	11
			18.25	0.5863	0.0660	0.0014	338	11
			18.84	0.5819	0.0701	0.0015	326	10
		Inc. g rim II	17.29	0.5830	0.1119	0.0033	336	11
			17.70	0.5511	0.1205	0.0026	324	10
			16.82	0.5131	0.1220	0.0037	340	11
			16.05	0.5187	0.1524	0.0034	341	11
			16.53	0.5944	0.1419	0.0043	337	12
			17.48	0.6230	0.1205	0.0076	328	12
			16.64	0.5202	0.1314	0.0038	339	11
			16.19	0.5289	0.1380	0.0044	345	12
			16.72	0.5563	0.1347	0.0032	336	11
			18.02	0.5684	0.1151	0.0025	321	10
			17.65	0.5681	0.1152	0.0040	327	11
			17.45	0.5921	0.1183	0.0025	330	11
			17.12	0.5255	0.1296	0.0030	331	10
			17.47	0.5582	0.1258	0.0040	326	11
			17.92	0.5945	0.0990	0.0027	330	11
			17.36	0.6341	0.1123	0.0028	334	12
			17.51	0.6984	0.1222	0.0051	327	13
			17.47	0.5626	0.1194	0.0035	329	11
			16.92	0.5323	0.1146	0.0029	342	11
			17.06	0.6198	0.1211	0.0035	336	12
		M3 matrix	19.02	0.5933	0.0543	0.0016	330	10
			19.19	0.6117	0.0544	0.0015	327	10
			19.09	0.6672	0.0540	0.0013	329	11
			19.41	0.6377	0.0557	0.0012	323	10
			19.43	0.5946	0.0541	0.0018	323	10
			18.62	0.5817	0.0532	0.0012	337	10
			19.19	0.6816	0.0536	0.0012	327	11
			19.75	0.6062	0.0535	0.0011	318	10
			19.68	0.6613	0.0537	0.0012	319	11
			19.06	0.5927	0.0531	0.0012	330	10
			18.13	0.6191	0.0535	0.0012	346	12
			18.89	0.6095	0.0541	0.0011	332	11
			19.03	0.5864	0.0541	0.0012	330	10
			18.86	0.5728	0.0532	0.0012	333	10
			18.71	0.5859	0.0539	0.0012	335	10
			18.59	0.6067	0.0534	0.0012	338	11
			19.01	0.6952	0.0545	0.0013	330	12
			19.14	0.5953	0.0534	0.0012	328	10
			19.39	0.6115	0.0544	0.0013	323	10
			19.26	0.6093	0.0573	0.0014	324	10
			17.95	0.6824	0.0576	0.0024	348	13
			18.75	0.5959	0.0565	0.0014	334	10
			18.86	0.5842	0.0554	0.0011	332	10
			17.47	0.5443	0.0638	0.0020	354	11
			19.30	0.5997	0.0544	0.0012	325	10
			19.44	0.6287	0.0532	0.0011	323	10
			19.30	0.6460	0.0534	0.0011	325	11
			18.93	0.5945	0.0606	0.0013	329	10
			19.19	0.6117	0.0570	0.0013	326	10
			18.74	0.5861	0.0542	0.0012	335	10
			19.67	0.6416	0.0536	0.0011	319	10
			18.77	0.5796	0.0558	0.0015	333	10
			18.56	0.5789	0.0529	0.0011	338	10
			19.76	0.6720	0.0535	0.0011	318	11
			19.43	0.6104	0.0554	0.0016	323	10
			18.85	0.5747	0.0536	0.0014	333	10
			19.80	0.8360	0.0543	0.0012	317	13
			19.47	0.5972	0.0564	0.0016	321	10
			19.56	0.6054	0.0554	0.0014	320	10
			18.43	0.5793	0.0535	0.0013	341	11
			19.21	0.6509	0.0597	0.0018	324	11
			19.80	0.6478	0.0550	0.0013	317	10

Table S.II.3 (continued)

Sample	Analysis from thin-section or mount	Analysis location in the thin-section or in the monazite	$^{238}U/^{206}Pb$	± 2 se	$^{207}Pb/^{206}Pb$	± 2 se	Intercept Age (Ma)**	± 2 se
MJ62B	Thin-section	Inc. g rim I	18.67	0.5789	0.0739	0.0018	328	10
			18.28	0.5818	0.0669	0.0014	337	11
			18.85	0.5821	0.0676	0.0015	327	10
			18.79	0.6228	0.0681	0.0016	328	11
			18.29	0.5709	0.0652	0.0015	338	10
			18.41	0.5946	0.0649	0.0013	336	11
			18.77	0.5743	0.0668	0.0015	329	10
			19.12	0.5819	0.0660	0.0015	323	10
		Inc. g rim II	18.89	0.5911	0.0668	0.0015	327	10
			18.19	0.6049	0.0647	0.0014	340	11
			18.11	0.5925	0.0644	0.0014	342	11
			18.86	0.6417	0.0669	0.0014	327	11
			19.39	0.5980	0.0677	0.0014	318	10
			18.66	0.5843	0.0666	0.0015	331	10
			18.60	0.5659	0.0670	0.0014	332	10
			18.79	0.5962	0.0662	0.0014	329	10
		M1-M2 matrix	18.57	0.5699	0.0648	0.0013	333	10
			18.60	0.5652	0.0660	0.0014	332	10
			18.95	0.6289	0.0677	0.0014	326	11
			19.23	0.5825	0.0667	0.0015	321	10
			19.12	0.5834	0.0664	0.0014	323	10
			18.43	0.5628	0.0655	0.0014	335	10
			18.84	0.5820	0.0635	0.0013	329	10
			19.78	0.6065	0.0643	0.0016	313	9
			18.88	0.5895	0.0664	0.0015	327	10
			19.05	0.5776	0.0658	0.0013	325	10
			18.64	0.6004	0.0661	0.0014	332	11
			18.67	0.6082	0.0634	0.0013	332	11
			18.82	0.5848	0.0636	0.0015	329	10
			18.44	0.5981	0.0623	0.0013	337	11
			18.84	0.5872	0.0639	0.0013	329	10
			18.89	0.5819	0.0648	0.0014	328	10
			18.38	0.6650	0.0623	0.0014	338	12
			18.17	0.5811	0.0619	0.0013	342	11
			18.45	0.5935	0.0634	0.0014	336	11
			18.33	0.5769	0.0643	0.0015	338	10
			18.20	0.5704	0.0626	0.0013	341	11
			18.88	0.5793	0.0629	0.0014	329	10
			18.88	0.5857	0.0626	0.0014	329	10
			18.54	0.6021	0.0626	0.0014	335	11
			18.22	0.5581	0.0608	0.0014	341	10
			18.67	0.5921	0.0615	0.0013	333	10
			18.98	0.5864	0.0635	0.0013	327	10
			18.77	0.5721	0.0694	0.0016	328	10
			19.01	0.5749	0.0649	0.0014	326	10
			18.81	0.5713	0.0667	0.0016	328	10
			18.28	0.5670	0.0652	0.0013	338	10
			18.38	0.5633	0.0660	0.0014	336	10
			18.59	0.5927	0.0648	0.0013	333	10
			18.89	0.5941	0.0653	0.0014	328	10
		M3 matrix	19.10	0.5991	0.0639	0.0013	325	10
			19.07	0.5971	0.0637	0.0013	325	10
			18.95	0.5767	0.0640	0.0014	327	10
			18.69	0.6024	0.0637	0.0014	332	11
			18.38	0.5686	0.0723	0.0056	333	10
			18.18	0.5739	0.0653	0.0014	340	11
			19.51	0.5987	0.0679	0.0014	316	10
			18.25	0.5566	0.0689	0.0018	337	10
			18.59	0.5624	0.0737	0.0017	329	10
			18.73	0.5817	0.0644	0.0014	331	10
			18.04	0.5499	0.0652	0.0013	343	10
			18.53	0.5860	0.0620	0.0015	335	10
			19.01	0.5892	0.0651	0.0014	326	10
			18.79	0.5952	0.0640	0.0014	330	10
			18.52	0.5663	0.0628	0.0013	335	10

Table S.II.4: Monazite REE MC-ICP-MS data of the micaschists samples: MJ218A, MJ58D2, MJ58G, MJ11C and MJ62B. (The table continues next pages)

Sample	Analysis from thin-section or mount	Analysis location in the thin-section or in the monazite	Number of analysis	U ppm	Th ppm	La ppm	Ce ppm	Pr ppm	Nd ppm	Sm ppm	Eu ppm	Gd ppm	Tb ppm	Dy ppm	Ho ppm	Er ppm	Tm ppm	Yb ppm	Lu ppm
MJ218A	Thin-section	Inc. g rim I	7	3630	29600	119000	236000	26000	94000	19600	4720	12390	1450	5050	462	559	27.8	58.0	5.9
			8	4140	24700	114000	241000	27400	109000	23200	4550	10300	700	840	31	23	0.2	2.9	0.3
			9	4070	21100	109000	227000	27600	108000	19800	4270	9080	476	626	21	21	0.6	2.3	0.3
			10	4790	29900	124000	252000	26900	114000	23000	4320	9840	518	588	20	25	0.8	2.8	0.2
			11	4830	34100	117000	240000	30100	97400	21000	5240	13500	1500	4000	357	290	13.3	35.2	3.4
		Inc. g rim II	1	5490	32800	127500	274000	31900	107900	21100	5130	14400	1710	5160	472	490	30.6	61.4	7.0
			2	6430	31500	115000	225000	26600	95000	17200	4210	11600	1200	3470	320	317	20.0	42.2	4.9
			3	4480	29900	118000	250000	26800	88000	18600	4560	12400	1310	4340	345	365	21.2	46.8	3.6
			4	5100	35400	120000	240000	30800	93100	19800	4970	13800	1580	5070	444	470	25.8	59.9	4.5
			5	8240	43900	99650	217000	24500	88000	23000	5340	13900	1430	4240	358	357	21.3	52.9	5.9
			6	25100	63300	61000	207000	31900	146000	37000	11800	22700	1460	1540	65	75	7.4	33.9	5.4
			12	4790	39000	99000	223000	28500	85000	19800	4460	11900	1440	4460	457	477	43.6	139.0	10.3
		M1-M2 matrix	15	4190	43900	138000	249000	29600	106000	17500	4000	7100	366	488	27	33	1.2	5.7	0.7
			16	3410	40100	132000	240000	26500	97000	16100	3570	6520	326	418	24	30	1.2	3.6	0.5
			17	2330	32800	141200	255000	27000	96000	14300	2940	4750	226	264	13	25	1.1	7.4	1.0
			23	4940	25200	150000	264000	27200	89900	13450	3510	7860	521	654	33	47	3.0	12.1	1.2
			24	5200	35900	117000	254000	30300	104200	17100	4060	9080	514	578	31	38	2.0	5.5	0.6
			25	4380	30300	117000	259000	29000	108000	16100	4170	9020	491	596	34	44	1.7	8.2	1.0
			26	5160	25600	144000	267000	27300	92400	14700	3670	7790	521	619	28	32	1.4	3.0	0.5
			27	2930	34400	103000	243000	27900	107000	16000	4060	5180	284	330	20	27	1.2	4.4	0.6
			28	2780	32700	113000	248000	27800	109500	15100	3790	5400	301	390	21	34	1.2	2.6	0.6
			29	4110	34900	113000	233000	30100	109000	14900	4220	7550	423	506	23	31	0.8	4.5	0.2
			30	5410	35300	109000	260000	29400	114000	19100	4460	9110	519	646	31	34	1.7	5.4	0.8
			31	4220	33500	128000	256000	26700	102000	17700	3910	8370	490	537	28	32	2.1	3.4	0.7
			33	4810	33100	121000	250000	28700	106000	17000	3920	8370	475	574	29	34	1.1	4.8	0.9
			34	6370	38500	120000	263000	27700	99510	19200	4700	9960	598	632	31	39	2.0	5.5	1.0
			35	5160	35300	112500	219000	24400	92500	17000	3420	9040	600	785	39	37	2.5	12.8	1.4
			36	4840	42600	125000	239000	26800	93100	17200	3910	9170	524	600	26	35	1.7	6.9	0.7
			37	4150	46900	115000	229000	26400	90000	18000	3650	8040	475	552	31	34	1.6	5.6	0.9
			38	6240	32700	116000	234000	28500	107000	18900	4270	10800	670	1060	67	73	5.9	26.0	3.1
			39	11500	53800	84700	226000	27400	114000	27700	6730	16300	906	1030	44	35	1.6	8.9	0.6
			40	8200	41200	107000	252000	29200	105000	23400	5070	12500	695	719	33	39	1.7	4.5	0.9
			41	8180	39500	108000	236000	26700	96000	20500	4780	12200	654	697	32	38	1.8	7.1	1.0
			42	6800	39200	138200	239000	28700	99000	17700	4540	10330	598	667	30	32	1.3	4.5	0.6
			43	7140	41200	128000	229000	26400	111000	21700	5250	11250	644	732	31	36	2.1	6.3	0.8
			44	12900	67800	88700	194000	28400	115000	29800	7320	18800	1150	1210	45	43	2.1	15.8	0.6
			45	6820	33400	114000	264000	28300	118000	20000	4840	8560	467	481	21	32	1.2	5.7	1.2
			46	13700	43900	92000	231000	28600	110000	22600	6640	14400	850	822	32	32	1.5	5.8	0.7
			47	12600	49200	104900	235000	30000	125000	26800	6060	15300	749	778	31	38	1.1	7.6	0.6
			48	11860	60200	107000	239000	27500	114000	26500	5860	15800	830	737	33	43	1.8	8.8	0.7
			51	7710	31200	120000	257000	29400	108000	22800	5700	11100	614	573	22	32	0.9	7.9	0.5
			52	10910	83000	86000	188000	24900	105000	28100	5630	14700	694	598	27	33	1.6	6.5	0.9
			54	5490	29100	124000	243000	28100	95000	14000	3290	7600	356	388	21	29	1.5	5.9	1.2
			55	4170	26700	149600	269000	25600	103000	15500	3360	7220	403	413	20	30	1.6	5.9	0.8
			56	4580	22800	143000	299000	28300	84400	16000	3540	7030	353	388	21	28	1.7	5.2	0.8
			57	6140	28700	126000	256000	29100	96000	15700	3500	6900	334	399	17	28	1.8	5.5	0.9
			58	4340	27100	117800	235000	28500	99000	16600	3530	6940	346	360	17	25	1.3	4.0	0.5
			59	5300	31400	114000	270000	30600	106000	15000	3750	7400	377	376	18	28	1.2	4.7	0.4
		M3 matrix	14	2470	20280	127000	239000	24200	66100	10200	3330	4480	330	791	87	192	30.3	127.0	17.3
			18	12670	46300	82800	189000	24900	103000	26400	6740	19100	1030	1230	52	54	3.5	14.2	1.9
			19	8800	45500	104700	238000	28600	121000	22200	6130	15000	791	951	38	45	1.5	6.5	0.5
			20	5920	39100	122000	224000	27200	94700	18800	4280	12400	878	1620	145	216	19.3	97.0	9.3
			21	8410	44500	114000	247000	29200	111000	22400	5480	13100	755	862	40	43	1.7	5.6	0.8
			22	4910	41500	132000	225000	27300	89300	17600	4110	10140	613	807	49	63	3.6	13.0	2.2
			49	21500	54900	71200	205000	29400	131000	36100	10400	24200	1390	1270	54	57	4.4	16.4	2.0
			50	10230	75500	85200	189000	26000	116000	29300	6170	15800	772	964	60	95	12.6	54.0	5.6
			60	18700	56800	112000	233000	26400	106400	33200	5280	15200	526	485	24	36	3.3	12.8	1.8

Table S.II.4 (continued)

Sample	Analysis from thin-section or mount	Analysis location in the thin-section or in the monazite	Number of analysis	U ppm	Th ppm	La ppm	Ce ppm	Pr ppm	Nd ppm	Sm ppm	Eu ppm	Gd ppm	Tb ppm	Dy ppm	Ho ppm	Er ppm	Tm ppm	Yb ppm	Lu ppm
MJ58D2	Thin-section	Inc. g rim	1	9160	60400	192000	431000	41600	178000	31500	8470	21900	2160	4470	291	226	8.5	27.0	2.0
			2	8390	56400	175000	367000	46000	168000	30700	7550	20700	1870	3780	203	173	6.5	15.3	2.3
			3	7650	48700	182000	377000	43800	156000	27600	7290	19900	1780	4100	250	211	9.1	21.3	1.7
			5	8670	59900	181000	374000	41400	154000	29900	7800	22000	2030	4290	301	235	8.5	25.5	1.8
			6	8440	53800	187000	363000	41500	141000	27900	7120	20300	2030	4430	279	246	12.1	25.0	1.7
			7	9020	53900	170000	322000	40600	144000	30000	7510	22500	2350	5690	421	385	19.9	46.0	3.5
			8	9480	63300	167000	359000	46500	147000	29500	9400	23700	2240	5730	403	372	19.6	44.2	2.5
			9	8140	58300	189000	348000	37900	143000	29000	7370	20300	1940	4580	303	239	10.4	24.2	1.7
			10	9100	64600	176000	382000	42600	158000	29500	7830	21800	2150	4950	349	285	11.5	29.9	2.8
			11	12420	43000	181000	362000	40900	142400	23900	6320	9790	574	777	55	65	2.8	8.1	1.0
			12	14600	47300	213000	405000	48800	163000	30100	6980	10420	547	835	47	87	2.6	6.9	1.0
			13	8540	65300	171000	332000	41100	137000	28000	7060	18800	2100	5010	377	310	15.5	36.5	3.4
			16	8390	63100	176000	347000	41000	144000	27600	7010	19000	1980	5330	363	306	14.8	35.4	2.4
			19	7780	54200	197000	395000	38900	148000	28600	6970	20900	1790	4550	319	275	17.3	34.2	2.9
			22	7770	56100	176000	332000	35800	136000	26800	7040	20400	2000	4830	328	326	16.6	30.7	3.4
			23	16530	62100	164000	374000	44300	139000	25600	6130	12400	875	1440	93	120	8.5	26.6	3.0
			24	9710	61900	191000	348000	43700	157900	31000	8040	20300	2070	4790	401	334	18.6	40.2	3.7
			25	18000	63000	178000	350000	39600	141000	28500	7100	15100	1390	3440	283	431	47.1	110.0	9.7
			26	13010	49800	161000	339000	40700	134000	24700	6270	17000	1610	4930	501	760	72.0	185.0	19.6
			27	7540	56200	185000	381000	39800	155000	29400	7120	19800	2000	5100	359	329	17.2	32.0	3.5
			36	8300	54700	186000	367000	44500	151000	29800	7260	21700	2050	4090	227	163	8.1	16.6	2.0
			53	11800	57200	135000	307000	26600	106000	23300	5640	10600	810	1260	75	67	3.3	12.8	0.7
			62	12220	29700	167000	340000	42200	149000	28200	7170	15800	1430	5160	591	897	82.0	252.0	27.2
			63	9710	40400	181000	367000	44600	150000	27000	6740	7580	384	500	29	40	1.9	5.8	0.4
			65	9390	58000	186000	358000	39600	154000	27300	5240	15600	1336	3360	330	388	24.8	55.4	4.4
			66	9500	60900	181000	367000	40800	159000	27600	5290	14500	1200	2980	262	309	19.3	49.0	4.5
			67	13840	43100	167000	323000	37100	133000	26900	5830	14100	1281	2950	196	219	13.5	45.0	2.9
			68	11400	58400	171200	340000	39000	139000	26400	5340	13600	1270	3080	260	363	22.6	46.8	4.8
			69	8590	37900	119000	315000	23700	88000	21200	4280	11400	1150	3020	267	268	23.1	31.0	2.6
		M1-M2 matrix	28	8420	63600	181000	386000	44400	157000	27800	7190	18300	1500	3130	166	155	8.5	24.0	2.3
			29	7510	57400	191000	340000	41100	158000	30100	7230	19200	1560	2930	144	102	4.5	12.7	1.4
			30	10370	68000	171000	383000	41400	144000	27100	7060	19600	1680	3610	189	147	6.0	15.5	1.3
			31	7950	50100	204000	415000	45400	177000	32100	7550	18700	1750	3280	182	134	5.6	12.8	2.0
			32	7380	51100	172000	382000	41600	150000	27600	6980	17100	1560	2810	130	115	4.9	16.8	1.6
			33	7160	59200	182000	382000	45500	160000	29400	6810	17600	1560	2880	150	111	4.1	15.3	1.7
			34	7670	64100	195000	367000	43800	157000	28600	6790	20500	1730	2910	152	128	4.5	14.9	1.1
			35	7950	64300	184000	340000	42100	143000	28000	6800	17700	1700	2800	134	109	4.0	12.8	1.5
			45	8730	56400	190000	361000	42900	159000	30600	8100	19900	1890	3820	250	207	11.9	31.0	3.7
			46	10650	72200	177000	361000	43100	159000	32500	7630	22700	2370	5880	428	368	16.6	34.5	2.8
			47	9600	67500	163000	351000	40100	154000	29900	7600	20200	2240	6200	373	363	17.4	39.8	2.4
			48	6630	36000	196000	344000	42000	156000	30500	7410	19400	2030	4540	314	269	12.6	28.7	3.5
			49	7390	57500	172000	346000	35600	154000	28300	7310	19300	1780	4400	296	285	12.1	26.7	2.5
			50	8490	67800	181000	358000	36700	145000	27700	7190	18400	1860	4970	320	264	14.3	31.3	3.2
			51	6760	39300	165000	316000	39800	132000	30200	6790	19800	2000	4370	307	237	13.5	30.0	2.3
			52	7550	42900	219000	410000	43700	165000	30400	7980	19700	1760	2980	137	110	3.0	11.6	0.8
			54	7890	62700	188000	345000	41400	153000	25700	6160	17300	1460	2530	113	100	2.8	11.5	0.9
			55	7860	59900	189000	382000	41400	156000	32000	7390	18800	1600	2540	128	97	2.7	15.2	2.4
			56	8950	53200	182000	366000	41200	144000	27000	7000	17600	1510	2520	124	110	3.9	12.3	1.2
			57	10230	63300	191000	386000	44200	157000	28700	7350	18300	1570	2520	142	123	4.5	9.1	1.9
			58	9220	57400	176000	350000	39900	129000	25500	6540	16900	1480	2450	126	106	4.6	14.2	1.3
			59	7760	63900	202000	395000	45000	146000	27000	6980	17000	1570	2600	128	121	4.5	18.0	1.4
			60	7460	54700	188000	322000	41100	136400	26800	6840	17100	1450	2270	117	88	4.6	8.8	1.0
		M3 matrix	14	11830	53600	176000	364000	39500	143000	29900	5670	19400	1640	3820	261	332	24.4	101.0	10.3
			15	11110	54000	174000	363000	36500	135000	25700	5670	14300	1260	3510	348	478	35.5	87.0	8.0
			17	12070	52300	200000	382000	43800	155000	32100	6320	17200	1220	2970	240	320	21.3	75.0	9.1
			18	10580	49500	156000	345000	36500	103900	26000	5360	14600	1130	2920	269	327	28.3	90.0	13.4
			20	15200	43700	177000	340000	46200	161000	26500	6510	14300	1120	1850	158	223	13.6	44.6	4.8
			37	8870	62400	187000	375000	39500	141000	27800	6340	19500	1540	2720	137	140	9.6	33.0	4.1
			38	9650	50200	179000	376000	37300	134000	29100	6720	16900	1291	2210	105	107	5.9	18.2	3.4
			39	6940	54500	183000	383000	40200	150000	28200	6840	19100	1470	2740	141	125	4.3	13.5	0.9
			40	8000	58100	182000	371000	46700	163000	32800	7340	20100	1760	2750	152	110	4.3	13.3	1.6
			41	7600	48800	186000	378000	44200	163000	30300	7470	18700	1520	2890	135	118	3.3	13.9	1.3
			42	11810	57500	165800	364000	40800	149000	27300	5590	16600	1550	4030	359	407	37.5	124.0	18.1
			43	5110	49500	164000	324000	38500	131000	26500	4660	18200	1920	5320	588	1050	141.0	579.0	91.0
			44	8930	53300	203000	372000	42400	142000	29100	6610	17810	1640	2930	159	113	4.4	13.7	1.3
			61	8090	49200	161000	353000	39100	160000	27200	5020	17900	1750	4290	452	643	77.8	294.0	45.8

Table S.II.4 (continued)

Sample	Analysis from thin-section or mount	Analysis location in the thin-section or in the monazite	Number of analysis	U ppm	Th ppm	La ppm	Ce ppm	Pr ppm	Nd ppm	Sm ppm	Eu ppm	Gd ppm	Tb ppm	Dy ppm	Ho ppm	Er ppm	Tm ppm	Yb ppm	Lu ppm
MJ58G	Mount	Monazite core	4	10720	64300	184000	342000	40800	150000	26700	6590	16300	1380	2490	139	126	4.3	18.3	2.0
			5	10600	67500	176000	358000	46400	134000	25100	6170	16300	1330	2460	133	121	4.1	17.3	1.5
			6	11220	71900	194000	357000	43700	151000	27800	6890	17400	1530	2540	149	130	4.6	16.5	2.3
			7	10600	66800	196000	353000	44200	144000	27700	6700	16800	1370	2670	130	125	4.9	15.5	1.8
			8	9360	52000	180000	391000	44100	144000	30400	6820	17300	1524	2590	127	121	5.1	15.2	1.9
			9	12300	80000	225000	390000	47300	153000	31300	7570	18700	1460	3070	162	142	6.0	15.7	1.9
			10	11540	74800	185000	388000	43200	149000	27100	6880	17200	1530	2640	158	120	5.6	16.3	2.6
			11	12600	82400	194000	394000	45600	170000	27700	6730	18400	1660	3050	159	125	6.5	13.2	2.2
			12	10630	69100	179000	361000	40800	150000	25400	6780	18100	1370	2570	136	123	4.5	14.3	1.9
			13	9440	59200	156000	330000	37500	131000	24900	6210	15900	1270	2260	135	108	4.2	15.9	1.3
			14	9400	57900	176000	382000	39400	140000	28100	6650	16600	1310	2170	124	100	4.5	10.0	1.5
			17	11050	58200	179000	427000	45300	146000	31200	7500	19600	1600	2810	189	187	9.1	23.2	2.3
			18	11500	56100	214000	360000	43500	149000	28700	7230	16100	1065	1430	70	76	4.2	14.9	1.6
			19	13300	48400	164000	349000	40900	159000	29100	7110	19000	1470	3090	220	187	9.5	31.5	3.9
			20	11200	51600	195000	381000	45400	169000	31900	7200	20000	1670	3600	227	206	12.2	40.0	5.4
			21	9300	50400	194000	348000	45100	161000	27400	7000	19700	1800	3420	217	216	9.4	26.4	3.4
			22	8120	54900	198000	386000	45200	160000	31600	7400	19900	1670	2850	176	156	5.1	15.8	1.4
			23	8830	55100	187000	368000	45000	166000	31600	7350	20700	1700	3630	234	196	10.2	25.9	2.6
			24	10050	58100	202000	371000	47000	156000	29200	7380	18700	1760	3520	264	213	9.1	25.1	2.1
			25	8830	56900	195000	386000	45500	149000	29800	7410	20600	1420	2260	135	128	5.2	15.7	2.0
			26	10340	61400	192000	356000	45200	169000	29800	7460	19700	1430	1940	94	88	2.8	15.8	1.5
			27	7990	50000	179000	362000	45400	151000	27700	7110	17800	1590	2880	164	126	4.6	16.4	1.9
			28	8680	53800	179000	362000	46600	146000	30100	7640	19300	1530	3000	176	147	6.7	21.9	1.6
			29	9300	56500	176000	360000	42800	152000	27900	7220	17700	1580	2860	168	136	6.4	21.0	2.0
			30	9040	57200	192000	364000	47000	184000	31200	7760	19000	1210	1620	98	98	3.8	17.0	0.8
			31	11300	56800	195000	373000	46400	165000	30700	7200	20000	1290	1800	104	115	7.8	32.0	3.3
			32	10380	58000	172000	360000	38200	135000	28100	6000	18900	1280	2180	107	96	3.0	15.8	1.7
			33	12950	72000	173000	355000	43900	154000	32300	7610	19200	1500	2300	118	96	2.3	13.8	2.0
			34	12780	73800	171000	317000	40100	148000	26300	6920	18700	1370	2160	120	109	3.2	11.8	1.1
			35	13700	76400	183000	373000	43500	151000	30100	8600	19900	1720	2620	139	117	4.5	14.6	1.7
			36	13800	79500	172000	357000	42500	145000	28300	6890	18200	1610	2420	137	106	4.2	15.1	1.5
			37	12950	74200	199000	352000	39400	161000	30300	7440	18600	1500	2380	120	97	4.0	11.7	1.0
			39	14300	81900	199000	348000	44300	175000	31500	8030	19200	1580	2450	120	99	3.6	13.7	1.5
			40	9700	58600	159000	342000	42700	147000	25000	6890	18200	1460	2930	188	189	11.2	26.8	2.7
			41	11200	62500	190000	382000	43200	158000	29100	7070	19400	1840	3770	272	274	14.5	36.5	2.6
			43	8720	55500	157000	341000	39400	133000	23300	6130	15610	1320	2490	174	173	9.2	18.1	1.7
			44	8460	42700	175000	345000	40500	135000	27000	7000	19200	1820	3800	255	237	13.4	31.7	2.1
			45	9690	47700	185000	371000	45600	166000	29600	7790	22400	1950	4070	251	217	12.7	25.2	2.5
			46	8690	42900	219000	387000	46600	154000	30500	7650	22900	1920	3840	287	219	11.7	33.2	2.6
			47	8360	38600	195000	370000	40300	151000	29000	7030	21000	1910	3880	263	250	12.2	31.2	3.3
			64	9050	45400	182000	369000	42900	150000	28700	7120	18100	1630	3570	275	271	14.1	28.7	1.2
			65	9070	43900	185000	391000	43100	158000	31200	7430	19400	1700	4050	295	275	14.6	30.9	1.6
			66	9570	50600	187000	421000	45000	166000	30500	7330	19000	1560	3070	207	185	7.9	21.4	2.0
			67	12700	74900	172000	384000	43400	141000	32800	6910	19300	1690	4440	321	303	13.3	28.6	2.0
			68	11220	59300	162000	395000	42700	151000	28800	6710	19300	1710	3550	268	240	11.9	25.8	2.2
			69	12320	63300	193000	343000	43800	148000	29100	7470	18600	1920	4230	265	269	12.6	20.7	2.6
			70	10300	52300	189000	343000	41400	146000	27100	6640	17400	1670	3400	226	217	10.8	26.3	2.3
			71	10880	61800	181000	362000	41000	153000	27000	6660	19100	1580	3380	199	201	8.8	19.1	1.3
			73	7060	50500	167000	356000	40200	148000	27900	6380	18200	1590	2860	192	157	7.8	18.6	1.7
			74	9530	56800	187000	366000	38900	144000	27600	6430	16100	1410	2300	123	124	6.2	17.8	1.0
			75	9770	59900	193000	311000	39500	155000	29600	6880	19300	1570	2790	154	159	7.2	21.9	1.5
			76	10160	66600	187000	338000	43100	162000	29100	6830	20200	1440	2580	156	142	7.2	15.8	1.6
			77	12000	60500	187000	341000	39100	161000	31200	7340	19700	1640	2830	191	186	7.1	28.2	2.3
			78	12880	67900	194000	342000	40700	139000	28300	6680	19100	1710	3000	206	207	9.6	27.7	2.1
			79	8540	63000	187000	355000	41700	139000	28200	7170	17800	1930	3170	200	162	6.9	24.2	2.4
		Monazite rim	1	7080	41500	181000	368000	42200	152000	28000	7300	17200	1140	1950	117	111	4.6	17.8	0.8
			2	6960	42700	190000	391000	45400	147000	29300	6480	16200	957	1400	75	73	2.8	10.4	2.4
			3	8970	47700	192000	369000	44400	145000	27800	6400	16800	1380	2540	171	147	5.4	17.2	2.1
			15	8150	55200	203000	395000	43600	147000	25800	6910	16300	844	710	27	39	1.6	9.5	0.7
			16	8590	55000	186000	391000	40400	142000	26200	6330	14100	730	661	24	38	0.8	9.2	1.3
			48	9200	67400	182000	363000	40000	135000	26400	6270	15500	860	736	23	37	1.3	3.7	0.8
			49	9020	57000	207000	387000	46500	167000	28400	7340	17300	823	761	23	45	0.5	10.0	0.5
			50	8040	49900	199000	382000	41800	168000	28700	6670	14800	832	700	22	37	1.4	10.6	1.1
			51	8840	55300	169000	359000	41700	137300	28200	6710	14800	708	718	23	35	0.8	4.3	0.9
			52	10850	72200	196000	390000	42700	156000	27800	7310	17800	952	1030	35	42	0.9	10.6	0.7
			53	7800	51600	184000	376000	43700	145000	28200	7150	16300	808	653	16	39	0.7	6.4	1.0
			54	9220	61700	182000	388000	40700	148700	28300	6840	14600	898	866	27	37	1.1	7.9	0.8
			56	9900	82300	185000	364000	40400	146000	25500	6250	14600	863	739	19	31	0.7	6.1	1.2
			57	10480	75900	175000	374000	42100	149000	25500	6710	14600	675	667	19	39	0.8	6.3	0.5
			58	9840	73500	186000	368000	38200	138000	26300	6450	14600	747	671	20	37	1.0	5.1	0.4
			59	7930	51300	165000	341000	40500	144000	27400	7130	15000	865	733	21	36	0.5	7.1	0.3
			60	7360	52500	178000	355000	40500	142000	25800	6460	15700	849	840	21	37	1.0	6.3	0.6
			61	11080	77500	180000	370000	36600	144000	26000	6610	15900	942	997	30	36	0.9	5.5	0.7
			62	10770	74000	178000	369000	38400	141000	29000	6820	15500	927	939	24	45	0.8	7.9	0.8
			72	7620	55400	202000	377000	47400	156000	31100	7700	19100	1820	3540	205	185	7.4	22.7	1.9

Table S.II.4 (continued)

Sample	Analysis from thin-section or mount	Analysis location in the thin-section or in the monazite	Number of analysis	U ppm	Th ppm	La ppm	Ce ppm	Pr ppm	Nd ppm	Sm ppm	Eu ppm	Gd ppm	Tb ppm	Dy ppm	Ho ppm	Er ppm	Tm ppm	Yb ppm	Lu ppm
MJ11C	Thin-section	Inc. g rim I	68	5630	22460	114000	212000	25000	99680	19300	3450	10300	860	1370	86	69	2.3	10.6	0.5
			69	4880	18350	121000	235000	26600	101100	18700	3760	11000	883	1580	88	64	4.0	9.7	0.4
			70	4000	14050	117000	231000	26000	99600	21000	3630	10700	860	1390	72	65	2.4	8.4	0.2
			71	4290	29000	88200	218000	27400	120000	32600	5880	21200	1750	2710	170	149	9.5	50.6	6.2
			72	3420	24450	100500	221000	27800	103000	29600	4940	19500	1610	2550	182	167	10.3	29.7	4.7
			73	5860	21160	104200	219000	27600	101000	18900	3310	12600	1130	2430	185	189	11.5	25.7	3.0
			75	4090	22120	113000	246000	28300	110000	19100	3330	11400	851	1240	73	63	1.8	10.4	1.1
			76	4248	25590	101500	222000	29300	114000	18200	3260	10200	742	1048	59	49	1.8	7.3	0.6
			77	4270	24270	105400	212000	27500	100100	18600	3130	9980	636	980	55	51	1.5	9.2	1.0
		Inc. g rim II	43	1078	30130	119000	253000	26100	96000	11820	1660	3940	152	316	34	100	12.1	62.0	13.3
			44	1886	35300	87800	213000	23000	86200	13400	1780	4100	152	289	37	111	13.8	64.1	8.4
			45	1180	28700	109500	251000	29400	98000	12200	1750	4180	156	338	56	131	13.8	44.8	4.3
			46	791	28780	115000	260000	27100	107000	10500	1550	3300	114	170	20	58	6.8	35.7	5.6
			47	812	30000	94000	233000	26300	102000	12700	1620	3820	141	213	35	77	8.1	38.1	3.7
			48	1477	32100	99000	191000	26300	89700	14500	2040	4250	153	245	33	75	9.8	42.0	4.2
			49	965	36000	99000	250000	23000	98000	13500	1820	4360	141	160	16	42	5.9	32.6	4.6
			52	1171	39690	96000	219000	23300	97000	13200	1850	3990	176	239	26	69	7.2	32.9	4.0
			53	1238	38500	92000	205000	23600	91900	13400	2020	4380	201	333	40	110	11.6	36.7	6.4
			54	2420	48200	92000	264000	24900	95000	14600	2050	4110	163	258	37	106	11.2	43.8	4.1
			56	1640	49440	84000	192000	24000	87500	14600	2060	4980	175	202	18	41	5.1	25.7	3.1
			57	1725	48490	99000	211000	25100	102000	15400	2120	5080	191	247	22	60	7.9	51.7	6.4
			58	1529	49000	94600	213000	22900	99800	16000	2140	5200	169	236	20	54	4.0	28.9	3.6
			59	1625	48900	90000	221000	22600	88000	13900	1870	4090	172	244	31	76	9.3	39.4	5.1
			60	1440	44500	105700	252000	26500	93000	15900	1620	4160	186	323	33	75	9.1	47.2	9.6
			61	1730	50500	89400	220000	25700	93000	13400	1830	4380	169	244	28	62	7.2	34.4	4.4
			62	1541	42100	106000	246000	29200	97000	15000	2050	4240	165	258	32	73	7.7	22.2	3.5
			63	1466	43420	107400	246000	26800	106000	16100	2070	4590	175	288	31	79	8.1	22.4	2.5
			64	1378	43950	84700	204000	22500	74500	11200	1230	3400	143	232	28	64	9.1	50.2	6.6
			65	1685	39800	91100	224000	25100	93200	14600	1780	4340	163	287	43	109	12.7	50.1	4.8
		M3 matrix	1	1020	9200	116000	263000	26400	116000	20700	3220	12100	1003	3170	316	520	57.7	214.0	25.6
			2	1500	10750	115000	255000	28700	111000	21100	3030	11400	718	2120	270	536	60.4	235.0	34.6
			3	1175	10690	119000	247000	31000	127000	22300	3000	11390	794	2100	265	488	57.3	217.0	34.8
			4	1990	18830	104000	203000	23100	100000	19600	2780	11300	810	2540	339	598	66.0	262.0	34.5
			5	1157	10710	95100	232000	25400	106000	20300	2510	9060	689	1730	260	474	59.5	209.0	30.9
			6	1730	11850	118000	227000	25200	109000	20600	2720	10300	707	2080	261	477	63.5	246.0	35.8
			7	3092	11600	97000	247000	24700	101000	22300	2840	10210	701	2190	285	608	71.4	305.0	40.2
			8	4610	14510	111000	263000	29500	110000	25400	3330	13800	1000	2760	372	735	109.0	471.0	67.7
			9	5050	14300	105000	263000	32000	113000	21400	2830	11200	826	2650	321	695	96.0	548.0	84.3
			10	2920	9580	120000	257000	26300	108000	21500	2770	10500	725	2290	294	643	82.0	399.0	52.0
			11	1279	9040	109000	253000	28700	111000	21900	2600	9300	675	2050	245	426	49.6	208.0	27.1
			12	2990	15300	111000	222000	26000	105000	23100	3130	11100	910	2720	406	650	85.0	341.0	56.3
			13	2186	16420	113000	246000	28100	108000	20100	2840	10650	710	2270	290	526	66.1	254.0	34.0
			14	3300	14430	109000	258000	27900	107000	20900	2770	10800	715	2230	245	495	58.9	278.0	39.2
			15	2202	12800	103000	281000	26100	113000	19600	2320	9600	721	1800	226	435	54.0	218.0	34.4
			16	2640	11670	111000	234000	28900	106000	20600	2610	9700	672	2100	271	517	66.0	257.0	36.6
			17	2249	13160	110000	210000	23900	89000	19000	2630	9370	632	1830	241	424	52.4	203.0	30.2
			18	5450	17280	115100	239000	25700	104000	22200	2820	11700	897	2530	376	758	113.0	524.0	79.0
			19	3608	37100	97000	215000	27000	103000	20400	2640	11800	997	3390	442	830	99.7	433.0	67.5
			20	3720	24840	115000	231000	27800	101000	18900	2980	11230	641	1500	162	301	31.4	120.0	15.9
			21	2180	30100	98000	215000	26200	99200	18300	2610	10600	758	2100	265	509	59.1	225.0	33.3
			22	1685	37500	107000	220000	24700	99790	17900	2350	10300	846	2470	299	599	69.1	269.0	39.9
			23	1795	17360	128000	225000	29100	113000	20500	2860	12200	946	2760	368	677	82.6	340.0	46.0
			24	1310	23100	95000	207000	24400	103000	17300	3120	12400	1090	3310	347	551	57.7	190.0	29.0
			25	3452	26890	109000	239000	29000	113000	19800	3050	11350	870	2500	316	636	109.0	511.0	80.0
			26	4320	18430	115200	219000	30200	106100	19400	2970	12100	924	2750	338	675	88.0	387.0	55.4
			27	3534	29300	102000	214000	27600	106000	19400	2570	9800	711	1890	259	474	59.8	272.0	35.5
			28	4240	24530	122700	244000	28900	108000	18800	2770	9150	516	907	90	146	12.9	59.5	7.3
			29	5370	26020	102400	242000	25800	108000	18300	2860	9580	570	1020	99	137	10.1	32.1	4.1
			30	3880	9500	117000	244000	27200	110000	20700	2780	12100	948	2850	362	600	76.9	293.0	42.2
			31	5466	10500	120000	230000	29800	110000	21000	2740	12700	886	2780	315	557	65.0	259.0	36.5
			32	3470	9560	112000	237000	29100	107000	19900	2470	10860	865	2620	302	560	54.5	221.0	28.9
			33	6970	17710	108000	227000	25100	108000	18500	2630	11700	1110	3520	491	854	131.0	600.0	100.0
			34	7130	17890	121000	241000	29100	117000	23500	3190	13700	1320	4340	623	1071	153.0	630.0	94.0
			35	2682	16710	123000	281000	31900	127000	19200	2360	10100	661	1930	215	417	45.6	202.0	26.3
			36	3481	12770	110200	233000	26300	99000	17200	2360	9400	710	1890	221	440	50.0	232.0	33.0
			37	5020	20350	110000	239000	25800	107000	18900	2840	11600	798	2510	357	687	86.0	431.0	59.7
			38	1630	7900	111000	274000	28300	104000	20500	2780	11400	786	1890	248	483	51.0	242.0	30.3
			39	5530	14380	114000	236000	26700	105000	19100	2510	10900	738	2300	321	602	76.6	332.0	49.5
			40	1913	9310	121000	238000	29100	113000	18400	2670	10300	829	2070	273	456	54.2	205.0	28.3
			41	1843	9010	126000	266000	28400	113000	18900	2800	10300	709	2140	236	464	63.4	239.0	31.1
			42	5400	15130	113000	257000	31300	103900	22000	3000	12300	894	2800	371	722	107.0	478.0	68.1

Table S.II.4 (continued)

Sample	Analysis from thin-section or mount	Analysis location in the thin-section or in the monazite	Number of analysis	U ppm	Th ppm	La ppm	Ce ppm	Pr ppm	Nd ppm	Sm ppm	Eu ppm	Gd ppm	Tb ppm	Dy ppm	Ho ppm	Er ppm	Tm ppm	Yb ppm	Lu ppm
MJ62B	Thin-section	Inc. g rim I	40	10290	48900	221000	405000	44700	166000	33700	7340	20900	2170	5420	400	337	13.5	26.9	2.7
			58	8570	49300	191000	347000	41200	155000	27400	6540	18600	1990	5320	422	339	13.5	32.1	2.0
			59	9460	50800	212000	395000	47000	150000	31700	7040	17700	1620	4270	245	225	9.7	19.6	1.1
			60	10700	59700	188000	368000	41800	146000	29400	5720	12000	676	1450	88	105	5.0	12.0	0.8
			61	11900	61500	204000	367000	43800	146000	26400	6480	11800	784	1750	103	108	6.3	14.8	1.6
			62	10720	61500	161000	363000	41500	155000	27200	6530	13300	1020	1880	123	125	4.9	11.7	2.0
			63	8550	51100	175000	378000	38900	150000	29600	6910	15700	1460	2950	185	147	7.0	16.8	1.3
			64	11000	62700	191000	427000	43400	155000	33000	7800	19600	2220	5510	415	335	14.3	24.7	2.9
		Inc. g rim II	9	9300	64900	192000	389000	40000	167000	30000	6760	17900	1590	3170	182	161	6.0	14.2	2.7
			13	9610	67700	190000	382000	41700	145000	30500	6640	17600	1380	2690	184	139	5.7	16.6	1.8
			18	8670	57600	165000	330000	40900	135000	26300	5950	15000	1330	2740	151	132	5.9	13.5	1.4
			23	10330	78100	171000	362000	40900	140000	30500	5900	14200	1130	1970	143	148	7.7	19.1	1.4
			28	9900	60900	161000	324000	39500	152000	27800	5570	13300	1020	1740	130	153	7.7	17.6	1.6
			33	10980	74600	193000	361000	40500	160000	30700	6860	15500	1110	2470	143	157	6.9	16.4	1.9
			34	8400	57800	173000	319000	41700	161000	30900	6580	18500	1930	4730	291	243	10.7	23.5	2.2
			35	8620	61000	171000	357000	37500	144000	29600	6500	18100	2160	5780	400	339	14.2	25.0	2.7
		M1-M2 matrix	1	8410	53400	187000	395000	44700	158000	31000	7490	20500	2650	8470	800	760	43.9	96.0	7.5
			2	10060	66200	165000	352000	36000	146000	31400	6300	18100	1930	4580	357	342	18.7	42.5	2.9
			3	11530	74900	197000	397000	46100	179000	33800	7470	19100	1840	4410	322	320	16.1	32.0	4.8
			4	9640	74900	193000	372000	43100	154500	32000	7040	18600	1880	4380	305	322	13.1	33.7	2.7
			5	9980	76300	166000	344000	41200	153000	28000	6210	17700	1680	3850	281	274	15.4	26.1	2.9
			6	10690	70800	197000	402000	46600	176000	36100	7100	21400	2050	5100	362	349	17.6	39.5	3.4
			7	10170	60600	184000	343000	43900	163000	30700	6690	20100	2270	5750	531	481	23.9	48.0	4.1
			8	19600	53600	183000	393000	40700	157000	29200	5730	15700	1190	2210	133	136	6.9	16.8	1.9
			10	8830	58700	181000	366000	44400	152000	30000	6570	17200	1850	4490	306	293	16.1	33.7	2.5
			11	11810	71900	180000	340000	38000	158000	27600	6450	15300	1095	2570	206	262	15.1	29.2	4.4
			12	10080	75000	182000	354000	39700	154000	31600	6710	18100	1660	3890	268	284	14.8	36.1	2.5
			41	11450	65900	171000	362000	39400	152000	29100	6870	20600	2420	8150	793	835	52.7	103.0	9.8
			42	11980	64000	173000	362000	40900	155000	29700	7730	21400	2430	8050	820	959	58.5	135.0	11.7
			43	12230	61900	170000	363000	40700	156000	28400	7140	21000	2480	7930	844	950	56.8	135.0	12.8
			44	12700	65200	169000	361000	43500	159000	32600	6980	21200	2310	7220	786	960	61.8	153.0	13.0
			45	12800	78000	180000	342000	37300	142000	30100	6340	20500	2570	7690	759	1060	59.1	125.0	9.4
			46	12800	66800	177000	361000	46400	159000	31200	7600	23100	2790	9070	890	886	58.9	119.0	12.7
			47	13230	71300	202000	381000	39900	158000	32100	7640	23400	2840	9960	940	961	58.0	112.0	9.8
			48	11020	49800	168000	335000	37500	155000	29800	5920	18300	2560	8800	808	830	46.7	81.0	7.9
			49	11100	59700	181000	338000	43400	149000	31700	7570	20700	2560	8900	806	789	41.9	81.0	5.6
			50	11700	67200	179000	389000	39400	164000	30800	7730	22900	2810	9900	843	814	48.6	84.3	6.9
			51	9630	47600	162000	319000	38400	147000	29100	6780	19800	2650	9400	810	731	43.9	69.8	6.9
			52	9970	52400	159000	341000	39300	149000	30600	6970	21500	2620	9100	788	717	45.3	87.0	8.0
			53	10690	52300	157500	328000	40800	144000	29000	6990	21000	2690	9060	858	859	48.5	100.0	8.5
			54	10910	50900	188000	401000	40200	165000	35000	8080	23300	2950	9560	936	835	45.0	78.0	7.3
			55	9760	45900	181000	361000	38100	150000	30300	7600	22100	2610	8770	751	710	36.1	74.0	7.0
			56	11000	49800	178000	342000	41700	148000	31800	7330	20400	2550	9200	750	870	42.3	75.0	7.1
			65	8490	55200	183000	394000	42200	139000	29800	6350	20300	2180	7280	598	585	32.3	60.9	5.6
			66	9730	59200	191000	364000	40000	173000	30600	7240	20000	1680	4060	314	303	16.9	36.3	3.2
			67	7790	48900	173000	336000	41700	160000	30200	6400	19200	2490	8430	678	747	39.3	70.0	6.0
			68	9580	66400	182000	375000	39600	144000	28500	6460	17700	1690	4520	315	321	15.7	35.6	2.2
			69	9760	75500	163000	344000	38300	145000	28700	6670	18100	1690	4980	309	257	13.6	25.8	2.7
			70	10460	67600	182000	383000	45700	146000	31300	6350	19900	1850	4190	290	277	14.5	34.2	3.2
			71	10440	66700	195000	377000	41600	149000	29100	6330	18700	1860	4860	388	423	23.2	42.2	4.1
		M3 matrix	14	10730	59900	181000	373000	40800	154000	32100	7530	21500	2610	9150	916	1180	68.2	136.0	12.9
			15	11330	62400	181000	345000	39200	144000	29600	7220	19200	2160	5990	574	668	39.4	110.0	7.3
			16	10010	56100	184000	340000	40400	146000	29000	7090	19400	2090	5330	501	546	36.1	76.0	6.7
			17	10840	67400	187000	350000	40400	132000	31400	7060	20900	2320	7200	669	751	48.3	96.3	8.7
			20	10410	62300	178000	382000	41100	161000	28900	6840	20200	2100	7290	739	945	63.6	156.0	15.4
			21	8550	45700	168000	325000	39200	146000	27300	5930	16300	1590	5330	654	780	54.1	111.0	11.5
			22	22600	50900	191000	345000	41200	144000	28200	5350	15580	1410	3460	334	410	30.0	104.0	12.4
			24	9070	66400	188000	394000	43600	156000	32000	6840	25100	3210	11500	1230	1270	92.0	186.0	14.0
			25	8460	68600	158000	324000	39200	145000	30400	6650	21300	2760	11000	1026	1190	78.5	148.0	12.6
			26	10340	53400	178000	335000	40700	152000	30000	6570	20900	2390	8340	796	930	54.5	123.0	10.8
			27	9580	75000	176000	383000	40600	168000	31100	7380	22900	2950	10870	1120	1239	85.0	158.0	14.5
			29	9000	42400	179000	362000	39800	148000	29100	6320	19500	2530	7370	779	820	49.1	113.0	11.2
			30	9830	59000	170000	386000	39600	161000	32100	7220	21100	1870	5430	426	406	23.4	61.7	5.5
			31	10190	55100	170000	359000	42000	159000	29000	6340	16600	1370	3820	350	417	25.0	55.3	5.1
			32	9580	44200	177000	401000	43900	153000	32800	7230	21200	2430	7800	634	802	46.5	96.0	7.4

Table S.II.5: ^{40}Ar/^{39}Ar CO$_2$-laser step-heating analytical data of **phengite** populations from the **phyllite sample MJ69G**.

Step #	^{39}Ar$_K$ (V)	^{36}Ar$_{atm}$/^{39}Ar$_K$ (± 1σ)	^{37}Ar$_{Ca}$/^{39}Ar$_K$ (± 1σ)	^{38}Ar$_{Cl}$/^{39}Ar$_K$ (± 1σ)	% ^{40}Ar*	^{40}Ar*/^{39}Ar$_K$ (± 1σ)	Age (Ma) (± 1σ)
MJ69-G	**J = .2730E-02 ± .2926E-04**						
# 1	5,59E-06	2,06E-03 ± 4,55E-03	1,01E-01 ± 1,89E-01	-3,80E-04 ± 3,82E-03	98,9	52,83 ± 1,89	243,1 ± 8,1
# 2	7,60E-06	-1,25E-03 ± 3,21E-03	8,05E-02 ± 1,38E-01	1,75E-03 ± 2,97E-03	100,6	63,53 ± 1,32	288,6 ± 5,6
# 3	1,11E-05	-3,83E-03 ± 2,19E-03	-3,76E-02 ± 1,06E-01	-2,85E-03 ± 2,27E-03	101,5	77,14 ± 1,10	344,8 ± 4,5
# 4	2,11E-05	-1,05E-03 ± 1,25E-03	-3,38E-02 ± 5,30E-02	-7,15E-05 ± 1,53E-03	100,4	75,48 ± 0,60	338,1 ± 2,4
# 5	2,00E-05	-3,83E-04 ± 1,23E-03	-4,56E-02 ± 5,48E-02	-1,12E-03 ± 1,28E-03	100,1	77,41 ± 0,71	345,9 ± 2,9
# 6	1,01E-05	6,30E-04 ± 2,45E-03	3,60E-02 ± 1,03E-01	-6,62E-03 ± 2,30E-03	99,8	80,65 ± 1,19	359,0 ± 4,8
# 7	9,69E-06	-2,81E-03 ± 2,64E-03	-4,19E-02 ± 1,08E-01	-3,96E-03 ± 2,42E-03	101,1	77,80 ± 1,17	347,5 ± 4,7
# 8	1,26E-05	-4,29E-04 ± 1,99E-03	-2,90E-02 ± 8,74E-02	-2,23E-03 ± 1,95E-03	100,2	76,70 ± 1,06	343,0 ± 4,3
# 9	2,26E-05	3,16E-03 ± 1,07E-03	-1,77E-04 ± 4,77E-02	-3,03E-03 ± 1,15E-03	98,8	76,29 ± 0,69	341,3 ± 2,8
# 10	2,05E-05	4,40E-03 ± 1,29E-03	-3,24E-02 ± 5,05E-02	-2,36E-03 ± 1,47E-03	98,3	76,26 ± 0,89	341,2 ± 3,6
# 11	9,54E-06	1,62E-03 ± 2,65E-03	7,67E-02 ± 1,14E-01	-1,70E-04 ± 2,53E-03	99,4	78,47 ± 1,31	350,2 ± 5,3
# 12	7,26E-06	-5,82E-05 ± 3,55E-03	6,77E-02 ± 1,54E-01	1,32E-03 ± 3,58E-03	100,0	77,12 ± 1,48	344,7 ± 6,0
# 13	1,04E-05	1,21E-03 ± 2,42E-03	3,93E-02 ± 1,01E-01	-7,22E-04 ± 2,32E-03	99,5	75,83 ± 1,04	339,5 ± 4,2
# 14	1,37E-05	2,67E-03 ± 1,91E-03	-5,86E-02 ± 7,87E-02	-2,41E-03 ± 1,70E-03	99,0	75,54 ± 1,05	338,3 ± 4,3
# 15	1,23E-05	8,98E-03 ± 2,04E-03	2,33E-02 ± 8,62E-02	-8,23E-04 ± 2,05E-03	96,7	77,25 ± 1,14	345,3 ± 4,6
# 16	6,94E-06	7,29E-03 ± 3,69E-03	1,51E-01 ± 1,73E-01	1,15E-04 ± 3,32E-03	97,3	78,23 ± 1,81	349,2 ± 7,4
# 17	8,70E-06	5,40E-03 ± 3,12E-03	-4,99E-02 ± 1,33E-01	-4,46E-03 ± 2,79E-03	97,9	75,81 ± 1,35	339,4 ± 5,5
# 18	5,02E-06	8,45E-03 ± 4,98E-03	-2,23E-01 ± 2,36E-01	-2,01E-03 ± 5,11E-03	96,9	76,66 ± 2,41	342,9 ± 9,8
# 19	3,20E-06	2,39E-02 ± 8,13E-03	-3,14E-01 ± 3,38E-01	-5,81E-03 ± 7,09E-03	92,1	81,56 ± 3,08	362,7 ± 12
# 20	2,33E-06	2,85E-02 ± 1,07E-02	-2,18E-01 ± 5,03E-01	-9,87E-03 ± 9,55E-03	89,6	72,34 ± 4,30	325,2 ± 18
# 21	1,61E-06	2,38E-02 ± 1,52E-02	-1,04E+00 ± 6,62E-01	-1,33E-02 ± 1,35E-02	91,2	73,24 ± 5,83	328,9 ± 24
# 22	2,59E-06	8,00E-03 ± 9,76E-03	-1,90E-01 ± 4,46E-01	-2,90E-03 ± 8,77E-03	96,8	70,62 ± 3,79	318,1 ± 16
# 23	2,08E-06	4,09E-02 ± 1,28E-02	-5,10E-01 ± 5,73E-01	-7,50E-03 ± 1,16E-02	84,4	65,46 ± 5,00	296,6 ± 21
# 24	2,52E-06	7,83E-02 ± 1,11E-02	-6,02E-01 ± 4,31E-01	-5,55E-03 ± 1,01E-02	74,0	65,77 ± 4,17	297,9 ± 17
Total	2,29E-04	3,77E-03 ± 5,44E-04	-3,31E-02 ± 2,36E-02	-2,12E-03 ± 5,27E-04	98,6	75,52 ± 0,26	338,2 ± 3,5
Weighted Mean Age (integrated over steps marked in blue)			*MSWD/(N-1) = 1,55*				**343,1 ± 1,0**

Table S.II.6: First measure: ^{40}Ar/^{39}Ar CO$_2$-laser step-heating analytical data of **phengite** populations from the **phyllite sample MJ52F**

Step #	^{39}Ar$_K$ (V)	^{36}Ar$_{atm}$/^{39}Ar$_K$ (± 1σ)	^{37}Ar$_{Ca}$/^{39}Ar$_K$ (± 1σ)	^{38}Ar$_{Cl}$/^{39}Ar$_K$ (± 1σ)	% ^{40}Ar*	^{40}Ar*/^{39}Ar$_K$ (± 1σ)	Age (Ma) (± 1σ)
MJ52F	**J = .2737E-02 ± .2934E-04**	**N291.MS3**					
# 1	7,86E-08	5,87E-01 ± 3,96E-01	1,83E+01 ± 4,41E+01	-2,26E-01 ± 2,79E-01	-95,1	-84,57 ± 106,10	-475,0 ± 682
# 2	1,76E-06	2,31E-02 ± 1,30E-02	-1,38E+00 ± 1,83E+00	-4,83E-03 ± 1,18E-02	91,5	73,11 ± 4,93	329,1 ± 20
# 3	5,84E-06	4,66E-03 ± 3,47E-03	-4,87E-01 ± 5,35E-01	-2,30E-03 ± 3,59E-03	97,9	65,05 ± 1,57	295,6 ± 6,6
# 4	9,11E-06	-4,84E-05 ± 2,26E-03	-1,74E-01 ± 3,45E-01	2,51E-03 ± 2,35E-03	100,0	55,60 ± 1,16	255,6 ± 5,0
# 5	3,24E-05	-3,66E-05 ± 6,31E-04	-8,06E-03 ± 1,09E-01	5,64E-04 ± 9,66E-04	100,0	62,12 ± 0,40	283,3 ± 1,7
# 6	3,13E-05	2,28E-04 ± 6,52E-04	-5,34E-02 ± 1,07E-01	4,84E-04 ± 1,05E-03	99,9	68,04 ± 0,64	308,1 ± 2,7
# 7	2,48E-05	1,10E-03 ± 8,93E-04	2,55E-02 ± 1,36E-01	9,13E-04 ± 1,07E-03	99,5	70,48 ± 0,64	318,2 ± 2,7
# 8	1,75E-05	-1,25E-03 ± 1,18E-03	4,63E-02 ± 1,94E-01	1,70E-03 ± 1,62E-03	100,5	73,82 ± 0,85	332,0 ± 3,5
# 9	2,21E-05	-7,83E-04 ± 1,04E-03	-1,72E-01 ± 1,45E-01	8,58E-04 ± 1,02E-03	100,3	74,37 ± 0,92	334,3 ± 3,8
# 10	1,64E-05	-1,60E-04 ± 1,26E-03	1,77E-01 ± 2,05E-01	-2,06E-03 ± 1,29E-03	100,1	75,54 ± 0,78	339,0 ± 3,2
# 11	1,52E-05	-1,59E-03 ± 1,41E-03	5,55E-02 ± 2,17E-01	-7,14E-05 ± 1,47E-03	100,6	75,53 ± 0,72	339,0 ± 2,9
# 12	5,75E-05	3,30E-04 ± 3,87E-04	1,78E-02 ± 5,78E-02	-5,57E-04 ± 6,34E-04	99,9	76,21 ± 0,36	341,8 ± 1,5
# 13	2,08E-05	1,89E-04 ± 1,04E-03	2,99E-03 ± 1,55E-01	-5,71E-05 ± 1,31E-03	99,9	78,19 ± 0,69	349,9 ± 2,8
# 14	3,17E-05	3,64E-04 ± 6,64E-04	-1,76E-02 ± 1,10E-01	-1,15E-03 ± 8,94E-04	99,9	77,49 ± 0,54	347,0 ± 2,2
# 15	3,03E-05	5,85E-04 ± 7,08E-04	-3,95E-02 ± 1,12E-01	-2,11E-03 ± 9,31E-04	99,8	76,56 ± 0,56	343,2 ± 2,3
# 16	1,79E-05	-1,13E-03 ± 1,20E-03	-6,95E-02 ± 1,79E-01	-1,52E-03 ± 1,22E-03	100,4	78,78 ± 0,86	352,3 ± 3,5
# 17	1,52E-05	6,55E-04 ± 1,41E-03	-1,39E-01 ± 2,22E-01	-9,76E-04 ± 1,82E-03	99,8	76,04 ± 0,64	341,1 ± 2,6
# 18	2,59E-05	6,77E-04 ± 7,99E-04	6,42E-02 ± 1,29E-01	-7,59E-04 ± 1,23E-03	99,7	75,78 ± 0,77	340,0 ± 3,1
# 19	2,24E-05	-3,11E-04 ± 9,10E-04	2,58E-01 ± 1,49E-01	-6,70E-04 ± 1,39E-03	100,1	75,70 ± 0,54	339,7 ± 2,2
# 20	2,10E-05	1,27E-04 ± 1,05E-03	9,29E-02 ± 1,66E-01	-2,24E-03 ± 1,43E-03	100,0	76,35 ± 0,80	342,4 ± 3,2
# 21	2,41E-05	-4,83E-04 ± 8,61E-04	8,00E-02 ± 1,37E-01	-1,12E-03 ± 9,64E-04	100,2	76,14 ± 0,64	341,5 ± 2,6
# 22	1,41E-05	1,11E-03 ± 1,51E-03	2,15E-01 ± 2,58E-01	-3,69E-03 ± 1,76E-03	99,6	74,28 ± 0,85	333,9 ± 3,5
# 23	1,77E-05	1,82E-03 ± 1,20E-03	2,50E-02 ± 1,91E-01	-1,42E-03 ± 1,57E-03	99,3	74,86 ± 0,82	336,3 ± 3,4
# 24	1,32E-05	-6,67E-05 ± 1,59E-03	2,96E-02 ± 2,66E-01	-6,71E-04 ± 1,82E-03	100,0	75,48 ± 0,88	338,8 ± 3,6
# 25	1,97E-05	2,40E-03 ± 1,18E-03	1,66E-01 ± 1,82E-01	3,77E-04 ± 1,25E-03	99,1	75,95 ± 0,86	340,7 ± 3,5
# 26	1,76E-05	2,58E-03 ± 1,16E-03	1,11E-01 ± 1,95E-01	-1,89E-04 ± 1,23E-03	99,0	75,00 ± 0,92	336,8 ± 3,8
# 27	7,00E-06	1,64E-02 ± 3,04E-03	1,50E-01 ± 4,87E-01	-4,03E-03 ± 3,05E-03	94,2	78,59 ± 1,42	351,5 ± 5,8
# 28	5,03E-06	-2,08E-03 ± 4,03E-03	2,32E-01 ± 6,53E-01	-3,83E-03 ± 4,14E-03	100,8	78,45 ± 1,91	350,9 ± 7,8
# 29	3,22E-06	8,61E-03 ± 6,34E-03	2,01E-01 ± 1,04E+00	-3,57E-03 ± 7,33E-03	96,6	71,50 ± 2,69	322,4 ± 11
# 30	1,14E-06	2,59E-02 ± 1,90E-02	-8,69E-01 ± 2,93E+00	-2,10E-02 ± 1,78E-02	89,2	63,31 ± 7,16	288,3 ± 30
Total	5,42E-04	7,86E-04 ± 2,15E-04	2,27E-02 ± 3,40E-02	-7,30E-04 ± 2,61E-04	99,7	73,99 ± 0,14	332,7 ± 3,3
Weighted Mean Age (integrated over steps marked in blue)			*MSWD/(N-1) = 1,11*				**340,0 ± 0,9**

Table S.II.7: Second measure: ^{40}Ar/^{39}Ar CO$_2$-laser step-heating analytical data of **phengite** populations from the **phyllite sample MJ52F**

Step #	^{39}Ar$_K$ (V)	^{36}Ar$_{atm}$/^{39}Ar$_K$ (± 1σ)			^{37}Ar$_{Ca}$/^{39}Ar$_K$ (± 1σ)			^{38}Ar$_{Cl}$/^{39}Ar$_K$ (± 1σ)			%^{40}Ar*	^{40}Ar*/^{39}Ar$_K$ (± 1σ)			Age (Ma) (± 1σ)		
MJ52F	**J = .2737E-02 ± .2934E-04**				**N273.MS3**												
# 1	7,46E-06	1,16E-02	±	4,02E-03	7,35E-02	±	8,65E-02	6,01E-03	±	3,00E-03	94,6	59,77	±	1,62	273,3	±	6,9
# 2	2,88E-06	-4,13E-03	±	9,50E-03	-9,99E-02	±	2,26E-01	1,11E-02	±	8,36E-03	102,5	49,88	±	3,46	230,9	±	15
# 3	2,07E-05	-9,07E-04	±	1,45E-03	-3,30E-02	±	3,10E-02	6,54E-04	±	1,19E-03	100,4	63,19	±	0,65	287,8	±	2,7
# 4	1,02E-05	-1,58E-03	±	2,82E-03	2,23E-02	±	6,90E-02	6,22E-04	±	2,14E-03	100,7	70,96	±	1,30	320,2	±	5,4
# 5	4,86E-05	3,10E-03	±	5,79E-04	-4,94E-03	±	1,35E-02	-1,23E-03	±	6,27E-04	98,8	73,59	±	0,54	331,1	±	2,2
# 6	1,73E-05	-1,79E-03	±	1,61E-03	3,18E-03	±	4,23E-02	-2,17E-04	±	1,40E-03	100,7	78,98	±	0,94	353,0	±	3,8
# 7	1,12E-05	-5,60E-03	±	2,47E-03	9,28E-02	±	6,47E-02	2,29E-03	±	1,84E-03	102,1	80,30	±	1,23	358,4	±	5,0
# 8	1,71E-05	-1,15E-03	±	1,65E-03	2,60E-03	±	4,00E-02	-2,14E-03	±	1,65E-03	100,4	76,30	±	1,07	342,1	±	4,4
# 9	3,08E-05	-6,51E-04	±	9,13E-04	3,18E-02	±	2,42E-02	1,77E-03	±	9,59E-04	100,3	76,22	±	0,60	341,8	±	2,5
# 10	6,77E-06	1,22E-03	±	4,19E-03	-7,80E-03	±	1,11E-01	-4,91E-03	±	3,25E-03	99,6	78,98	±	1,72	353,1	±	7,0
# 11	1,85E-05	7,09E-04	±	1,53E-03	-9,15E-03	±	3,53E-02	-2,57E-03	±	1,27E-03	99,7	76,76	±	0,79	344,0	±	3,2
# 12	7,73E-06	1,79E-03	±	3,65E-03	-2,91E-02	±	8,68E-02	-4,40E-03	±	3,10E-03	99,3	79,33	±	1,68	354,5	±	6,8
# 13	7,31E-06	7,85E-04	±	4,06E-03	-2,14E-02	±	9,24E-02	2,73E-03	±	3,41E-03	99,7	76,32	±	1,64	342,2	±	6,7
# 14	6,64E-06	2,21E-03	±	4,55E-03	-1,01E-01	±	1,01E-01	-3,16E-03	±	3,14E-03	99,1	75,40	±	2,08	338,5	±	8,5
# 15	1,22E-05	2,56E-03	±	2,36E-03	-4,07E-03	±	6,02E-02	3,09E-03	±	1,71E-03	99,0	76,19	±	0,98	341,7	±	4,0
# 16	2,80E-06	8,63E-03	±	6,74E-03	1,37E-01	±	2,47E-01	7,45E-03	±	7,08E-03	96,9	79,63	±	2,96	355,7	±	12
# 17	2,59E-06	1,53E-03	±	6,70E-03	-1,07E-02	±	2,85E-01	-1,89E-03	±	8,70E-03	99,4	80,81	±	3,03	360,5	±	12
# 18	2,76E-06	1,07E-02	±	6,71E-03	1,13E-01	±	2,33E-01	2,00E-03	±	8,58E-03	96,1	78,10	±	3,13	349,5	±	13
# 19	7,41E-06	4,52E-03	±	2,41E-03	1,29E-01	±	1,03E-01	-1,24E-04	±	2,84E-03	98,3	77,70	±	1,36	347,9	±	5,5
# 20	1,02E-05	1,04E-02	±	1,80E-03	2,80E-02	±	7,13E-02	-3,24E-04	±	2,30E-03	96,3	80,13	±	1,49	357,7	±	6,0
# 21	3,82E-06	6,73E-03	±	4,83E-03	7,53E-02	±	1,84E-01	-7,23E-03	±	5,23E-03	97,5	78,02	±	2,74	349,2	±	11
# 22	1,47E-05	4,10E-03	±	1,19E-03	-1,78E-02	±	4,78E-02	-4,77E-03	±	1,54E-03	98,4	74,40	±	1,05	334,4	±	4,3
# 23	1,15E-06	2,08E-02	±	1,51E-02	1,16E-01	±	6,06E-01	3,54E-03	±	1,88E-02	92,5	75,48	±	5,94	338,8	±	24
# 24	5,93E-06	6,85E-03	±	2,97E-03	-1,06E-01	±	1,16E-01	-4,62E-03	±	3,55E-03	97,3	74,21	±	1,44	333,6	±	5,9
# 25	6,96E-07	5,10E-02	±	2,59E-02	4,23E-01	±	9,95E-01	-1,02E-02	±	2,75E-02	81,0	64,17	±	9,09	291,9	±	38
# 26	2,45E-06	8,95E-03	±	7,23E-03	1,75E-02	±	2,96E-01	-5,15E-04	±	8,85E-03	96,2	66,53	±	3,15	301,8	±	13
# 27	1,69E-06	1,52E-02	±	1,18E-02	-1,16E-01	±	3,95E-01	-1,22E-03	±	1,39E-02	94,1	71,95	±	4,77	324,3	±	20
# 28	1,22E-06	6,66E-02	±	1,83E-02	-1,18E-01	±	5,83E-01	-1,36E-02	±	1,61E-02	74,6	57,63	±	6,28	264,2	±	27
Total	2,83E-04	2,32E-03	±	4,57E-04	6,33E-03	±	1,30E-02	-4,66E-04	±	4,32E-04	99,1	74,37	±	0,24	334,2	±	3,4
Weighted Mean Age (integrated over steps marked in blue)					*MSWD/(N-1) = 1,41*										**343,4**	**±**	**1,3**

Table S.II.8: ^{40}Ar/^{39}Ar CO$_2$-laser **step-heating** analytical data of **phengite** populations from the **phyllite sample MJ22B**

Step #	^{39}Ar$_K$ (V)	^{36}Ar$_{atm}$/^{39}Ar$_K$ (± 1σ)			^{37}Ar$_{Ca}$/^{39}Ar$_K$ (± 1σ)			^{38}Ar$_{Cl}$/^{39}Ar$_K$ (± 1σ)			%^{40}Ar*	^{40}Ar*/^{39}Ar$_K$ (± 1σ)			Age (Ma) (± 1σ)		
MJ22-B	**J = .2744E-02 ± .2942E-04**																
# 1	5,61E-07	4,76E-01	±	6,32E-02	4,61E+00	±	6,65E+00	-9,60E-02	±	4,52E-02	21,6	38,78	±	14,71	182,4	±	66
# 2	2,03E-07	6,07E-02	±	1,21E-01	4,03E+00	±	1,84E+01	7,81E-03	±	1,19E-01	81,0	76,55	±	43,04	344,0	±	176
# 3	2,69E-07	-6,19E-02	±	8,37E-02	-6,37E-01	±	1,35E+01	-4,78E-02	±	8,48E-02	131,4	76,56	±	30,53	344,0	±	125
# 4	1,09E-06	1,80E-02	±	2,17E-02	-2,58E+00	±	3,28E+00	2,17E-02	±	2,23E-02	93,3	74,67	±	8,24	336,3	±	34
# 5	5,11E-06	6,79E-04	±	4,47E-03	-1,04E+00	±	7,53E-01	7,41E-04	±	4,56E-03	99,7	71,84	±	1,98	324,6	±	8,2
# 6	6,13E-06	-4,51E-03	±	3,69E-03	8,76E-02	±	6,07E-01	8,02E-04	±	4,17E-03	101,7	79,95	±	1,98	357,9	±	8,1
# 7	7,23E-06	-1,86E-04	±	3,08E-03	6,40E-01	±	5,10E-01	-2,28E-03	±	3,30E-03	100,1	77,28	±	1,45	347,0	±	5,9
# 8	6,31E-05	3,82E-04	±	3,47E-04	-1,51E-02	±	5,57E-02	1,73E-04	±	5,00E-04	99,9	73,70	±	0,44	332,3	±	1,8
# 9	7,86E-06	2,24E-03	±	2,92E-03	-2,47E-01	±	4,95E-01	5,58E-04	±	3,66E-03	99,2	77,28	±	1,45	347,0	±	5,9
# 10	1,11E-05	6,63E-04	±	2,16E-03	-2,39E-01	±	3,26E-01	-9,05E-04	±	2,23E-03	99,7	76,43	±	1,25	343,5	±	5,1
# 11	1,93E-05	1,87E-04	±	1,16E-03	-3,02E-01	±	1,85E-01	-2,33E-03	±	1,35E-03	99,9	74,40	±	0,79	335,2	±	3,2
# 12	1,34E-04	-6,36E-06	±	1,72E-04	2,15E-03	±	2,87E-02	-6,44E-04	±	4,18E-04	100,0	74,63	±	0,38	336,1	±	1,5
# 13	3,99E-05	1,12E-03	±	5,64E-04	-3,10E-03	±	8,88E-02	-9,77E-04	±	7,85E-04	99,6	72,82	±	0,38	328,7	±	1,6
# 14	4,51E-05	2,74E-04	±	5,04E-04	-2,36E-02	±	8,05E-02	-1,85E-03	±	6,44E-04	99,9	73,05	±	0,39	329,6	±	1,6
# 15	2,18E-05	2,32E-03	±	1,00E-03	1,51E-01	±	1,76E-01	-7,22E-04	±	1,43E-03	99,1	71,86	±	0,73	324,7	±	3,0
# 16	1,36E-05	1,12E-03	±	1,71E-03	-1,06E-02	±	2,89E-01	-3,31E-04	±	2,02E-03	99,6	74,72	±	0,86	336,5	±	3,5
# 17	1,24E-05	-9,89E-04	±	1,79E-03	-2,75E-01	±	3,00E-01	-3,18E-03	±	2,17E-03	100,4	74,03	±	0,99	333,7	±	4,1
# 18	3,38E-05	3,97E-04	±	6,56E-04	6,79E-02	±	1,17E-01	6,89E-04	±	9,86E-04	99,8	73,08	±	0,58	329,7	±	2,4
# 19	2,73E-05	1,03E-03	±	8,11E-04	1,60E-01	±	1,44E-01	-2,35E-03	±	9,90E-04	99,6	72,44	±	0,68	327,1	±	2,8
# 20	1,37E-05	-5,64E-04	±	1,70E-03	9,96E-02	±	2,90E-01	-2,84E-03	±	1,76E-03	100,2	73,64	±	0,89	332,1	±	3,7
# 21	7,47E-06	1,21E-03	±	3,07E-03	-3,20E-02	±	5,09E-01	-1,03E-03	±	2,95E-03	99,5	72,32	±	1,60	326,6	±	6,6
# 22	4,96E-06	-1,42E-03	±	4,36E-03	5,85E-01	±	7,88E-01	2,67E-03	±	5,12E-03	100,5	77,73	±	1,87	348,8	±	7,6
# 23	8,50E-06	3,00E-03	±	2,75E-03	1,77E-01	±	4,67E-01	7,90E-04	±	2,87E-03	98,9	76,48	±	1,25	343,7	±	5,1
# 24	9,52E-06	-2,04E-03	±	2,56E-03	-1,02E-01	±	3,90E-01	2,11E-03	±	3,15E-03	100,8	74,77	±	1,18	336,7	±	4,9
# 25	1,10E-05	-4,13E-04	±	2,06E-03	1,96E-01	±	3,55E-01	-2,59E-04	±	2,46E-03	100,2	74,02	±	1,17	333,6	±	4,8
# 26	3,72E-05	1,02E-04	±	6,11E-04	-1,38E-02	±	1,06E-01	6,61E-04	±	7,85E-04	100,0	73,97	±	0,38	333,4	±	1,6
# 27	2,14E-05	1,88E-03	±	1,04E-03	-1,79E-01	±	1,74E-01	-2,51E-03	±	1,18E-03	99,3	73,71	±	0,82	332,3	±	3,4
# 28	9,14E-06	6,11E-03	±	2,48E-03	-3,70E-01	±	4,13E-01	-2,37E-03	±	2,78E-03	97,6	74,24	±	1,13	334,5	±	4,6
# 29	3,24E-06	7,26E-03	±	7,09E-03	1,34E-01	±	1,17E+00	9,33E-04	±	7,50E-03	97,1	70,98	±	3,15	321,0	±	13
# 30	8,94E-07	6,82E-02	±	2,54E-02	-1,92E+00	±	4,14E+00	-2,59E-02	±	2,52E-02	71,3	50,12	±	9,31	232,5	±	41
Total	5,76E-04	1,11E-03	±	2,17E-04	-1,37E-02	±	3,58E-02	-8,29E-04	±	2,67E-04	99,6	73,91	±	0,15	333,2	±	3,3
Weighted Mean Age (integrated over steps marked in blue)					*MSWD/(N-1) = 2,74*										**332,5**	**±**	**0,6**

Table S.II.9: ***In-situ*** UV-laser 40Ar/39Ar analytical data of **phengite** grains from the **phyllite sample MJ22**.

Spot #	$^{39}Ar_K$ (V)	$^{36}Ar_{atm}/^{39}Ar_K$ (± 1σ)	$^{37}Ar_{Ca}/^{39}Ar_K$ (± 1σ)	$^{38}Ar_{Cl}/^{39}Ar_K$ (± 1σ)	%$^{40}Ar^*$	$^{40}Ar^*/^{39}Ar_K$ (± 1σ)	Age (Ma) (± 1σ)
MJ22: phyllite (phengite)		**J = 0.002720 ± 0.00002913**					
# 1	8,83E-06	3,37E-03 ± 2,56E-03	1,12E-01 ± 1,66E-01	-1,01E-03 ± 2,88E-03	98,7	76,85 ± 1,33	342,4 ± 5,4
# 2	1,41E-05	5,73E-04 ± 1,54E-03	-2,76E-02 ± 1,02E-01	-3,37E-03 ± 1,60E-03	99,8	73,77 ± 0,67	329,9 ± 2,8
# 3	2,49E-05	2,95E-03 ± 1,00E-03	3,63E-02 ± 6,17E-02	-2,75E-04 ± 1,08E-03	98,8	74,10 ± 0,52	331,2 ± 2,1
# 4	2,88E-05	2,16E-03 ± 7,77E-04	4,27E-02 ± 5,45E-02	4,05E-04 ± 9,37E-04	99,2	74,45 ± 0,50	332,6 ± 2,0
# 5	2,62E-05	4,50E-03 ± 8,65E-04	2,78E-02 ± 5,57E-02	-1,17E-03 ± 9,39E-04	98,2	74,04 ± 0,61	331,0 ± 2,5
# 6	2,80E-05	1,83E-03 ± 7,99E-04	5,85E-02 ± 5,38E-02	2,25E-04 ± 7,69E-04	99,3	74,48 ± 0,50	332,8 ± 2,1
# 7	2,84E-05	4,37E-03 ± 8,04E-04	2,19E-02 ± 5,64E-02	-1,38E-04 ± 9,15E-04	98,3	74,40 ± 0,50	332,5 ± 2,1
# 8	1,83E-08	-1,24E+01 ± 2,71E+01	9,74E+00 ± 8,24E+01	1,07E+00 ± 2,50E+00	-4,1	145 ± 485	598 ± 1708
# 9	1,33E-05	9,62E-03 ± 1,76E-03	6,31E-02 ± 1,12E-01	-6,06E-04 ± 1,57E-03	96,5	78,36 ± 0,88	348,6 ± 3,6
# 10	1,07E-05	9,14E-03 ± 2,09E-03	5,71E-02 ± 1,40E-01	4,57E-04 ± 1,75E-03	96,5	75,39 ± 0,99	336,5 ± 4,0
# 11	9,81E-06	2,02E-02 ± 2,53E-03	-9,70E-02 ± 1,48E-01	1,61E-04 ± 2,45E-03	92,6	74,63 ± 1,05	333,4 ± 4,3
# 12	1,32E-05	7,77E-03 ± 1,75E-03	1,72E-01 ± 1,40E-01	2,42E-03 ± 1,77E-03	97,1	77,34 ± 1,00	344,4 ± 4,0
# 13	2,02E-05	7,17E-03 ± 1,15E-03	-4,05E-02 ± 7,33E-02	3,81E-04 ± 1,18E-03	97,2	73,94 ± 0,66	330,6 ± 2,7
# 14	2,35E-05	3,96E-03 ± 9,59E-04	-7,10E-03 ± 6,67E-02	-4,91E-04 ± 1,15E-03	98,5	75,09 ± 0,60	335,3 ± 2,5
# 15	2,04E-05	5,47E-03 ± 1,14E-03	-7,33E-02 ± 7,11E-02	-1,73E-03 ± 1,28E-03	97,9	75,54 ± 0,69	337,1 ± 2,8
# 16	8,65E-06	5,14E-03 ± 2,72E-03	-8,85E-02 ± 1,69E-01	1,60E-03 ± 2,12E-03	98,1	76,98 ± 1,09	343,0 ± 4,4
# 17	1,05E-05	7,87E-03 ± 2,23E-03	-3,54E-02 ± 1,41E-01	1,61E-03 ± 2,21E-03	97,1	76,73 ± 0,85	342,0 ± 3,4
# 18	1,01E-05	7,60E-03 ± 2,33E-03	-4,42E-02 ± 1,50E-01	-2,06E-03 ± 1,94E-03	97,1	76,20 ± 1,11	339,8 ± 4,5
# 19	7,38E-06	1,46E-02 ± 2,99E-03	1,39E-01 ± 2,05E-01	-1,27E-03 ± 2,59E-03	94,8	78,03 ± 1,57	347,2 ± 6,4
# 20	9,63E-06	1,25E-02 ± 2,30E-03	-5,76E-02 ± 1,61E-01	-1,76E-03 ± 2,15E-03	95,4	76,22 ± 1,15	339,9 ± 4,7
# 21	6,93E-06	2,19E-02 ± 3,25E-03	-1,10E-01 ± 2,26E-01	-4,37E-03 ± 2,61E-03	92,2	76,27 ± 1,76	340,1 ± 7,1
# 22	6,92E-06	1,21E-02 ± 3,22E-03	9,23E-02 ± 2,18E-01	-2,54E-03 ± 2,67E-03	95,6	77,05 ± 1,40	343,3 ± 5,7
# 23	5,90E-06	1,88E-02 ± 3,65E-03	1,88E-01 ± 2,57E-01	-3,56E-05 ± 3,06E-03	93,5	79,50 ± 1,31	353,2 ± 5,3
# 24	1,06E-06	1,36E-01 ± 2,21E-02	2,32E-01 ± 1,47E+00	-3,34E-02 ± 1,60E-02	65,7	77,03 ± 7,38	343,2 ± 30
# 25	3,67E-06	2,67E-02 ± 5,99E-03	3,93E-01 ± 4,32E-01	-6,35E-03 ± 5,30E-03	90,8	77,62 ± 2,23	345,6 ± 9,0
# 26	3,66E-06	4,36E-02 ± 6,52E-03	3,29E-01 ± 4,34E-01	-9,19E-03 ± 5,44E-03	85,4	75,46 ± 2,27	336,8 ± 9,2
# 27	3,29E-06	4,33E-02 ± 6,82E-03	1,21E-01 ± 4,39E-01	-2,10E-03 ± 5,14E-03	85,0	72,28 ± 2,79	323,8 ± 11
# 28	5,68E-06	2,14E-02 ± 3,90E-03	3,55E-01 ± 2,93E-01	-5,24E-03 ± 3,15E-03	92,6	79,29 ± 1,68	352,3 ± 6,8
# 29	2,00E-05	1,13E-02 ± 1,11E-03	1,35E-02 ± 7,88E-02	-2,40E-03 ± 1,36E-03	95,8	75,52 ± 0,90	337,0 ± 3,7
# 30	1,78E-05	5,60E-03 ± 1,24E-03	4,54E-02 ± 9,12E-02	-1,62E-03 ± 1,15E-03	97,8	74,06 ± 0,70	331,1 ± 2,8
# 31	2,23E-05	4,02E-03 ± 9,91E-04	-1,18E-02 ± 6,45E-02	1,31E-04 ± 1,17E-03	98,5	75,78 ± 0,48	338,1 ± 2,0
# 32	2,50E-05	7,86E-03 ± 9,45E-04	-7,25E-03 ± 6,08E-02	-3,47E-04 ± 7,72E-04	97,1	76,28 ± 0,59	340,1 ± 2,4
Total	4,39E-04	7,23E-03 ± 2,93E-04	2,74E-02 ± 1,97E-02	-7,86E-04 ± 2,83E-04	97,2	75,40 ± 0,15	336,5 ± 3,3
Weighted Mean Age (integrated over steps marked in blue)			*MSWD/(N-1) = 2,67*				**335,8 ± 0,6**

Table S.II.10: $^{40}Ar/^{39}Ar$ CO_2-laser step-heating analytical data of **phengite** populations from the **phyllite sample MJ92C**

Step #	$^{39}Ar_{K}$ (V)	$^{36}Ar_{atm}/^{39}Ar_{K}$ (± 1σ)	$^{37}Ar_{Ca}/^{39}Ar_{K}$ (± 1σ)	$^{38}Ar_{Cl}/^{39}Ar_{K}$ (± 1σ)	% $^{40}Ar^{*}$	$^{40}Ar^{*}/^{39}Ar_{K}$ (± 1σ)	Age (Ma) (± 1σ)
MJ92-C	**J = .2726E-02 ± .2921E-04**						
# 1	3,66E-06	3,80E-03 ± 4,96E-03	-1,96E-01 ± 2,62E-01	8,21E-03 ± 6,50E-03	98,5	73,96 ± 2,12	331,4 ± 8,7
# 2	1,00E-05	-3,33E-03 ± 2,03E-03	-3,68E-02 ± 8,94E-02	3,51E-04 ± 2,57E-03	101,5	64,65 ± 0,87	292,9 ± 3,7
# 3	1,48E-05	-1,37E-03 ± 1,19E-03	-3,80E-03 ± 6,34E-02	-2,73E-03 ± 1,69E-03	100,8	52,26 ± 0,76	240,3 ± 3,3
# 4	1,88E-05	-1,57E-03 ± 9,88E-04	-3,21E-02 ± 4,96E-02	-2,81E-03 ± 1,34E-03	100,7	68,09 ± 0,67	307,2 ± 2,8
# 5	2,21E-05	-1,54E-03 ± 8,18E-04	-2,54E-02 ± 3,93E-02	-4,27E-04 ± 1,27E-03	100,6	73,90 ± 0,80	331,2 ± 3,3
# 6	1,84E-05	-1,65E-03 ± 9,08E-04	2,95E-02 ± 5,85E-02	-1,01E-03 ± 1,39E-03	100,7	72,79 ± 0,77	326,6 ± 3,2
# 7	6,36E-05	-4,90E-04 ± 2,55E-04	4,31E-03 ± 1,45E-02	-9,52E-04 ± 4,31E-04	100,2	72,97 ± 0,32	327,4 ± 1,3
# 8	3,03E-05	-2,88E-04 ± 5,74E-04	-5,97E-03 ± 3,09E-02	-2,90E-04 ± 9,51E-04	100,1	74,44 ± 0,55	333,4 ± 2,2
# 9	3,43E-05	6,32E-04 ± 5,32E-04	-2,53E-02 ± 2,73E-02	-2,11E-03 ± 7,56E-04	99,8	73,69 ± 0,44	330,3 ± 1,8
# 10	2,73E-05	2,52E-04 ± 7,09E-04	2,44E-02 ± 3,31E-02	2,24E-04 ± 1,19E-03	99,9	74,89 ± 0,72	335,2 ± 3,0
# 11	1,48E-05	-1,37E-03 ± 1,30E-03	-4,89E-02 ± 6,43E-02	-2,71E-04 ± 1,84E-03	100,5	75,64 ± 0,87	338,3 ± 3,5
# 12	1,53E-05	-1,81E-03 ± 1,19E-03	-3,99E-02 ± 5,88E-02	-2,08E-03 ± 1,81E-03	100,7	76,02 ± 1,04	339,8 ± 4,3
# 13	3,76E-05	-1,54E-03 ± 5,11E-04	-3,17E-02 ± 2,46E-02	-9,19E-04 ± 7,36E-04	100,6	72,62 ± 0,46	325,9 ± 1,9
# 14	1,03E-04	2,40E-05 ± 2,05E-04	-5,25E-03 ± 9,58E-03	-1,53E-03 ± 4,41E-04	100,0	73,39 ± 0,39	329,1 ± 1,6
# 15	3,76E-05	-4,62E-04 ± 6,02E-04	-1,94E-03 ± 2,46E-02	-1,32E-03 ± 1,02E-03	100,2	74,04 ± 0,58	331,7 ± 2,4
# 16	2,03E-05	-1,46E-03 ± 1,07E-03	-2,94E-02 ± 4,52E-02	-2,81E-03 ± 1,30E-03	100,6	74,44 ± 0,89	333,4 ± 3,6
# 17	1,52E-05	-2,12E-03 ± 1,46E-03	-6,20E-02 ± 5,88E-02	-3,33E-04 ± 1,62E-03	100,9	73,88 ± 0,86	331,1 ± 3,5
# 18	1,12E-05	6,97E-03 ± 2,04E-03	-4,61E-02 ± 8,72E-02	-1,28E-03 ± 2,09E-03	97,4	76,25 ± 0,99	340,7 ± 4,0
# 19	2,76E-05	-3,95E-04 ± 7,71E-04	-3,74E-02 ± 3,44E-02	-1,53E-03 ± 9,51E-04	100,2	75,11 ± 0,57	336,1 ± 2,3
# 20	2,93E-05	-5,11E-04 ± 7,71E-04	-8,15E-03 ± 3,23E-02	-1,36E-03 ± 9,04E-04	100,2	71,81 ± 0,54	322,6 ± 2,2
# 21	2,14E-05	5,40E-04 ± 1,02E-03	-2,32E-02 ± 4,33E-02	-1,37E-03 ± 1,25E-03	99,8	72,90 ± 0,59	327,0 ± 2,4
# 22	1,14E-05	-3,63E-03 ± 1,84E-03	-1,31E-01 ± 8,35E-02	-1,11E-03 ± 2,07E-03	101,4	77,22 ± 1,26	344,7 ± 5,1
# 23	1,42E-05	2,73E-04 ± 1,53E-03	-2,63E-02 ± 6,80E-02	-1,10E-04 ± 1,81E-03	99,9	73,61 ± 0,81	330,0 ± 3,3
# 24	1,86E-05	5,90E-04 ± 1,20E-03	2,75E-02 ± 5,23E-02	-1,61E-03 ± 1,38E-03	99,8	72,82 ± 0,69	326,7 ± 2,8
# 25	3,36E-05	6,29E-04 ± 6,29E-04	1,24E-02 ± 3,26E-02	-5,19E-04 ± 9,23E-04	99,7	72,31 ± 0,62	324,6 ± 2,5
# 26	4,68E-05	1,01E-03 ± 3,46E-04	-6,26E-03 ± 2,23E-02	2,47E-05 ± 6,36E-04	99,6	71,65 ± 0,35	321,9 ± 1,4
# 27	1,69E-05	-2,16E-03 ± 9,39E-04	-4,62E-02 ± 6,22E-02	-6,07E-04 ± 1,33E-03	100,9	71,92 ± 0,70	323,0 ± 2,9
# 28	7,73E-06	-2,03E-03 ± 2,01E-03	8,05E-02 ± 1,34E-01	-3,29E-03 ± 3,22E-03	100,8	75,15 ± 1,23	336,3 ± 5,0
# 29	8,89E-06	-1,26E-03 ± 1,72E-03	-1,29E-01 ± 1,16E-01	-3,06E-03 ± 2,91E-03	100,5	75,68 ± 0,98	338,4 ± 4,0
# 30	1,14E-05	-2,84E-03 ± 1,43E-03	6,99E-02 ± 1,06E-01	-1,14E-03 ± 2,37E-03	101,2	72,62 ± 0,78	325,9 ± 3,2
# 31	7,84E-06	-6,18E-03 ± 2,11E-03	-9,43E-02 ± 1,28E-01	-3,61E-03 ± 2,94E-03	102,5	75,13 ± 1,20	336,2 ± 4,9
# 32	9,84E-06	-1,49E-04 ± 1,61E-03	4,75E-03 ± 1,04E-01	3,55E-03 ± 2,32E-03	100,1	73,70 ± 0,90	330,3 ± 3,7
# 33	1,28E-05	-2,48E-03 ± 1,16E-03	9,76E-02 ± 8,25E-02	-4,10E-03 ± 1,83E-03	101,0	74,37 ± 0,97	333,1 ± 4,0
# 34	2,60E-05	-1,02E-04 ± 6,31E-04	-2,07E-02 ± 3,83E-02	-2,34E-04 ± 1,03E-03	100,0	72,08 ± 0,51	323,7 ± 2,1
# 35	1,88E-05	6,33E-04 ± 8,25E-04	2,34E-03 ± 5,38E-02	1,66E-03 ± 1,56E-03	99,8	74,24 ± 0,60	332,5 ± 2,4
# 36	1,25E-05	-7,75E-04 ± 1,23E-03	-5,80E-02 ± 7,96E-02	-2,28E-03 ± 1,97E-03	100,3	73,97 ± 0,66	331,4 ± 2,7
# 37	9,05E-06	-6,15E-04 ± 1,62E-03	-9,38E-02 ± 1,09E-01	-1,20E-03 ± 3,03E-03	100,2	75,61 ± 1,11	338,2 ± 4,5
# 38	3,21E-06	1,12E-02 ± 4,82E-03	-1,07E-01 ± 3,18E-01	-1,05E-03 ± 7,09E-03	95,3	66,16 ± 2,10	299,2 ± 8,8
Total	8,45E-04	-4,37E-04 ± 1,36E-04	-1,47E-02 ± 7,13E-03	-1,05E-03 ± 1,99E-04	100,2	72,93 ± 0,11	327,2 ± 3,2
Weighted Mean Age (integrated over steps marked in blue)			*MSWD/(N-1) = 3,88*				**329,0 ± 0,4**

Table S.II.11: ^{40}Ar/^{39}Ar CO$_2$-laser step-heating analytical data of **phengite** populations from the **phyllite sample S3-051**

Step #	^{39}Ar$_K$ (V)	^{36}Ar$_{atm}$/^{39}Ar$_K$ (± 1σ)	^{37}Ar$_{Ca}$/^{39}Ar$_K$ (± 1σ)	^{38}Ar$_{Cl}$/^{39}Ar$_K$ (± 1σ)	%^{40}Ar*	^{40}Ar*/^{39}Ar$_K$ (± 1σ)	Age (Ma) (± 1σ)
S3-051	**J = .2718E-02 ± .2911E-04**						
# 1	2,74E-06	1,72E-01 ± 9,27E-03	3,98E-01 ± 2,12E-01	-1,22E-02 ± 7,13E-03	31,1	22,95 ± 2,52	109,2 ± 11,6
# 2	3,56E-06	1,68E-02 ± 6,85E-03	1,39E-01 ± 1,66E-01	-2,62E-04 ± 5,73E-03	90,0	44,86 ± 2,24	207,6 ± 9,8
# 3	6,29E-06	5,81E-03 ± 3,44E-03	-5,93E-03 ± 9,96E-02	-1,54E-04 ± 3,28E-03	97,1	58,07 ± 1,42	264,4 ± 6,0
# 4	2,24E-05	1,79E-03 ± 9,68E-04	5,07E-03 ± 2,72E-02	4,05E-04 ± 9,36E-04	99,3	74,22 ± 0,77	331,5 ± 3,1
# 5	1,25E-05	-9,44E-05 ± 1,81E-03	6,88E-03 ± 4,81E-02	3,89E-06 ± 1,78E-03	100,0	74,41 ± 0,82	332,3 ± 3,3
# 6	8,58E-06	-3,82E-04 ± 2,84E-03	-4,46E-02 ± 6,56E-02	-2,33E-03 ± 2,65E-03	100,2	74,83 ± 1,33	334,0 ± 5,4
# 7	5,62E-05	5,07E-04 ± 4,31E-04	8,33E-03 ± 1,16E-02	-8,32E-04 ± 4,98E-04	99,8	73,89 ± 0,37	330,2 ± 1,5
# 8	3,08E-05	-5,93E-04 ± 7,11E-04	-9,13E-03 ± 1,95E-02	-1,11E-03 ± 7,89E-04	100,2	74,94 ± 0,72	334,4 ± 2,9
# 9	1,63E-05	-6,33E-04 ± 1,42E-03	-2,93E-02 ± 3,74E-02	8,97E-05 ± 1,54E-03	100,2	75,93 ± 0,85	338,5 ± 3,4
# 10	2,69E-05	-1,77E-04 ± 7,90E-04	-1,04E-02 ± 2,26E-02	-2,17E-03 ± 1,00E-03	100,1	73,27 ± 0,49	327,7 ± 2,0
# 11	1,31E-05	-4,04E-03 ± 1,60E-03	-2,51E-02 ± 4,70E-02	-5,34E-04 ± 1,51E-03	101,6	74,07 ± 1,12	330,9 ± 4,6
# 12	6,45E-05	-8,71E-04 ± 3,24E-04	7,68E-04 ± 9,56E-03	-1,22E-03 ± 4,68E-04	100,4	72,76 ± 0,48	325,6 ± 2,0
# 13	5,17E-05	-1,14E-04 ± 3,97E-04	2,80E-02 ± 1,40E-02	-6,81E-04 ± 5,96E-04	100,0	72,44 ± 0,45	324,2 ± 1,9
# 14	5,15E-05	-5,87E-04 ± 4,16E-04	6,47E-03 ± 1,17E-02	-1,48E-03 ± 4,87E-04	100,2	73,80 ± 0,48	329,8 ± 1,9
# 15	2,13E-05	-9,60E-04 ± 1,00E-03	-9,27E-03 ± 3,06E-02	-3,04E-04 ± 1,16E-03	100,4	73,13 ± 0,61	327,1 ± 2,5
# 16	2,29E-05	-7,76E-04 ± 9,44E-04	3,72E-02 ± 3,04E-02	-1,76E-03 ± 1,25E-03	100,3	73,89 ± 0,64	330,2 ± 2,6
# 17	1,27E-05	-1,01E-03 ± 1,62E-03	-3,22E-02 ± 4,71E-02	-2,73E-03 ± 1,88E-03	100,4	75,75 ± 0,82	337,8 ± 3,3
# 18	1,31E-05	5,13E-04 ± 1,77E-03	1,10E-02 ± 4,45E-02	-1,12E-03 ± 1,69E-03	99,8	70,59 ± 0,81	316,6 ± 3,3
# 19	2,24E-05	6,19E-04 ± 1,01E-03	-2,28E-02 ± 2,63E-02	-4,50E-04 ± 1,10E-03	99,8	72,36 ± 0,74	323,9 ± 3,0
# 20	2,49E-05	3,84E-06 ± 8,77E-04	-1,42E-02 ± 2,42E-02	-2,30E-03 ± 1,15E-03	100,0	73,56 ± 0,61	328,8 ± 2,5
# 21	1,50E-05	1,40E-03 ± 1,43E-03	3,77E-03 ± 4,22E-02	-1,43E-04 ± 1,59E-03	99,5	74,11 ± 0,68	331,1 ± 2,8
# 22	6,43E-06	2,26E-04 ± 3,45E-03	-5,98E-02 ± 8,93E-02	-7,14E-04 ± 3,03E-03	99,9	73,01 ± 1,54	326,6 ± 6,3
# 23	1,41E-05	4,28E-03 ± 1,50E-03	2,84E-02 ± 4,66E-02	-2,08E-03 ± 1,50E-03	98,3	71,77 ± 0,62	321,5 ± 2,5
# 24	7,38E-05	8,05E-04 ± 3,02E-04	-3,90E-03 ± 8,08E-03	-8,31E-04 ± 6,55E-04	99,7	73,57 ± 0,39	328,9 ± 1,6
# 25	2,94E-05	6,35E-03 ± 7,72E-04	-1,35E-02 ± 2,18E-02	-9,70E-04 ± 8,24E-04	97,5	71,89 ± 0,52	322,0 ± 2,1
# 26	2,30E-05	4,79E-03 ± 1,03E-03	-2,83E-03 ± 2,75E-02	1,35E-03 ± 1,06E-03	98,1	74,22 ± 0,74	331,5 ± 3,0
# 27	1,03E-05	3,44E-03 ± 2,15E-03	5,06E-02 ± 6,83E-02	-3,74E-03 ± 2,13E-03	98,7	74,57 ± 1,09	332,9 ± 4,4
# 28	1,28E-05	-7,41E-04 ± 1,76E-03	5,71E-02 ± 5,31E-02	6,76E-05 ± 1,88E-03	100,3	72,71 ± 1,00	325,4 ± 4,1
# 29	9,00E-06	1,04E-02 ± 2,75E-03	-8,26E-03 ± 6,52E-02	1,83E-03 ± 3,29E-03	96,0	74,47 ± 1,38	332,6 ± 5,6
# 30	1,12E-05	7,10E-04 ± 2,05E-03	-1,36E-02 ± 5,32E-02	-1,97E-03 ± 2,12E-03	99,7	73,97 ± 1,03	330,5 ± 4,2
# 31	1,44E-05	-8,52E-04 ± 1,61E-03	-4,01E-02 ± 4,10E-02	-2,70E-03 ± 1,48E-03	100,3	72,60 ± 1,07	324,9 ± 4,4
# 32	1,06E-05	-2,62E-03 ± 2,22E-03	3,75E-03 ± 5,96E-02	-1,36E-03 ± 1,91E-03	101,1	72,89 ± 1,09	326,1 ± 4,5
# 33	8,12E-06	-7,43E-04 ± 2,77E-03	-6,80E-02 ± 7,59E-02	-3,22E-03 ± 2,60E-03	100,3	69,17 ± 1,48	310,8 ± 6,1
# 34	4,57E-05	7,79E-04 ± 5,24E-04	8,83E-03 ± 1,35E-02	1,33E-03 ± 8,51E-04	99,7	72,17 ± 0,40	323,1 ± 1,6
# 35	3,00E-06	1,03E-02 ± 7,79E-03	5,63E-01 ± 2,57E-01	-4,69E-03 ± 6,43E-03	95,6	66,46 ± 3,53	299,6 ± 15
# 36	3,56E-06	9,66E-03 ± 6,78E-03	-4,54E-02 ± 1,97E-01	-6,30E-03 ± 5,64E-03	96,2	72,44 ± 3,09	324,2 ± 13
Total	7,75E-04	1,34E-03 ± 1,76E-04	4,10E-03 ± 4,85E-03	-9,53E-04 ± 1,96E-04	99,5	72,88 ± 0,12	326,0 ± 3,2
Weighted Mean Age (integrated over steps marked in blue)			*MSWD/(N-1) = 2,54*				**328,2 ± 0,5**

Table S.II.12: First measure: $^{40}Ar/^{39}Ar$ CO_2-laser step-heating analytical data of **phengite** populations from the **phyllite sample S3-180**

Step #	$^{39}Ar_K$ (V)	$^{36}Ar_{atm}/^{39}Ar_K$ (± 1σ)	$^{37}Ar_{Ca}/^{39}Ar_K$ (± 1σ)	$^{38}Ar_{Cl}/^{39}Ar_K$ (± 1σ)	% $^{40}Ar^*$	$^{40}Ar^*/^{39}Ar_K$ (± 1σ)	Age (Ma) (± 1σ)
S3-180	**J = .2714E-02 ± .2907E-04**		**N290.MS3**				
# 1	7,82E-07	1,26E-01 ± 3,11E-02	1,81E+00 ± 4,68E+00	-5,79E-04 ± 2,06E-02	35,0	20,01 ± 10,47	95,4 ± 49
# 2	2,17E-07	1,30E-01 ± 1,13E-01	-2,89E+00 ± 1,61E+01	-3,21E-02 ± 7,09E-02	-152,2	-23,20 ± 37,85	-117,3 ± 198
# 3	1,02E-06	3,85E-02 ± 2,36E-02	-1,21E-01 ± 3,76E+00	8,45E-03 ± 1,59E-02	78,1	40,51 ± 8,20	188,2 ± 36
# 4	6,15E-06	7,83E-03 ± 4,00E-03	-3,79E-01 ± 5,61E-01	2,53E-03 ± 2,96E-03	96,0	55,12 ± 1,50	251,5 ± 6,4
# 5	5,56E-06	8,73E-04 ± 4,27E-03	1,11E-01 ± 6,57E-01	-2,43E-04 ± 3,11E-03	99,6	67,23 ± 1,92	302,4 ± 7,9
# 6	5,70E-06	9,65E-03 ± 4,38E-03	-2,78E-01 ± 5,68E-01	-5,27E-03 ± 2,82E-03	96,1	70,32 ± 1,76	315,1 ± 7,2
# 7	2,05E-05	8,00E-04 ± 1,24E-03	-5,38E-02 ± 1,78E-01	-3,12E-04 ± 9,79E-04	99,7	73,38 ± 0,60	327,7 ± 2,4
# 8	1,10E-05	1,28E-03 ± 2,23E-03	-1,19E-02 ± 3,09E-01	-1,25E-03 ± 1,50E-03	99,5	75,56 ± 0,98	336,5 ± 4,0
# 9	1,06E-05	1,08E-03 ± 2,35E-03	8,08E-02 ± 3,25E-01	-1,53E-03 ± 1,88E-03	99,6	75,81 ± 1,22	337,6 ± 5,0
# 10	2,68E-05	2,20E-04 ± 9,14E-04	-1,23E-01 ± 1,27E-01	-5,25E-04 ± 9,14E-04	99,9	73,75 ± 0,67	329,2 ± 2,7
# 11	1,59E-05	5,44E-04 ± 1,49E-03	-1,47E-01 ± 2,07E-01	-4,97E-03 ± 1,32E-03	99,8	73,52 ± 0,86	328,2 ± 3,5
# 12	3,45E-05	1,78E-04 ± 7,12E-04	-1,29E-01 ± 1,02E-01	-2,79E-03 ± 7,82E-04	99,9	73,81 ± 0,52	329,4 ± 2,1
# 13	3,13E-05	-8,00E-04 ± 7,88E-04	-7,57E-02 ± 1,20E-01	6,09E-04 ± 6,96E-04	100,3	73,75 ± 0,57	329,2 ± 2,3
# 14	4,53E-05	7,74E-05 ± 5,33E-04	-1,29E-01 ± 7,16E-02	-2,22E-03 ± 5,77E-04	100,0	71,97 ± 0,35	321,9 ± 1,4
# 15	2,55E-05	-4,82E-04 ± 8,90E-04	1,50E-02 ± 1,43E-01	-2,18E-03 ± 6,98E-04	100,2	73,90 ± 0,68	329,8 ± 2,8
# 16	1,22E-05	1,53E-03 ± 1,81E-03	9,47E-02 ± 3,18E-01	-2,45E-03 ± 1,44E-03	99,4	72,95 ± 1,21	325,9 ± 4,9
# 17	8,17E-06	5,44E-03 ± 2,63E-03	3,71E-01 ± 4,37E-01	-2,07E-03 ± 1,99E-03	97,9	75,70 ± 1,67	337,1 ± 6,8
# 18	1,76E-05	3,08E-03 ± 1,31E-03	-1,41E-01 ± 1,96E-01	5,51E-05 ± 1,53E-03	98,8	73,93 ± 1,01	329,9 ± 4,1
# 19	4,49E-05	3,66E-04 ± 4,82E-04	-6,42E-02 ± 7,82E-02	-1,01E-03 ± 5,17E-04	99,9	71,54 ± 0,40	320,1 ± 1,7
# 20	3,65E-05	1,48E-03 ± 6,32E-04	-3,12E-02 ± 9,27E-02	-3,49E-04 ± 7,98E-04	99,4	73,45 ± 0,64	328,0 ± 2,6
# 21	2,82E-05	1,22E-03 ± 7,67E-04	9,10E-02 ± 1,21E-01	-9,49E-04 ± 9,32E-04	99,5	73,86 ± 0,69	329,6 ± 2,8
# 22	2,89E-05	-1,28E-04 ± 7,62E-04	-6,89E-02 ± 1,20E-01	-3,77E-05 ± 6,75E-04	100,1	72,97 ± 0,57	326,0 ± 2,3
# 23	1,21E-05	-1,24E-03 ± 1,95E-03	-1,27E-01 ± 2,91E-01	1,13E-03 ± 1,70E-03	100,5	75,31 ± 1,11	335,5 ± 4,5
# 24	7,19E-06	5,40E-03 ± 2,98E-03	-2,31E-01 ± 5,03E-01	6,31E-04 ± 2,68E-03	97,9	73,50 ± 1,58	328,2 ± 6,5
# 25	2,61E-05	1,12E-03 ± 8,61E-04	7,32E-02 ± 1,29E-01	-3,91E-04 ± 8,76E-04	99,6	72,55 ± 0,79	324,3 ± 3,2
# 26	2,26E-05	2,69E-04 ± 9,78E-04	4,74E-02 ± 1,49E-01	7,62E-05 ± 7,96E-04	99,9	71,38 ± 0,78	319,5 ± 3,2
# 27	1,32E-05	2,77E-04 ± 1,67E-03	-3,21E-01 ± 2,57E-01	-2,67E-03 ± 1,11E-03	99,9	71,97 ± 0,92	321,9 ± 3,8
# 28	8,80E-06	3,49E-04 ± 2,54E-03	-2,36E-01 ± 3,93E-01	-2,53E-03 ± 2,26E-03	99,9	73,58 ± 1,46	328,5 ± 5,9
# 29	1,72E-05	9,32E-04 ± 1,24E-03	5,55E-03 ± 2,03E-01	-3,72E-03 ± 1,04E-03	99,6	71,93 ± 0,92	321,7 ± 3,8
# 30	5,58E-05	2,95E-04 ± 4,10E-04	1,19E-02 ± 6,56E-02	-1,46E-03 ± 5,54E-04	99,9	72,58 ± 0,36	324,4 ± 1,5
# 31	2,46E-05	9,61E-04 ± 9,13E-04	1,65E-01 ± 1,42E-01	-5,95E-04 ± 1,01E-03	99,6	73,17 ± 0,67	326,8 ± 2,7
# 32	1,09E-05	-1,50E-03 ± 1,96E-03	-2,02E-02 ± 3,17E-01	-2,61E-03 ± 1,77E-03	100,6	72,16 ± 1,14	322,7 ± 4,7
# 33	2,24E-05	-4,27E-04 ± 1,07E-03	4,86E-02 ± 1,67E-01	-1,28E-03 ± 8,33E-04	100,2	72,42 ± 0,75	323,7 ± 3,1
# 34	3,52E-05	-5,83E-04 ± 6,17E-04	6,79E-02 ± 1,05E-01	-1,10E-03 ± 8,02E-04	100,2	73,51 ± 0,55	328,2 ± 2,3
# 35	4,52E-07	-1,31E-01 ± 5,29E-02	1,39E+00 ± 7,43E+00	2,77E-02 ± 3,32E-02	153,1	111,30 ± 23,15	476,4 ± 87
Total	6,74E-04	7,98E-04 ± 2,04E-04	-3,05E-02 ± 3,09E-02	-1,19E-03 ± 1,85E-04	99,7	72,75 ± 0,13	325,1 ± 3,2
Weighted Mean Age (integrated over steps marked in blue)			*MSWD/(N-1) = 1,20*				**325,7 ± 0,7**

Table S.II.13: Second measure: ^{40}Ar/^{39}Ar CO_2-laser step-heating analytical data of **phengite** populations from the **phyllite sample S3-180**

Step #	$^{39}Ar_K$ (V)	$^{36}Ar_{atm}/^{39}Ar_K$ (± 1σ)	$^{37}Ar_{Ca}/^{39}Ar_K$ (± 1σ)	$^{38}Ar_{Cl}/^{39}Ar_K$ (± 1σ)	% $^{40}Ar^*$	$^{40}Ar^*/^{39}Ar_K$ (± 1σ)	Age (Ma) (± 1σ)
S3-180	**J = .2714E-02 ± .2907E-04**	**N311.MS3**					
# 1	1,74E-06	1,58E-01 ± 1,51E-02	-1,65E-01 ± 7,98E-02	2,18E-03 ± 1,07E-02	45,0	38,36 ± 4,53	178,7 ± 20,1
# 2	3,67E-06	5,50E-03 ± 5,67E-03	1,13E-02 ± 3,81E-02	3,41E-03 ± 6,73E-03	97,0	51,64 ± 1,92	236,6 ± 8,3
# 3	6,25E-06	1,07E-02 ± 3,42E-03	3,21E-02 ± 2,51E-02	-4,29E-03 ± 3,07E-03	95,5	67,25 ± 1,59	302,5 ± 6,6
# 4	5,60E-06	-2,85E-03 ± 3,70E-03	1,11E-02 ± 2,69E-02	-1,91E-04 ± 3,28E-03	101,1	77,94 ± 2,06	346,2 ± 8,3
# 5	9,36E-06	-2,34E-03 ± 2,23E-03	-8,15E-03 ± 1,50E-02	7,71E-04 ± 2,20E-03	100,9	74,55 ± 1,58	332,4 ± 6,4
# 6	3,28E-05	-2,96E-04 ± 6,49E-04	-4,89E-03 ± 4,15E-03	4,50E-04 ± 7,30E-04	100,1	75,01 ± 0,63	334,3 ± 2,6
# 7	1,39E-05	4,52E-04 ± 1,50E-03	-3,64E-03 ± 1,06E-02	-1,89E-03 ± 1,40E-03	99,8	76,78 ± 0,72	341,5 ± 2,9
# 8	1,83E-05	-1,70E-03 ± 1,18E-03	7,42E-04 ± 7,54E-03	-3,69E-03 ± 1,05E-03	100,7	74,38 ± 0,83	331,7 ± 3,4
# 9	2,13E-05	-6,12E-04 ± 1,00E-03	2,08E-02 ± 7,45E-03	-1,05E-04 ± 1,12E-03	100,2	73,97 ± 0,85	330,1 ± 3,5
# 10	2,21E-05	-1,20E-03 ± 9,26E-04	-4,64E-03 ± 6,23E-03	-1,39E-03 ± 1,10E-03	100,5	74,08 ± 0,64	330,5 ± 2,6
# 11	1,56E-05	-2,22E-03 ± 1,31E-03	1,99E-03 ± 8,96E-03	-2,72E-04 ± 1,57E-03	100,9	75,07 ± 0,88	334,6 ± 3,6
# 12	8,04E-05	-2,42E-04 ± 2,76E-04	9,78E-04 ± 1,67E-03	-2,78E-04 ± 5,14E-04	100,1	74,05 ± 0,32	330,4 ± 1,3
# 13	1,13E-04	1,06E-04 ± 1,88E-04	-1,36E-03 ± 1,19E-03	-9,59E-05 ± 7,03E-04	100,0	73,86 ± 0,27	329,6 ± 1,1
# 14	4,77E-05	-3,61E-05 ± 4,58E-04	-1,41E-03 ± 2,96E-03	-7,34E-04 ± 7,90E-04	100,0	72,77 ± 0,46	325,2 ± 1,9
# 15	1,70E-05	-6,74E-04 ± 1,24E-03	-5,83E-03 ± 8,34E-03	1,75E-05 ± 1,31E-03	100,3	74,96 ± 0,81	334,1 ± 3,3
# 16	4,58E-05	-6,05E-04 ± 4,80E-04	9,36E-04 ± 3,28E-03	-1,45E-03 ± 6,76E-04	100,2	72,56 ± 0,48	324,3 ± 1,9
# 17	3,03E-05	-9,58E-04 ± 6,89E-04	-7,09E-03 ± 4,55E-03	-5,66E-04 ± 1,03E-03	100,4	73,44 ± 0,60	327,9 ± 2,4
# 18	1,83E-05	-1,78E-03 ± 1,16E-03	-3,60E-03 ± 7,87E-03	-2,08E-03 ± 1,40E-03	100,7	74,62 ± 0,81	332,7 ± 3,3
# 19	7,79E-06	-3,05E-03 ± 2,64E-03	-5,67E-03 ± 1,95E-02	6,42E-04 ± 2,41E-03	101,2	75,09 ± 1,96	334,7 ± 8,0
# 20	6,52E-06	-2,25E-03 ± 3,27E-03	-1,94E-04 ± 2,23E-02	-5,64E-03 ± 2,69E-03	100,9	76,88 ± 1,69	341,9 ± 6,8
# 21	1,78E-05	-1,22E-03 ± 1,16E-03	2,18E-03 ± 9,00E-03	-1,16E-03 ± 1,33E-03	100,5	73,10 ± 0,77	326,5 ± 3,2
# 22	1,65E-05	-2,32E-03 ± 1,35E-03	8,75E-03 ± 9,02E-03	4,52E-04 ± 1,44E-03	100,9	75,07 ± 0,87	334,6 ± 3,5
# 23	9,49E-06	-1,21E-03 ± 2,17E-03	1,85E-03 ± 1,69E-02	-1,29E-03 ± 2,58E-03	100,5	73,20 ± 1,31	326,9 ± 5,3
# 24	6,09E-06	-6,67E-03 ± 3,53E-03	9,84E-04 ± 2,28E-02	-6,94E-05 ± 3,63E-03	102,7	76,11 ± 1,81	338,8 ± 7,3
# 25	2,60E-05	-5,28E-04 ± 8,22E-04	2,87E-03 ± 6,18E-03	-7,38E-04 ± 8,95E-04	100,2	73,39 ± 0,70	327,7 ± 2,8
# 26	2,78E-05	-9,54E-04 ± 7,91E-04	9,90E-03 ± 5,72E-03	-7,90E-05 ± 9,43E-04	100,4	72,58 ± 0,58	324,4 ± 2,4
# 27	1,76E-05	-1,09E-03 ± 1,19E-03	1,53E-03 ± 7,50E-03	-1,65E-03 ± 1,24E-03	100,4	75,26 ± 0,76	335,3 ± 3,1
# 28	1,85E-05	-4,92E-04 ± 1,21E-03	2,66E-03 ± 7,76E-03	-1,20E-03 ± 1,44E-03	100,2	72,27 ± 0,72	323,1 ± 2,9
# 29	1,19E-05	-1,25E-03 ± 1,78E-03	5,70E-04 ± 1,19E-02	-3,41E-04 ± 1,86E-03	100,5	75,01 ± 0,88	334,3 ± 3,6
# 30	7,67E-06	-2,52E-03 ± 2,89E-03	-5,33E-03 ± 1,79E-02	1,29E-03 ± 2,48E-03	101,0	74,48 ± 1,22	332,2 ± 5,0
# 31	1,00E-05	-4,87E-03 ± 2,09E-03	-3,32E-03 ± 1,37E-02	-9,14E-04 ± 2,14E-03	102,0	74,90 ± 1,24	333,9 ± 5,0
# 32	1,71E-05	-1,15E-03 ± 1,32E-03	-4,20E-03 ± 7,73E-03	-1,44E-03 ± 1,29E-03	100,5	74,67 ± 0,74	332,9 ± 3,0
# 33	3,93E-05	-9,06E-04 ± 5,68E-04	-2,09E-04 ± 3,63E-03	-8,71E-04 ± 6,41E-04	100,4	72,65 ± 0,61	324,7 ± 2,5
# 34	2,01E-05	-9,58E-04 ± 1,04E-03	1,80E-03 ± 7,29E-03	-1,86E-03 ± 1,15E-03	100,4	73,72 ± 0,55	329,1 ± 2,2
# 35	1,26E-05	-3,64E-03 ± 1,66E-03	1,68E-03 ± 1,12E-02	7,52E-04 ± 1,93E-03	101,4	76,32 ± 0,99	339,6 ± 4,0
# 36	4,77E-06	-8,84E-03 ± 4,31E-03	-3,72E-03 ± 2,75E-02	-4,19E-03 ± 3,49E-03	103,4	78,76 ± 1,87	349,5 ± 7,6
# 37	5,25E-06	-6,11E-03 ± 4,00E-03	-9,14E-03 ± 2,56E-02	-1,95E-03 ± 3,85E-03	102,4	78,56 ± 2,31	348,7 ± 9,3
# 38	9,96E-06	-3,50E-03 ± 2,24E-03	4,28E-03 ± 1,46E-02	-2,16E-03 ± 2,24E-03	101,4	76,28 ± 1,14	339,5 ± 4,6
Total	7,96E-04	-5,35E-04 ± 1,66E-04	1,38E-04 ± 1,11E-03	-7,32E-04 ± 2,09E-04	100,2	73,82 ± 0,12	329,5 ± 3,3
Weighted Mean Age (integrated over steps marked in blue)			*MSWD/(N-1) = 1,85*				**329,2 ± 0,5**

Table S.II.14: ^{40}Ar/^{39}Ar CO_2-laser step-heating analytical data of **phengite** populations from the **phyllite sample S3-375**

Step #	$^{39}Ar_K$ (V)	$^{36}Ar_{atm}/^{39}Ar_K$ (± 1σ)	$^{37}Ar_{Ca}/^{39}Ar_K$ (± 1σ)	$^{38}Ar_{Cl}/^{39}Ar_K$ (± 1σ)	% $^{40}Ar^*$	$^{40}Ar^*/^{39}Ar_K$ (± 1σ)	Age (Ma) (± 1σ)
S3-375	**J = .2711E-02 ± .2903E-04**						
# 1	7,88E-09	-5,15E+00 ± 2,54E+01	3,50E+02 ± 1,72E+03	-1,82E+00 ± 9,28E+00	-133,8	871,70 ± 4363	2188,0 ± 6344
# 2	8,28E-08	1,56E-01 ± 2,78E-01	1,12E+01 ± 1,11E+01	-3,54E-03 ± 2,48E-01	31,2	20,84 ± 87	99,2 ± 403
# 3	1,64E-06	1,54E-02 ± 1,34E-02	1,69E-01 ± 4,75E-01	-1,35E-02 ± 1,27E-02	88,7	35,54 ± 4,57	165,9 ± 20
# 4	2,81E-06	4,98E-04 ± 8,55E-03	3,16E-01 ± 2,78E-01	2,80E-04 ± 7,53E-03	99,7	54,84 ± 2,86	250,1 ± 12
# 5	7,23E-06	2,91E-03 ± 3,15E-03	5,06E-02 ± 1,25E-01	2,35E-03 ± 3,47E-03	98,8	70,53 ± 1,42	315,7 ± 5,8
# 6	7,56E-06	3,56E-03 ± 3,00E-03	-3,59E-02 ± 9,50E-02	1,15E-03 ± 3,42E-03	98,6	75,32 ± 1,59	335,2 ± 6,5
# 7	9,55E-06	2,20E-03 ± 2,36E-03	-1,13E-01 ± 7,56E-02	-1,13E-03 ± 2,37E-03	99,2	75,24 ± 1,37	334,9 ± 5,5
# 8	2,17E-05	-3,65E-04 ± 1,07E-03	-3,30E-02 ± 3,35E-02	-1,84E-05 ± 1,12E-03	100,1	76,28 ± 0,83	339,1 ± 3,4
# 9	2,25E-05	6,40E-04 ± 1,01E-03	-3,45E-03 ± 3,79E-02	-2,06E-03 ± 1,22E-03	99,8	76,21 ± 0,52	338,8 ± 2,1
# 10	9,78E-06	-1,86E-03 ± 2,45E-03	-5,32E-02 ± 8,65E-02	-2,09E-03 ± 2,13E-03	100,7	78,67 ± 1,00	348,8 ± 4,0
# 11	6,11E-06	-6,83E-03 ± 3,62E-03	2,23E-02 ± 1,29E-01	6,36E-04 ± 3,50E-03	102,6	78,68 ± 1,89	348,8 ± 7,6
# 12	1,32E-05	-3,48E-03 ± 1,72E-03	8,19E-02 ± 6,16E-02	-3,62E-03 ± 1,61E-03	101,4	75,30 ± 0,88	335,1 ± 3,6
# 13	5,03E-05	1,20E-04 ± 4,55E-04	2,45E-03 ± 1,48E-02	1,05E-04 ± 6,67E-04	100,0	75,37 ± 0,60	335,4 ± 2,4
# 14	4,08E-05	-1,01E-03 ± 5,63E-04	-8,09E-03 ± 1,87E-02	-1,84E-03 ± 5,48E-04	100,4	74,42 ± 0,47	331,5 ± 1,9
# 15	6,50E-05	-5,24E-04 ± 3,63E-04	-2,01E-03 ± 1,14E-02	-1,69E-04 ± 5,20E-04	100,2	74,36 ± 0,35	331,3 ± 1,4
# 16	4,47E-05	-6,72E-04 ± 5,15E-04	-6,29E-03 ± 1,60E-02	-1,34E-03 ± 6,32E-04	100,3	73,23 ± 0,44	326,7 ± 1,8
# 17	2,23E-05	-3,78E-04 ± 1,09E-03	1,21E-03 ± 3,33E-02	-6,46E-04 ± 1,03E-03	100,2	73,78 ± 0,61	328,9 ± 2,5
# 18	2,18E-05	-1,42E-03 ± 1,14E-03	1,22E-02 ± 3,54E-02	2,49E-04 ± 1,01E-03	100,6	72,86 ± 0,84	325,2 ± 3,4
# 19	1,95E-05	-1,87E-03 ± 1,14E-03	5,04E-02 ± 4,13E-02	9,12E-04 ± 1,39E-03	100,7	74,63 ± 0,79	332,4 ± 3,2
# 20	3,01E-05	-9,56E-04 ± 7,49E-04	-7,25E-03 ± 2,54E-02	-1,81E-03 ± 1,06E-03	100,4	74,37 ± 0,53	331,3 ± 2,2
# 21	3,32E-05	-7,81E-04 ± 6,65E-04	2,05E-02 ± 2,51E-02	-1,15E-03 ± 8,05E-04	100,3	73,13 ± 0,48	326,3 ± 2,0
# 22	2,20E-05	3,65E-04 ± 1,16E-03	2,89E-02 ± 4,01E-02	-1,72E-03 ± 1,13E-03	99,9	72,32 ± 0,59	323,0 ± 2,4
# 23	9,44E-05	-2,32E-04 ± 2,39E-04	2,61E-03 ± 8,85E-03	-4,95E-05 ± 4,99E-04	100,1	73,93 ± 0,32	329,6 ± 1,3
# 24	9,84E-06	-2,81E-03 ± 2,23E-03	-6,43E-02 ± 7,71E-02	-2,20E-03 ± 2,55E-03	101,1	75,75 ± 1,16	336,9 ± 4,7
# 25	1,04E-05	-3,22E-03 ± 2,19E-03	3,79E-03 ± 8,84E-02	-4,65E-04 ± 2,20E-03	101,2	79,35 ± 1,17	351,5 ± 4,7
# 26	1,10E-05	-5,41E-03 ± 2,07E-03	-4,21E-02 ± 7,31E-02	-5,28E-04 ± 1,96E-03	102,2	75,24 ± 0,98	334,9 ± 4,0
# 27	1,57E-05	4,74E-03 ± 1,47E-03	9,02E-05 ± 5,00E-02	2,04E-03 ± 1,62E-03	98,2	74,70 ± 0,91	332,7 ± 3,7
# 28	1,25E-05	-3,18E-03 ± 1,82E-03	4,64E-02 ± 6,99E-02	-3,11E-03 ± 2,06E-03	101,2	76,85 ± 0,85	341,4 ± 3,4
# 29	1,37E-05	-2,10E-03 ± 1,65E-03	9,95E-02 ± 6,86E-02	-2,68E-04 ± 1,65E-03	100,8	76,10 ± 0,88	338,4 ± 3,6
# 30	4,78E-06	-1,56E-03 ± 4,99E-03	-4,20E-02 ± 1,67E-01	-2,20E-03 ± 4,43E-03	100,6	75,17 ± 2,09	334,6 ± 8,5
# 31	6,87E-06	1,75E-03 ± 3,45E-03	3,53E-02 ± 1,09E-01	-3,95E-03 ± 2,90E-03	99,3	68,80 ± 1,49	308,5 ± 6,1
# 32	6,82E-06	6,94E-03 ± 3,51E-03	1,07E-01 ± 1,17E-01	-4,54E-03 ± 3,15E-03	97,1	69,57 ± 1,43	311,7 ± 5,9
# 33	5,04E-06	2,56E-03 ± 4,53E-03	8,94E-02 ± 1,54E-01	7,56E-04 ± 3,96E-03	98,9	69,67 ± 1,90	312,1 ± 7,8
Total	6,43E-04	-5,05E-04 ± 2,06E-04	1,23E-02 ± 7,16E-03	-7,88E-04 ± 2,27E-04	100,2	74,23 ± 0,13	330,8 ± 3,3
Weighted Mean Age (integrated over steps marked in blue)			*MSWD/(N-1) = 3,74*				**330,7 ± 0,6**

Table S.II.15: $^{40}Ar/^{39}Ar$ CO_2-laser step-heating analytical data of **phengite** populations from the **phyllite sample MJ46E**

	$^{39}Ar_K$	$^{36}Ar_{atm}/^{39}Ar_K$			$^{37}Ar_{Ca}/^{39}Ar_K$			$^{38}Ar_{Cl}/^{39}Ar_K$			%$^{40}Ar^*$	$^{40}Ar^*/^{39}Ar_K$			Age (Ma)		
Step #	**(V)**	**(± 1σ)**			**(± 1σ)**			**(± 1σ)**				**(± 1σ)**			**(± 1σ)**		
MJ46-E	**J = .2742E-02 ± .2940E-04**																
# 1	4,77E-10	-1,41E+01	±	1,68E+03	-1,13E+03	±	1,35E+05	-2,07E+01	±	2,47E+03	-1889,0	3946	±	471200	4456,0	±	#####
# 2	6,32E-07	2,08E-02	±	4,29E-02	1,67E+00	±	1,05E+00	8,72E-03	±	3,60E-02	76,3	19,80	±	13,59	95,4	±	64
# 3	2,81E-07	6,54E-02	±	9,80E-02	1,20E+00	±	2,35E+00	1,75E-02	±	7,77E-02	45,7	16,26	±	30,66	78,7	±	145
# 4	4,76E-07	1,57E-02	±	5,74E-02	-9,49E-01	±	1,35E+00	1,66E-02	±	4,81E-02	91,7	51,21	±	19,14	237,0	±	83
# 5	9,28E-07	2,24E-03	±	2,95E-02	1,85E-01	±	7,00E-01	3,20E-03	±	2,35E-02	98,5	43,92	±	9,62	205,1	±	42
# 6	1,78E-06	4,35E-02	±	1,52E-02	1,82E-01	±	3,82E-01	9,96E-03	±	1,36E-02	82,8	61,62	±	5,49	281,6	±	23
# 7	3,90E-06	-6,80E-03	±	6,85E-03	-2,41E-02	±	1,67E-01	3,48E-03	±	5,69E-03	103,0	68,61	±	2,74	310,9	±	11
# 8	4,28E-06	-2,44E-03	±	6,34E-03	-9,21E-02	±	1,49E-01	6,20E-03	±	5,37E-03	100,9	81,27	±	2,50	362,9	±	10
# 9	1,92E-05	-1,52E-03	±	1,44E-03	-4,42E-03	±	3,13E-02	-3,64E-04	±	1,43E-03	100,6	75,46	±	0,85	339,2	±	3,5
# 10	2,32E-05	1,59E-03	±	1,26E-03	-2,03E-02	±	2,77E-02	-2,17E-03	±	1,17E-03	99,4	71,17	±	0,82	321,6	±	3,4
# 11	2,63E-05	-3,08E-04	±	1,04E-03	1,49E-02	±	2,57E-02	-3,75E-04	±	9,60E-04	100,1	71,38	±	0,58	322,5	±	2,4
# 12	1,68E-05	-5,42E-04	±	1,66E-03	2,90E-02	±	4,00E-02	-1,19E-04	±	1,57E-03	100,2	74,21	±	0,91	334,1	±	3,7
# 13	6,55E-05	5,28E-04	±	4,25E-04	-1,47E-03	±	9,51E-03	-2,44E-03	±	5,27E-04	99,8	72,15	±	0,44	325,7	±	1,8
# 14	1,35E-04	-9,58E-05	±	2,01E-04	6,05E-03	±	4,53E-03	1,92E-04	±	3,61E-04	100,0	76,99	±	0,29	324,4	±	1,2
# 15	5,87E-05	8,78E-04	±	4,65E-04	6,11E-03	±	1,09E-02	-8,34E-04	±	5,94E-04	99,7	72,97	±	0,49	329,0	±	2,0
# 16	1,17E-05	2,83E-03	±	2,32E-03	2,82E-02	±	5,26E-02	-4,39E-03	±	2,00E-03	98,8	70,65	±	1,12	319,5	±	4,6
# 17	1,27E-05	9,35E-04	±	2,13E-03	7,23E-02	±	4,84E-02	2,70E-04	±	1,87E-03	99,6	73,57	±	1,10	331,5	±	4,5
# 18	3,34E-05	1,23E-03	±	8,21E-04	-2,13E-03	±	2,03E-02	-1,44E-03	±	8,77E-04	99,5	70,73	±	0,60	319,8	±	2,5
# 19	1,78E-05	2,51E-03	±	1,56E-03	6,27E-02	±	3,79E-02	-1,39E-03	±	1,76E-03	99,0	70,79	±	0,77	320,0	±	3,2
# 20	1,20E-05	4,18E-03	±	2,24E-03	-7,89E-02	±	5,25E-02	-3,18E-03	±	2,02E-03	98,3	71,21	±	1,02	321,8	±	4,2
# 21	6,25E-05	8,91E-04	±	4,27E-04	2,12E-02	±	1,05E-02	-2,91E-03	±	4,83E-04	99,6	71,94	±	0,34	324,8	±	1,4
# 22	1,82E-05	2,92E-04	±	1,52E-03	2,61E-03	±	3,66E-02	-2,02E-03	±	1,45E-03	99,9	73,93	±	1,08	333,0	±	4,4
# 23	2,78E-05	2,24E-03	±	1,02E-03	3,68E-02	±	2,76E-02	-8,24E-04	±	1,31E-03	99,1	71,63	±	0,52	323,5	±	2,2
# 24	1,72E-05	2,18E-03	±	1,57E-03	-2,02E-02	±	3,93E-02	-3,06E-03	±	1,51E-03	99,1	71,05	±	0,83	321,1	±	3,4
# 25	1,37E-05	1,06E-02	±	2,05E-03	4,63E-02	±	5,37E-02	1,94E-04	±	2,15E-03	96,0	73,91	±	1,05	332,9	±	4,3
# 26	6,83E-06	7,23E-03	±	4,00E-03	-2,03E-02	±	1,00E-01	8,46E-04	±	4,26E-03	97,1	70,70	±	1,66	319,6	±	6,9
# 27	9,92E-06	-2,20E-03	±	2,66E-03	2,62E-02	±	6,56E-02	-5,23E-03	±	2,43E-03	100,9	74,13	±	1,29	333,8	±	5,3
# 28	4,64E-06	-6,95E-03	±	5,72E-03	-1,45E-01	±	1,51E-01	3,56E-03	±	5,09E-03	102,8	74,62	±	2,38	335,8	±	9,8
# 29	4,35E-06	-4,15E-03	±	6,03E-03	1,79E-02	±	1,46E-01	-8,43E-03	±	5,19E-03	101,6	77,87	±	2,44	349,1	±	9,9
# 30	5,97E-06	1,19E-03	±	4,48E-03	-1,68E-01	±	1,06E-01	1,95E-03	±	3,71E-03	99,5	76,48	±	1,79	343,4	±	7,3
# 31	5,68E-06	4,74E-03	±	4,74E-03	6,58E-02	±	1,35E-01	-1,08E-03	±	4,10E-03	98,2	77,78	±	1,93	348,8	±	7,9
# 32	1,21E-05	2,34E-03	±	2,31E-03	4,27E-01	±	7,00E-02	-2,47E-03	±	2,13E-03	99,1	72,57	±	1,06	327,4	±	4,4
# 33	4,85E-06	1,76E-02	±	5,66E-03	-1,21E-01	±	1,32E-01	-8,90E-05	±	5,39E-03	92,7	66,36	±	2,09	301,6	±	8,7
# 34	3,51E-06	5,51E-03	±	7,59E-03	-2,24E-01	±	1,94E-01	1,52E-03	±	7,43E-03	97,6	66,76	±	2,84	303,2	±	12
Total	6,42E-04	1,22E-03	±	2,48E-04	1,50E-02	±	6,08E-03	-1,09E-03	±	2,48E-04	99,5	73,19	±	0,15	329,9	±	3,3
Weighted Mean Age (integrated over steps marked in blue)					*MSWD/(N-1) = 2,05*										**324,8**	**±**	**0,6**

Table S.II.16: ^{40}Ar/^{39}Ar CO_2-laser step-heating analytical data of **phengite** populations from the **micaschist sample MJ213A**

Step #	$^{39}Ar_K$ (V)	$^{36}Ar_{atm}/^{39}Ar_K$ (± 1σ)	$^{37}Ar_{Ca}/^{39}Ar_K$ (± 1σ)	$^{38}Ar_{Cl}/^{39}Ar_K$ (± 1σ)	% $^{40}Ar^*$	$^{40}Ar^*/^{39}Ar_K$ (± 1σ)	Age (Ma) (± 1σ)
MJ213-A	**J = .2720E-02 ± .2914E-04**						
# 1	2,57E-07	2,54E+00 ± 4,62E-01	-2,61E+00 ± 4,53E+00	4,62E-03 ± 9,73E-02	4,9	38,66 ± 39,03	180,4 ± 173
# 2	6,58E-07	2,03E-01 ± 4,13E-02	4,44E-01 ± 1,87E+00	2,60E-02 ± 3,62E-02	56,1	76,54 ± 15,41	341,2 ± 63
# 3	1,76E-06	5,35E-02 ± 1,37E-02	1,23E+00 ± 6,63E-01	7,15E-03 ± 1,34E-02	67,5	32,82 ± 5,25	154,3 ± 24
# 4	3,28E-06	1,85E-02 ± 8,22E-03	3,93E+00 ± 4,18E-01	1,14E-03 ± 6,71E-03	92,8	69,88 ± 3,35	314,0 ± 14
# 5	6,31E-06	-1,50E-03 ± 3,83E-03	2,60E+00 ± 2,76E-01	3,29E-03 ± 3,65E-03	100,6	78,14 ± 1,74	347,7 ± 7,0
# 6	8,74E-06	-1,42E-03 ± 2,68E-03	2,27E-01 ± 1,47E-01	-2,42E-04 ± 2,96E-03	100,6	74,28 ± 1,31	332,0 ± 5,3
# 7	9,05E-06	1,65E-03 ± 2,62E-03	-4,91E-02 ± 1,36E-01	-2,13E-03 ± 2,58E-03	99,4	79,10 ± 1,43	351,6 ± 5,8
# 8	4,84E-05	2,92E-03 ± 4,88E-04	1,87E-02 ± 2,80E-02	-4,99E-04 ± 7,88E-04	98,8	73,70 ± 0,53	329,6 ± 2,2
# 9	3,13E-05	-2,25E-04 ± 7,59E-04	-1,06E-04 ± 3,92E-02	-1,18E-03 ± 1,03E-03	100,1	74,08 ± 0,52	331,2 ± 2,1
# 10	8,35E-05	6,06E-04 ± 2,88E-04	-3,52E-03 ± 1,49E-02	-4,17E-04 ± 4,04E-04	99,8	75,39 ± 0,30	336,5 ± 1,2
# 11	5,19E-05	7,87E-04 ± 4,41E-04	1,10E-02 ± 2,38E-02	-1,21E-03 ± 7,03E-04	99,7	74,03 ± 0,33	331,0 ± 1,3
# 12	2,62E-05	1,31E-04 ± 8,89E-04	-2,11E-02 ± 4,65E-02	-1,19E-03 ± 9,78E-04	100,0	74,23 ± 0,72	331,8 ± 2,9
# 13	1,86E-05	-1,26E-03 ± 1,35E-03	-1,17E-01 ± 6,66E-02	1,50E-03 ± 1,38E-03	100,4	90,53 ± 1,15	397,2 ± 4,5
# 14	1,47E-05	-1,27E-03 ± 1,59E-03	4,51E-03 ± 8,94E-02	6,10E-05 ± 1,53E-03	100,5	73,87 ± 0,94	330,4 ± 3,8
# 15	1,68E-05	-8,65E-04 ± 1,37E-03	-9,33E-03 ± 7,21E-02	-7,17E-04 ± 1,44E-03	100,3	74,25 ± 1,03	331,9 ± 4,2
# 16	2,04E-05	-1,33E-03 ± 1,18E-03	4,97E-03 ± 6,05E-02	1,33E-04 ± 1,30E-03	100,5	73,24 ± 0,62	327,8 ± 2,5
# 17	2,08E-05	-2,81E-04 ± 1,15E-03	-2,50E-02 ± 6,05E-02	-2,00E-04 ± 1,46E-03	100,1	74,92 ± 0,74	334,6 ± 3,0
# 18	1,94E-05	-5,88E-04 ± 1,22E-03	5,52E-02 ± 6,36E-02	-3,43E-03 ± 1,43E-03	100,2	73,41 ± 0,67	328,5 ± 2,7
# 19	1,55E-05	1,17E-03 ± 1,53E-03	-1,10E-03 ± 8,93E-02	-2,52E-04 ± 1,59E-03	99,5	73,68 ± 0,89	329,6 ± 3,6
# 20	9,01E-06	5,69E-04 ± 2,58E-03	-8,41E-02 ± 1,48E-01	-2,44E-03 ± 2,62E-03	99,8	75,62 ± 1,67	337,5 ± 6,8
# 21	5,72E-05	9,75E-05 ± 4,12E-04	5,79E-02 ± 2,36E-02	-6,48E-04 ± 6,10E-04	100,0	73,50 ± 0,57	328,9 ± 2,3
# 22	3,74E-05	-7,50E-04 ± 6,16E-04	2,37E-02 ± 3,62E-02	-1,20E-03 ± 7,11E-04	100,3	74,81 ± 0,49	334,2 ± 2,0
# 23	1,85E-05	-8,36E-04 ± 1,31E-03	-5,65E-02 ± 7,15E-02	-1,25E-03 ± 1,28E-03	100,3	74,60 ± 0,71	333,3 ± 2,9
# 24	7,44E-06	-6,27E-03 ± 3,10E-03	-4,78E-02 ± 1,79E-01	2,41E-04 ± 2,92E-03	102,5	75,78 ± 1,72	338,1 ± 7,0
# 25	6,21E-06	-4,00E-03 ± 3,91E-03	-1,09E-01 ± 2,12E-01	1,28E-03 ± 3,68E-03	101,6	74,30 ± 2,16	332,1 ± 8,8
# 26	1,16E-05	-8,76E-04 ± 2,03E-03	9,30E-02 ± 1,08E-01	-6,48E-04 ± 2,07E-03	100,3	76,31 ± 1,22	340,3 ± 5,0
# 27	1,12E-05	-2,98E-03 ± 2,10E-03	-4,62E-02 ± 1,17E-01	3,42E-03 ± 2,67E-03	101,2	76,65 ± 1,22	341,7 ± 5,0
# 28	1,28E-05	-1,57E-03 ± 1,88E-03	-3,51E-02 ± 9,89E-02	2,03E-04 ± 1,99E-03	100,6	75,09 ± 1,10	335,3 ± 4,5
# 29	2,73E-05	-2,79E-04 ± 9,04E-04	1,09E-02 ± 4,85E-02	-2,82E-03 ± 9,98E-04	100,1	74,66 ± 0,63	333,6 ± 2,6
# 30	6,10E-06	-4,16E-03 ± 3,91E-03	-3,15E-01 ± 2,04E-01	4,29E-03 ± 3,85E-03	101,6	76,65 ± 2,27	341,7 ± 9,2
# 31	1,02E-05	1,03E-03 ± 2,27E-03	3,50E-02 ± 1,23E-01	3,20E-03 ± 2,70E-03	99,6	74,46 ± 1,28	332,8 ± 5,2
# 32	1,71E-05	-1,76E-04 ± 1,42E-03	1,06E-01 ± 7,52E-02	5,35E-04 ± 1,71E-03	100,1	75,62 ± 0,99	337,5 ± 4,0
# 33	1,40E-05	4,60E-05 ± 1,71E-03	-9,34E-02 ± 9,09E-02	-7,04E-04 ± 1,77E-03	100,0	75,56 ± 1,05	337,2 ± 4,3
# 34	1,74E-05	-3,28E-05 ± 1,47E-03	1,88E-02 ± 8,85E-02	-3,21E-04 ± 1,36E-03	100,0	71,99 ± 0,90	322,6 ± 3,7
# 35	1,48E-06	9,70E-03 ± 1,65E-02	2,81E-01 ± 9,86E-01	-2,67E-03 ± 1,60E-02	96,7	84,52 ± 8,22	373,3 ± 33
# 36	3,12E-06	-4,47E-03 ± 7,97E-03	-3,30E-01 ± 4,31E-01	1,66E-03 ± 7,45E-03	101,7	79,40 ± 3,96	352,8 ± 16
Total	6,65E-04	1,33E-03 ± 2,17E-04	4,80E-02 ± 1,18E-02	-4,78E-04 ± 2,41E-04	99,5	74,90 ± 0,14	335,0 ± 3,3
Weighted Mean Age (integrated over steps marked in blue)			*MSWD/(N-1) = 1,47*				**332,8 ± 0,5**

Table S.II.17: ^{40}Ar/^{39}Ar CO$_2$-laser step-heating analytical data of **phengite** populations from the **micaschist sample MJ216**

Step #	**^{39}Ar$_K$ (V)**	**^{36}Ar$_{atm}$/^{39}Ar$_K$ (± 1σ)**	**^{37}Ar$_{Ca}$/^{39}Ar$_K$ (± 1σ)**	**^{38}Ar$_{Cl}$/^{39}Ar$_K$ (± 1σ)**	**% ^{40}Ar***	**^{40}Ar*/^{39}Ar$_K$ (± 1σ)**	**Age (Ma) (± 1σ)**
MJ216	**J = .2719E-02 ± .2912E-04**						
# 3	3,61E-07	1,57E-02 ± 6,23E-02	-6,28E-01 ± 1,87E+00	-7,98E-03 ± 5,62E-02	91,1	47,57 ± 19,93	219,4 ± 87
# 4	3,53E-07	-8,59E-02 ± 6,48E-02	2,66E+00 ± 2,55E+00	-1,04E-02 ± 5,52E-02	157,8	69,28 ± 21,15	311,3 ± 87
# 5	1,94E-06	9,45E-03 ± 1,17E-02	1,74E-01 ± 3,59E-01	3,76E-03 ± 1,13E-02	95,6	60,64 ± 4,12	275,3 ± 17
# 6	1,65E-06	5,76E-02 ± 1,53E-02	-2,34E-01 ± 4,15E-01	2,43E-03 ± 1,22E-02	81,2	73,46 ± 5,46	328,5 ± 22
# 7	6,19E-06	1,24E-02 ± 3,68E-03	-1,39E-02 ± 1,09E-01	-3,26E-03 ± 3,55E-03	95,5	77,76 ± 1,81	346,0 ± 7,3
# 8	1,29E-05	3,64E-03 ± 1,73E-03	-3,83E-02 ± 5,53E-02	-2,27E-03 ± 1,76E-03	98,7	79,46 ± 0,87	352,9 ± 3,5
# 9	1,54E-05	2,46E-03 ± 1,55E-03	7,66E-02 ± 4,86E-02	-1,13E-03 ± 1,62E-03	99,1	77,74 ± 0,82	345,9 ± 3,3
# 10	1,02E-05	-1,13E-03 ± 2,09E-03	3,45E-02 ± 6,62E-02	-2,42E-03 ± 2,49E-03	100,4	76,92 ± 1,19	342,6 ± 4,8
# 11	1,21E-05	6,01E-03 ± 2,01E-03	6,01E-02 ± 6,85E-02	-2,80E-03 ± 1,92E-03	97,7	74,64 ± 0,82	333,3 ± 3,3
# 12	9,57E-05	2,36E-03 ± 2,44E-04	1,01E-02 ± 7,44E-03	-5,32E-04 ± 4,20E-04	99,1	74,95 ± 0,27	334,6 ± 1,1
# 13	2,27E-05	-2,51E-04 ± 1,01E-03	1,45E-02 ± 2,91E-02	-3,25E-04 ± 1,02E-03	100,1	72,84 ± 0,71	326,0 ± 2,9
# 14	4,07E-05	-1,20E-04 ± 5,40E-04	5,90E-03 ± 1,90E-02	3,80E-04 ± 6,11E-04	100,0	72,35 ± 0,61	324,0 ± 2,5
# 15	2,29E-05	-1,28E-03 ± 9,48E-04	9,03E-03 ± 3,18E-02	1,33E-03 ± 1,10E-03	100,5	74,39 ± 0,78	332,3 ± 3,2
# 16	2,21E-05	-1,80E-03 ± 1,09E-03	-5,71E-03 ± 3,17E-02	-1,21E-03 ± 1,06E-03	100,7	74,71 ± 0,88	333,6 ± 3,6
# 17	1,91E-05	-1,84E-03 ± 1,15E-03	-1,10E-02 ± 4,03E-02	-1,74E-03 ± 1,42E-03	100,8	72,93 ± 0,64	326,3 ± 2,6
# 18	1,68E-05	-2,09E-03 ± 1,29E-03	-5,21E-02 ± 3,92E-02	-1,25E-03 ± 1,65E-03	100,8	74,14 ± 0,70	331,3 ± 2,8
# 19	1,19E-05	-7,26E-04 ± 1,87E-03	-6,75E-02 ± 5,84E-02	-1,26E-03 ± 1,83E-03	100,3	75,59 ± 0,87	337,2 ± 3,6
# 20	1,11E-05	-2,08E-03 ± 2,04E-03	4,45E-02 ± 6,40E-02	-5,20E-04 ± 2,18E-03	100,8	74,16 ± 1,17	331,4 ± 4,8
# 21	8,80E-06	8,63E-04 ± 2,60E-03	-2,61E-02 ± 7,68E-02	-2,87E-03 ± 2,42E-03	99,7	74,77 ± 1,16	333,8 ± 4,7
# 22	5,90E-05	9,41E-04 ± 3,89E-04	-1,53E-02 ± 1,13E-02	-1,39E-03 ± 4,52E-04	99,6	72,51 ± 0,41	324,6 ± 1,7
# 23	1,03E-04	4,67E-05 ± 1,51E-04	-6,13E-03 ± 5,71E-03	2,18E-04 ± 4,13E-04	100,0	73,42 ± 0,36	328,4 ± 1,5
# 24	6,08E-05	2,11E-04 ± 2,75E-04	-3,56E-03 ± 1,02E-02	-1,89E-04 ± 7,19E-04	99,9	73,49 ± 0,35	328,6 ± 1,4
# 25	2,89E-05	3,29E-04 ± 5,17E-04	-4,78E-03 ± 2,00E-02	-1,94E-04 ± 1,02E-03	99,9	73,90 ± 0,59	330,3 ± 2,4
# 26	4,29E-05	-4,19E-05 ± 4,09E-04	-3,28E-03 ± 1,38E-02	-7,58E-04 ± 7,84E-04	100,0	72,33 ± 0,53	323,9 ± 2,2
# 27	1,76E-05	-1,18E-03 ± 8,36E-04	1,72E-02 ± 3,37E-02	-5,51E-04 ± 1,63E-03	100,5	75,02 ± 1,00	334,9 ± 4,1
# 28	1,27E-05	4,42E-04 ± 1,18E-03	2,13E-02 ± 4,75E-02	-3,38E-03 ± 1,99E-03	99,8	72,60 ± 0,76	325,0 ± 3,1
# 29	1,06E-05	-9,04E-04 ± 1,66E-03	-2,99E-02 ± 5,52E-02	1,38E-04 ± 2,98E-03	100,4	74,80 ± 0,96	334,0 ± 3,9
# 30	1,17E-05	-2,20E-03 ± 1,30E-03	-2,90E-02 ± 5,56E-02	-4,87E-03 ± 2,37E-03	100,9	73,54 ± 1,04	328,9 ± 4,2
# 31	1,24E-05	-1,09E-04 ± 1,19E-03	-8,48E-02 ± 4,24E-02	-2,71E-03 ± 2,21E-03	100,0	73,46 ± 0,99	328,5 ± 4,0
# 32	2,35E-05	-3,11E-04 ± 6,90E-04	-1,95E-02 ± 2,37E-02	-1,63E-03 ± 1,24E-03	100,1	74,13 ± 0,76	331,2 ± 3,1
# 33	3,61E-05	6,18E-04 ± 4,63E-04	-2,08E-02 ± 1,93E-02	2,50E-04 ± 7,94E-04	99,8	72,11 ± 0,56	323,0 ± 2,3
# 34	2,55E-05	6,72E-04 ± 6,48E-04	-1,60E-02 ± 2,27E-02	-1,92E-03 ± 1,34E-03	99,7	72,38 ± 0,61	324,1 ± 2,5
# 35	2,83E-05	2,79E-04 ± 6,00E-04	1,73E-02 ± 2,04E-02	-6,01E-04 ± 1,10E-03	99,9	73,18 ± 0,51	327,4 ± 2,1
# 36	4,83E-05	-2,01E-04 ± 3,67E-04	-1,26E-02 ± 1,35E-02	-1,48E-03 ± 7,19E-04	100,1	72,56 ± 0,50	324,8 ± 2,1
# 37	2,80E-05	-8,28E-04 ± 5,47E-04	-2,46E-02 ± 1,98E-02	-1,02E-03 ± 1,22E-03	100,3	73,30 ± 0,61	327,9 ± 2,5
# 38	3,95E-05	2,52E-02 ± 5,71E-04	-1,26E-02 ± 1,31E-02	9,79E-04 ± 1,01E-03	90,8	73,18 ± 0,53	327,4 ± 2,2
# 39	7,49E-06	-9,46E-04 ± 3,47E-03	1,73E-02 ± 9,02E-02	-2,40E-03 ± 3,09E-03	100,4	74,37 ± 1,40	332,2 ± 5,7
# 40	5,74E-06	-5,02E-03 ± 4,28E-03	-1,17E-01 ± 1,16E-01	-5,90E-03 ± 4,07E-03	102,1	73,71 ± 1,91	329,5 ± 7,8
# 41	3,85E-06	-6,14E-03 ± 6,55E-03	-3,70E-02 ± 1,70E-01	5,79E-04 ± 6,06E-03	102,4	78,40 ± 3,05	348,6 ± 12
# 42	5,08E-06	-8,69E-03 ± 5,13E-03	-1,45E-01 ± 1,35E-01	7,62E-04 ± 4,97E-03	103,5	75,18 ± 2,32	335,5 ± 9,5
# 43	6,81E-06	-2,57E-03 ± 3,85E-03	-1,46E-03 ± 1,01E-01	-4,06E-03 ± 3,67E-03	101,0	73,95 ± 1,79	330,5 ± 7,3
# 44	2,40E-05	-1,28E-04 ± 1,03E-03	-4,75E-02 ± 2,67E-02	2,83E-04 ± 1,16E-03	100,1	72,07 ± 0,65	322,8 ± 2,7
# 45	2,16E-05	-7,14E-04 ± 1,15E-03	-4,90E-03 ± 3,47E-02	-2,42E-03 ± 1,60E-03	100,3	73,99 ± 0,82	330,7 ± 3,4
# 46	1,89E-06	-1,25E-02 ± 1,31E-02	1,72E-01 ± 4,06E-01	8,48E-03 ± 1,19E-02	105,3	73,44 ± 4,90	328,5 ± 20
Total	9,98E-04	1,24E-03 ± 1,41E-04	-6,12E-03 ± 4,46E-03	-7,72E-04 ± 1,87E-04	99,5	73,65 ± 0,11	329,3 ± 3,3
Weighted Mean Age (integrated over steps marked in blue)			*MSWD/(N-1) = 1,56*				**327,6 ± 0,5**

Table S.II.18: ^{40}Ar/^{39}Ar CO$_2$-laser **step-heating** analytical data of **phengite** populations from the **micaschist sample MJ11I**

	^{39}Ar$_K$	**^{36}Ar$_{atm}$/^{39}Ar$_K$**			**^{37}Ar$_{Ca}$/^{39}Ar$_K$**			**^{38}Ar$_{Cl}$/^{39}Ar$_K$**			**%^{40}Ar***	**^{40}Ar*/^{39}Ar$_K$**			**Age (Ma)**		
Step #	**(V)**	**(± 1σ)**			**(± 1σ)**			**(± 1σ)**				**(± 1σ)**			**(± 1σ)**		
MJ11I	**J = .2746E-02 ± .2944E-04**																
# 1	4,36E-08	9,22E-02	±	3,41E-01	-5,04E+00	±	1,36E+01	8,40E-02	±	5,80E-01	69,1	60,88	±	125,00	278,8	±	531
# 2	3,34E-08	6,31E-01	±	7,75E-01	-4,01E+00	±	1,72E+01	5,37E-01	±	9,13E-01	12,9	27,58	±	163,70	131,7	±	754
# 3	1,43E-09	-2,27E+01	±	4,77E+02	-5,37E+02	±	1,13E+04	7,63E+00	±	1,61E+02	-61,8	-	±	-	-	±	-
# 4	1,19E-06	8,77E-01	±	3,98E-02	-8,31E-02	±	4,54E-01	-2,24E-02	±	2,50E-02	7,4	20,79	±	5,52	100,2	±	26
# 5	1,00E-06	2,09E-01	±	2,25E-02	-4,76E-01	±	4,93E-01	3,10E-02	±	2,98E-02	33,8	31,57	±	6,69	150,0	±	30
# 6	2,53E-06	3,42E-02	±	5,97E-03	6,56E-02	±	2,18E-01	2,40E-03	±	9,89E-03	80,9	42,77	±	2,21	200,3	±	9,8
# 7	4,74E-06	3,34E-02	±	3,00E-03	-2,47E-02	±	1,10E-01	-6,84E-04	±	5,59E-03	87,0	65,80	±	1,41	299,6	±	5,9
# 8	1,35E-05	1,53E-02	±	1,49E-03	1,65E-03	±	3,76E-02	2,18E-03	±	2,01E-03	94,3	74,49	±	1,14	335,7	±	4,7
# 9	1,19E-05	1,14E-02	±	1,32E-03	3,66E-03	±	4,49E-02	2,03E-03	±	2,44E-03	95,6	73,96	±	0,91	333,5	±	3,7
# 10	1,03E-05	8,37E-03	±	2,62E-03	-4,79E-02	±	5,15E-02	-1,61E-03	±	2,65E-03	97,1	81,38	±	1,41	363,8	±	5,7
# 11	8,27E-05	7,83E-03	±	3,38E-04	4,30E-03	±	6,53E-03	6,82E-05	±	4,59E-04	97,0	73,83	±	0,32	333,0	±	1,3
# 12	1,00E-04	1,25E-03	±	2,60E-04	4,96E-03	±	5,06E-03	-3,28E-04	±	5,10E-04	99,5	72,87	±	0,42	329,0	±	1,7
# 13	6,83E-05	9,10E-04	±	3,77E-04	-3,65E-03	±	8,04E-03	-4,59E-04	±	6,89E-04	99,6	73,29	±	0,30	330,8	±	1,2
# 14	2,45E-05	-6,67E-04	±	1,08E-03	1,77E-02	±	2,37E-02	-2,14E-03	±	1,28E-03	100,3	73,26	±	0,71	330,6	±	2,9
# 15	6,63E-05	1,58E-03	±	3,75E-04	-9,51E-03	±	8,51E-03	3,82E-04	±	7,01E-04	99,4	74,10	±	0,33	334,1	±	1,4
# 16	3,53E-05	1,02E-03	±	7,27E-04	-1,60E-03	±	1,49E-02	-1,55E-03	±	7,85E-04	99,6	73,38	±	0,68	331,1	±	2,8
# 17	3,23E-05	1,15E-04	±	7,78E-04	5,70E-03	±	1,57E-02	-8,11E-04	±	8,90E-04	100,0	71,95	±	0,54	325,2	±	2,2
# 18	3,66E-05	1,32E-03	±	7,41E-04	-3,60E-03	±	1,41E-02	-1,70E-03	±	9,64E-04	99,5	71,91	±	0,65	325,0	±	2,7
# 19	3,27E-05	8,51E-04	±	7,83E-04	-1,28E-03	±	1,51E-02	-1,12E-03	±	1,05E-03	99,7	71,86	±	0,48	324,9	±	2,0
# 20	1,28E-05	-1,14E-03	±	2,02E-03	-2,94E-02	±	4,46E-02	-1,62E-03	±	2,17E-03	100,5	72,43	±	0,97	327,2	±	4,0
# 21	9,03E-06	1,02E-03	±	2,94E-03	-2,47E-02	±	6,74E-02	1,83E-03	±	3,07E-03	99,6	76,91	±	1,31	345,6	±	5,3
# 22	2,07E-05	1,50E-03	±	1,31E-03	-1,83E-02	±	2,63E-02	-1,80E-03	±	1,51E-03	99,4	71,71	±	0,89	324,2	±	3,7
# 23	2,72E-05	2,39E-03	±	9,73E-04	-2,20E-02	±	1,90E-02	-7,84E-04	±	1,21E-03	99,0	71,91	±	0,49	325,1	±	2,0
# 24	1,65E-05	2,53E-03	±	1,55E-03	4,14E-03	±	3,31E-02	1,96E-04	±	1,87E-03	99,0	73,18	±	1,01	330,3	±	4,1
# 25	2,83E-05	2,57E-03	±	9,51E-04	-7,46E-03	±	1,83E-02	-1,12E-03	±	1,05E-03	99,0	71,60	±	0,60	323,8	±	2,5
# 26	2,20E-05	4,57E-03	±	1,15E-03	-2,15E-02	±	2,57E-02	-3,14E-03	±	1,41E-03	98,2	72,89	±	0,66	329,1	±	2,7
# 27	2,17E-05	2,97E-03	±	1,19E-03	2,56E-02	±	2,41E-02	2,66E-03	±	1,55E-03	98,8	72,60	±	0,76	327,9	±	3,1
# 28	1,20E-05	5,27E-03	±	2,12E-03	1,68E-02	±	4,15E-02	2,03E-03	±	2,58E-03	98,0	75,28	±	1,03	339,0	±	4,2
# 29	2,42E-05	2,32E-03	±	1,07E-03	-2,97E-03	±	2,22E-02	-1,27E-03	±	1,33E-03	99,1	72,99	±	0,55	329,5	±	2,3
# 30	5,76E-06	-1,41E-03	±	4,76E-03	-7,73E-03	±	9,51E-02	-2,07E-04	±	4,83E-03	100,6	75,91	±	2,17	341,5	±	8,9
# 31	2,06E-05	2,92E-03	±	1,24E-03	1,61E-02	±	2,66E-02	1,01E-03	±	1,55E-03	98,8	72,92	±	0,72	329,3	±	3,0
# 32	1,03E-05	2,80E-02	±	2,74E-03	-2,17E-02	±	5,21E-02	5,08E-04	±	3,06E-03	90,3	76,79	±	1,08	345,1	±	4,4
# 33	6,63E-05	2,02E-03	±	4,08E-04	-9,52E-03	±	8,00E-03	-1,37E-03	±	6,47E-04	99,2	72,79	±	0,39	328,7	±	1,6
# 34	8,80E-07	1,01E-01	±	2,91E-02	1,64E-01	±	6,44E-01	-2,11E-02	±	3,03E-02	67,2	60,85	±	10,30	278,7	±	44
# 35	4,21E-06	2,94E-02	±	6,25E-03	4,22E-02	±	1,17E-01	6,99E-03	±	6,52E-03	88,1	64,38	±	2,50	293,7	±	11
# 36	1,71E-06	1,11E-01	±	1,61E-02	4,05E-01	±	3,00E-01	-2,00E-02	±	1,57E-02	49,0	31,59	±	5,51	150,0	±	25
Total	8,28E-04	5,16E-03	±	1,76E-04	-2,50E-03	±	3,88E-03	-5,19E-04	±	2,33E-04	98,0	72,81	±	0,12	328,8	±	3,3
Weighted Mean Age (integrated over steps marked in blue)					*MSWD/(N-1) = 3,29*										**329,9**	**±**	**0,5**

Table S.II.19: ***In-situ*** UV-laser 40Ar/39Ar analytical data of single **phengite** grains from the **garnet-micaschist sample MJ11I**.

Spot #	$^{39}Ar_K$ (V)	$^{36}Ar_{atm}/^{39}Ar_K$ (± 1σ)	$^{37}Ar_{Ca}/^{39}Ar_K$ (± 1σ)	$^{38}Ar_{Cl}/^{39}Ar_K$ (± 1σ)	%$^{40}Ar^*$	$^{40}Ar^*/^{39}Ar_K$ (± 1σ)	Age (Ma) (± 1σ)
MJ11I: garnet-micaschist (phengite)		**J = 0.002720 ± 0.00002913**					
# 1	3,19E-06	9,09E-03 ± 4,94E-03	-2,08E-02 ± 4,00E-01	1,26E-02 ± 4,82E-03	96,3	70,77 ± 2,42	317,6 ± 10
# 2	1,07E-05	2,39E-03 ± 1,56E-03	9,67E-02 ± 1,01E-01	1,56E-03 ± 1,77E-03	99,1	75,56 ± 1,14	337,2 ± 4,6
# 3	1,67E-05	3,04E-03 ± 9,75E-04	6,49E-02 ± 7,80E-02	-2,54E-04 ± 1,26E-03	98,8	76,03 ± 0,92	339,1 ± 3,7
# 4	6,35E-06	8,57E-03 ± 2,53E-03	2,15E-01 ± 1,69E-01	-9,68E-05 ± 2,74E-03	96,7	73,90 ± 1,14	330,4 ± 4,7
# 5	4,40E-05	1,40E-03 ± 3,44E-04	1,93E-02 ± 2,44E-02	-2,03E-03 ± 5,11E-04	99,4	73,89 ± 0,26	330,4 ± 1,1
# 6	2,48E-05	6,41E-03 ± 7,02E-04	-5,46E-03 ± 4,27E-02	3,15E-04 ± 1,15E-03	97,5	73,58 ± 0,50	329,1 ± 2,0
# 7	2,80E-05	5,57E-04 ± 5,52E-04	2,17E-02 ± 3,92E-02	-2,32E-03 ± 7,42E-04	99,8	73,19 ± 0,66	327,5 ± 2,7
# 8	8,75E-06	1,72E-03 ± 1,72E-03	1,02E-01 ± 1,23E-01	4,15E-04 ± 1,72E-03	99,3	73,02 ± 1,06	326,8 ± 4,3
# 9	3,76E-05	1,04E-03 ± 4,17E-04	1,94E-02 ± 2,73E-02	4,02E-04 ± 6,23E-04	99,6	75,57 ± 0,28	337,2 ± 1,2
# 10	2,80E-05	1,68E-03 ± 5,70E-04	1,65E-03 ± 4,00E-02	2,92E-04 ± 6,47E-04	99,3	74,91 ± 0,26	334,5 ± 1,0
# 11	2,92E-05	1,52E-03 ± 5,39E-04	1,49E-02 ± 3,85E-02	-9,87E-04 ± 7,12E-04	99,4	74,58 ± 0,40	333,2 ± 1,7
# 12	2,51E-05	2,48E-03 ± 6,64E-04	-4,54E-02 ± 4,05E-02	1,21E-03 ± 9,39E-04	99,1	76,35 ± 0,34	340,4 ± 1,4
# 13	2,75E-05	1,64E-03 ± 5,63E-04	2,26E-02 ± 4,35E-02	1,04E-04 ± 9,72E-04	99,4	75,00 ± 0,51	334,9 ± 2,1
# 14	2,82E-05	2,93E-03 ± 5,47E-04	7,45E-02 ± 5,57E-02	-2,37E-03 ± 4,99E-04	98,9	74,34 ± 0,36	332,2 ± 1,5
# 15	2,75E-05	1,11E-03 ± 5,60E-04	-2,74E-02 ± 3,87E-02	1,86E-03 ± 8,06E-04	99,6	77,89 ± 0,48	346,6 ± 1,9
# 16	2,80E-05	1,69E-03 ± 5,54E-04	3,69E-02 ± 4,10E-02	-9,11E-04 ± 6,15E-04	99,4	76,64 ± 0,71	341,6 ± 2,9
# 17	2,80E-05	2,28E-03 ± 5,75E-04	-2,70E-02 ± 3,88E-02	-2,04E-03 ± 8,31E-04	99,1	74,75 ± 0,53	333,9 ± 2,1
# 18	2,90E-05	1,51E-03 ± 5,57E-04	-9,62E-03 ± 3,94E-02	-3,08E-04 ± 9,39E-04	99,4	75,84 ± 0,78	338,3 ± 3,2
# 19	2,69E-05	2,12E-03 ± 5,90E-04	2,95E-03 ± 4,15E-02	-1,00E-03 ± 5,16E-04	99,2	76,85 ± 0,61	342,4 ± 2,5
# 20	2,66E-05	1,07E-03 ± 5,67E-04	-9,06E-03 ± 5,09E-02	6,88E-04 ± 7,42E-04	99,6	74,63 ± 0,69	333,4 ± 2,8
# 21	7,37E-06	7,87E-04 ± 2,08E-03	1,38E-02 ± 1,59E-01	-1,95E-03 ± 1,78E-03	99,7	79,03 ± 1,43	351,3 ± 5,8
# 22	1,38E-05	4,27E-04 ± 1,10E-03	6,86E-02 ± 7,79E-02	-1,33E-03 ± 1,05E-03	99,8	75,51 ± 1,01	337,0 ± 4,1
# 23	1,86E-05	2,32E-03 ± 8,41E-04	-5,17E-02 ± 5,77E-02	5,12E-04 ± 8,71E-04	99,1	72,78 ± 0,61	325,8 ± 2,5
# 24	1,85E-05	1,38E-03 ± 8,31E-04	-2,99E-02 ± 6,11E-02	1,08E-03 ± 9,53E-04	99,5	76,27 ± 0,59	340,1 ± 2,4
# 25	1,94E-05	1,36E-03 ± 7,80E-04	-1,12E-02 ± 6,03E-02	1,92E-03 ± 1,48E-03	99,5	75,18 ± 0,51	335,6 ± 2,1
# 26	1,86E-05	1,71E-03 ± 8,43E-04	-1,50E-03 ± 6,12E-02	1,66E-04 ± 9,33E-04	99,3	75,02 ± 0,45	335,0 ± 1,8
# 27	1,65E-05	6,70E-03 ± 9,27E-04	-2,41E-02 ± 7,73E-02	-1,88E-03 ± 1,20E-03	97,5	76,64 ± 0,86	341,6 ± 3,5
# 28	1,77E-05	1,12E-03 ± 9,22E-04	1,87E-02 ± 7,05E-02	1,80E-03 ± 1,52E-03	99,6	76,82 ± 0,85	342,3 ± 3,5
# 29	2,50E-05	1,56E-03 ± 6,58E-04	-9,79E-02 ± 4,39E-02	-7,11E-04 ± 7,01E-04	99,4	74,62 ± 0,42	333,4 ± 1,7
# 30	2,25E-05	8,79E-04 ± 6,87E-04	-5,20E-02 ± 4,90E-02	4,58E-04 ± 9,73E-04	99,7	75,31 ± 0,69	336,2 ± 2,8
# 31	2,43E-05	2,35E-03 ± 6,87E-04	-3,40E-02 ± 4,34E-02	5,25E-04 ± 8,19E-04	99,1	74,08 ± 0,57	331,2 ± 2,3
# 32	1,98E-05	3,62E-03 ± 7,89E-04	-5,00E-02 ± 5,87E-02	-4,17E-03 ± 8,00E-04	98,6	76,01 ± 0,51	339,0 ± 2,1
# 33	8,36E-06	2,31E-02 ± 2,14E-03	-1,45E-02 ± 1,34E-01	-6,90E-04 ± 2,54E-03	91,7	75,22 ± 1,39	335,8 ± 5,7
# 34	2,56E-05	2,19E-03 ± 6,17E-04	-3,58E-02 ± 4,15E-02	1,29E-04 ± 8,03E-04	99,1	74,58 ± 0,54	333,2 ± 2,2
# 35	2,44E-05	1,99E-03 ± 6,41E-04	-5,45E-02 ± 4,58E-02	-3,48E-04 ± 8,55E-04	99,2	76,11 ± 0,69	339,4 ± 2,8
# 36	8,16E-06	5,55E-04 ± 1,93E-03	-1,87E-01 ± 1,35E-01	1,58E-03 ± 1,79E-03	99,8	77,60 ± 1,32	345,5 ± 5,4
# 37	1,06E-05	1,68E-03 ± 1,43E-03	-3,93E-02 ± 1,14E-01	7,67E-04 ± 1,54E-03	99,3	73,05 ± 0,72	327,0 ± 2,9
# 38	4,67E-08	-7,10E-01 ± 7,22E-01	-4,40E+01 ± 4,67E+01	4,90E-02 ± 2,64E-01	7,8	-17,66 ± 99,86	-88,8 ± 515
# 39	1,93E-05	1,49E-04 ± 7,92E-04	-4,10E-02 ± 5,82E-02	-1,63E-03 ± 7,50E-04	99,9	73,14 ± 0,72	327,3 ± 2,9
# 40	2,08E-05	8,58E-04 ± 7,67E-04	-1,66E-02 ± 5,56E-02	-7,41E-04 ± 8,27E-04	99,7	75,14 ± 0,74	335,5 ± 3,0
# 41	1,39E-05	3,22E-03 ± 1,11E-03	6,16E-04 ± 8,16E-02	-4,06E-03 ± 1,29E-03	98,7	73,36 ± 0,53	328,2 ± 2,2
# 42	2,33E-05	1,89E-03 ± 6,49E-04	1,29E-02 ± 4,79E-02	-1,50E-03 ± 8,22E-04	99,3	73,83 ± 0,63	330,1 ± 2,6
# 43	2,64E-05	2,81E-03 ± 6,45E-04	-7,26E-02 ± 4,23E-02	-2,02E-04 ± 7,51E-04	98,9	75,58 ± 0,52	337,3 ± 2,1
# 44	2,53E-05	1,89E-03 ± 6,33E-04	-3,25E-03 ± 4,14E-02	-5,92E-04 ± 6,71E-04	99,3	74,97 ± 0,64	334,8 ± 2,6
Total	9,12E-04	2,17E-03 ± 1,15E-04	-8,64E-03 ± 8,31E-03	-4,00E-04 ± 1,44E-04	99,2	75,09 ± 0,10	335,3 ± 3,3
Weighted Mean Age (integrated over steps marked in blue)			*MSWD/(N-1) = 4,60*				**334,8 ± 0,3**

Table S.II.20: ^{40}Ar/^{39}Ar CO$_2$-laser step-heating analytical data of **phengite** populations from the **micaschist sample MJ62G**

Step #	^{39}Ar$_K$ (V)	^{36}Ar$_{atm}$/^{39}Ar$_K$ (± 1σ)	^{37}Ar$_{Ca}$/^{39}Ar$_K$ (± 1σ)	^{38}Ar$_{Cl}$/^{39}Ar$_K$ (± 1σ)	% ^{40}Ar*	^{40}Ar*/^{39}Ar$_K$ (± 1σ)	Age (Ma) (± 1σ)
MJ62-G	**J = .2734E-02 ± .2930E-04**						
# 1	4,08E-07	8,83E-01 ± 1,39E-01	-5,06E+00 ± 2,82E+00	-4,63E-03 ± 5,57E-02	12,7	37,79 ± 20,83	177,4 ± 93
# 2	3,99E-07	1,03E-01 ± 6,51E-02	-1,40E+00 ± 3,03E+00	-2,38E-02 ± 5,07E-02	60,3	45,94 ± 21,08	213,4 ± 92
# 3	4,28E-07	1,08E-02 ± 5,90E-02	1,10E+00 ± 2,61E+00	-1,69E-02 ± 4,43E-02	95,9	74,59 ± 20,89	334,8 ± 86
# 4	1,45E-06	1,81E-02 ± 1,88E-02	-2,95E-01 ± 8,13E-01	-3,36E-03 ± 1,52E-02	94,1	85,23 ± 6,99	377,9 ± 28
# 5	2,77E-06	3,61E-02 ± 9,43E-03	-1,62E-01 ± 4,21E-01	8,99E-03 ± 8,12E-03	88,3	80,25 ± 3,58	357,9 ± 14
# 6	3,98E-06	1,16E-02 ± 6,46E-03	2,47E-01 ± 3,24E-01	4,19E-03 ± 5,12E-03	96,0	81,40 ± 2,49	362,5 ± 10
# 7	1,19E-05	5,43E-03 ± 2,30E-03	-8,40E-02 ± 9,03E-02	1,70E-03 ± 2,07E-03	98,0	77,31 ± 1,19	345,9 ± 4,8
# 8	4,95E-05	3,76E-04 ± 5,32E-04	-1,14E-02 ± 2,24E-02	8,92E-04 ± 6,15E-04	99,9	74,12 ± 0,51	332,9 ± 2,1
# 9	3,57E-05	7,28E-04 ± 7,07E-04	-3,52E-02 ± 3,32E-02	4,77E-04 ± 8,77E-04	99,7	74,27 ± 0,56	333,5 ± 2,3
# 10	8,53E-05	3,32E-04 ± 2,97E-04	8,20E-03 ± 1,32E-02	-6,60E-04 ± 4,43E-04	99,9	74,67 ± 0,36	335,1 ± 1,5
# 11	4,73E-05	4,73E-04 ± 5,55E-04	9,05E-03 ± 2,65E-02	-1,75E-05 ± 7,19E-04	99,8	73,25 ± 0,32	329,3 ± 1,3
# 12	3,83E-05	4,39E-04 ± 6,60E-04	-1,74E-03 ± 2,80E-02	-1,45E-03 ± 6,71E-04	99,8	72,76 ± 0,43	327,3 ± 1,8
# 13	2,47E-05	8,50E-04 ± 1,06E-03	-7,16E-04 ± 4,71E-02	-1,20E-03 ± 9,66E-04	99,7	73,16 ± 0,62	329,0 ± 2,5
# 14	4,68E-05	-8,41E-04 ± 5,56E-04	-3,44E-02 ± 2,36E-02	-3,22E-04 ± 6,12E-04	100,3	72,78 ± 0,58	327,4 ± 2,4
# 15	1,88E-05	-8,86E-04 ± 1,33E-03	3,96E-02 ± 6,45E-02	-5,19E-04 ± 1,64E-03	100,4	73,62 ± 0,75	330,8 ± 3,1
# 16	9,86E-06	1,39E-03 ± 2,55E-03	2,31E-01 ± 1,23E-01	-1,04E-03 ± 2,17E-03	99,5	73,79 ± 1,22	331,5 ± 5,0
# 17	2,20E-05	1,84E-03 ± 1,16E-03	-1,52E-02 ± 5,12E-02	-1,96E-03 ± 1,03E-03	99,3	72,21 ± 0,64	325,0 ± 2,7
# 18	1,83E-05	-1,04E-03 ± 1,34E-03	1,42E-02 ± 6,49E-02	1,29E-03 ± 1,34E-03	100,4	80,11 ± 0,85	357,3 ± 3,4
# 19	3,44E-05	4,95E-04 ± 7,50E-04	5,83E-03 ± 3,20E-02	-6,56E-04 ± 8,06E-04	99,8	72,36 ± 0,55	325,7 ± 2,2
# 20	3,19E-05	5,58E-04 ± 8,17E-04	4,31E-02 ± 3,91E-02	-7,45E-04 ± 9,66E-04	99,8	72,47 ± 0,60	326,1 ± 2,5
# 21	1,56E-05	-2,99E-04 ± 1,59E-03	-1,85E-02 ± 7,47E-02	-3,40E-04 ± 1,50E-03	100,1	73,07 ± 1,02	328,6 ± 4,2
# 22	2,29E-05	1,56E-03 ± 1,09E-03	-6,69E-03 ± 4,79E-02	-6,62E-04 ± 9,80E-04	99,4	72,61 ± 0,76	326,7 ± 3,1
# 23	3,47E-05	3,39E-04 ± 7,28E-04	2,55E-03 ± 3,13E-02	-3,46E-04 ± 8,56E-04	99,9	72,39 ± 0,58	325,8 ± 2,4
# 24	1,28E-05	-8,19E-04 ± 2,07E-03	4,21E-02 ± 9,39E-02	-2,17E-03 ± 1,94E-03	100,3	74,76 ± 1,06	335,5 ± 4,3
# 25	1,50E-05	-1,44E-03 ± 1,66E-03	1,83E-02 ± 7,33E-02	5,48E-04 ± 1,52E-03	100,6	72,32 ± 0,84	325,5 ± 3,5
# 26	1,10E-05	-8,22E-04 ± 2,35E-03	7,63E-02 ± 1,12E-01	4,39E-04 ± 2,64E-03	100,3	73,33 ± 1,16	329,6 ± 4,7
# 27	1,78E-05	2,53E-04 ± 1,50E-03	-1,27E-02 ± 6,36E-02	-2,31E-03 ± 1,45E-03	99,9	71,66 ± 0,72	322,8 ± 3,0
# 28	8,91E-06	-2,33E-03 ± 2,81E-03	7,54E-02 ± 1,26E-01	1,49E-03 ± 2,25E-03	100,9	76,41 ± 1,21	342,3 ± 4,9
# 29	1,36E-05	-7,59E-04 ± 1,87E-03	5,20E-02 ± 8,53E-02	-1,08E-04 ± 1,90E-03	100,3	74,04 ± 0,86	332,6 ± 3,5
# 30	7,94E-06	-4,37E-03 ± 3,23E-03	3,74E-02 ± 1,46E-01	-4,77E-03 ± 2,52E-03	101,7	77,81 ± 1,45	348,0 ± 5,9
# 31	9,38E-06	-3,55E-03 ± 2,68E-03	-1,66E-02 ± 1,34E-01	-3,45E-03 ± 2,65E-03	101,4	75,58 ± 1,29	338,9 ± 5,3
# 32	1,04E-04	5,46E-04 ± 2,50E-04	-8,34E-03 ± 1,17E-02	-1,70E-03 ± 4,66E-04	99,8	74,96 ± 0,38	336,3 ± 1,6
# 33	7,34E-07	4,78E-02 ± 3,67E-02	1,42E+00 ± 1,61E+00	6,03E-03 ± 2,88E-02	82,2	65,24 ± 13,59	296,1 ± 57
# 34	1,29E-06	-6,46E-03 ± 1,95E-02	6,66E-01 ± 9,71E-01	-1,32E-02 ± 1,54E-02	102,6	74,01 ± 7,73	332,4 ± 32
# 35	2,10E-06	3,58E-02 ± 1,22E-02	9,37E-02 ± 5,79E-01	-1,18E-02 ± 9,42E-03	87,0	71,12 ± 4,94	320,6 ± 20
Total	7,62E-04	1,12E-03 ± 2,00E-04	3,84E-03 ± 9,07E-03	-6,63E-04 ± 2,05E-04	99,6	73,90 ± 0,13	332,0 ± 3,3
Weighted Mean Age (integrated over steps marked in blue)			*MSWD/(N-1) = 0,86*				**327,6 ± 0,6**

Table S.II.21: ^{40}Ar/^{39}Ar CO_2-laser step-heating analytical data of **phengite** populations from the **paragneiss sample MJ61B**

Step #	$^{39}Ar_K$	$^{36}Ar_{atm}/^{39}Ar_K$			$^{37}Ar_{Ca}/^{39}Ar_K$			$^{38}Ar_{Cl}/^{39}Ar_K$			$\%^{40}Ar^*$	$^{40}Ar^*/^{39}Ar_K$			Age (Ma)		
	(V)	(± 1σ)			(± 1σ)			(± 1σ)				(± 1σ)			(± 1σ)		
MJ61-B (Muscovite)		**J = .2736E-02 ± .2932E-04**															
# 1	6,22E-07	1,61E-01	±	4,80E-02	2,97E-01	±	2,28E+00	-2,11E-02	±	3,28E-02	57,9	65,26	±	16,65	296,3	±	70
# 2	2,32E-06	4,27E-02	±	1,24E-02	2,00E-01	±	6,03E-01	7,69E-03	±	1,03E-02	86,1	78,38	±	4,61	350,5	±	19
# 3	1,09E-05	1,69E-02	±	2,69E-03	1,41E-01	±	1,29E-01	-4,37E-03	±	1,99E-03	93,8	75,14	±	1,10	337,2	±	4,5
# 4	1,19E-05	7,18E-03	±	2,43E-03	2,31E-02	±	1,20E-01	-1,84E-03	±	1,84E-03	97,3	77,17	±	1,09	345,5	±	4,4
# 5	3,15E-05	1,11E-02	±	1,00E-03	1,47E-02	±	4,44E-02	7,66E-04	±	1,21E-03	95,8	75,16	±	0,55	337,3	±	2,3
# 6	5,70E-05	1,57E-03	±	5,29E-04	5,76E-03	±	2,55E-02	-9,75E-04	±	5,79E-04	99,4	74,79	±	0,44	335,8	±	1,8
# 7	1,97E-05	5,86E-05	±	1,44E-03	7,40E-02	±	7,12E-02	-1,48E-03	±	1,29E-03	100,0	76,83	±	0,84	344,1	±	3,4
# 8	2,27E-05	-8,48E-04	±	1,22E-03	3,75E-02	±	6,31E-02	-5,74E-04	±	1,42E-03	100,3	74,80	±	0,60	335,8	±	2,5
# 9	1,18E-05	-9,31E-04	±	2,34E-03	1,95E-01	±	1,26E-01	-2,62E-03	±	2,00E-03	100,4	75,26	±	1,13	337,7	±	4,6
# 10	3,54E-05	9,80E-04	±	8,00E-04	-9,75E-04	±	4,28E-02	7,38E-04	±	8,23E-04	99,6	73,32	±	0,43	329,8	±	1,8
# 11	1,07E-04	2,22E-03	±	2,82E-04	-1,02E-02	±	1,35E-02	-9,15E-04	±	3,94E-04	99,1	74,52	±	0,38	334,7	±	1,6
# 12	2,05E-05	2,72E-04	±	1,35E-03	2,18E-03	±	7,37E-02	3,55E-05	±	1,23E-03	99,9	74,56	±	0,72	334,9	±	3,0
# 13	7,70E-06	-1,58E-03	±	3,71E-03	-4,26E-03	±	1,95E-01	-4,71E-04	±	3,14E-03	100,6	77,26	±	1,59	345,9	±	6,5
# 14	9,24E-06	9,42E-03	±	3,10E-03	9,57E-02	±	1,68E-01	-5,64E-03	±	2,23E-03	96,5	75,92	±	1,38	340,4	±	5,6
# 15	1,80E-05	4,09E-03	±	1,64E-03	1,68E-02	±	8,37E-02	-1,15E-03	±	1,34E-03	98,4	72,17	±	0,85	325,1	±	3,5
# 16	7,11E-06	2,94E-03	±	3,98E-03	-6,37E-02	±	2,61E-01	-1,79E-03	±	3,53E-03	98,9	76,56	±	1,93	343,0	±	7,9
# 17	2,06E-05	6,95E-04	±	1,36E-03	1,63E-02	±	9,00E-02	-2,09E-03	±	1,24E-03	99,7	76,68	±	0,97	343,5	±	4,0
# 18	1,49E-05	-1,91E-03	±	1,88E-03	2,06E-01	±	1,21E-01	-2,31E-03	±	1,63E-03	100,7	77,91	±	1,05	348,5	±	4,3
# 19	9,04E-06	-2,20E-03	±	3,04E-03	-1,45E-01	±	2,09E-01	2,22E-03	±	2,80E-03	100,8	77,26	±	1,37	345,9	±	5,6
# 20	2,58E-05	-8,69E-05	±	1,10E-03	-5,21E-02	±	6,96E-02	-2,03E-03	±	8,89E-04	100,0	74,71	±	0,64	335,5	±	2,6
# 21	3,71E-05	-3,90E-05	±	8,03E-04	-6,75E-02	±	4,81E-02	-3,08E-04	±	7,75E-04	100,0	73,06	±	0,59	328,7	±	2,4
# 22	7,47E-06	-2,10E-03	±	3,79E-03	-3,46E-01	±	2,39E-01	-2,22E-03	±	3,03E-03	100,8	79,90	±	1,59	356,6	±	6,4
# 23	4,32E-06	-9,11E-03	±	6,39E-03	-3,27E-01	±	4,19E-01	3,82E-03	±	5,01E-03	103,5	79,50	±	2,81	355,0	±	11
# 24	2,15E-06	-2,26E-02	±	1,35E-02	-1,23E-01	±	8,46E-01	1,48E-02	±	9,88E-03	108,6	84,55	±	5,47	375,4	±	22
# 25	4,98E-06	-1,95E-03	±	5,57E-03	2,69E-01	±	3,98E-01	-1,71E-03	±	4,45E-03	100,8	77,41	±	2,53	346,5	±	10
# 26	3,26E-06	-3,11E-03	±	8,52E-03	-9,63E-03	±	5,98E-01	6,01E-03	±	7,02E-03	101,2	77,97	±	3,44	348,8	±	14
# 27	7,60E-06	-1,78E-03	±	3,64E-03	7,39E-03	±	2,47E-01	-1,99E-03	±	2,87E-03	100,7	75,28	±	1,61	337,8	±	6,6
# 28	4,71E-06	3,80E-03	±	6,21E-03	-4,13E-01	±	3,92E-01	-7,06E-03	±	4,85E-03	98,5	72,45	±	2,68	326,2	±	11
# 29	1,08E-05	1,12E-03	±	2,68E-03	-1,48E-01	±	1,70E-01	-2,35E-03	±	2,38E-03	99,6	73,93	±	1,27	332,3	±	5,2
# 30	4,57E-06	-4,68E-03	±	6,07E-03	3,49E-02	±	4,21E-01	-9,24E-04	±	4,80E-03	101,9	75,70	±	2,49	339,5	±	10
Total	5,30E-04	2,19E-03	±	2,95E-04	-1,11E-03	±	1,72E-02	-9,15E-04	±	2,67E-04	99,2	75,04	±	0,17	336,8	±	3,4
Weighted Mean Age (integrated over steps marked in blue)					*MSWD/(N-1) = 2,84*										**335,7**	**±**	**0,6**

Table S.II.22: $^{40}Ar/^{39}Ar$ CO_2-laser step-heating analytical data of **biotite** populations from the **paragneiss sample MJ61B**

Step #	$^{39}Ar_K$ (V)	$^{36}Ar_{atm}/^{39}Ar_K$ (± 1σ)	$^{37}Ar_{Ca}/^{39}Ar_K$ (± 1σ)	$^{38}Ar_{Cl}/^{39}Ar_K$ (± 1σ)	$\%^{40}Ar^*$	$^{40}Ar^*/^{39}Ar_K$ (± 1σ)	Age (Ma) (± 1σ)
MJ61-B (Biotite)		**J = .2736E-02 ± .2932E-04**					
# 1	2,46E-08	-4,04E-01 ± 1,33E+00	2,85E+01 ± 8,71E+01	-2,25E-01 ± 1,06E+00	174,7	279,10 ± 574,50	1023,0 ± 1608
# 2	3,35E-07	1,38E-01 ± 9,15E-02	5,50E+00 ± 5,23E+00	-4,24E-02 ± 7,22E-02	65,1	76,29 ± 31,14	341,9 ± 127
# 3	1,76E-06	2,68E-02 ± 1,63E-02	3,94E-01 ± 1,10E+00	-1,84E-02 ± 1,48E-02	89,1	64,58 ± 5,95	293,5 ± 25
# 4	7,73E-06	2,33E-02 ± 4,01E-03	-3,02E-01 ± 2,11E-01	-3,14E-03 ± 3,48E-03	91,3	72,33 ± 1,56	325,7 ± 6,4
# 5	2,08E-05	5,79E-03 ± 1,37E-03	-7,02E-02 ± 8,94E-02	1,08E-03 ± 1,30E-03	97,6	70,31 ± 0,73	317,4 ± 3,0
# 6	3,61E-05	4,57E-03 ± 8,12E-04	2,05E-02 ± 5,33E-02	-6,36E-04 ± 1,17E-03	98,1	70,37 ± 0,58	317,6 ± 2,4
# 7	5,78E-05	2,76E-03 ± 5,16E-04	-4,01E-03 ± 2,98E-02	-6,78E-04 ± 6,57E-04	98,9	70,73 ± 0,32	319,1 ± 1,3
# 8	2,14E-05	9,41E-04 ± 1,39E-03	4,97E-02 ± 8,09E-02	1,15E-03 ± 1,50E-03	99,6	69,37 ± 0,67	313,5 ± 2,8
# 9	1,15E-05	-5,15E-04 ± 2,50E-03	7,65E-02 ± 1,69E-01	-1,88E-03 ± 2,57E-03	100,2	73,15 ± 1,21	329,1 ± 5,0
# 10	3,15E-05	5,67E-04 ± 9,06E-04	-1,95E-02 ± 5,79E-02	-1,64E-03 ± 9,97E-04	99,8	71,13 ± 0,56	320,8 ± 2,3
# 11	2,02E-05	7,60E-04 ± 1,45E-03	-3,59E-02 ± 9,46E-02	-2,00E-03 ± 1,63E-03	99,7	71,95 ± 0,92	324,1 ± 3,8
# 12	1,97E-05	1,23E-03 ± 1,46E-03	-1,06E-01 ± 9,05E-02	-7,14E-04 ± 1,79E-03	99,5	70,74 ± 0,96	319,1 ± 4,0
# 13	1,43E-05	-1,42E-03 ± 2,02E-03	-1,24E-01 ± 1,17E-01	-2,23E-03 ± 1,79E-03	100,6	68,97 ± 1,09	311,8 ± 4,5
# 14	3,93E-05	4,63E-04 ± 7,47E-04	-3,79E-03 ± 4,59E-02	1,42E-03 ± 1,04E-03	99,8	70,81 ± 0,39	319,4 ± 1,6
# 15	3,10E-05	5,06E-04 ± 9,24E-04	-1,84E-02 ± 5,81E-02	-1,91E-04 ± 1,19E-03	99,8	70,80 ± 0,55	319,4 ± 2,3
# 16	1,64E-05	4,82E-04 ± 1,78E-03	-1,90E-02 ± 1,08E-01	-2,81E-03 ± 1,73E-03	99,8	72,49 ± 0,82	326,3 ± 3,4
# 17	9,44E-06	1,72E-03 ± 3,09E-03	1,49E-02 ± 1,98E-01	-1,15E-03 ± 2,93E-03	99,3	73,42 ± 1,27	330,2 ± 5,2
# 18	1,63E-05	-9,27E-04 ± 1,75E-03	1,56E-02 ± 1,16E-01	-4,85E-04 ± 1,74E-03	100,4	72,47 ± 1,03	326,3 ± 4,2
# 19	3,54E-05	5,66E-04 ± 8,15E-04	2,36E-02 ± 4,89E-02	1,14E-03 ± 9,64E-04	99,8	70,41 ± 0,53	317,8 ± 2,2
# 20	3,43E-05	1,14E-03 ± 8,42E-04	5,49E-02 ± 5,09E-02	-1,41E-03 ± 7,98E-04	99,5	70,36 ± 0,60	317,6 ± 2,5
# 21	1,78E-05	-4,96E-04 ± 1,60E-03	-3,68E-02 ± 9,70E-02	2,39E-03 ± 1,64E-03	100,2	71,33 ± 0,90	321,6 ± 3,7
# 22	1,23E-05	-3,61E-04 ± 2,35E-03	-8,54E-02 ± 1,57E-01	3,60E-04 ± 2,24E-03	100,2	68,91 ± 1,11	311,6 ± 4,6
# 23	1,53E-05	1,65E-03 ± 1,87E-03	6,62E-02 ± 1,13E-01	-2,46E-03 ± 1,77E-03	99,3	71,95 ± 0,87	324,1 ± 3,6
# 24	1,41E-05	-1,41E-03 ± 2,07E-03	1,72E-01 ± 1,43E-01	1,42E-03 ± 1,89E-03	100,6	72,65 ± 0,97	327,0 ± 4,0
# 25	1,51E-05	1,31E-04 ± 1,95E-03	3,55E-02 ± 1,16E-01	1,95E-03 ± 1,86E-03	100,0	74,04 ± 1,07	332,7 ± 4,4
# 26	2,62E-05	7,38E-04 ± 1,11E-03	-1,66E-02 ± 6,32E-02	-2,50E-04 ± 1,32E-03	99,7	70,85 ± 0,61	319,6 ± 2,5
# 27	2,87E-05	-2,24E-04 ± 9,98E-04	-2,00E-02 ± 6,00E-02	1,06E-03 ± 1,04E-03	100,1	70,43 ± 0,71	317,8 ± 2,9
# 28	1,27E-05	9,17E-05 ± 2,30E-03	-2,95E-02 ± 1,50E-01	-2,81E-03 ± 2,00E-03	100,0	70,92 ± 1,06	319,9 ± 4,4
# 29	7,64E-06	1,20E-03 ± 3,70E-03	8,41E-02 ± 2,37E-01	6,18E-03 ± 3,55E-03	99,5	73,03 ± 1,54	328,6 ± 6,3
# 30	9,90E-06	-7,80E-04 ± 2,89E-03	3,50E-02 ± 1,74E-01	-1,08E-03 ± 2,65E-03	100,3	73,19 ± 1,27	329,3 ± 5,2
# 31	1,46E-05	-1,24E-03 ± 1,96E-03	-4,14E-02 ± 1,21E-01	1,47E-03 ± 2,33E-03	100,5	72,95 ± 1,02	328,2 ± 4,2
# 32	2,09E-05	1,79E-03 ± 1,36E-03	1,62E-02 ± 8,59E-02	6,95E-04 ± 1,43E-03	99,3	71,52 ± 0,83	322,4 ± 3,4
# 33	8,44E-06	-4,07E-05 ± 3,52E-03	-1,46E-01 ± 2,13E-01	3,90E-03 ± 3,24E-03	100,0	71,26 ± 1,36	321,3 ± 5,6
# 34	6,09E-06	-3,03E-03 ± 4,82E-03	1,35E-01 ± 3,06E-01	-1,94E-03 ± 4,27E-03	101,3	72,23 ± 1,95	325,3 ± 8,0
# 35	1,66E-05	9,53E-04 ± 1,69E-03	1,17E-01 ± 1,12E-01	-1,98E-03 ± 1,77E-03	99,6	71,26 ± 0,94	321,3 ± 3,9
# 36	1,67E-06	-1,18E-02 ± 1,76E-02	1,17E+00 ± 1,12E+00	-5,77E-03 ± 1,48E-02	105,2	70,35 ± 6,20	317,5 ± 26
Total	6,53E-04	1,33E-03 ± 2,67E-04	5,94E-03 ± 1,66E-02	-2,70E-04 ± 2,77E-04	99,5	71,12 ± 0,14	320,7 ± 3,2
Weighted Mean Age (integrated over steps marked in blue)			*MSWD/(N-1) = 1,60*				**320,2 ± 0,5**

Table S.II.23: ^{40}Ar/^{39}Ar CO_2-laser step-heating analytical data of **phengite** populations from the **orthogneiss sample MJ212**

Step #	**^{39}Ar$_K$ (V)**	**^{36}Ar$_{atm}$/^{39}Ar$_K$ (± 1σ)**			**^{37}Ar$_{Ca}$/^{39}Ar$_K$ (± 1σ)**			**^{38}Ar$_{Cl}$/^{39}Ar$_K$ (± 1σ)**			**%^{40}Ar***	**^{40}Ar*/^{39}Ar$_K$ (± 1σ)**			**Age (Ma) (± 1σ)**		
MJ212	**J = .2723E-02 ± .2917E-04**																
#1	1,44E-06	2,44E-01	±	2,02E-02	-4,11E-01	±	6,85E-01	1,81E-03	±	1,70E-02	25,0	24,03	±	6,66	114,3	±	31
#2	1,66E-06	6,02E-02	±	1,64E-02	3,86E-02	±	5,85E-01	-1,00E-04	±	1,28E-02	67,4	36,85	±	5,83	172,5	±	26
#3	2,83E-06	1,75E-02	±	9,59E-03	1,99E-01	±	3,89E-01	4,28E-03	±	7,87E-03	90,1	46,82	±	3,49	216,5	±	15
#4	1,29E-05	1,28E-02	±	2,05E-03	-1,61E-02	±	7,37E-02	-6,74E-04	±	2,17E-03	94,7	67,20	±	0,87	303,2	±	3,6
#5	1,38E-05	1,16E-02	±	1,99E-03	-7,14E-03	±	6,47E-02	-1,97E-03	±	1,95E-03	95,2	68,29	±	1,17	307,7	±	4,8
#6	2,62E-05	1,14E-02	±	1,04E-03	4,88E-02	±	3,66E-02	-3,65E-05	±	1,25E-03	95,6	72,87	±	0,54	326,6	±	2,2
#7	2,65E-05	2,85E-03	±	1,06E-03	2,22E-02	±	3,78E-02	-1,38E-03	±	1,14E-03	98,9	73,52	±	0,51	329,2	±	2,1
#8	1,25E-05	2,82E-03	±	2,13E-03	4,02E-03	±	8,52E-02	-1,97E-03	±	2,17E-03	98,9	74,74	±	1,06	334,2	±	4,3
#9	1,65E-05	3,34E-03	±	1,62E-03	-6,28E-02	±	5,94E-02	-1,58E-03	±	1,70E-03	98,7	73,00	±	0,93	327,1	±	3,8
#10	5,13E-05	7,01E-03	±	5,60E-04	2,69E-02	±	2,07E-02	-8,24E-04	±	6,17E-04	97,3	73,31	±	0,48	328,4	±	2,0
#11	2,91E-05	2,57E-03	±	9,22E-04	-2,21E-02	±	3,38E-02	-4,50E-04	±	1,06E-03	99,0	72,91	±	0,65	326,7	±	2,6
#12	5,17E-05	1,66E-03	±	5,21E-04	6,33E-03	±	1,80E-02	-1,60E-04	±	5,32E-04	99,3	74,43	±	0,41	333,0	±	1,7
#13	2,09E-05	-1,96E-04	±	1,29E-03	4,28E-02	±	5,06E-02	-3,90E-03	±	1,24E-03	100,1	72,48	±	0,63	325,0	±	2,6
#14	2,29E-05	8,29E-04	±	1,20E-03	-7,42E-02	±	4,05E-02	-1,45E-03	±	1,14E-03	99,7	73,36	±	0,87	328,6	±	3,6
#15	2,64E-05	1,36E-03	±	9,98E-04	-3,93E-02	±	3,42E-02	3,91E-04	±	1,34E-03	99,5	74,30	±	0,76	332,4	±	3,1
#16	2,17E-05	2,17E-04	±	1,23E-03	-1,37E-02	±	5,21E-02	-1,56E-03	±	1,35E-03	99,9	73,48	±	0,62	329,1	±	2,5
#17	3,83E-05	1,08E-03	±	6,92E-04	-6,48E-03	±	2,48E-02	-7,83E-04	±	9,97E-04	99,6	72,68	±	0,46	325,8	±	1,9
#18	2,39E-05	4,95E-04	±	1,13E-03	-2,13E-02	±	4,57E-02	9,49E-04	±	1,30E-03	99,8	74,74	±	0,65	334,2	±	2,7
#19	1,52E-05	-2,52E-04	±	1,74E-03	-7,86E-02	±	6,86E-02	-4,53E-03	±	1,54E-03	100,1	74,16	±	0,86	331,9	±	3,5
#20	2,83E-05	3,71E-04	±	9,41E-04	-1,18E-02	±	3,87E-02	7,22E-04	±	1,04E-03	99,9	73,73	±	0,76	330,1	±	3,1
#21	2,40E-05	1,86E-04	±	1,13E-03	-1,82E-02	±	3,93E-02	1,17E-03	±	1,35E-03	99,9	73,24	±	0,58	328,1	±	2,4
#22	1,54E-05	1,30E-03	±	1,82E-03	-5,19E-03	±	6,32E-02	-3,34E-03	±	1,75E-03	99,5	73,30	±	1,05	328,3	±	4,3
#23	1,98E-05	7,55E-04	±	1,32E-03	-1,47E-02	±	5,01E-02	3,98E-06	±	1,29E-03	99,7	78,38	±	0,74	349,0	±	3,0
#24	2,87E-05	8,09E-04	±	9,58E-04	-3,91E-02	±	3,28E-02	-1,20E-03	±	9,22E-04	99,7	72,90	±	0,51	326,7	±	2,1
#25	1,75E-05	-1,07E-04	±	1,58E-03	6,56E-03	±	6,65E-02	-1,54E-03	±	1,53E-03	100,0	73,91	±	0,84	330,8	±	3,4
#26	3,92E-05	6,98E-04	±	7,00E-04	-7,82E-03	±	2,43E-02	4,59E-04	±	7,47E-04	99,7	73,70	±	0,62	330,0	±	2,5
#27	1,94E-05	1,07E-03	±	1,38E-03	-6,12E-03	±	5,83E-02	-1,32E-03	±	1,22E-03	99,6	73,35	±	0,80	328,5	±	3,3
#28	1,08E-05	8,55E-03	±	2,62E-03	4,63E-02	±	9,82E-02	-3,02E-03	±	2,33E-03	96,7	74,63	±	1,18	333,8	±	4,8
#29	1,45E-05	-4,37E-03	±	1,84E-03	5,94E-02	±	6,82E-02	-1,75E-03	±	1,88E-03	101,8	73,41	±	0,95	328,8	±	3,9
#30	4,24E-08	-5,68E+00	±	5,01E+00	3,29E+00	±	2,37E+01	1,33E-01	±	4,96E-01	-8,3	128,00	±	247	539,6	±	898
#31	7,66E-06	7,64E-04	±	3,44E-03	6,56E-02	±	1,28E-01	4,26E-03	±	3,00E-03	99,7	73,80	±	1,64	330,4	±	6,7
#32	6,41E-06	1,69E-02	±	4,37E-03	2,94E-02	±	1,51E-01	-3,74E-03	±	3,39E-03	93,7	74,30	±	1,84	332,4	±	7,5
#33	7,35E-06	-3,19E-03	±	3,67E-03	7,62E-02	±	1,40E-01	-2,26E-03	±	3,12E-03	101,3	71,58	±	1,65	321,3	±	6,8
#34	7,48E-06	-3,17E-03	±	3,72E-03	-1,79E-02	±	1,38E-01	7,00E-03	±	3,12E-03	101,0	90,57	±	1,75	397,7	±	6,9
#35	6,16E-06	4,76E-03	±	4,41E-03	1,93E-01	±	1,69E-01	-1,33E-03	±	3,81E-03	98,2	75,25	±	2,06	336,3	±	8,4
#36	6,01E-06	-2,17E-03	±	4,51E-03	-2,18E-01	±	1,61E-01	-7,22E-03	±	3,90E-03	100,9	75,46	±	1,97	337,2	±	8,0
Total	6,74E-04	2,83E-03	±	2,41E-04	-3,70E-03	±	8,98E-03	-7,70E-04	±	2,43E-04	98,9	73,35	±	0,14	328,6	±	3,3
Weighted Mean Age (integrated over steps marked in blue)					*MSWD/(N-1) =*	*0,99*									**329,1**	**±**	**0,5**